Aggregation Phenomena in Atomic Layer Deposition

Bridging Macro and Nano

Grillo, Fabio

DOI
10.4233/uuid:97fabd08-203c-4471-9596-7ad91f7eb2c0

Publication date
2018

Document Version
Final published version

Citation (APA)
Grillo, F. (2018). *Aggregation Phenomena in Atomic Layer Deposition: Bridging Macro and Nano*. [Dissertation (TU Delft), Delft University of Technology]. https://doi.org/10.4233/uuid:97fabd08-203c-4471-9596-7ad91f7eb2c0

Aggregation Phenomena in Atomic Layer Deposition

Bridging Macro and Nano

Aggregation Phenomena in Atomic Layer Deposition

Bridging Macro and Nano

Proefschrift

ter verkrijging van de graad van doctor
aan de Technische Universiteit Delft,
op gezag van de Rector Magnificus prof. dr. ir. T. H. J. J. van der Hagen,
voorzitter van het College voor Promoties,
in het openbaar te verdedigen op
woensdag 23 mei 2018 om
10:00 uur

door

Fabio Grillo

Master of Science in Chemical Engineering,
Sapienza University of Rome, Rome, Italië,
geboren te Anzio, Italië.

Dit proefschrift is goedgekeurd door de promotoren:

Prof. dr. ir. J. R. van Ommen
Prof. dr. ir. M. T. Kreutzer

Samenstelling promotiecommissie:

Rector Magnificus,	voorzitter
Prof. dr. ir. J. R. van Ommen,	TU Delft
Prof. dr. ir. M. T. Kreutzer,	TU Delft
Onafhankelijke leden:	
Prof. dr. R. A Adomaitis,	University of Maryland
Dr. A. Delabie,	KU Leuven
Prof. dr. W.A. Groen,	TU Delft
Prof. dr. ir. W.M.M. Kessels,	TU Eindhoven
Prof. dr. E.H. Brück,	TU Delft

Keywords: Atomic layer deposition, nanoparticles, nanorods, particle size distribution, modeling, atomistic processes, fluidized bed reactors

Front & Back: While my window gently weeps, Fabio Grillo

ISBN 978-90-65624-23-9

An electronic version of this dissertation is available at
`http://repository.tudelft.nl/`.

If you are certain, you are certainly wrong
because nothing deserves certainty.

Bertrand Russell

Contents

Summary

Atomic layer deposition (ALD) is a gas-phase thin film technology that boasts atomic-level control over the amount of material being deposited. A great deal of research effort has been devoted to the exploitation of ALD precision for the synthesis of nanostructures other than thin films such as supported nanoparticles (NPs). ALD is not only precise but also scalable to high-surface-area supports such as powders, which are relevant to a wide range of applications in fields spanning catalysis, energy storage and conversion, and medicine. Yet, translating the precision of ALD of thin films to the synthesis of NPs is not straightforward. In fact, ALD is mostly understood in terms of self-limiting surface reactions leading to a layer-by-layer conformal growth. However, the formation and growth of NPs is bound to be dictated by atomistic processes other than ALD surface reactions, such as the diffusion and aggregation of atoms and NPs. Understanding the role of such non-equilibrium processes is the key to achieving atomic-level control over the morphology of ALD-grown NPs and, in particular, their particle size distribution (PSD) and shape. This thesis is aimed at expanding our atomic-scale understanding of the mechanisms behind the formation of NPs during ALD. In particular, this thesis is based on experiments and models that were devised with an eye to scalability.

The first chapter presents a review of the current understanding of ALD. The fundamentals of ALD are illustrated by means of two examples: $AlCH_3/H_2O$ ALD of Al_2O_3, which is known to result in conformal films; and $MeCpPtMe_3/O_2$ ALD of Pt, which instead often results in the formation of NPs during the early stages of growth. The thermodynamic driving forces behind the formation of either films or NPs and the kinetic processes that work in the direction of thermodynamic equilibrium are also introduced. Furthermore, this chapter presents a discussion on the effect and the choice of temperature, time, and pressure. Finally, ALD performed in fluidized bed reactors (FBRs) is introduced. FBRs are a type of reactor that enable ALD on bulk quantities of high-surface-area supports and, in particular, nanopowders. Most of the experimental work presented in this thesis regards ALD performed on nanopowders via such reactors.

The second chapter presents a mean-field population-balance model capable of describing the formation and growth of NPs during ALD by accounting for: cyclic deposition of atoms on both the substrate and the NPs; diffusion and aggregation of atoms and NPs; atom attachment to NPs; and gas-phase-mediated Ostwald ripening. This model is used to assess the effect of different growth mechanism on experimental observables such as the PSD, number density, and amount of material being deposited. The main conclusion of the analysis presented in this chapter is that the PSD offers a clue into the mechanisms of NP formation and growth.

In *the third chapter*, the population-balance model described in the second chapter is used to interpret the evolution of the PSD as function of the temperature and the number

of cycles in $MeCpPtMe_3/O_2$ ALD of Pt on gram-scale batches of graphene nanoplatelets. The model clearly shows that Ostwald ripening and layer-by-layer growth, which were previously believed to be the dominant mechanisms, play a minor role. Instead, the NP growth is best described in terms of Smoluchowski aggregation, that is, NP diffusion and coalescence. In particular, we describe the effect of the deposition temperature by allowing for a temperature dependent scaling of the NP mobility. Low temperatures translate into an NP mobility that quickly decays with the NP size, whereas high temperatures result in virtually size-independent NP mobility. Furthermore, the NPs are found to form and grow mostly during the ligand-removal step. This led us to conclude that the local pressure and temperature gradients arising from the combustion of the carbon ligands induce transient NP mobility.

In *the fourth chapter*, we leverage the atomic-scale understanding presented in the second and the third chapter to fabricate gram-scale batches of catalysts based on Pt NPs with tailored PSDs supported on graphene nanoplatelets. By using low and high deposition temperatures we fabricate Pt catalysts with narrow and broad PSDs, respectively. This allows us to study the effect of the shape of the PSD on the activity and the stability of the catalysts against propene oxidation. We find that narrow PSDs, and thus low-temperature ALD, lead to more stable and active Pt catalysts. In particular, the knowledge of the mass-based PSD after the catalytic test allows us to test a simple geometrical model for the activity of the Pt NPs. This analysis led us to conclude that integral properties such as average diameter and dispersion are poor descriptors of the catalytic activity.

In *the fifth chapter*, we explain the effect of the oxygen exposure (P_{O_2} x t) on the ligand-removal kinetics and the degree of metal aggregation in ALD of Pt on TiO_2 nanopowders. We find that the ligand-removal kinetics, and thus the amount of Pt being deposited at a given number of cycles, exhibits a sigmoidal (S-shaped) curve as a function of the oxygen exposure. We describe such a curve via a two-step kinetic model accounting for the autocatalytic nature of combustion reactions. In particular, we find that the low oxygen exposures typically used for ALD on flat substrates result in incomplete ligand-removal steps. As a result, negligible amounts of Pt are deposited after the first cycle. Also, the Pt deposited after the first cycle remains mostly atomically dispersed. On the other hand, the high oxygen exposures typically used for ALD on powders effectively remove the carbon ligands, thus enabling Pt deposition after the first cycle and the formation of NPs as large as 5-6 nm even after only 5 cycles. This reconciles the discrepancies between the literature on Pt ALD on flat substrates and that on Pt ALD on powders. Crucially, we find that high partial oxygen pressures ($\geq$ 5 mbar) mitigate metal aggregation, thus leading to narrow PSDs.

The sixth chapter is dedicated to the discovery of the formation of TiO_2 nanorods during $TiCl_4/H_2O$ ALD on graphene nanoplatelets performed at 300 °C. Our analysis shows that the nanorods form via oriented attachment. The latter is a variant of Smoluchowski aggregation where NPs not only diffuse and collide but also align and fuse along a preferential crystallographic orientation. We find that the emergence of asymmetric growth, and thus of nanorods, is a non-linear function of the exposure time of both precursors. Crucially, we find that the lattices of TiO_2 and graphene nanoplatelets are in a rotational

alignment driven by lattice matching. This is a strong indication that the aggregation process is substrate-mediated.

The seventh chapter presents a multi-scale reaction engineering model devised to understand the effect of precursor transport on ALD in FBRs on nanostructured materials such as nanopowders and nano-porous powders. The model is used to carry out a conservative analysis of the impact of mass-transfer limitations on the precursor utilization efficiency. The latter is crucial for the scale-up of the process. We find that precursor utilization efficiencies close to 100% can be obtained in a wide range of operating conditions. However, at high pressures mass-transfer limitations can result in an inhomogeneous deposition process if the supports consist of porous powders and if the ALD reactions are not carried out to completion.

The eight chapter presents a summary of the main results of this thesis, a discussion on the limitations of its approach, and an outlook for further research.

Samenvatting

Atoomlaagdepositie (ALD) is een gasfase-dunnefilmtechnologie die boogt op de controle op atomair niveau van de hoeveelheid materiaal die wordt gedeponeerd. Er is veel onderzoek verricht naar het gebruik van ALD-precisie voor de synthese van nanostructuren anders dan dunne films, zoals gedragen nanodeeltjes. ALD is niet alleen precies maar ook schaalbaar naar dragers met een groot oppervlakte, zoals poeders, die relevant zijn voor een breed scala aan toepassingen op het gebied van katalyse, energieopslag en –conversie en medicijnen. Het vertalen van de ALD-precisie van dunne films naar de synthese van nanodeeltjes is echter niet rechttoe rechtaan. ALD wordt immers vooral begrepen in termen van zelflimiterende oppervlaktereacties die leiden tot een laagsgewijze conforme groei, terwijl de vorming en groei van nanodeeltjes onvermijdelijk wordt bepaald door processen op atomaire schaal anders dan ALD-oppervlaktereacties, zoals de diffusie en aggregatie van atomen en nanodeeltjes. Het begrijpen van de rol van dergelijke niet-evenwichtsprocessen is de sleutel tot het bereiken van controle op atomair niveau over de morfologie van de via ALD gegroeide nanodeeltjes en, in het bijzonder, hun deeltjesgrootteverdeling (PSD) en vorm. Dit proefschrift is gericht op het uitbreiden van ons begrip op atomaire schaal aangaande de mechanismen achter de vorming van nanodeeltjes tijdens ALD. Dit proefschrift is met name gebaseerd op experimenten en modellen die zijn ontworpen met het oog op de opschaalbaarheid.

Het eerste hoofdstuk geeft een bespreking van de huidige inzichten omtrent ALD. De grondbeginselen van ALD worden geïllustreerd aan de hand van twee voorbeelden: $AlCH_3/H_2O$ ALD van Al_2O_3, waarvan bekend is dat het resulteert in conforme films; en $MeCpPtMe_3/O_2$ ALD van Pt, dat daarentegen vaak resulteert in de vorming van nanodeeltjes tijdens de vroege stadia van de groei. De thermodynamische drijvende krachten achter de vorming van ofwel films ofwel nanodeeltjes en het kinetische proces dat werkt in de richting van het thermodynamisch evenwicht worden ook geïntroduceerd. Daarnaast presenteert dit hoofdstuk een discussie aangaande het effect en de keuze van de temperatuur, tijd en druk. Ten slotte wordt de uitvoering van ALD in reactoren met een gefluïdiseerde bed (FBR's) geïntroduceerd. Een FBR is een reactortype dat ALD mogelijk maakt op grote hoeveelheden dragers met een groot oppervlakte en, in het bijzonder, op nanopoeders. Het merendeel van het experimentele werk dat gepresenteerd wordt in dit proefschrift heeft betrekking op ALD op nanopoeders via dergelijke reactoren.

Het tweede hoofdstuk presenteert een gemiddeld-veld-populatiebalansmodel dat de vorming en groei van nanodeeltjes tijdens ALD kan beschrijven door rekening te houden met: cyclische depositie van atomen op zowel het substraat als de nanodeeltjes, diffusie en aggregatie van atomen en nanodeeltjes, aanhechting van atomen aan nanodeeltjes en gasfase-gemedieerde Ostwaldrijping. Dit model wordt gebruikt om het effect te bepalen van verschillende groeimechanismen op experimentele observabelen, zoals de PSD, de aantaldichtheid en de hoeveelheid gedeponeerd materiaal. De belangrijkste conclusie van de analyse die in dit hoofdstuk wordt gepresenteerd, is dat de PSD een aanwijzing biedt voor

de groei- en vormingsmechanismen van nanodeeltjes.

In *het derde hoofdstuk* wordt het populatiebalansmodel dat in het tweede hoofdstuk is beschreven, gebruikt om de evolutie van de PSD te interpreteren als functie van de temperatuur en het aantal cycli in $MeCpPtMe_2/O_3$ ALD van Pt op gramschaalladingen van grafeen nanoplaatjes. Het model laat duidelijk zien dat Ostwaldrijping en laagsgewijze groei, waarvan men voorheen dacht dat het de dominante mechanismen waren, een ondergeschikte rol spelen. In plaats daarvan wordt de groei van nanodeeltjes het beste beschreven in termen van Smoluchowski-aggregatie, oftewel de diffusie en samensmelting van nanodeeltjes. In het bijzonder beschrijven we het effect van de depositietemperatuur door een temperatuurafhankelijke schaling van de nanodeeltjesmobiliteit mogelijk te maken. Lage temperaturen vertalen zich in een nanodeeltjesmobiliteit die snel afneemt met de grootte van de nanodeeltjes, terwijl hoge temperaturen resulteren in een praktisch grootte-onafhankelijke nanodeeltjesmobiliteit. Bovendien bleken de nanodeeltjes voornamelijk te vormen en te groeien tijdens de ligandverwijderingsstap, waaruit we concludeerden dat de lokale druk- en temperatuurgradiënten die voortkomen uit de verbranding van de koolstofliganden, de vergankelijke nanodeeltjesmobiliteit op gang brengen.

In *het vierde hoofdstuk* gebruiken we de inzichten op atomaire schaal, die gepresenteerd zijn in het tweede en derde hoofdstuk, voor het fabriceren van ladingen op gramschaal van katalysatoren op basis van Pt nanodeeltjes met op maat gemaakte PSD's op dragers van grafeen nanoplaatjes. Door lage en hoge depositietemperaturen te gebruiken, fabriceren we Pt katalysatoren met respectievelijk smalle en brede PSD's. Dit geeft ons de mogelijkheid het effect van de vorm van de PSD op de activiteit en de stabiliteit van de katalysatoren tegen propeenoxidatie te bestuderen. We komen te weten dat smalle PSD's, en dus ALD bij lage temperatuur, leidt tot stabielere en actievere katalysatoren. Met name de kennis van de op massa gebaseerde PSD na de katalytische test stelt ons in staat een eenvoudig geometrisch model voor de activiteit van de Pt nanodeeltjes te testen. Uit deze analyse concludeerden we dat de integrale eigenschappen zoals de gemiddelde diameter en de dispersie slechte descriptoren zijn van de katalytische activiteit.

In *het vijfde hoofdstuk* verklaren we het effect van de zuurstofblootstelling (PO_2 x t) op de ligandverwijderingskinetiek en de mate van metaalaggregatie in ALD van Pt op TiO_2 nanopoeders. We komen te weten dat de ligandverwijderingskinetiek, en dus de hoeveelheid Pt die gedeponeerd wordt bij een gegeven aantal cycli, een sigmoïdale (S-vormige) kromme vertoont als functie van de zuurstofblootstelling. We beschrijven een dergelijke kromme via een tweetraps kinetisch model dat rekening houdt met de autokatalytische aard van verbrandingsreacties. In het bijzonder komen we te weten dat de lage zuurstofblootstellingen die gewoonlijk toegepast worden voor ALD op vlakke substraten, resulteert in onvolledige ligandverwijderingsstappen. Ten gevolge hiervan worden verwaarloosbare hoeveelheden Pt gedeponeerd na de eerste cyclus. Ook blijft de Pt die gedeponeerd wordt na de eerste cyclus grotendeels atomair dispers. Aan de andere kant verwijderen de hoge zuurstofblootstellingen die gewoonlijk gebruikt worden voor ALD op poeders, de koolstofliganden effectief, waardoor depositie van Pt na de eerste cyclus en de vorming van nanodeeltjes tot wel 5-6 nm na slechts 5 cycli mogelijk worden gemaakt. Dit verzoent de discrepanties in de literatuur

tussen Pt ALD op vlakke substraten en Pt ALD op poeders. Cruciaal is dat een hoge partiële zuurstofdruk (≥ 5 mbar) de metaalaggregatie vermindert en dus leidt tot een smalle PSD.

Het zesde hoofdstuk is gewijd aan de ontdekking van de vorming van TiO_2 nanostaafjes tijdens $TiCl_4/H_2O$ ALD op grafeen nanoplaatjes uitgevoerd bij 300 °C. Onze analyse laat zien dat de nanostaafjes vormen via georiënteerde aanhechting. Dit laatste is een variant op Smoluchowski-aggregatie waarbij nanodeeltjes niet alleen diffunderen en botsen maar ook uitlijnen en fuseren langs een preferentiële kristallografische oriëntatie. We komen te weten dat de opkomst van asymmetrische groei, en dus van nanostaafjes, een niet-lineaire functie is van de blootstellingstijd van beide precursors. Cruciaal is dat de TiO_2 roosters en grafeen nanoplaatjes zich in een rotatie-uitlijning bevinden die wordt aangedreven door aanpassing aan het rooster. Dit is een sterke indicatie dat het aggregatieproces substraat-gemedieerd is.

Het zevende hoofdstuk presenteert een multischaal-reactietechniekmodel dat is ontworpen om het effect van het precursortransport op ALD in FBR's op nanogestructureerde materialen zoals nanopoeders en nanoporeuze poeders te begrijpen. Het model wordt gebruikt om een behoudende analyse uit te voeren omtrent de impact van massa-overdrachtsbeperkingen op de precursorgebruiksefficiëntie. Dit laatste is cruciaal voor de opschaling van het proces. We komen te weten dat een precursorgebruiksefficiëntie nabij de 100% kan worden verkregen in een breed scala van operationele condities, maar bij hoge druk kunnen massa-overdrachtsbeperkingen resulteren in een inhomogeen depositieproces als de dragers bestaan uit poreuze nanopoeders en als de ALD-reacties niet volledig worden uitgevoerd.

In *het achtste hoofdstuk* wordt een samenvatting gegeven van de belangrijkste resultaten van dit proefschrift, een discussie aangaande de beperkingen van de aanpak en een vooruitblik op verder onderzoek.

Saint Petersburg, Russia 2016.

Preface

The writing of it was the culminating act of a long mental process,
the drawing together of scattered threads of thought
and the final generalizing upon all the data
with which his mind was burdened.

Jack London. Martin Eden (pp. 224-225)

In the nature of the use of chance operations
is the belief that all answers answer all questions

John Cage

The research behind this thesis was performed with no specific application in mind. The writing of this thesis was instead orchestrated by curiosity and mediated by a series of chance operations, including a couple of catastrophes. I hope that this thesis can give a glimpse of the sheer complexity of the processes behind the formation of nanoparticles and nanorods during atomic layer deposition.

Fabio Grillo
Delft, February 2018

Park of the national palace of Pena, Sintra, Portugal 2016.

I

Introduction

There is no more self-indulgent idea than the idea of "rigor"
and no more impervious fantasy than the fantasy of escape from fantasy.

Steven Connor

Historical breakthroughs are often marked by the advent of new materials. Consider for example the impact that the invention of materials such as bronze, steel, glass, paper, and plastic has had on the development of civilization as we know it. In like manner, the advent of nanostructured materials (NMs) promises to revolutionize several fields of science and technology. The ever-increasing capability of technology to manipulate matter at the nanoscale, the so-called 'room at the bottom', has added a new dimension to the tunability of material properties [1–4]. Structuring materials down to the nanoscale gives rise, in fact, to unique properties with far-reaching applications, which bulk materials would not otherwise exhibit [3–9]. However, for NMs to truly have an impact on most practical applications these have to become available in large quantities and at an affordable price. In other words, whether NMs will indeed effect a revolution ultimately depends on the development of synthesis routes that can reconcile atomic-level precision with production schemes that are relevant to the industrial scale [4, 8, 10–13].

This thesis is concerned with the problem of synthesizing NMs by growing adlayers on nanopowders via atomic layer deposition (ALD) performed in fluidized bed reactors (FBRs). ALD is a thin film technique and FBRs are reactors that enable the processing of bulk quantities of powders [14–18]. Because the latter are inherently scalable and ALD boasts atomic-level control over the amount of material being deposited, the combination of the two has indeed the potential for delivering the sought large-scale synthesis of NMs. Yet, ALD was originally developed for the layer-by-layer deposition of thin films and the understanding of the ALD of more complex nanostructures is still limited. The precision of ALD relies, in fact, on cyclic repetitions of self-saturating surface reactions that lead to the deposition of less than a monolayer per cycle. It follows that, if the growth proceeds in a layer-by-layer fashion, as is the case with ALD of thin films, varying the number of cycles translates into atomic-level precision over the thickness of the adlayer [14, 19]. In contrast, if the adlayer assembles into more complex structures such as nanoparticles and nanorods,

Parts of this chapter have been published in *Chemical Communications* 53, 45-71, 2017.

depositing less than a monolayer per cycle does not necessarily entail atomic-level control over the morphology. This is because the latter can be dictated by atomistic processes, other than "ALD reactions", such as surface diffusion and aggregation of atoms and nanoclusters. Understanding the interplay between ALD reactions and aggregation phenomena is therefore crucial to the development of ALD routes for the synthesis of NMs with a well-defined morphology and thus functionality.

Using FBRs to carry out ALD on bulk quantities of nanopowders adds another layer of complexity to the conventional ALD process. (I) Large quantities of nanopowders translate into large areas, and thus into large amounts of precursor molecules that are needed for depositing the desired structure. Understanding the transport of the precursor molecules within and without the FBRs is therefore crucial for steering the process towards the minimization of precursor waste, which would otherwise compromise scale-up efforts. (II) FBRs of nanopowders are characterized by a perpetual state of agitation that induces the dynamic agglomeration and fragmentation of the nanopowders into hierarchical porous structures of sizes spanning from hundreds of nanometers to hundreds of microns. This dynamic process has a direct influence on the transport of the precursors. As such, it can affect, not only the efficiency of the deposition process, but also the kinetic processes behind the formation of the desired nanostructure.

Ultimately, this work seeks to expand the understanding of the governing processes underpinning the synthesis of NMs via ALD on fluidized nanopowders. In particular, this thesis presents fundamental insights into: (I) the aggregation of adatoms into nanoparticles and nanorods, and (II) the influence of the transport of precursor molecules on the precursor utilization and on the deposition homogeneity.

In the following sections I will present a critical review of the current understanding of ALD, and in particular of ALD of nanostructures on high-surface-area substrates. The review will be critical in that I will place the emphasis on the gaps of knowledge and on those aspects that although currently unexplored might offer opportunities for the advancement of the field. Furthermore, I will elaborate on the fluidization of nanopowders and on the use of fluidized bed reactors for ALD. Finally, I will present a summary of this introductory chapter.

1.1. ALD: the Current Understanding

Towards reconciling Atomic-Level Control with Scalability

Since the early days of chemistry, liquid-phase processes have always had a predominant role in the synthesis and the discovery of new compounds. This is mostly due to the fact that wet chemistry enables complex synthesis routes by means of apparatuses that can be as simple as a few pieces of glassware. However, despite their simplicity, wet chemistry routes have several shortcomings. For instance, the low diffusion rates inherent to any liquid-phase process often translate into long processing times and poor mixing of the reacting mixture, which in turn can result in poor product homogeneity. Furthermore, when the desired product is a solid, further separation steps need to be added to the process. This not only

results in the incorporation of significant levels of impurities in the final product but also adds to the process cost and complexity, thus hampering potential scale-up efforts. Such limitations have become particularly relevant since the advent of nanotechnology. In fact, the full potential of nanostructured materials can only be harnessed by means of synthesis routes that are at once scalable and capable of controlling the properties of the product down to the nanoscale. ALD is emerging as an attractive synthesis route that has the potential to address the shortcomings of conventional chemistry routes when it comes to controllability and scalability.

An 'Historical' Perspective

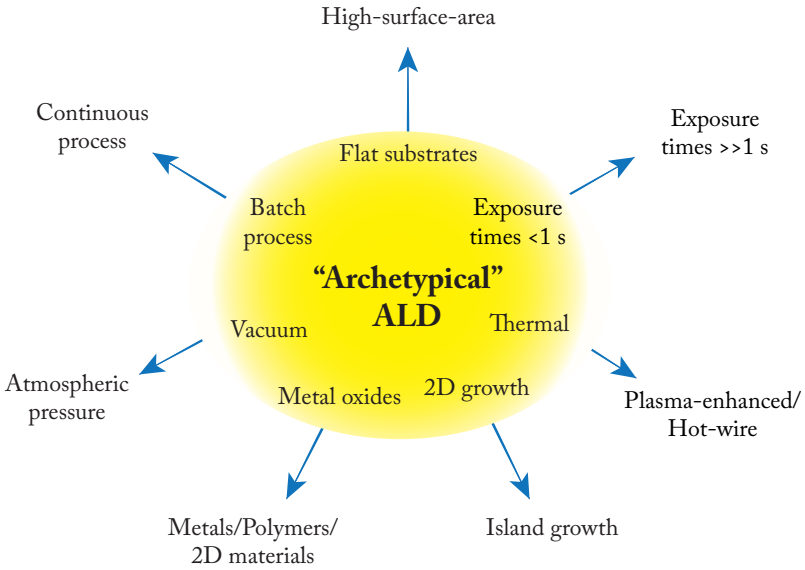

Figure 1.1: ALD archetype and deviations from it.

The first forms of ALD date back to as early as the 1960s-70s. It was previously believed that the first instance of ALD was to be found in a technology called 'atomic layer epitaxy' developed in Finland in the 1970s. However, a recent initiative called 'Virtual Project on the History of ALD' (www.vph-ald.com), has pointed out that the characteristics of ALD could already be found in a technology that was invented in the Soviet Union back in the 1960s called "molecular layering". Historically, the development of ALD has been mostly driven by its application in the semiconductor industry. As a result, the most well established ALD systems are the thermal ALD of films of ceramic oxides, such as alumina and hafnium oxide, on wafers (i.e., flat substrates). Such processes can be regarded as the "archetypes" of ALD as they have set the standard for ALD processes for many years now. Accordingly, the "archetypical ALD" is a thermal process carried out at vacuum (10^{-1}-10^{-6} mbar) for the deposition of highly conformal and pinhole-free metal oxides films, typically on wafers, where the precursor exposure times can be as short as a few milliseconds (see Figure 1.1).

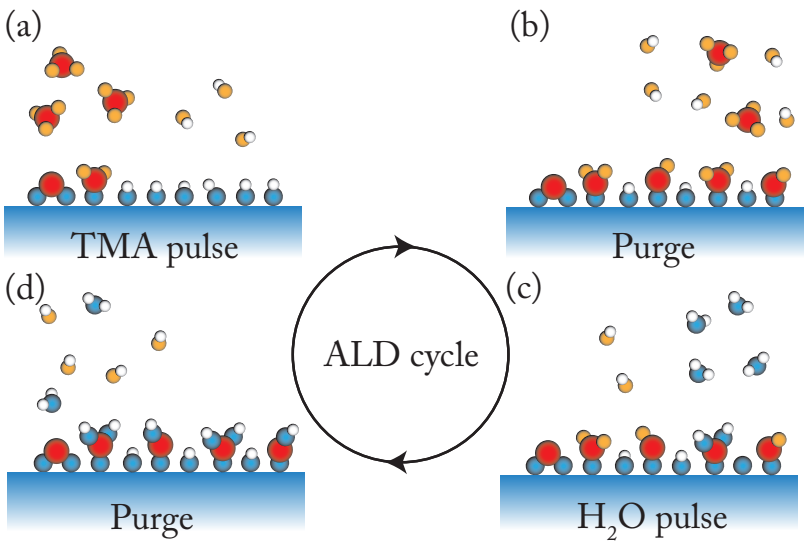

Figure 1.2: Schematic representation of the working principle of ALD of Al_2O_3 based on trimethylaluminum (TMA) and H_2O: (a) Exposure of the substrate surface to TMA and reactions between TMA and surface active sites (e.g., ⊦OH and oxygen bridges); (b) purging of excess TMA and reaction by-product (i.e., CH_4); (c) exposure of the substrate surface to H2O and reaction between H_2O and precursor ligands; (d) purging of excess H_2O and reaction by-product (i.e., CH_4); the four steps (a) to (d) compose one ALD cycle.

As ALD is finding promising applications that go beyond the fabrication of ever-shrinking electronic devices, its recent development has seen a considerable departure from its archetypical forms. In fact, as already discussed in a number of recent reviews [14, 20–27], ALD provides viable synthesis routes for the fabrication and/or functionalization of a wide range of materials whose functionality is inherently tied to nanoscale features such as NPs-based catalysts, quantum dots, dye-sensitized solar cells, hybrid materials, and nanostructured electrodes for enhanced batteries. However, such novel applications often require process conditions, surface chemistries, and reactor designs that transcend the archetypical ALD. Consequently, a new understanding of ALD has to be sought.

1.1.1. The Fundamentals

In ALD the compound which makes up the coating is synthesized directly on the substrate surface

ALD is a deposition technique that enables digital control over the amount of deposited material by relying on sequential self-limiting surface reactions. In ALD the compound to be deposited is synthesized directly on the substrate surface instead of being deposited from the vapor phase as it is the case in conventional thin film techniques such as physical vapor deposition (PVD). As such ALD can be regarded as a bottom-up synthesis route. The synthesis of the desired compound is split into two or more reacting steps, depending on the ALD chemistry of choice and the compound to be deposited, that are separated by purge steps (see Figure 1.2). Each reacting step involves self-saturating chemisorption reactions between a precursor and the substrate surface. The purge step after each reactive step is crucial to preserve the self-limiting nature of ALD reactions, since it prevents the

uncontrolled reactions that would result from the intermixing between different precursors, and between precursors and reaction by-products. By repeating these steps in a cyclic fashion one can grow the desired material with a resolution that is defined by the amount of material deposited in each cycle, the so-called 'growth per cycle' (GPC), which is typically a fraction of a monolayer [14, 19, 28]. This in principle translates into atomic-level control over the material properties. Finally, in virtue of being a surface-driven process, ALD lends itself to the deposition of conformal coatings over substrates with complex geometries such as high-aspect-ratio structures for electronic devices, powders, and porous media [14, 18, 19].

Although ALD allows the deposition of a wealth of materials on virtually every substrate, whether the surface of the substrate of choice is reactive towards a given ALD precursor depends on the specific interaction between surface and precursor chemistry at the deposition conditions (e.g., temperature and pressure). In some instances, such as ALD on graphene or hydrogen-terminated silicon, the substrate surface might lack active sites even towards reactive precursors such as trimethylaluminum [29, 30]. Nonetheless, chemisorption and thus deposition can still occur at surface defects, as these can act as preferential sites for the precursor chemisorption [30–32]. Preferential adsorption of ALD precursors on specific active sites, either already present or created by appropriate surface treatments, can be exploited for the nanopatterning of surfaces. Such process is usually referred to as area-selective ALD [31, 33–37]. Ultimately, the nature, the density and the spatial distribution of active sites play a crucial role in determining the GPC and the positioning of the as-deposited atoms, especially during the initial stages of growth, that is, the first cycles [31, 38]. In particular, first principles calculations show that the most favorable adsorption pathway itself, which is specific to each precursor/surface combination, can lead to either crystalline or disordered growth [39, 40]. Finally, if the deposition conditions allow atom mobility, the atoms comprising the ALD-grown adlayer can undergo further rearrangements in order to minimize the energy of the system. It follows that, depending on the affinity between the adlayer and the substrate, ALD can result in materials with various morphologies, including, but not limited to, films (layer-by-layer growth), which can be amorphous or crystalline, and nanoparticles (NPs) (island growth) [14, 19, 28].

The nature, the density and the spatial distribution of active sites play a crucial role in determining the GPC and the initial spatial arrangement of deposited atoms

Thermodynamic growth regimes: layer-by-layer vs island growth

Thermodynamics dictates the preferred growth mode of an adlayer. Yet, the latter can differ considerably from the actual growth mode because the growth conditions are typically far from equilibrium [41–43]. In other words, the growth mode is often kinetically determined. This is especially the case in ALD since it usually takes place at low temperatures (e.g., 100–250 °C). Nonetheless, thermodynamics still defines the driving forces of kinetic processes. Hence, elucidating the thermodynamics behind the growth of an adlayer is a necessary step in the pursuit of a complete understanding of growth dynamics.

Thermodynamics allows the prediction of the preferred growth mode

The thermodynamic stability of the heterostructure resulting from the deposition of a certain amount of material over a substrate depends on the work of adhesion and the strain energy introduced by the formation of an interface between different materials with different lattice constants and surface energies [41, 44–47]. In lattice matched systems, if the binding energy between the adlayer and the substrate is higher than the binding energy between adatoms, the adlayer will tend to grow in a layer-by-layer fashion following the

crystal structure of the substrate. This growth mode is usually referred to as layer-by-layer or Stranski–Krastanov growth [41].

Moderate strains can be accommodated by a positive work of adhesion

If there is a lattice mismatch between the adlayer and substrate, coherent growth results in a strained adlyaer. For a moderate lattice mismatch, the increase in strain energy can be compensated by the decrease in the Gibbs free energy due to a positive work of adhesion, that is $W_{sc} = \gamma_s + \gamma_a - \gamma_{int} > 0$, where γ_s, γ_a, γ_{int} are the surface energy density of the substrate, the adlayer, and of the interface, respectively. In this case, the strained adlyaer can still grow in a layer-by-layer fashion [41, 45–47]. In a flat configuration the specific strain energy accumulated in the adlayer, assuming the substrate to be unstrained, is proportional to the thickness of the adlayer h and the square of the lattice mismatch f:

$$E_s = \alpha f^2 h \tag{1.1}$$

where α is a constant which depends upon the elastic moduli of the adlayer material. On the other hand, the decrease in the adlayer specific energy due to the work of adhesion scales as the inverse of the adlayer thickness:

$$E_a = -W_{sc}/h \tag{1.2}$$

Therefore there exists a critical thickness h_c after which further increase in strain energy will not be compensated by the work of adhesion:

$$E_s + E_a = 0 \longrightarrow h_c = \frac{\sqrt{W_{sc}/\alpha}}{f} \tag{1.3}$$

In lattice mismatched systems the formation of islands might be favored as they relax strain energy

This phenomenon is referred to as the Asaro-Tiller-Grinfeld instability [48]. Once the critical thickness has been reached, further growth will see the relaxation of the strain energy either by the formation of defects such as dislocations, or by lateral relaxation via formation of either coherent or incoherent islands on the already deposited layer, usually referred to as wetting layer. Such growth mode is referred to as layer-plus-island or Stranski-Krastanov growth [41, 45]. The efficiency with which the islands relax the strain energy depends on their shape and surface density. Consequently, the geometry and the density of the islands are bound to change as more material is deposited and more strain energy has to be relaxed. In addition, as the island geometry and density affect the strain field in the islands they also affects the strain field on the wetting layer. The strain field on the wetting layer, in turn, interacts with the islands giving rise to an additional energy term due to the elastic interaction between islands [41, 45, 47, 49, 50]. The coupling between islands due to elastic interaction might lead to their self-assembly [45, 46]. For this reason, the Stranski-Krastonow growth has been receiving growing interest as it can be exploited for fabrication of quantum dots with properties that, in principle, can be tuned by varying the growth conditions.

A third possible thermodynamic growth regime, which is particularly relevant to ALD of nanoparticles, is the island or Volmer-Weber growth [41, 45]. Island growth can take place when $\gamma_s < \gamma_{int} + \gamma_c$. It must be noted that so far we have considered γ_{int} and γ_c not to be a function of the amount of deposited material, nonetheless these can vary with the adlayer thickness. In virtue of this, in some cases, after a certain thickness a layer-by-layer growth can

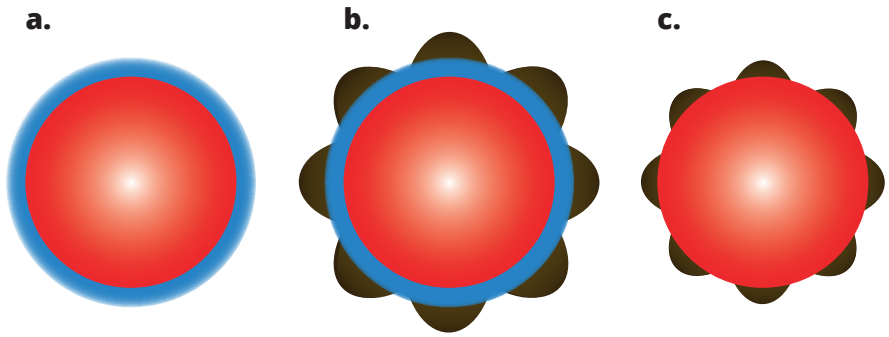

Figure 1.3: Schematic representation of possible thermodynamic growth modes on NPs: a. layer-by-layer, b. layer-plus-island and c. island growth.

turn in island growth because the condition $\gamma_s > \gamma_{int} + \gamma_c$ does not apply anymore due to a change in either γ_{int} or γ_c or both. Moreover, from the previous analysis of layer-plus-island growth, is also clear that for highly mismatched systems the critical thickness h_c approaches zero and island growth can become the preferred growth mode already after a small fraction of a monolayer. It must be noted that thermodynamic treatment given here, despite capturing the essence of the problem, is still a simplified picture. A more complete thermodynamic picture for the growth on flat substrates is given by Daruka and Barási [44, 47]. In their pioneering work[47], the authors depict the growth regimes described here, together with a number of intermediate regimes, into a phase diagram in function of the lattice mismatch and amount of deposited material.

High lattice mismatches and/or a negative work of adhesion lead to island growth

The simplified thermodynamic picture given in the previous section highlights how the preferred growth mode is the result of the competition between bulk effects (e.g. strain energy) and surface effects (e.g. work of adhesion). This is true for the growth of thin films on flat substrates as well as on substrates with more complex topographies such as nanopowders. A number of thermodynamic models capable of predicting the preferred growth mode on flat substrates, which take into account the effect of strain, surface, and island-island interaction energy, are already available [45–47, 51, 52]. Some work on the thermodynamics of growth on nanowires has also been done [45]. Nevertheless, to the best of my knowledge, a comprehensive thermodynamic model for the prediction of the preferred growth mode on nanoparticles is still not available. The same growth regimes identified for the growth on flat substrates (layer-by-layer, layer-plus-island and island growth) are expected for the growth on nanopowders (see Fig. 1.3). Only in this case a thermodynamic description is complicated by geometry and size effects. For example, when the size of a system approaches the nanoscale, thermodynamic properties such as surface energies can still be defined, but these will differ from their bulk counterparts as a function of the size and the geometry [45, 53]. Also, if the nanoparticle is faceted, each facet will contribute differently on the work of adhesion, due to the different surface energy of each facet [32, 54, 55]. A common assumption in thermodynamic models for flat substrates is to consider the substrate to be unstrained with a lattice constant equal to its bulk value. Nevertheless, due to the finite size and curvature of the nanoparticles, the also the substrate is expected to be strained due to the presence of an

Curvature and size affect the preferred growth mode on NPs

adlayer, and its lattice constant will differ from the its bulk counterpart [56, 57]. In addition, for spherical nanoparticles with diameter $d < 50$ nm, the curvature $(1/R)$ will result in a not negligible stress σ_{rr} due to the surface tension τ_s according to the Young-Laplace equation:

$$\sigma_{rr} = 2\tau_s / R \tag{1.4}$$

Small nanoparticles are inheritably strained due to surface tension

That is to say that even an uncoated nanoparticle with $d < 50$ nm will be inheritably strained [58–61]. Anisotropy in the nanoparticle and the adlayer crystal structure will also inheritably affect the strain field and thus the strain energy of the whole structure [56, 57]. Finally, the geometry has a direct effect on the relative contribution of bulk and surface effects as a function of the adlayer thickness, since the volume of the coated nanoparticle scales as its thickness to the third power and the surface of the interface stays constant [45, 62].

A deposition technique based on surface chemistry: ALD of alumina

To illustrate the working principles of ALD I will use two examples, namely ALD of alumina, which typically results in layer-by-layer growth, and ALD of platinum, which depending on the substrate often results in island growth. In the first example, I will therefore highlight the role of surface chemistry, whereas in the second I will emphasize the interplay between surface chemistry, thermodynamics and diffusional processes.

ALD of alumina can be performed by splitting the gas phase reaction between trimethylaluminum (TMA) and water:

$$2\,Al(CH_3)_3(g) \;+\; 3\,H_2O(g) \longrightarrow Al_2O_3(s) \;+\; 6\,CH_4(g)$$

into the two sets of gas-solid reactions, referred to as half-reactions, given in Table 7.1. In the

TMA half-reaction
$a\ Al(CH_3)_3(g) + b\ \underset{\perp}{S} \longrightarrow a\ \underset{\perp}{Al(CH_3)_x} + a(3\text{-}x)\ CH_4(g)$
H_2O half-reaction
$a\ \underset{\perp}{Al(CH_3)_x} + \frac{3}{2}a\ H_2O \longrightarrow \frac{a}{2}\ Al_2O_3(s) + b\ \underset{\perp}{S} + ax\ CH_4(g)$

Table 1.1: Half-reactions in ALD of Al_2O_3

TMA half-reaction, TMA is fed in gaseous form to the reaction chamber, wherein it reacts with the active sites (⊢S) on the substrate surface till the surface reactions reach saturation due to either lack of actives sites or steric hinderance between adsorbed species (⊢$Al(CH_3)_x$) (see Figure 1.2). In this case, the surface sites (⊢S) that are active towards to the chemisorption of TMA can be either surface hydroxyl groups (⊢OH) or oxygen bridges (-O-). Depending on the degree of the hydroxylation of the surface and the operating conditions, the surface reactions will take different paths, which result in different surface states and thus different concentrations of adsorbed species at saturation. For instance, the more hydroxylated the surface the more pronounced the removal of methyl groups upon chemisorption of TMA ($x \rightarrow 0$), the less the steric hinderance between adsorbed species (⊢$Al(CH_3)_x$), the higher the amount of Al deposited per cycle (assuming the number of active sites not to be limiting with respect to saturation) [14, 19, 28, 63–67]. Once the surface is saturated with adsorbed

The purge step is crucial to preserve the self-limiting nature of ALD surface chemistry

species, the unreacted precursor molecules and reaction by-products are evacuated from the reaction chamber via either a vacuum system or the flow of an inert gas.

During the second half-reaction water molecules react with the residual surface methyl groups releasing methane and resulting in a fraction of a monolayer of aluminum oxide and a certain degree of surface hydroxylation. The surface state after each half-reaction, depends on the starting surface and the operating conditions. If the latter are kept constant, after a certain number of cycles, referred to as "nucleation period", the surface state will evolve within a cyclic steady-state (i.e., a limit cycle). During the nucleation period the gas-solid reactions gradually shift the surface chemistry from the one of the initial substrate to the one of the ALD-grown material. As a result, the GPC will vary in the first cycles according to the cycle-to-cycle evolution of the ALD surface chemistry, before settling down to a steady-state value after the "nucleation period" [14, 66, 68].

The steady-state operation can be depicted as a limit-cycle solution in the phase portrait of the surface coverage

Thermodynamics vs Kinetics: ALD of Platinum

So far this treatment has emphasized the kinetic aspects of the growth related to the ALD surface chemistry. However, the picture is usually more complex and the growth dynamics is not only determined by the ALD surface chemistry but also by the interplay between thermodynamic driving forces and diffusional processes. This is the case for ALD of noble metals on oxides, where the interaction between thermodynamics and kinetics is particularly pronounced. One of the most well-established ALD process for depositing platinum is the

$MeCpPtMe_3$ half-reaction
$a\ MeCpPtMe_3(g) + b\ O^* \longrightarrow a\ Pt(C_xH_y) + c\ C_zH_w + d\ CH_4(g) + e\ CO_2(g) + f\ H_2O(g)$
O_2 half-reaction
$a\ Pt(C_xH_y) + c\ C_zH_w + b\ O_2 \longrightarrow a\ Pt + b\ O^* + l\ CO_2(g) + m\ H_2O(g)$

Table 1.2: Half-reactions in Pt ALD

$MeCpPt(IV)Me_3/O_2$ process. As in the TMA/H_2O system, the synthesis of platinum is split in two half-reactions (see Table 7.2), but in this case the surface chemistry at play is somewhat more complex. In the first half-reaction, the precursor $MeCpPtMe_3$ decomposes on the substrate surface by reacting with adsorbed molecular oxygen ($\vdash O^*$) through a series of combustion and dehydrogenation reactions, with methane, carbon dioxide and water being the main reaction products. The decomposition of the precursor upon adsorption results in platinum atoms and a carbonaceous layer adsorbed on the surface [69–71]. The saturation in this case is reached when all the active oxygen adsorbed on the surface has been depleted. Thus, the amount of platinum that can be deposited per cycle strongly depends on the activity and surface coverage of the chemisorbed molecular oxygen present on the substrate surface before the $MeCpPtMe_3$ exposure.In fact, the highest GPCs for Pt ALD are reported for depositions on surfaces that are particularly active towards molecular oxygen adsorption and dissociation such as $SrTiO_3(001)$ and Pt(111) [69, 72]. The chemistry at play during the oxygen half-reaction is not too far from the one taking place during well established catalyst regeneration processes such as the removal of coke from the FCC catalyst via combustion. The oxygen exposure is in fact meant to remove the carbonaceous layer and replenish the surface of chemisorbed molecular oxygen. Again, given the importance of the

The same ALD chemistry leads to different GPCs on different surfaces and in particular on different crystal facets

latter for the subsequent chemisorption of $MeCpPtMe_3$, the operating conditions during the oxygen exposure such as temperature, oxygen partial pressure and exposure time, have all an important effect on the GPC [69, 73]. That being said about the surface chemistry of the $MeCpPtMe_3/O_2$ ALD system, I will now discuss how surface chemistry, thermodynamics, and diffusional processes act in concert in determining the nucleation and growth dynamics of ALD-grown Pt films and ALD-grown adlayers in general.

Temperature and co-reactant pressure and exposure time all affect the GPC

Experimental evidence shows that even after one cycle of Pt ALD on oxides the submonolayer of Pt is arranged in nanoclusters or 3D islands of sizes on the order of 1 nm [69, 73–76]. This suggest that, as the platinum adatoms form on the substrate surface these have sufficient mobility to form into islands, even at ALD temperatures (e.g. 200-300 °C). The tendency of Pt adatoms to form into clusters on oxide surfaces is usually ascribed to the fact that the binding energy between platinum atoms is much higher than the binding energy between platinum and oxide atoms [42, 43, 45, 77]. In a simplified picture this can be translated in terms of surface energies. In analogy with liquid-solid systems, by using Young's equation [78]:

Pt adatoms are mobile even at ALD temperatures

$$\gamma_s = \gamma_{int} + \gamma_c \cos\vartheta \tag{1.5}$$

where ϑ is the contact angle between the NP and the substrate, respectively. The coating material will then "wet" the substrate surface if the following condition applies:

Pt and other noble metals have the tendency to agglomerate on oxides to minimize the energy of the system

$$\gamma_s \geq \gamma_{int} + \gamma_c \tag{1.6}$$

That is to say that the contact angle will be zero if the surface energy of the substrate is higher than the sum of the surface energy of the coating material and the interfacial energy. Given that platinum, as other noble metals, has a much higher surface energy density than oxides, this condition is unlikely to apply to Pt ALD on oxides [79]. Hence, this simple thermodynamic argument suggests that, during ALD growth, platinum adatoms will have the tendency to agglomerate into islands to minimize the surface-to-volume ratio and thus the energy of the system. Yet, the extent to which platinum adlayers do agglomerate into islands, or in other words the number and the size of the islands, depends on kinetics rather thermodynamics [42, 43, 77].

The number and the size of the islands depend on kinetics rather thermodynamics

Mackus et al. [73] have shown that the oxygen partial pressure and exposure time have a dramatic effect on the cluster size distribution of platinum islands deposited on alumina at 300 °C. In particular, they observed that higher oxygen partial pressures and longer exposures times resulted in large clusters or nanoparticles. In the catalysis literature the coarsening of Pt nanoparticles induced in the presence of oxygen is typically ascribed to Ostwald ripening [80]. The latter is the growth of larger clusters at the expenses of smaller ones due inter-cluster exchange of atoms driven by the Gibbs-Thompson effect: clusters of different sizes have different chemical potentials μ_c depending on their radius of curvature R: [81]:

$$\mu_c = \mu_0 + 2\gamma_c V_a / R \tag{1.7}$$

where μ_0 is the chemical potential of an infinite sized cluster and V_a is the atomic volume. Ostwald ripening has been widely studied given its impact on cluster stability in supported metal catalysts [81–83]. There are three possible pathways for the inter-cluster exchange of

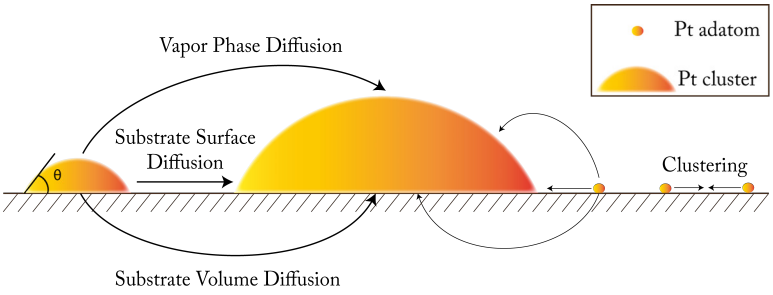

Figure 1.4: Schematic representation of the possible atom transport mechanisms between partially wetting platinum nanoclusters and adatoms on a substrate surface.

atomic species and adatoms transport: surface diffusion, diffusion through the vapor phase and diffusion through the substrate [82] (see Fig. 3.3). The third path inhabits time scales much larger than the first two mechanisms and thus it will not be further discussed. Surface diffusion is an activated process that involves the migration of an adatom from a surface site to the another by surmounting a certain migration energy. The latter is a function of the specific interaction between adatom and surface site. For this reason, surface diffusion strongly depends on the surface properties. The same adatom can behave differently on different facets of the same material. In particular, surface diffusion is an anisotropic process on anisotropic surfaces. Surface diffusion might be also affected by the concentration of adatoms on the surface due to adatom-adatom interactions [42, 43, 81–83]. The diffusion through the vapor phase is a mechanism of particular relevance to noble metals clusters in oxidizing environments [73, 81–83]. The energy required to transfer a metal to the vapor phase in vacuum or in a reducing environment, referred to as sublimation energy, is relatively high. Nevertheless, platinum and other noble metals have a relatively volatile metal oxide and the energy required to transfer a metal atom in the form of a metal oxide is much lower than the sublimation energy. In virtue of this, during the oxygen exposure in Pt ALD, platinum atoms can be transported between clusters through the gas phase in the form of platinum oxide according to the reversible oxidation reaction:

Surface diffusion is a function of the crystal facet

Diffusion through the vapor phase might be relevant to ALD of noble metals

$$Pt(s) + x/2\ O_2(g) \rightleftharpoons PtO_x(g)$$

Although gas-phase-mediated ripening is in principle relevant to ALD of noble metals based on oxidation chemistry, in the work of Mackus et al. [73] is not clear whether the the oxygen exposure affected the cluster size distribution due to enhanced inter-cluster transport or simply because higher oxygen partial pressures and longer exposure times led to a higher degree of removal of organic ligands and thus to more platinum deposited in each cycle, which would in turn result in larger clusters. Moreover, Pt clusters have a catalytic effect on the adsorption and dissociation of molecular oxygen that vary with the cluster size. In sum, in ALD of noble metals on oxides, surface chemistry, thermodynamic driving forces and kinetic processes are all intimately correlated.

It is not clear whether Ostwald ripening is a governing process in ALD of noble metals

Other kinetic processes relevant to ALD of noble metals and of nanoparticles in general are: cluster diffusion (as a whole) and coalescence, transition between 2D clusters to 3D

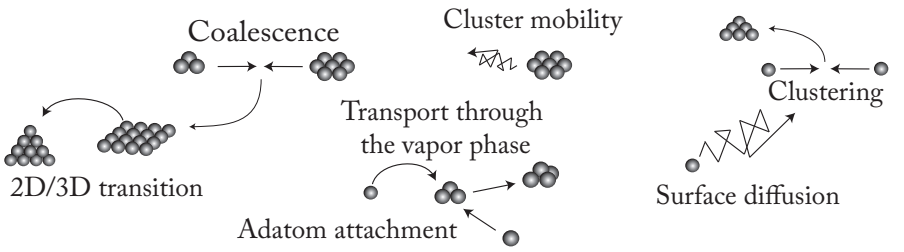

Figure 1.5: Schematic representation of atomistic processes relevant to ALD of noble metals and to ALD processes exhibiting island growth in general.

clusters, and nucleation-inhibited growth of clusters due to cluster faceting (see Figure 1.5). A theoretical framework for the treatment of the thermodynamic driving forces and diffusional processes described above is already available [41–45, 77, 81–91]. The description of such processes is particularly relevant to ALD of noble metals but also to the study of ALD dynamics in general. Nevertheless, to the best of my knowledge nobody has yet attempted to couple such understanding with a suitable description of the surface chemistry and sequential dynamic nature of ALD to derive simple models capable of describing the nucleation and growth of ALD films. Such models would help elucidating how GPC, diffusional processes, material properties, and operating conditions all concur in the determination of the morphology of ALD-grown adlayers, and thus provide invaluable insights for the further development and application of ALD technology.

1.1.2. On the Effect of Temperature, Pressure, and Time

ALD processing conditions and reactor designs can vary considerably depending on the nature of the substrate and the material to be deposited. However, the design rationale of an ALD process is typically dictated by the need for minimizing operating times, thus maximizing throughput, while retaining a self-limiting deposition. ALD surface reactions are active, that is fast enough, and self-limiting only within a certain region or "window" in the parameter space of temperature, time and pressure. Identifying such a region is therefore the first step towards the design of every ALD process. Historically, the "ALD window" was described solely in terms of temperature range, probably due to the fact that most deposition experiments were carried out at fixed exposures (pressure x time) [14]. Recently it has become clear that to fully understand the self-limiting nature of ALD growth one has to include time and pressure in the picture. In fact, ALD surface chemistry has often been depicted in terms of sequential chemisorption reactions, while reality is more complex. At every stage of the ALD process, several reactions take place simultaneously and at different rates, including those which are not self-terminating. It follows that whether the growth is dominated by ALD reactions (e.g., precursor chemisorption) or by undesired reactions (e.g., precursor decomposition and desorption, and etching reactions) depends on the relative magnitude of the reaction rates and on the timescale of the experiment, or in other words on kinetics [92, 93].

ALD surface reactions are active and self-limiting only within a certain region or "window"

The ALD window is a function of temperature, time, and pressure

Since reactions rates are finite functions of the temperature and the partial pressure of

reactants, one can in principle tune temperature, pressure, and time so as to selectively suppress undesired reactions and "activate" the desired ALD reactions. Furthermore, if the substrate is heterogeneous, reaction rates on different part of the substrate will inherently have different temperature and pressure dependence. Such principle has been recently exploited to achieve area-selective ALD [73]. Hence, in ALD the choice of the process conditions is strongly tied to surface chemistry considerations. However, it must be noted that ultimately self-limiting deposition can only be achieved by solving two mass transfer problems, namely, the delivering of gaseous precursors to the substrate surface and the complete removal of reaction by-products and unreacted precursors after each reacting step. In the following paragraphs, I will illustrate in greater detail how temperature, time, and pressure can be chosen on account of their effect on surface chemistry and mass transfer. Emphasis will be placed on those effects that, despite being partially unexplored, could open up new avenues for the development of novel ALD processes.

The process conditions are bounded by surface chemistry and mass transfer considerations

Temperature

The strong reliance of ALD on surface reactions, and thus activated processes, makes the temperature one of the most important parameters in every ALD process. As already mentioned, ALD has often been described in terms of the temperature range (ALD window) within which ALD reactions are both active and self-limiting. As such the ALD window is dictated by both the intrinsic properties of the precursors and the unique precursor-substrate chemistry. With regard to the latter, ALD growth can proceed only if the chemisorption reactions are fast and irreversible in relation to the time scale of the ALD experiment. For this reason, the ALD window is bounded at one end by low precursor reactivity at low temperatures, and at the other by the onset of desorption reactions at high temperatures.

The precursor itself can disrupt the self-limiting behaviour, thus further narrowing the ALD region, both at low temperatures due to uncontrolled condensation and at high temperatures due to thermal decomposition (CVD-like reactions). Most ALD chemistries are based on sequential exposures of CVD precursors at low temperatures. However, this transposition is not always possible as the precursor chemisorption might not be fast enough at temperatures below the decomposition temperature. For this reason, the advent of ALD has spurred the development of dedicated ALD precursors that can outperform CVD precursors in terms of volatility, reactivity, and thermal stability [14, 19, 28, 94].

Within the ALD window, the GPC can vary with the temperature. For example, this can be due to the fact that the temperature can change the nature and the number of active sites. In the trimethylaluminum/water process the GPC is known to be a decreasing function of the temperature [14, 63]. Such dependency has been ascribed to the temperature-dependent desorption of hydroxyl groups, which are considered the main active site for the chemisorption of trimethylaluminum [63]. Another reason behind the temperature dependence of the GPC is the fact that, in each precursor exposure, several surface reactions take place at the same time and the dominant reactions, and thus the number and the nature of surface species that remain adsorbed in the timescale of the ALD experiment, can in principle vary with the temperature [14, 65, 92, 93]. Nevertheless, such variations are usually of the order of a fraction of a sub-monolayer, therefore when compared with CVD or wet-chemistry synthesis routes, ALD is virtually insensitive to the deposition temperature (within the

The GPC at saturation is a function of temperature

ALD window).

In sum, the range within which the deposition temperature can be chosen is set by the ALD chemistry of choice. Once the range is defined, the optimal temperature depends on the nature of the substrate, the desired morphology, and energy consumption considerations. In most cases, it is desirable to choose the deposition temperature as close as possible to the lower end of the ALD window. ALD surface reactions lead to the deposition of atoms that are not arranged in the most thermodynamically stable form and the degree to which they approach it largely depends on the deposition temperature. For this reason, the lowest deposition temperature is chosen when the thermal budget has to be minimized in order to avoid interdiffusion between the ALD-grown material and the substrate [19]. Furthermore, as a rule, low deposition temperatures usually translate into amorphous films, whereas high deposition temperatures promote the formation of crystalline films [28]. Therefore, depending on the final application, one can tune the deposition temperature so as to obtain either an amorphous or a crystalline film. If conformality is the main concern, low deposition temperatures are again desirable, as ALD-grown amorphous films tend to have the better conformality and lower roughness than crystalline films [28, 54, 95]. Moreover, when the affinity between substrate and ALD-grown material is such that island growth is the preferred growth regime: the surface density, the size, and the shape of the deposited islands or nanoclusters strongly depend on the temperature. Hence, if ALD is to be used for the deposition of size-selected NPs, the lowest temperature should be chosen in order to minimize NPs sintering and thus the undesired broadening of their size distribution. Finally, low deposition temperatures are also preferred when the substrate is heat-sensitive and/or energy consumption is a major concern [19].

the surface density, the size, and the shape of the ALD-grown NPs strongly depend on the temperature

Pressure

The choice of the operating pressure in ALD processes is usually based on considerations on mass transfer and process scale-up rather than on surface chemistry. However, the pressure represents another handle for steering the surface chemistry towards the desired reaction path, which is up to now hardly exploited. For the sake of clarity, it is worth to emphasize the distinction between the absolute operating pressure and the partial pressure of precursors. At any given time, the absolute pressure in an ALD reactor is given by the sum of the partial pressures of the precursors, the reaction by-products, and the carrier gas, if present. ALD surface chemistry is mostly dependent on the partial pressure of precursors as it rests on adsorption reactions. However, in some instances, the partial pressure of the reaction by-products and the carrier gas can be expected to also affect the growth. For example, both reaction by-products and carrier gas molecules could mediate the precursor adsorption by competitive physisorption. Even though in most instances the carrier gas is not expected to participate directly in adsorption reactions, as it is usually an inert gas, it can still affect ALD growth by mediating the surface diffusion of adsorbed species via weak gas-solid interactions [96]. In principle, high inert gas pressures can also thermodynamically stabilize adsorbates that would otherwise desorb at lower pressures. Furthermore, by-products formed upon adsorption can lead to subsequent etching reactions that can effectively change the nature and the density of surface active sites during both the reacting and the purge steps. This is especially the case for halogen-based precursors. That being said, the effect of pressure on ALD surface chemistry remains largely unexplored. This is mostly

the pressure represents another handle for steering the surface chemistry towards the desired reaction path

the effect of pressure on ALD surface chemistry remains largely unexplored

due to the fact that studying the effect of the pressure on the concentration of adsorbed species is extremely challenging as they both vary continuously during an ALD cycle. Several studies report the effect of the partial pressure of precursors on the GPC at a given exposure time [14, 97]. However, it must be noted that the reported partial pressure is hardly the one experienced by the surface of the substrate. In fact, since most ALD chemistries enjoy fast kinetics and precursors are usually not supplied in great excess, the precursor partial pressure inside the reaction chamber rapidly drops upon exposure, as the ALD surface reactions deplete precursor molecules. Even when the precursor is supplied in excess, the typically fast ALD surface reactions are likely to deplete the precursor molecules at a higher rate than diffusion would allow, thus resulting in a gradient in the partial pressure between the substrate surface and the bulk of the gas [97, 98]. As a result, most of the reported changes in GPC with the partial pressure have usually little to do with the actual ALD surface chemistry. Instead, they are mostly an empirical measure of the amount of precursor that has to be introduced in the reaction chamber to obtain saturation at a given exposure time and for a given reactor design [98, 99]. In recent years, this gap of knowledge has seen several researchers devoting considerable effort in the deconvolution of reactor dynamics and surface chemistry via both mathematical modelling and in-situ measurements [98–104].

reported precursor partial pressures are hardly the ones experienced by the surface

Since most ALD reactions reach saturation on time scales of the order of milliseconds over wide ranges of precursor partial pressure, the lack of a detailed understanding of the ALD surface chemistry has not hampered the development and application of most ALD processes. On the other hand, the role of pressure is still particularly relevant to ALD processes that are based on inherently slow kinetics. For example, ALD of catalytic metals often relies on the combustion of organic ligands via exposure to an oxidizer [14, 19, 28]. The rate of combustion of adsorbed carbonaceous material is known from heterogeneous catalysis to be strongly dependent on the partial pressure of the oxidizer and the nature of the underlying substrate. Mackus et al. [73] recently achieved selective growth on alumina-supported platinum NPs by exploiting the fact that, below a certain oxygen partial pressure, combustion reactions are active on pre-existing Pt NPs and effectively suppressed on bare alumina, on the timescale of their ALD experiments. Finally, pressure is expected to have an important role in all the ALD processes that result in the deposition of NPs, as the latter form and grow via surface diffusion, which in turn is known to be strongly affected by the nature and the partial pressure of the chemical species present in the reactive environment.

the role of pressure is still particularly relevant to ALD processes that are based on inherently slow kinetics

Most conventional ALD reactors operate at vacuum (<1 mbar). Low operating pressures are typically preferred as they facilitate the purge step and help mitigating the incorporation of impurities[19]. However, since the cost and the complexity of vacuum equipment represent an obstacle to the scale-up of the process, great effort has been devoted to the development of atmospheric pressure ALD [19, 75, 97, 103]. Operating at atmospheric pressure, not only simplifies the reactor equipment, but also widens the range of precursor partial pressures that can be employed. This is especially relevant for ALD on high-surface-area substrates, which typically require large amounts of precursor for reaching surface saturation. In fact, given that the amount of precursor delivered to the reactor is proportional to the product of the precursor partial pressure and the exposure time, it follows that high precursor partial pressures are desirable if throughput is to be maximized.

Operating at atmospheric pressure widens the range of precursor partial pressures that can be employed

Time

Despite the inherent dynamic nature of ALD, the current understanding of self-limiting deposition is mostly framed in thermodynamics rather than kinetics [105]. In the classic picture of ALD, the surface species formed upon precursor chemisorption must be thermodynamically stable for the surface chemistry to be self-limiting [14, 19, 28]. However, as recently pointed out by Pedersen [106], even when the adsorbed monolayer is not thermally stable, one could in principle adjust the exposure and purge times to kinetically prevent the onset of desorption and CVD reactions. In fact, as long as the adsorbed monolayer is stable until the next precursor pulse, the deposition can still be self-limiting. From this perspective, it is clear how the ALD window should also be defined in the parameter space of time. Furthermore, recent studies have shown that time not only is crucial for the definition of self-limiting deposition, but can also have pronounced effects on the GPC. In fact, the precursor chemisorption, which is usually characterized by fast kinetics, can be followed by a series of subsequent slow reactions such as ligand removal and surface diffusion. Travis et al. [105] have shown that ligand removal reactions, normally attributed to a specific precursor pulse can also take place during the purge step and the subsequent exposure to another precursor. Several ALD chemistries terminate due to the steric hindrance brought about by the precursor ligands that remain on the surface upon chemisorption. Since slow surface reactions following chemisorption can result in further ligands removal, thus mitigating steric hindrance, proper adjustment of the precursor pulse length might result in higher GPCs. For example, Muneshwar et al. [107] have shown that dividing a single precursor pulse in a series of short pulses, while keeping the dose constant, can effectively increase the GPC due to the lower steric hindrance experienced by the precursor at the beginning of each short pulse. In virtue of this, one could also envision that distributing the same precursor dose over long exposure times might also result in higher GPCs. However, the gain in GPC might not compensate for the loss in throughput due to long cycle times.

There are certain ALD processes that inherently require long exposure times, namely ALD on high-aspect-ratio structures and ALD on high-surface-area substrates such as powders and porous media [14, 19]. High-aspect-ratio structures generally require longer exposure times as they bring about diffusion limitations. For example, the Al_2O_3 process, whose surface chemistry is known to reach saturation on time scales of the order of milliseconds, when applied to anodic aluminium oxide films that present pores 50 μm deep and 65 nm wide requires reactant exposures up to one minute to obtain a conformal coating [19]. While exposure times of the order of one minute can already be considered exotic for a conventional ALD process (i.e., ALD on flat substrates), the exposure times required for saturation in ALD on high-surface-area substrate are completely off the scale, as they are in the range of several minutes to few hours depending on the reactor design, the precursor partial pressure, and the amount of material to be coated [14, 18, 75, 104, 108]. Therefore, for such processes one can expect slow CVD-like reactions or surface diffusion, which have little to no effect in conventional ALD, to play a major role in ALD on high-surface-area substrates. However, despite its relevance, little research has been devoted to the understanding of ALD at time scales relevant to ALD on high-surface-area substrates.

Surface diffusion is expected to play a major role in ALD on high-surface-area substrates

1.2. Fluidization of Nanopowders

Fluidization is a process in which a bed of solid particles is suspended in a fluidlike state by an upward-flowing gas or liquid. When a fluid flows through a fixed bed of particles, this tends to expand due to the drag force between the particles and the fluid. As the superficial velocity of the gas reaches a critical value, referred to as the minimum fluidization velocity, the drag force equates the weight of the particles and the the bed of particles is said to be in a state of incipient fluidization. If the superficial velocity is further increased, the fluidized bed can exhibit different behaviours according to the property of the fluid and of the particles.

Liquid-solid systems are usually characterized by homogeneous or smooth fluidization, that is a progressive increase in the superficial velocity translates into a progressive expansion of the bed with no appreciable heterogeneities or voids of liquid. On the other hand, gas-solid systems can give rise to more complex behaviours arising from flow instabilities that manifest themselves in the form of gas voids or "bubbles" and of preferential channels through which the gas bypasses the bed. The fluidization regime in this case is referred to as heterogeneous fluidization or bubbling fluidization [15]. With regard to gas fluidization, solid particles were classified by Geldart [109] according to their fluidization behaviour into four groups:

- Group A: aeratable or materials having a small mean particle size and/or low particle density $\varrho_s < 1.4\ \mathrm{g/cm^3}$. These particles show high bed expansion, smooth fluidization at low gas flow rates and bubbling fluidization at higher flow rates but with small bubbles.
- Group B: sand-like or most particles of size $40\ \mu\mathrm{m} < d_p < 500\ \mu\mathrm{m}$ and density $1.4 < \varrho_s < 4\ \mathrm{g/cm^3}$. These particles show bubbling fluidization upon the onset of fluidization with bubbles growing larger with the height of the bed.
- Group C: cohesive or very fine powders $d_p < 30\ \mu\mathrm{m}$. These particles cannot be easily fluidized because of the interparticle forces such as van der Waals, electrostatic and capillary forces that are stronger than those resulting from the gas.
- Group D: spoutable or large and/or dense particles. These particles are not easy to be fluidized due to large bubbles and channeling of gas.

Gas fluidization of Geldart A and Geldart B has already been successfully employed in several industrial fields, such as, coal gasification, petroleum refining, metallurgy, chemical synthesis, drying and coating technology [15]. According to the Geldart classification, nanoparticles fall into group C, and thus one would expect their proper fluidization to be prevented by interparticle forces, which, given the size of the primary particles, are several orders of magnitude greater than the gravitational force and the drag force exerted by the gas flow. Nevertheless, there is ample experimental evidence that nanopowders can be indeed fluidized. In fact, nanoparticles are not fluidized individually, instead, they fluidize in the form of micron-sized highly porous agglomerates due to the aforementioned interparticle forces. Therefore, their fluidization behaviour is determined by the average agglomerate properties rather than by the properties of the primary particles [110–113].

NPs are not fluidized individually but rather in the form of μm-sized porous fractal-agglomerates

Nanoparticles agglomerates spontaneously form during fluidization and a dynamic equilibrium between breaking and cohesive forces determines their average properties. They undergo what has been described as a multi-stage aggregation process that results in hierarchical fractal structures [111, 113–116]. In fact, primary particles are arranged in very open chain-like structures of 200-300 nm in size (see Figure 1.6 and Figure 1.7), referred to as primary agglomerates, formed by either agglomeration due to interparticle forces (e.g., capillary and London-van der Waals forces) or sintering caused by the manufacturing process itself.

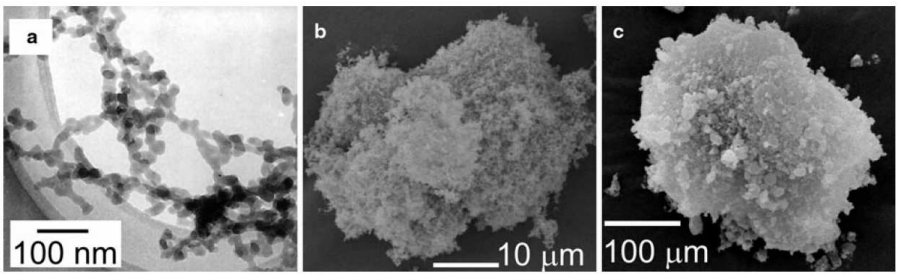

Figure 1.6: Illustration of the multistage agglomerate structure obtained by *ex-situ* analysis; a) TEM image of a network of silica NPs, b) SEM image of a simple agglomerate or sub-agglomerate built up from these networks, c) SEM image of a complex agglomerate consisting of several sub-agglomerates. (adapted from Yao et al. 2002 [111])

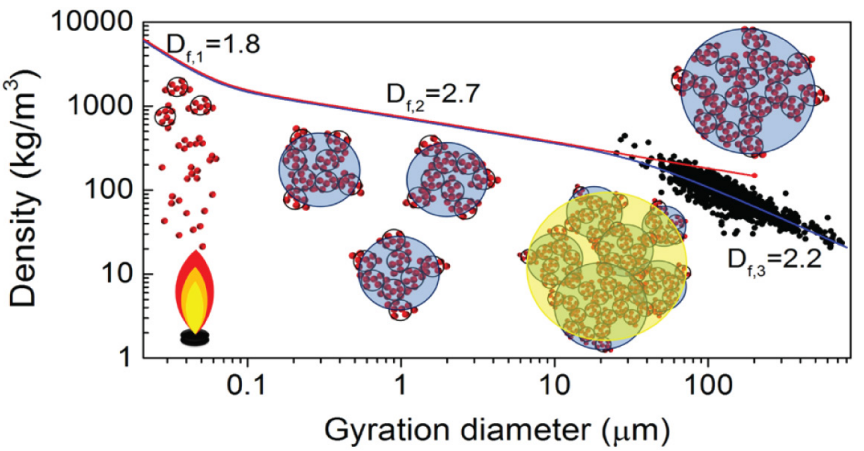

Figure 1.7: Conceptual variation of the agglomerate density as a function of size for fluidized P-25 TiO_2 nanoparticles. $D_{f,1}$, $D_{f,2}$, and $D_{f,3}$ are the fractal dimensions of the primary, simple, and complex agglomerates, respectively (adapted from De Martín et al. 2014 [114]).

Primary agglomerates, in turn, coalesce into bigger and more compact spherical or ellipsoidal agglomerates with typical sizes of 1-100 μm, called simple agglomerates. Finally, the latter further agglomerate into open structures of sizes ranging from 100-800 μm called complex

agglomerates [111–113, 117]. Finally, although the existence of a dynamic equilibrium between agglomeration and fragmentation is believed to be behind the size distribution of complex agglomerates, a fundamental understanding of the subject is still not available. In particular, it is not clear what is the breakage mechanism, and what is the effect of the structure of the simple agglomerates, of the interparticle forces, and of the gas velocity on the shape of the size distribution of the complex agglomerates. Understanding and controlling the latter is key to optimize not only the fluidization process but also the transport of precursor molecules within the agglomerates and thus the deposition process.

A fundamental understanding of the of the physics behind the size distribution of complex agglomerates is not available

Since nanoparticles are fluidized in the form of agglomerates, their fluidization is often referred to as agglomerate fluidization. The latter is furthermore distinguished into two categories: agglomerate bubbling fluidization (ABF) and agglomerate particulate fluidization (APF), according to the fluidization quality given by the agglomerates properties. ABF is characterized by vigorous bubbling at incipient fluidization and very low and almost constant expansion for superficial velocity above the minimum fluidization velocity, whereas APF is characterized by smooth fluidization and high bed expansion [111].

The fluidization quality of ABF systems can be drastically improved through assisting methods, such as, vibration, sound waves, micro-jets and stirring. The underlying idea of these methods is to introduce energy into the system so as to overcome inter-particle forces and thereby break down large agglomerates, which impair the fluidization quality, and/or break channels and bubbles of gas. Among other things, the assisting methods can decrease the minimum fluidization velocity so as to operate at lower superficial velocity, reducing the elutriation of nanoparticles [113, 116].

For example, figure 1.8 shows the normalized pressure drop along a bed of titania nanoparticles as a function of the superficial velocity, with and without vibration. Clearly, the fluidization and defluidization cycle exhibits hysteresis in both cases. The minimum fluidization at atmospheric pressure has been estimated to be 5 cm/s without vibration and 2.8 cm/s with a vertical vibration of 45 Hz. The use of other frequencies resulted in higher fluidization velocities. In the experiment without vibration, the pressure drop data shows an oscillating behaviour for superficial velocities lower than the minimum fluidization velocities. This is consistent with the formation of unstable channels of gas arising from the cohesive forces between the particles. In contrast, the vertical vibration aids the break-up of such channels and the pressure drop smoothly increases with the superficial velocity until the whole bed is fluidized.

1.2.1. ALD on Nanopowders in Fluidized Bed Reactors

The sequential steps of ALD can be performed in FBRs by properly modulating the composition of the fluidizing gas [17, 118]. Despite the tendency of NPs to agglomerate during fluidization, several experimental studies have proven that the coating of individual NPs via ALD in FBRs is indeed possible [16, 19, 118]. Such technology boasts the potential for attaining production schemes relevant to the industrial scale, thanks to the inherent scalability of FBRs, while retaining the capability of ALD to tune surfaces at the nanoscale [13, 17–19, 104, 113, 119]. In a foreseeable future, such potential could boost the application of NPs

ALD in FBRs enables nanotuning in an industrial scale

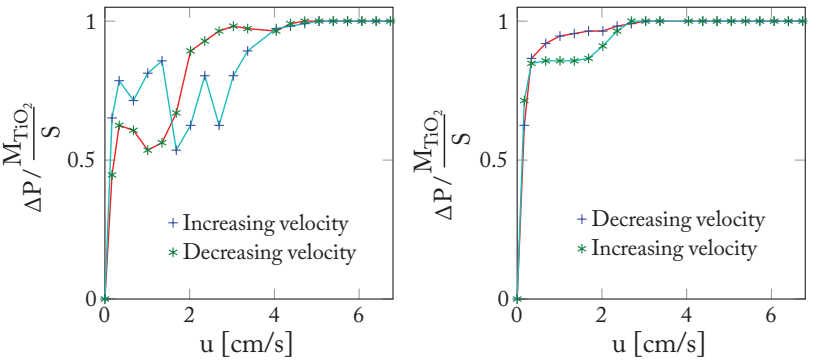

Figure 1.8: Normalized pressure drop along the bed without vibration (left) and with vibration (45 Hz) (right) vs the superficial gas velocity.

in fields such as the production of improved catalysts and enhanced materials for fuel cells and batteries [13, 16, 70, 74, 75, 118–120].

In ALD on NPs in FBRs, fluidization, NPs agglomeration and coating process are all interrelated

Given the high-surface area of nanopowders and the cost of ALD precursors, one of the main challenges in the scale-up of such process is to understand the governing processes behind the precursor utilization efficiency [17, 18, 104]. Another challenge is posed by the interaction between the nanopowder agglomeration and the deposition process. In fact, the latter affects the former as the nanopowder agglomeration process depends on surface properties which are continuously changed during ALD. Yet, the way fluidization and nanopowders agglomeration process affects the ALD dynamics and thus the morphology of the coating is still unclear. In particular, the time scales of ALD half-reactions in FBRs on NPs, given their high surface area, is orders of magnitude larger than in ALD on flat substrates. The effect of the half-reaction time scale on the final morphology of the coating is far from being understood. Finally, optimizing the operating conditions, especially the operating pressure which affects both fluidization and ALD dynamics is a challenge in itself. In particular, the fluidization process requires a viscous flow of gas to suspend the NPs and thus the use of vacuum ($P << 1$ mbar) to purge the system in between precursor exposures is not an option. A flow of inert gas is used instead. Therefore, assessing the effect of operating pressure, purging times and thus reactor scale on the feasibility of carrying out self-limiting ALD reactions in FBRs is crucial for its implementation in an industrial scale.

1.3. Summary

- In ALD, adlayers are synthesized on substrates via a series of surface reactions.

- The as-deposited position and the spatial arrangement of adatoms depend on the surface chemistry at play during the ALD half-reactions. In particular, the density of surface species after each half-reaction is a function of the density and the nature of the surface active sites.

- The atoms deposited as a result of ALD reactions might migrate from their as-deposited position via a number of diffusional processes in the direction of thermodynamic equilibrium.
- The surface density, the size, and the shape of ALD-grown nanostructures such as nanoparticles strongly depend on temperature, time, and pressure. In particular, the effect of precursor exposure time is still poorly understood, especially with regard to ALD on high-surface-area substrates.
- A fundamental understanding of the role of atomistic processes such as surface diffusion and aggregation of atoms and nanoclusters in ALD is still lacking. In particular, it is not clear whether Ostwald ripening is indeed relevant to ALD of Pt NPs and of noble metals in general.
- Nanoparticles are not fluidized individually. Instead, upon fluidization, they agglomerate into micron-sized fractal structures. As a result, the fluidization behaviour depends on the properties of such agglomerates (i.e., size and density) rather then on those of the individual particles. The fluidization dynamics as well as the structure of the nanoparticle agglomerates affect the transport of precursor molecules and thus the precursor utilization efficiency. Yet, a full account of the impact of the precursor transport on the efficiency of ALD carried out in FBRs is still not available.

References

[1] R. P. Feynman, *The pleasure of finding things out*, edited by J. Robbins (Perseus Books, Cambridge, MA, 2000).

[2] C. P. Poole and F. Owens, *Introduction to nanotechnology* (John Wiley & Sons, Inc., New York, NY, USA, 2003) pp. xii, 388 p.

[3] Q. Z. Qian, A. Boxman, and U. Chowdhry, *Nanotechnology in the chemical industry - Opportunities and challenges,* Journal of Nanoparticle Research 5, 567 (2003).

[4] B. Roldan Cuenya and F. Behafarid, *Nanocatalysis: Size- and shape-dependent chemisorption and catalytic reactivity,* Surface Science Reports 70, 135 (2015).

[5] F. Sanchez and K. Sobolev, *Nanotechnology in concrete - A review,* Construction and Building Materials 24, 2060 (2010).

[6] H. N. Cheng, K. T. Klasson, T. Asakura, and Q. Wu, *Nanotechnology in agriculture,* in *ACS Symposium Series*, Vol. 1224 (2016) pp. 233–242.

[7] D. Yohan and B. D. Chithrani, *Applications of nanoparticles in nanomedicine,* Journal of Biomedical Nanotechnology 10, 2371 (2014).

[8] B. R. Cuenya, *Synthesis and catalytic properties of metal nanoparticles: Size, shape, support, composition, and oxidation state effects,* Thin Solid Films 518, 3127 (2010).

[9] C. Santhosh, V. Velmurugan, G. Jacob, S. K. Jeong, A. N. Grace, and A. Bhatnagar, *Role of nanomaterials in water treatment applications: A review,* Chemical Engineering Journal 306, 1116 (2016).

[10] M. A. Watzky, E. E. Finney, and R. G. Finke, *Transition-metal nanocluster size vs formation time and the catalytically effective nucleus number: A mechanism-based treatment,* Journal of the American Chemical Society 130, 11959 (2008).

[11] J. E. Mondloch, E. Bayram, and R. G. Finke, *A review of the kinetics and mechanisms of formation of supported-nanoparticle heterogeneous catalysts,* Journal of Molecular Catalysis A: Chemical 355, 1 (2012).

[12] S. S. I. Baker C.C. Pradhan A., *Encyclopedia of nanoscience and nanotechnology* (CRC Press, Boca Raton, 2004) pp. 449–473.

[13] A. Goulas and J. van Ommen, *Scalable production of nanostructured particles using atomic layer deposition,* KONA Powder and Particle Journal 31, 234 (2014).

[14] R. L. Puurunen, *Surface chemistry of atomic layer deposition: A case study for the trimethylaluminum/water process,* Journal of Applied Physics 97 (2005).

[15] D. Kunii and O. Levenspiel, *Fluidization Engineering* (Butterworth-Heinemann, 1991).

[16] D. M. King, X. Liang, and A. W. Weimer, *Functionalization of fine particles using atomic and molecular layer deposition,* Powder Technology 221 (2012).

[17] D. M. King, J. A. Spencer II, X. Liang, L. F. Hakim, and A. W. Weimer, *Atomic layer deposition on particles using a fluidized bed reactor with in situ mass spectrometry,* Surface and Coatings Technology 201, 9163 (2007).

[18] D. Longrie, D. Deduytsche, and C. Detavernier, *Reactor concepts for atomic layer deposition on agitated particles: A review,* Journal of Vacuum Science & Technology A 32 (2014).

[19] S. M. George, *Atomic Layer Deposition: An Overview,* Chemical Reviews 110 (2010).

[20] B. J. O'Neill, D. H. K. Jackson, J. Lee, C. Canlas, P. C. Stair, C. L. Marshall, J. W. Elam, T. F. Kuech, J. A. Dumesic, and G. W. Huber, *Catalyst Design with Atomic Layer Deposition,* ACS Catalysis 5, 1804 (2015).

[21] J. Lu, J. W. Elam, and P. C. Stair, *Atomic layer deposition - Sequential self-limiting surface reactions for advanced catalyst "bottom-up" synthesis,* (2016).

[22] H. Kim, H. B. R. Lee, and W. J. Maeng, *Applications of atomic layer deposition to nanofabrication and emerging nanodevices,* (2009).

[23] R. W. Johnson, A. Hultqvist, and S. F. Bent, *A brief review of atomic layer deposition: From fundamentals to applications,* Materials Today 17, 236 (2014).

[24] S. M. George, *Atomic layer deposition: An overview,* Chemical Reviews 110, 111 (2010).

[25] M. Knez, K. Nielsch, and L. Niinistö, *Synthesis and Surface Engineering of Complex Nanostructures by Atomic Layer Deposition,* Advanced Materials 19, 3425 (2007).

[26] L. Wen, M. Zhou, C. Wang, Y. Mi, and Y. Lei, *Nanoengineering Energy Conversion and Storage Devices via Atomic Layer Deposition,* Advanced Energy Materials 6 (2016).

[27] C. Detavernier, J. Dendooven, S. Pulinthanathu Sree, K. F. Ludwig, and J. A. Martens, *Tailoring nanoporous materials by atomic layer deposition,* Chemical Society Reviews 40, 5242 (2011).

[28] V. Miikkulainen, M. Leskelä, M. Ritala, and R. L. Puurunen, *Crystallinity of inorganic films grown by atomic layer deposition: Overview and general trends,* Journal of Applied Physics 113, 021301 (2013).

[29] R. L. Puurunen, W. Vandervorst, W. F. A. Besling, O. Richard, H. Bender, T. Conard, C. Zhao, A. Delabie, M. Caymax, S. De Gendt, M. Heyns, M. M. Viitanen, M. de Ridder, H. H. Brongersma, Y. Tamminga, T. Dao, T. de Win, M. Verheijen, M. Kaiser, and M. Tuominen, *Island growth in the atomic layer deposition of zirconium oxide and aluminum oxide on hydrogen-terminated silicon: Growth mode modeling and transmission electron microscopy,* Journal of Applied Physics 96 (2004).

[30] K. Kwanpyo, H.-B.-R. Lee, R. W. Johnson, J. T. Tanskanen, N. Liu, M.-G. Kim, C. Pang, C. Ahn, S. F. Bent, and Z. Bao, *Selective metal deposition at graphene line defects by atomic layer deposition,* Nature Communications 5 (2014).

[31] N. Pinna and M. Knez, *Atomic Layer Deposition of Nanostructured Materials* (Wiley, 2011) pp. 193–225.

[32] H.-B.-R. Lee and S. F. Bent, *Microstructure-Dependent Nucleation in Atomic Layer Deposition of Pt on TiO2,* Chemistry of Materials 24, 279 (2012).

[33] W. Dong, K. Zhang, Y. Zhang, T. Wei, Y. Sun, X. Chen, and N. Dai, *Application of three-dimensionally area-selective atomic layer deposition for selectively coating the vertical surfaces of standing nanopillars,* Scientific Reports 4 (2014).

[34] H.-B.-R. Lee, M. N. Mullings, X. Jiang, B. M. Clemens, and S. F. Bent, *Nucleation-Controlled Growth of Nanoparticles by Atomic Layer Deposition,* Chemistry of Materials 24, 4051 (2012).

[35] E. Färm, S. Lindroos, M. Ritala, and M. Leskelä, *Microcontact Printed RuOx Film as an Activation Layer for Selective-Area Atomic Layer Deposition of Ruthenium,* Chemistry of Materials 24, 275 (2012).

[36] H.-B.-R. Lee, S. H. Baeck, T. F. Jaramillo, and S. F. Bent, *Growth of Pt Nanowires by Atomic Layer Deposition on Highly Ordered Pyrolytic Graphite,* Nano Letters 13, 457 (2013).

[37] A. Mackus, J. Mulders, M. van de Sanden, and W. Kessels, *Local deposition of high-purity Pt nanostructures by combining electron beam induced deposition and atomic layer deposition,* Journal of Applied Physics 107, 116102 (2010).

[38] R. Puurunen, *Random Deposition as a Growth Mode in Atomic Layer Deposition,* Chemical Vapor Deposition 10 (2004).

[39] B. Han, Q. Zhang, J. Wu, B. Han, E. J. Karwacki, A. Derecskei, M. Xiao, X. Lei, M. L. O'Neill, and H. Cheng, *On the Mechanisms of SiO2 Thin-Film Growth by the Full Atomic Layer Deposition Process Using Bis(t-butylamino)silane on the Hydroxylated SiO2(001) Surface,* The Journal of Physical Chemistry C 116, 947 (2012).

[40] L. Huang, B. Han, B. Han, A. Derecskei-Kovacs, M. Xiao, X. Lei, M. L. O'Neill, R. M. Pearlstein, H. Chandra, and H. Cheng, *Density functional theory study on the full ALD process of silicon nitride thin film deposition via BDEAS or BTBAS and NH3,* Phys. Chem. Chem. Phys. 16, 18501 (2014).

[41] J. A. Venables, G. D. T. Spiller, and M. Hanbucken, *Nucleation and growth of thin films,* Reports on Progress in Physics 47, 399 (1984).

[42] H. Brune, *Microscopic view of epitaxial metal growth: nucleation and aggregation,* Surface Science Reports 31, 121 (1998).

[43] C. T. Campbell, *Ultrathin metal films and particles on oxide surfaces: structural, electronic and chemisorptive properties,* Surface Science Reports 27, 1 (1997).

[44] K. W. Kolasinski, ed., *Surface Science: Foundations of Catalysis and Nanoscience*, third edition ed. (John Wiley & Sons, Ltd, 2012).

[45] X. Li, C. Wang, and G. Yang, *Thermodynamic theory of growth of nanostructures,* Progress in Materials Science 64, 121 (2014).

[46] A.-L. Barabási, *Thermodynamic and kinetic mechanisms in self-assembled quantum dot formation,* Materials Science and Engineering: B 67, 23 (1999).

[47] I. Daruka and A.-L. Barabási, *Dislocation-Free Island Formation in Heteroepitaxial Growth: A Study at Equilibrium,* Phys. Rev. Lett. 79, 3708 (1997).

[48] R. Asaro and W. Tiller, *Interface morphology development during stress corrosion cracking: Part I. Via surface diffusion,* Metallurgical Transactions 3, 1789 (1972).

[49] I. Daruka, J. Tersoff, and A.-L. Barabási, *Shape Transition in Growth of Strained Islands,* Phys. Rev. Lett. 82, 2753 (1999).

[50] J. Tersoff and R. M. Tromp, *Shape transition in growth of strained islands: Spontaneous formation of quantum wires,* Phys. Rev. Lett. 70, 2782 (1993).

[51] P. Thibault and L. J. Lewis, *Stability of strained heteroepitaxial systems in (1+1) dimensions,* Physical Review B 70, 035415 (2004).

[52] D. Zubia and S. D. Hersee, *Nanoheteroepitaxy: The Application of nanostructuring and substrate compliance to the heteroepitaxy of mismatched semiconductor materials,* Journal of Applied Physics 85, 6492 (1999).

[53] X. Li, *The influence of the atomic interactions in out-of-plane on surface energy and its applications in nanostructures,* Journal of Applied Physics 112 (2012).

[54] Q. Li, C. Dong, A. Nie, J. Liu, W. Zhou, and H. Wang, *Microstructure-Dependent Conformal Atomic Layer Deposition on 3D Nanotopography,* Langmuir 28, 15809 (2012).

[55] H.-B. Wang, F. Ma, Q.-Q. Li, C.-Z. Dong, D.-Y. Ma, H.-T. Wang, and K.-W. Xu, *Synthesis and stress relaxation of ZnO/Al-doped ZnO core-shell nanowires,* Nanoscale 5, 2857 (2013).

[56] S. Raychaudhuri and E. T. Yu, *Critical dimensions in coherently strained coaxial nanowire heterostructures,* Journal of Applied Physics 99 (2006).

[57] Ferrand, David and Cibert, Joël, *Strain in crystalline core-shell nanowires,* Eur. Phys. J. Appl. Phys. 67, 30403 (2014).

[58] I. Robinson, *Nanoparticle Structure by Coherent X-ray Diffraction,* Journal of the Physical Society of Japan 82, 021012 (2013).

[59] Y.-T. Cheng and M. W. Verbrugge, *The influence of surface mechanics on diffusion induced stresses within spherical nanoparticles,* Journal of Applied Physics 104, 083521 (2008).

[60] H. Duan, J. Wang, and B. Karihaloo, *Theory of Elasticity at the Nanoscale,* (Elsevier, 2009) pp. 1 – 68.

[61] F. Fischer, T. Waitz, D. Vollath, and N. Simha, *On the role of surface energy and surface stress in phase-transforming nanoparticles,* Progress in Materials Science 53, 481 (2008).

[62] Z.-J. Jiang and D. F. Kelley, *Stranski-Krastanov Shell Growth in ZnTe/CdSe Core/Shell Nanocrystals,* The Journal of Physical Chemistry C 117, 6826 (2013).

[63] R. L. Puurunen, *Correlation between the growth-per-cycle and the surface hydroxyl group concentration in the atomic layer deposition of aluminum oxide from trimethylaluminum and water,* Applied Surface Science 245, 6 (2005).

[64] R. A. Wind and S. M. George, *Quartz Crystal Microbalance Studies of Al_2O_3 Atomic Layer Deposition Using Trimethylaluminum and Water at 125 °C,* The Journal of Physical Chemistry A 114, 1281 (2010).

[65] S. D. Elliott and J. C. Greer, *Simulating the atomic layer deposition of alumina from first principles,* J. Mater. Chem. 14, 3246 (2004).

[66] M. Juppo, A. Rahtu, M. Ritala, and M. Leskelä, *In Situ Mass Spectrometry Study on Surface Reactions in Atomic Layer Deposition of Al_2O_3 Thin Films from Trimethylaluminum and Water,* Langmuir 16, 4034 (2000).

[67] R. Puurunen, *Growth Per Cycle in Atomic Layer Deposition: Real Application Examples of a Theoretical Model,* Chemical Vapor Deposition 9, 327 (2003).

[68] C. D. Travis and R. A. Adomaitis, *Modeling ALD Surface Reaction and Process Dynamics using Absolute Reaction Rate Theory,* Chemical Vapor Deposition 19, 4 (2013).

[69] A. J. M. Mackus, N. Leick, L. Baker, and W. M. M. Kessels, *Catalytic Combustion and Dehydrogenation Reactions during Atomic Layer Deposition of Platinum,* Chemistry of Materials 24, 1752 (2012).

[70] X. Liang, Y. Zhou, J. Li, and A. W. Weimer, *Reaction mechanism studies for platinum nanoparticle growth by atomic layer deposition,* Journal of Nanoparticle Research 13, 3781 (2011).

[71] T. Aaltonen, M. Ritala, T. Sajavaara, J. Keinonen, and M. Leskelä, *Atomic Layer Deposition of Platinum Thin Films,* Chemistry of Materials 15, 1924 (2003).

[72] S. T. Christensen, J. W. Elam, B. Lee, Z. Feng, M. J. Bedzyk, and M. C. Hersam, *Nanoscale Structure and Morphology of Atomic Layer Deposition Platinum on SrTiO3 (001),* Chemistry of Materials 21, 516 (2009).

[73] A. J. M. Mackus, M. A. Verheijen, N. Leick, A. A. Bol, and W. M. M. Kessels, *Influence of Oxygen Exposure on the Nucleation of Platinum Atomic Layer Deposition: Consequences for Film Growth, Nanopatterning, and Nanoparticle Synthesis,* Chemistry of Materials 25, 1905 (2013).

[74] J. Li, X. Liang, D. M. King, Y.-B. Jiang, and A. W. Weimer, *Highly dispersed Pt nanoparticle catalyst prepared by atomic layer deposition,* Applied Catalysis B: Environmental 97, 220 (2010).

[75] A. Goulas and J. R. van Ommen, *Atomic Layer Deposition of Platinum Clusters on Titania Nanoparticles at Atmospheric Pressure,* Journal of Materials Chemistry 15, 4647 (2013).

[76] J. A. Enterkin, K. R. Poeppelmeier, and L. D. Marks, *Oriented Catalytic Platinum Nanoparticles on High Surface Area Strontium Titanate Nanocuboids,* Nano Letters 11, 993 (2011).

[77] J. A. Venables, *Introduction to Surface and Thin Film Processes* (Cambridge University Press, 2000) cambridge Books Online.

[78] P.-G. de Gennes, F. Brochard-Wyart, and D. Quéré, *Capillarity and Wetting Phenomena* (Springer New York, 2004).

[79] L. Baker, A. S. Cavanagh, J. Yin, S. M. George, A. Kongkanand, and F. T. Wagner, *Growth of continuous and ultrathin platinum films on tungsten adhesion layers using atomic layer deposition techniques,* Applied Physics Letters 101, 111601 (2012).

[80] P. N. Plessow and F. Abild-Pedersen, *Sintering of Pt Nanoparticles via Volatile PtO2: Simulation and Comparison with Experiments,* ACS Catalysis 6, 7098 (2016).

[81] P. Wynblatt and N. Gjostein, *Supported metal crystallites,* Progress in Solid State Chemistry 9, 21 (1975).

[82] P. Wynblatt and N. Gjostein, *Particle growth in model supported metal catalysts—I. Theory,* Acta Metallurgica 24, 1165 (1976).

[83] P. Wynblatt and N. Gjostein, *Particle growth in model supported metal catalysts—II. Comparison of experiment with theory,* Acta Metallurgica 24, 1175 (1976).

[84] D. Walgraef, *Nanostructure evolution during thin film deposition,* Physica E: Low-dimensional Systems and Nanostructures 18, 393 (2003).

[85] D. Walgraef, *Nanostructure initiation during the early stages of thin film growth,* Physica E: Low-dimensional Systems and Nanostructures 15, 33 (2002).

[86] D. Walgraef, *Self-organization and nanostructure formation in chemical vapor deposition,* Phys. Rev. E 88, 042405 (2013).

[87] J. Christian, ed., *The Theory of Transformations in Metals and Alloys, Part I and II* (Pergamon, Oxford, 2002).

[88] J. A. Venables, *Rate equation approaches to thin film nucleation kinetics,* Philosophical Magazine 27, 697 (1973).

[89] C. Ratsch and J. A. Venables, *Nucleation theory and the early stages of thin film growth,* Journal of Vacuum Science & Technology A 21, S96 (2003).

[90] Y. Kajikawa and S. Noda, *Growth mode during initial stage of chemical vapor deposition,* Applied Surface Science 245, 281 (2005).

[91] J. Evans, P. Thiel, and M. Bartelt, *Morphological evolution during epitaxial thin film growth: Formation of 2D islands and 3D mounds,* Surface Science Reports 61, 1 (2006).

[92] C. D. Travis, *Model-based Analysis of Atomic Layer Deposition Growth Kinetics and Multiscale Process Dynamics*, Ph.D. thesis, University of Maryland (2014).

[93] M. Shirazi and S. D. Elliott, *Atomistic kinetic Monte Carlo study of atomic layer deposition derived from density functional theory,* Journal of Computational Chemistry 35, 244 (2014).

[94] T. J. Knisley, L. C. Kalutarage, and C. H. Winter, *Precursors and chemistry for the atomic layer deposition of metallic first row transition metal films,* Coordination Chemistry Reviews 257, 3222 (2013), chemical Vapor Deposition and Atomic Layer Deposition: Precursor Design and Application.

[95] A. Nie, J. Liu, Q. Li, Y. Cheng, C. Dong, W. Zhou, P. Wang, Q. Wang, Y. Yang, Y. Zhu, Y. Zeng, and H. Wang, *Epitaxial TiO2/SnO2 core-shell heterostructure by atomic layer deposition,* J. Mater. Chem. 22, 10665 (2012).

[96] S. Kukushkin and A. Osipov, *New phase formation on solid surfaces and thin film condensation,* Progress in Surface Science 51, 1 (1996).

[97] P. Poodt, J. van Lieshout, A. Illiberi, R. Knaapen, F. Roozeboom, and A. van Asten, *On the kinetics of spatial atomic layer deposition,* Journal of Vacuum Science & Technology A 31 (2013).

[98] T. J. Larrabee, T. E. Mallouk, and D. L. Allara, *An atomic layer deposition reactor with dose quantification for precursor adsorption and reactivity studies,* Review of Scientific Instruments 84, 014102 (2013).

[99] A. Holmqvist, T. Törndahl, F. Magnusson, U. Zimmermann, and S. Stenström, *Dynamic parameter estimation of atomic layer deposition kinetics applied to in situ quartz crystal microbalance diagnostics,* Chemical Engineering Science 111, 15 (2014).

[100] C. D. Travis and R. A. Adomaitis, *Dynamic Modeling for the Design and Cyclic Operation of an Atomic Layer Deposition (ALD) Reactor,* Processes 1, 128 (2013).

[101] A. Yanguas-Gil and J. W. Elam, *Simple model for atomic layer deposition precursor reaction and transport in a viscous-flow tubular reactor,* Journal of Vacuum Science & Technology A 30 (2012).

[102] A. Yanguas-Gil and J. W. Elam, *Analytic expressions for atomic layer deposition: Coverage, throughput, and materials utilization in cross-flow, particle coating, and spatial atomic layer deposition,* Journal of Vacuum Science & Technology A 32 (2014).

[103] M. B. M. Mousa, C. J. Oldham, and G. N. Parsons, *Atmospheric Pressure Atomic Layer Deposition of Al2O3 Using Trimethyl Aluminum and Ozone,* Langmuir 30, 3741 (2014), pMID: 24617608.

[104] F. Grillo, M. T. Kreutzer, and J. R. van Ommen, *Modeling the precursor utilization in atomic layer deposition on nanostructured materials in fluidized bed reactors,* Chemical Engineering Journal 268, 384 (2015).

[105] C. D. Travis and R. A. Adomaitis, *Modeling alumina atomic layer deposition reaction kinetics during the trimethylaluminum exposure,* Theoretical Chemistry Accounts 133, 1 (2013).

[106] H. Pedersen, *Time as the Fourth Dimension: Opening up New Possibilities in Chemical Vapor Deposition,* Chemistry of Materials 28, 691 (2016).

[107] T. Muneshwar and K. Cadien, *AxBAxB… pulsed atomic layer deposition: Numerical growth model and experiments,* Journal of Applied Physics 119, 085306 (2016).

[108] X. Liang, L. B. Lyon, Y.-B. Jiang, and A. W. Weimer, *Scalable synthesis of palladium nanoparticle catalysts by atomic layer deposition,* Journal of Nanoparticle Research 14, 943 (2012).

[109] D. Geldart, *Types of gas fluidization,* Powder Technology 7, 285 (1973).

[110] S. Morooka, K. Kusakabe, A. Kobata, and Y. Kato, *Fluidization state of ultrafine powders,* J. Chem. Eng. J. 21, 41 (1988).

[111] W. Yao, G. Guangsheng, W. Fei, and W. Jun, *Fluidization and agglomerate structure of SiO2 nanoparticles,* Powder Technology 124, 152 (2002).

[112] C. Zhu, Q. Yu, R. N. Dave, and R. Pfeffer, *Gas fluidization characteristics of nanoparticle agglomerates,* AIChE Journal 51, 426 (2005).

[113] J. R. Ommen, J. M. Valverde, and R. Pfeffer, *Fluidization of nanopowders: a review,* Springer Netherlands , 1 (2012).

[114] L. de Martín, W. G. Bouwman, and J. R. van Ommen, *Multidimensional Nature of Fluidized Nanoparticle Agglomerates,* Langmuir 30, 12696 (2014).

[115] M. Tahmasebpoor, L. de Martín, M. Talebi, N. Mostoufi, and J. R. van Ommen, *The role of the hydrogen bond in dense nanoparticle-gas suspensions,* Phys. Chem. Chem. Phys. 15, 5788 (2013).

[116] J. Shabanian, R. Jafari, and J. Chaouki, *Fluidization of ultrafine powders,* International Review of Chemical Engineering 4, 16 (2012).

[117] L. F. Hakim, J. L. Portman, M. D. Casper, and A. Weimer, *Aggregation behavior of nanoparticles in fluidized beds,* Powder Technology 160, 149 (2005).

[118] R. Beetstra, U. Lafont, J. Nijenhuis, E. Kelder, and J. R. van Ommen, *Atmospheric pressure process for coating particles using atomic layer deposition,* Chemical Vapor Deposition 15, 227 (2009).

[119] J. R. van Ommen, C. U. Yurteri, N. Ellis, and E. M. Kelder, *Scalable gas-phase processes to create nanostructured particles,* Particuology 8, 572 (2010).

[120] Y. Zhou, D. M. King, X. Liang, J. Li, and A. W. Weimer, *Optimal preparation of Pt/TiO2 photocatalysts using atomic layer deposition,* Applied Catalysis B: Environmental 101, 54 (2010).

Shafi Abad, Iran 2017.

2

Nanoparticle Sintering in Atomic Layer Deposition of Supported Catalysts: Kinetic Modeling of the Size Distribution

What I cannot model, I do not understand

In industrial catalysis, the sintering of supported nanoparticles (NPs) is often associated with the loss of catalyst activity and thus with periodic plant downtime and economic burdens. Yet, sintering mechanisms are at play also during the synthesis of the catalyst itself. They can, in fact, determine the size distribution of the NPs, and thus the activity and the stability of the catalyst. Here, we examine the role of nanoparticle sintering in a technique borrowed from the semiconductor industry that promises to reconcile atomic-scale precision with scalability: atomic layer deposition. By modeling the cyclic influx of single atoms in concomitance with NP sintering via either dynamic coalescence or Ostwald ripening, we establish the "signature" of different growth regimes: the size distribution. In contrast, we show that integral quantities such as the mean diameter, the number of NPs per unit area, and the material loading are poor indicators of the underlying growth mechanism. In particular, a constant number of NPs cannot be interpreted as a sign of no sintering. Finally, we argue that NP sintering, if properly understood, can open up new avenues for the control over the size distribution of NPs, and thus over their catalytic activity and stability.

Published as: Fabio Grillo, Jacob A. Moulijn, Michiel T. Kreutzer, J. Ruud van Ommen, Nanoparticle Sintering in Atomic Layer Deposition of Supported Catalysts: Kinetic Modeling of the Size Distribution, *Catalysis Today*, 2018.

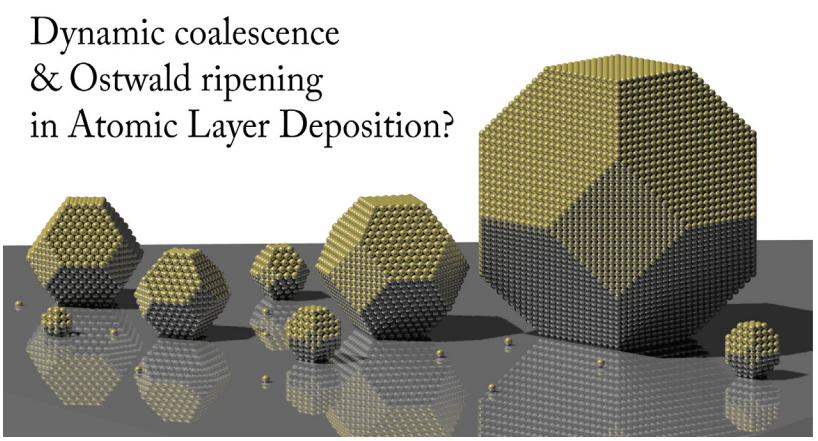

2.1. Introduction

Catalysis plays a key role in chemical conversion. In catalysis, precision can be reached in the sense that the desired products are formed at high rates without large amounts of by-products [1–3]. It is an enabling technology that has the potential of leading to breakthroughs in the Chemical Process Industry. It plays a central role in the development of sustainable technology and Process Intensification [4]. A catalyst is often named according to its composition, for instance as Co-Mo/A_2O_3 (3 wt% Co, 15 wt% Mo, 82 wt% Al_2O_3) or 5.2 wt% Pt-Al_2O_3. However, defining a catalyst in this way is an oversimplification. A catalyst is a chemical that performs several functions simultaneously. In this respect, catalysts are comparable to microchips, although nobody would refer to a microchip as "silica promoted by a certain amount of Au". The comparison with microchips goes further. There is no doubt that in the microchip industry scientists and engineers have benefited greatly from the recent developments in nanoscience and nanotechnology [5–8]. In catalysis this is less the case. We feel that catalysis can learn a great deal from the recent developments in the semiconductor industry, especially in the direction of atomic-scale precision in the synthesis of solid catalysts.

Solid catalysts can be subdivided in bulk catalysts and supported catalysts [1]. Here we will limit ourselves to supported catalysts. The major function of a support is to provide a surface where the active phase can be dispersed. The degree of dispersion, or simply the dispersion, is typically quantified as the fraction of atoms or molecules of the active phase that are exposed to the reaction environment. Often the active phase forms into clusters of atoms or nanoparticles (NPs) with a certain size distribution. Thus, in the limit of every atom having the same catalytic activity, the dispersion coincides with the average surface-to-volume ratio of the NP population. It follows that in most instances the preferred configurations are the ones in which the active phase is dispersed in the form of small NPs or even single atoms [9]. Yet, in some cases the catalytic activity is size-dependent and the small-NPs configuration might not be the most desirable [10]. In general, the ideal synthesis route for supported catalysts is the one that enables full control over the size distribution of NPs [8].

The support plays a crucial role in stabilizing the active phase against sintering: the process

that leads to a progressive loss of active surface area via NP growth [11–13]. In catalysis, sintering is typically an undesired process because it inevitably results in the deactivation of the catalyst. For this reason, over the years, a great research effort has been devoted to the understanding of the sintering mechanisms behind the deactivation of catalysts during industrially relevant reactions [11–19]. Supported NPs can sinter via two main pathways: Ostwald ripening and dynamic coalescence (Smoluchowski aggregation) [12, 16–18, 20–22]. Ostwald ripening is the growth of large NPs at the expenses of smaller ones via the exchange of single atoms. This process is driven by the Gibbs-Thompson effect: large NPs are more stable than smaller ones and thus less likely to shed atoms. The transport of single atoms between NPs can take place via surface diffusion, subsurface diffusion, or through the gas-phase [16, 20, 21]. The latter is particularly relevant to supported NPs of noble metals in oxidizing atmospheres because surface oxide species are more volatile than the pure metal [16]. On the other hand, dynamic coalescence is the process in which NPs diffuse over the support surface as a whole, collide, and coalesce [12, 17, 18, 21–25]. These mechanisms are not only relevant to the growth of supported NPs exposed to reaction conditions, but also to the synthesis of NPs in general [25–30]. In particular, the study of the role of sintering mechanisms in the synthesis of colloidal NPs is a very active field of research [27]. This is because a fundamental understanding of such processes might open up avenues for the tailoring of the size distribution and even the shape of colloidal NPs[27, 28]. On the other hand, very little research has been devoted to the understanding of the mechanisms behind the synthesis of supported NPs, which is of great relevance to the field of catalyst synthesis.

Current liquid- and gas-phase synthesis methods for supported NPs often lack the ability to tailor the size distribution with high precision or do not lend themselves to large scale production [8, 10, 31]. Atomic layer deposition (ALD), a thin-film technique derived from chemical vapor deposition, has the potential to reconcile atomic-scale precision with industrial scale production [10, 26, 31–35]. ALD has already established itself in the semiconductor industry thanks to its atomic scale-level precision in the deposition of thin films. In ALD solid materials (i.e., supports) are functionalized by thin films or nanoparticles [31, 36–39]. The latter are synthesized in a bottom-up fashion by means of reaction cycles. In each cycle the support is exposed to typically two gaseous reactants in a sequential fashion, that is, the support is exposed to one reactant at the time. Such reaction sequence brings about the deposition of no more than a monolayer of the desired material. This precision is achieved by relying on self-limiting surface chemistries, for example, the stoichiometric reaction of precursor molecules with the limited number of active surface sites. Varying the number of reaction cycles, therefore, enables digital control over the amount of deposited material[31, 36, 38]. Yet, exploiting the precision of ALD for the synthesis of supported NPs is not straightforward [10, 26, 40]. In fact, ALD of NPs can result in wide range of size distributions depending on the system at hand [26, 33, 40–45]. Different size distributions are bound to arise from different growth mechanisms and in particular sintering mechanisms. The role of the latter in ALD of NPs is still under debate [26, 40].

Here we present a general theoretical understanding of ALD of NPs by means of the mean-field rate-equation model approach that was developed in our previous work [26]. Our analysis is dedicated to two related questions: what are the growth pathways that lead from adsorbed single atoms to supported NPs? How do different growth pathways affect the NP population? The aim is twofold. First, to identify the observable (i.e., size distribution,

number of NPs, average size, and amount of material deposited) that varies the most across different growth mechanisms or, in other words, to establish the signature of each growth mechanism. Secondly, to identify the most desirable growth pathway and thus propose routes to improve the control over the size distribution. The first part of the paper will be dedicated to the description of the model and thus to the theory. The second part will discuss five case studies covering different growth scenarios designed to shed light on the role of dynamic coalescence and Ostwald ripening in ALD of NPs.

2.2. Theory and Model description

2.2.1. Observables in ALD of nanoparticles

The fundamentals of ALD of NPs can depart considerably from those of ALD of conformal films. The latter is entirely dependent on surface chemistry, since the extent and the nature of the reactions between the precursors and the support determine the amount of material deposited and thus the film thickness. In fact, if the growth proceeds in a 2D fashion and the underlying support has a flat surface, the amount of material deposited and the film thickness are linearly dependent. As a result, the vast majority of ALD processes is understood and described in terms of a single observable: the growth-per-cycle (GPC), which is expressed either as the increase in thickness per cycle (nm/cycle) or as the amount of material deposited per cycle (at nm^{-2}) [31, 36, 38, 46]. Clearly, ALD of nanoparticles does not enjoy the same simplicity. An ensemble of supported nanoparticles is in fact characterized by a number of observables:

i) the size distribution

ii) the number density, that is, the number of nanoparticles per unit area

iii) the shape

iv) the total number of atoms per unit area

Such observables not only can vary in a non-linear fashion with the number of cycles and the process conditions, but are also in a non-linear relationship with each other. In particular, the amount of material deposited in each cycle will vary depending on the additional surface area associated with the presence of nanoparticles and thus on i), ii), and iii). The latter are mostly dictated by kinetic processes such as surface diffusion and aggregation of adatoms and nanoparticles, and atom attachment and detachment to and from nanoparticles [47, 48]. In turn, such processes are affected by the total amount of material, that is, iv). In short, while ALD of thin films can be understood almost entirely in terms of surface chemistry, to understand ALD of nanoparticles one has to take into account diffusion phenomena because they play a major role in determining i-iv), as is discussed in detail in the following paragraphs.

2.2.2. Dynamic modeling of nanoparticle formation and growth

The governing mechanisms behind the growth of NPs can in principle vary on a case-by-case basis. Identifying such mechanisms has not only a fundamental value but also a practical one. This is because insights into the factors that affect the growth mechanism are the basis

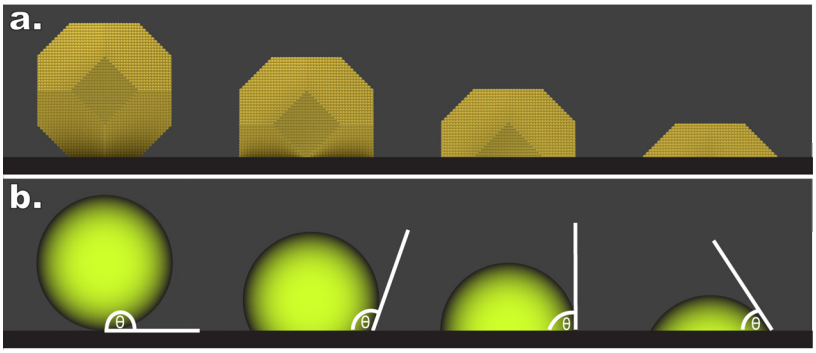

Figure 2.1: Schematic representation of an FCC nanoparticle that takes on the shape of a truncated cuboctahedron at increasing NP-support interaction (wetting) (a) and its representation in the spherical cap approximation (b).

for the development of recipes for the synthesis of the desired morphologies. Yet, the search for the underlying growth mechanism is complicated by the fact that different causes may have similar effects on certain observables. It is therefore crucial to identify the observable that varies the most across different mechanisms. In short, we need to establish the signature trends of the different kinetic processes on i), ii), iii), and iv). Here, we do so by means of a kinetic model that takes into account not only the formation and the growth of NPs due to the cyclic deposition of single atoms but also NP sintering via either dynamic coalescence or Ostwald ripening. In our treatment of the latter, we assume that the NPs exchange single atoms via the gas phase. This variant of Ostwald ripening is particularly relevant to the ALD of noble metals, that is the ALD system that is more likely to lead to the formation of nanoparticles as opposed to conformal films [31, 33, 40, 49]. In short, our model allows for the following processes:

1. Cyclic deposition of single atoms on the surface of both the support and the NPs
2. Diffusion and aggregation of single atoms, that is NP formation; and atom attachment to NPs
3. Diffusion and coalescence of NPs, that is, dynamic coalescence (DC)
4. Gas-phase-mediated Ostwald ripening (OR), that is, the growth of large NPs at the expenses of smaller one (Gibbs-Thompson effect) via the exchange of single atoms between NPs in the form of volatile compounds (e.g., PtO_x in the case of Pt NPs)

The above processes are modeled via a mean-field rate-equation approach. For a detailed description of the model, the reader is referred to the Appendix 3.A of chapter 3. Table 2.1 presents the main equations of the kinetic model. The deposition process is modeled by assuming that at the beginning of each cycle:

- The number of single atoms on the support n_1 increases by a constant value G_s (at nm^{-2}) times the fractional area not occupied by NPs (deposition on the substrate)
- The number of atoms k in each NP increases by a fraction of the number of surface atoms k_{surf}, that is, by G_p (deposition on the NPs)

Kinetic model (m = cycle number)
Cyclic deposition of single atoms on the support
$\Delta n_1 = G_s \left[1 - \sum_k n_k(m)\, \pi r_k^2(m)\right]$
Cyclic layer-by-layer growth of the nanoparticles
$\Delta k = G_p k(m) f_k(m)$
Population balance: evolution of the size distribution
$\frac{dn_k}{dt} = \left(B_k^{DC} - E_k^{DC}\right) + \left(B_k^{OR} - E_k^{OR}\right)$
Shape: projected radius (r_k) and dispersion (f_k)
$r_k = \alpha k^{1/3},\ \&\ \alpha = \sin\vartheta \sqrt[3]{\frac{3\Omega}{\pi(2-3\cos\vartheta+\cos^3\vartheta)}}$
$f_k = k_{surf}/k = \frac{30z^2-60z+36}{10z^3-15z^2+11z-3},\ \&\ z = \frac{\sqrt{2}r_k}{a} + \frac{1}{2}$
Loading (total number of atoms per unit area)
$L_{m+1} = \underbrace{L_m\left(1 + G_p\left\langle f_k(m)\right\rangle\right)}_{\text{NPs}} + \underbrace{G_s\left(1 - \sum_k n_k(m)\, \pi r_k^2(m)\right)}_{\text{Support}}$

Table 2.1: Main equations of the model.

whereas the evolution of the size distribution due to the kinetic processes (2-4) is described by a population balance that allows for the "birth" (B_k) and "extinction" E_k of the population of NPs consisting of k atoms n_k (nm^{-2}). B_k and E_k are expressed in terms of number of NPs per unit area per unit time (nm^{-2} s^{-1}). Here, the ratio between the number of surface atoms and the total number of atoms comprising an NP, that is, the dispersion, is denoted by f_k. The latter has been taken equal to the dispersion of an FCC NP assuming the shape of a perfect cuboctahedron [50](see Figure 2.1). This shape has been shown to mimic the fraction of surface sites of the most stable Pt clusters over a wide range of sizes [51]. Here, denotes the lattice constant. Instead, the relation between the number of atoms in an NP and its projected radius is described by approximating the NP to a spherical cap (see Figure 2.1b) characterized by a contact angle ϑ (Ω denotes the atomic volume) [20].

For a detailed description of birth and extinction rates the reader is referred to the appendix 3.A of chapter 3 and, in particular to Equations 3.1, 3.2, and 3.23-3.26. In short, for dynamic coalescence, B_k^{DC} and E_k^{DC} are calculated by assuming that single atoms and NPs undergo irreversible aggregation as a result of binary collisions. Clusters comprising as few as two atoms (i.e., dimers) are assumed to be stable. The collision frequency depends on the diffusion rate, the number, and the size of the surface species. The diffusion rate is assumed to follow the power law $D_k = D1k^{-s}$, where s is a positive number that typically ranges from

0 to 2 [18, 20, 22, 23, 52–56]. Accordingly, B_k^{DC} accounts for the increase in the number of NPs of size due to the "birth" of NPs resulting from the collision and subsequent coalescence of two NPs of size i and j, where $i+j=k$. Instead, E_k^{DC} accounts for the "extinction" of NPs of size k due to their collision with NPs of arbitrary size i, which result in NPs of size $i+k>k$.

Ostwald ripening is modeled by allowing for the detachment of atoms from the NP surface at a rate $\sim \exp^{\gamma/r_k}$, where γ is the surface energy of the NP material. In particular, we assume that, once detached, the atoms join a vapor basin that is in equilibrium with the NP ensemble: the inter-particle transport takes place through the vapor phase [16, 20]. Accordingly, B_k^{OR} accounts for the "birth" of NPs of size k due to atom detachment from NPs of size $k+1$ and atom attachment onto NPs of size $k-1$, and E_k^{OR} accounts for the "extinction" of NPs of size due to atom detachment/attachment. It is worth noting that simulating Ostwald ripening in concomitance with the cyclic generation of single atoms gives rise to a nucleation and growth problem: NPs of various sizes cyclically form as a result of the aggregation of single atoms, however, only NPs above a certain critical size survive and thus grow.

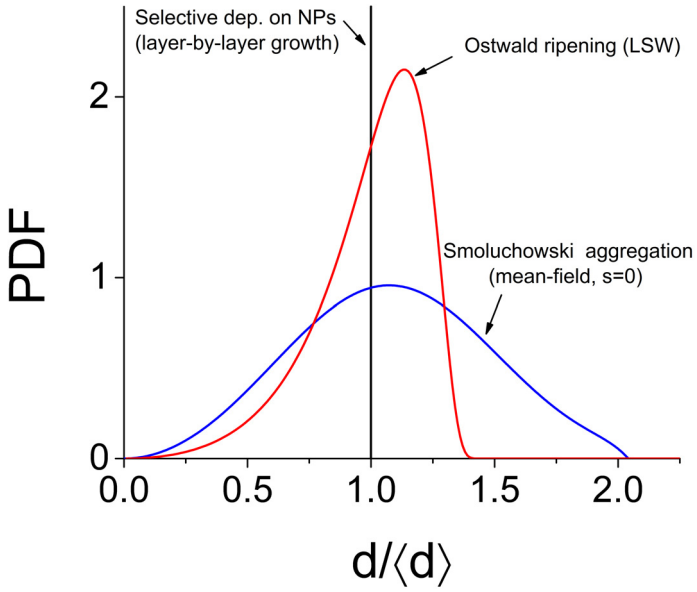

Figure 2.2: Size distributions rescaled with respect to the average diameter expressed in terms of probability density function in case of: ideal layer-by-layer growth of the NPs in the limit of infinite number of cycles and no NP sintering; diffusion-limited Ostwald ripening for an ensemble of (3D) NPs on a surface (LSW approximation) [25]; Smoluchowski aggregation of (3D) NPs on a surface for $D_k = D1$ (analytical approximation in the limit of long-times) [23].

2.2.3. Rescaled size distribution and clues offered by its asymptotic behavior

Now that we have established a theoretical framework for the description of the observables i), ii), iii), iv), we can seek the signatures of the growth mechanisms considered here. We anticipate that the observable carrying the most information is the size distribution (SD), and in particular the SD rescaled with respect to the average diameter. The latter gives a measure of the broadness of the distribution, or in other words, of the magnitude of the departure of all the sizes from the average size. For example, Figure 2.2 shows the shape that the rescaled SD attains in three limiting cases: no deposition and dynamic coalescence where the mobility of the NPs is size-independent; no deposition and surface-mediated Ostwald ripening; and the case in which the growth proceeds on the NPs alone and the NPs do not sinter. In fact, it can be shown that if an ensemble of an infinite number of NPs undergoes either dynamic coalescence or Ostwald ripening, the SD will keep broadening and shifting towards the large-size side, and yet the rates at which the broadness and the average size increase approach the same value in the limit of long times. The SD is then said to admit a self-similar solution, that is, the rescaled SDs all collapse onto a single curve [21, 23, 25, 57]. In the limiting case in which the NPs grow in a layer-by-layer fashion and do not sinter, each NP will grow at the same rate. As a result, the average size will increase while the broadness of the SD will remain constant, and thus the rescaled SD will gradually narrow and eventually approach a Dirac delta function centered on one. As a rule, the fact that the experimental rescaled SDs does not narrow with increasing number of cycles is a clear indication that a mechanism other than layer-by-layer growth is at play. The self-similar solutions in the case of pure dynamic coalesce or Ostwald ripening might offer a first clue, however, the cyclic generation of single atoms is bound to periodically induce transients in the SD evolution and thus disrupt the approach to the self-similar solution. In general, it is therefore crucial to resolve the full dynamic behavior by taking into account both deposition and sintering.

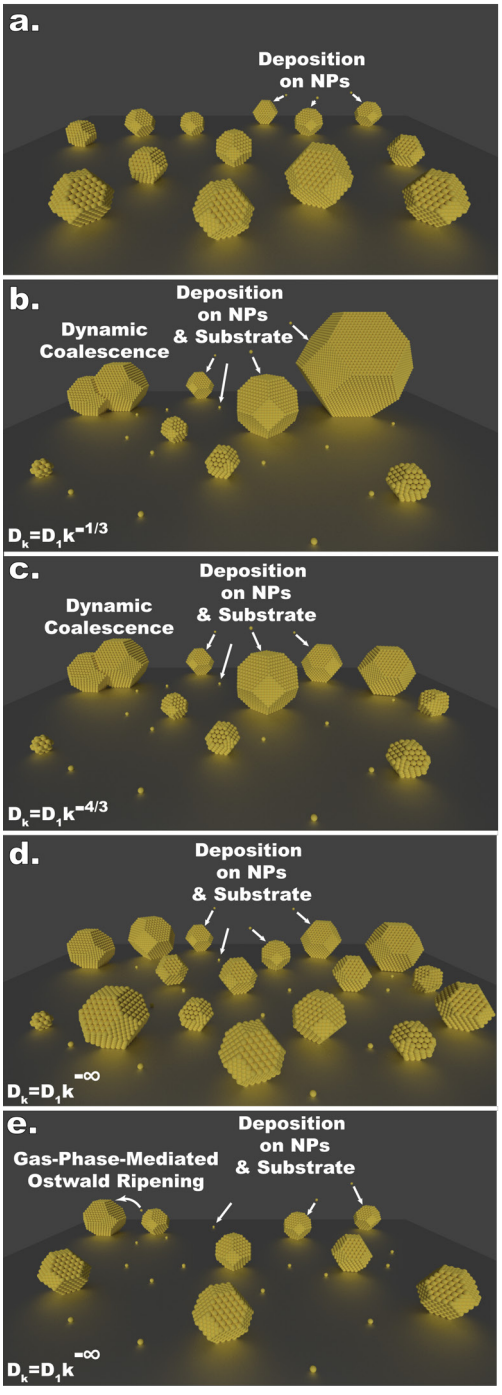

Figure 2.3: Schematic representation of the five growth scenarios considered here: layer-by-layer growth of NPs that do not sinter (a); cyclic deposition of single atoms on the substrate and the NPs, surface diffusion, attachment, and aggregation of single atoms, and dynamic coalescence characterized by an NP mobility that is either weakly (b) or strongly (c) size-dependent; cyclic deposition of single atoms on the substrate and the NPs, surface diffusion, attachment, and aggregation of single atoms (d); cyclic deposition of single atoms on the substrate and the NPs, surface diffusion, attachment, and aggregation of single atoms, and gas-phase-mediated Ostwald ripening (e).

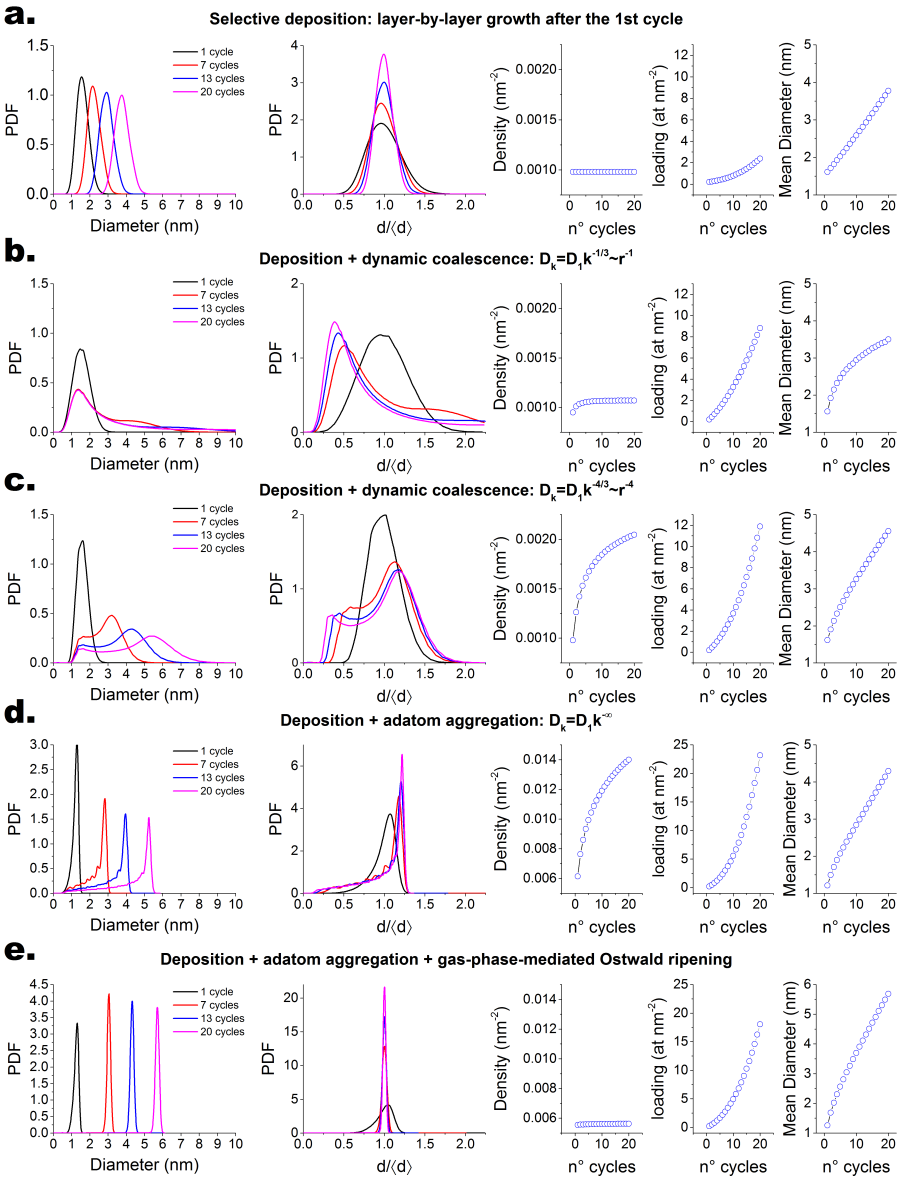

Figure 2.4: Simulated evolution of the size distribution and its rescaled counterpart, the nanoparticle number density, the loading, and the mean diameter with the number of cycles in the growth scenarios of Figure 2.3. The size distributions are expressed in terms of probability density function (PDF) vs diameter by taking into account that $f_r dr = f_k dk$ and , and thus $f_d = 8\alpha^{-3} d_k^2 f\left(dk_k^3/8\alpha^3\right)_k$

2.3. Results and Discussion

Here we examine the dynamic evolution of the size distribution, the number density, and the loading in five case studies covering the following growth scenarios (see Figure 2.3 and Table 2.2):

a) Formation of NPs in the first cycle via deposition of single atoms on the support and dynamic coalescence, followed by layer-by-layer growth ($G_s = 0$ & $\frac{dn_k}{dt} = 0$, if $m > 1$)

b) Deposition on both the support and the NPs; single atom diffusion and attachment to NPs; dynamic coalesce characterized by a weak size dependence of the NP mobility ($D_k = D_1 k^{-1/3} \sim 1/r_k$, $B_k^{OR} = E_k^{OR} = 0$)

c) Deposition on both the support and the NPs; single atom diffusion and attachment to NPs; dynamic coalesce characterized by a strong size dependence of the NP mobility ($D_k = D_1 k^{-4/3} \sim 1/r_k^4$, $B_k^{OR} = E_k^{OR} = 0$)

d) Deposition on both the support and the NPs; single atom diffusion and attachment to NPs ($D_k = D_1 k^{-\infty}$, $B_k^{OR} = E_k^{OR} = 0$)

e) Deposition on both the support and the NPs; single atom diffusion and attachment to NPs; and gas-phase-mediated Ostwald ripening ($D_k = D_1 k^{-\infty}$, $B_k^{DC} = E_k^{DC} = 0$)

Case Study	Deposition on		Single atoms	Nanoparticle	Ostwald Ripening
	NPs	Support	Diffusion & aggregation	Diffusion & Coalescence	(Gas-Phase-Mediated)
a	✓	✗	✗	✗(after the 1st cycle)	✗
b	✓	✓	✓	✓(weak size-dependence)	✗
c	✓	✓	✓	✓(strong size-dependence)	✗
d	✓	✓	✓	✗	✗
e	✓	✓	✓	✗	✓

Table 2.2: Simulation parameters for ALD on micron-sized nanoporous γ-alumina particles.

G_s and G_p were set equal to at nm^{-2} and 0.3 (at/k_{surf}), respectively, unless otherwise specified. To put these figures in perspective: the loading after one cycle of Pt ALD was reported to be ~0.1 at nm^{-2} on graphene nanoplatelets and ~0.4 at nm^{-2} on Si nanowires [26, 42]; whereas, given the above assumptions on the shape and the dispersion, a G_p of 0.3 translates into a radial growth per cycle of about 0.05 nm/cycle, which is close to the typical GPC of Pt ALD on platinum [49, 58]. The NPs were assumed to be hemispherical caps consisting of platinum atoms, that is, the contact angle ϑ was set equal to 90°. D_1 was varied across different growth scenarios so as to achieve about the same number density after one cycle in scenario (a) to (c) and in scenario (d) and (e). In scenario (e), Ostwald ripening was modeled by considering the exchange of volatile PtO_2 between Pt NPs by setting the temperature equal to 250 °C, the partial pressure of oxygen equal to 0.2 bar, and the cycle time equal to 900 s. The treatment of gas-phase-mediated Ostwald ripening is based on the work of Plessow and Abild-Pedersen [16]. Figure 2.4 shows the results of the simulations for the five growth scenarios within the cycle range 1-20.

2.3.1. Average size and loading across different growth scenarios

A striking feature of the simulation results (see Figure 2.4) is that the evolution of both the loading and the average size is qualitatively similar across considerably different growth mechanisms. Instead, the SD and its rescaled counterpart exhibit the most marked changes. It is clear that in scenario (a) the evolution of the average diameter is strictly linear, whereas in the other cases it exhibits varying degrees of non-linearity. The most pronounced non-linearity is observed for the case of simultaneous deposition and dynamic coalescence characterized by a weak size-dependence of the NP mobility, that is, scenario (b). Also, in this case, the average diameter after 20 cycles is the lowest across all the growth scenarios. This is somewhat counterintuitive, as one would naturally associate dynamic coalescence with the formation of larger NPs. In fact, large NPs do form, however, when the NP mobility is not a strong function of the size, the survival probability of small NPs becomes comparable to the one of large particles. This, in combination with the fact that small NPs are constantly forming as a result of the deposition process, results in a large fraction of small NPs, and thus in smaller average sizes. That being said, with the exception of scenario (b), the evolution of the diameter with the number of cycles is fairly linear and thus cannot be used as a signature of the underlying growth mechanism, especially if one allows for experimental variability.
As to the loading (at nm^{-2}), the differences are quantitative and not qualitative: in the limit of small loadings and low number of cycles the trend is linear, whereas at higher loading and number of cycles it eventually becomes exponential. Clearly, the rate at which the loading increases is higher when the deposition takes place on both the support and the NPs (compare Figure 2.4a and Figure 2.4b), and in correspondence of higher NP number densities (see Figure 2.4a-e) as more NPs translate into higher surface areas. Yet, in general, the latter is true only if the number of atoms that are being deposited per surface area is higher on the NPs than on the support. In contrast, if the opposite is true, the rate of change of the metal loading would actually decrease with the number of cycles. Also, it is important to point out that the loading will increase exponentially only if the material fed to the system is always in excess of the initial saturation value. In fact, the vast majority of ALD experiments is carried out with a fixed exposure of precursors throughout all the cycles. This exposure is typically established on the basis of the saturation of the loading at a fixed number of cycles [40]. However, from the equation describing the loading in Table 2.1 it is clear that the amount of material required for the saturation of the entire surface will vary from cycle to cycle. Therefore, we conclude that a linear trend in the metal loading is rather the exception than the rule, and that, if a linear trend is indeed observed, it will likely be the direct result of the use of a fixed exposure of precursors throughout the cycles.

2.3.2. The size distribution as a signature of the growth mechanism

We will now examine the effect of the different growth mechanisms on the SD, the rescaled SD, and the NP number density. While the average diameter and the metal loading exhibit similar trends across different mechanisms, the SD and in particular the rescaled SD exhibit marked qualitative and quantitative differences.
As already anticipated, in scenario (a), since the growth takes place on the NPs only and there is no sintering, the SD shifts towards larger sizes while its span or broadness remains

constant. As a result, the rescaled SD narrows down in every cycle. Instead, in scenario (b), each cycle results in the broadening of the SD, which becomes heavy-tailed in the large-size side, while the peak of the SD remains pinned on the small-size side. As expected, after the first cycle, the rescaled SD approaches the self-similar solution of the problem of pure dynamic coalescence for $D_k = D_1 k^{-1/3}$. However, in the subsequent cycles, the rescaled SD becomes markedly left-skewed with the mode at around 0.5, which does not change significantly with the number of cycles. This exemplifies how the cyclic formation of new NPs can disrupt the sintering dynamics and lead to quasi-stationary solutions that differ significantly from the self-similar solution to the dynamic coalescence problem (no single atoms influx). Moreover, as opposed to the case of exclusive dynamic and coalescence, where the NP density drops over time, the concomitant cyclic formation of NPs and their dynamic coalescence can lead to a dynamic equilibrium, and thus to a constant NP density. In fact, in scenario (b) the NP number density remains fairly constant throughout 20 cycles. This has important implications, because a constant NP number density is often interpreted as a sign of no sintering [43, 59].

Comparing scenario (c) with scenario (b) clearly demonstrates how the same mechanism, that is, dynamic coalescence, can lead to completely different morphologies depending on how the NP mobility scales with the NP size. In fact, when the NP mobility drops quickly with increasing NP size, the SD transits from being right-skewed to being left-skewed with increasing number of cycles. Also, in this case, the peak of the SD is not pinned and it shifts towards the large-size side. Again, the rescaled SD approaches the self-similar solution for $D_k = D_1 k^{-4/3}$ after the first cycle. Subsequent cycles result in a left-skewed rescaled SD with a mode above 1. Unlike scenario (b), here the NP density increases with the number of cycles. However, in the limit of large number of cycles the NP density saturates. Clearly, when the NP density tends to the critical value at which the center-to-center distance is equal to the NP diameter, that is, the percolation limit, the mean-field approximation breaks down. Thus, we expect that at high coverages the NP density will eventually drop due to static coalescence. Yet, in the early stages of growth (coverage < 5%), a drop in the NP density is not necessarily caused by dynamic coalescence alone. Interestingly, the evolution of the size distribution in scenario (b) is in qualitative agreement with the PSDs reported by Rontu et al. for plasma-enhanced ALD of Pt on TiO_2 at 300 °C [60].

In the extreme limit in which only single atoms are mobile ($D_k = D_1 k^{-\infty}$), that is, scenario (d), the evolution of the SD and of the NP number density is in qualitative agreement with the previous scenario: the SD are left-skewed and the NP number density increases with the number of cycles. The difference lies in the sharpness of the main peak: despite the tail on the small-size side, the SDs are quite narrow. This is particularly evident when the SD is rescaled. Another interesting feature is that each cycle results into a secondary peak since the "extinction" of NPs is not allowed for. Such features were indeed reported for the case of plasma-enhanced deposition of Pt NPs at room temperature [40].

The last scenario (e) adds Ostwald ripening to scenario (d). Ostwald ripening has been thought to be a governing mechanism in the growth of Pt NPs when oxygen is used as the second reactant, as this might promote the formation of volatile oxides that would in turn lead to gas-phase-mediate ripening. However, if Ostwald ripening was the governing mechanism then the SD should be extremely narrow. This may sound counterintuitive, given that Ostwald ripening is known to the catalysis community as a sintering mechanism

that leads to the broadening of the SD at high temperatures and on long time scales [12, 15]. Yet, if Ostwald ripening takes place concomitantly with the generation of single atoms and thus new NPs, it actually promotes the "focusing" or narrowing of the SD. In fact, this very mechanism is well known to the field of colloidal synthesis and it is exploited for the synthesis of NPs with very narrow SDs [27–29]. This is clearly illustrated by the evolution of the rescaled SD, which quickly approaches a Dirac delta. In analogy with scenario (b), also in this case the NP density remains fairly constant with the number of cycles as a result of a dynamic equilibrium between the formation of new NPs and their sintering. Again, this means that in ALD of NPs the observation of a fairly constant NP density cannot be used to rule out Ostwald ripening. Naturally, these conclusions have to be taken within the limits of the mean-field approximation and in the case in which the deposition on the support does lead to the formation of new NPs. For example, a considerable drop in the NP number density might suggest that single atoms are preferentially attached to preexisting NPs and that these are undergoing sintering either by Ostwald ripening or dynamic coalescence.

2.4. Conclusions

The sintering of supported nanoparticles plays a crucial role in industrial catalysis. Dynamic coalescence and Ostwald ripening –the main pathways for nanoparticle sintering- have been widely studied in an attempt to understand how to suppress sintering. This is because the sintering of supported nanoparticles under catalytic conditions invariably leads to a loss of catalytic activity. Nonetheless, nanoparticle sintering also plays a crucial role in the very synthesis of supported nanoparticles. In this case, sintering takes place while new nanoparticles are forming due to an influx of single atoms. Here, we studied how the cyclic influx of single atoms on a support affects nanoparticle sintering. In particular, we modeled the effect of sintering on the size distribution of nanoparticles synthesized via atomic layer deposition. We have established that the evolution with the number of cycles of the size distribution is a signature of the mechanisms underlying the nanoparticle growth. On the other hand, the evolution of the average diameter, of the nanoparticle number density, and of the amount of deposited material can exhibit similar behaviors across different growth mechanisms. Therefore, they are poor indicators of the underlying mechanisms. In particular, a linear trend in the evolution of the average diameter cannot be interpreted as a sign of no sintering. Moreover, a linear trend in the amount of deposited material should be the exception rather than the rule, as a non-linear trend should naturally arise at high coverages. Less trivially, also a constant nanoparticle number density cannot be interpreted as a sign of no sintering, since this can be the result of the dynamic equilibrium between nanoparticle formation and nanoparticle sintering via either dynamic coalescence or Ostwald ripening. In case of dynamic coalescence, if the nanoparticle mobility decreases quickly with the size, the nanoparticle number density is actually expected to increase, unless in proximity of the percolation limit. Surprisingly, the narrowest size distribution is obtained when Ostwald ripening takes place in concomitance with NP formation. In conclusion, if properly understood and harnessed, sintering mechanisms can be beneficial rather than disruptive to atomic layer deposition of nanoparticles.

References

[1] R. Schlögl, *Heterogeneous catalysis,* Angewandte Chemie - International Edition 54, 3465 (2015).

[2] E. F. A., *Industrial Catalysis,* Nature 122, 802 (1928).

[3] J. Moulijn, M. Makkee, and A. Van Diepen, *Chemical process technology*, 2nd ed. (Wiley, 2013) p. 566.

[4] A. C. Dimian, C. S. Bildea, and A. A. Kiss, *Process Intensification,* Chemical Engineering Progress , 397 (2014).

[5] J. Wu, Y.-L. Shen, K. Reinhardt, H. Szu, B. Dong, J. Wu, Y.-L. Shen, K. Reinhardt, H. Szu, and B. Dong, *A Nanotechnology Enhancement to Moore's Law,* Applied Computational Intelligence and Soft Computing 2013, 1 (2013).

[6] W. R. Fahrner, *Materials Today*, Vol. 7 (2005) p. 270.

[7] H. Choi and C. C. Mody, *The long history of molecular electronics: Microelectronics origins of nanotechnology,* (2009).

[8] B. Roldan Cuenya and F. Behafarid, *Nanocatalysis: Size- and shape-dependent chemisorption and catalytic reactivity,* Surface Science Reports 70, 135 (2015).

[9] J. Liu, *Catalysis by Supported Single Metal Atoms,* ACS Catalysis 7, 34 (2017).

[10] H. Van Bui, F. Grillo, S. S. Kulkarni, R. Bevaart, N. Van Thang, B. van der Linden, J. A. Moulijn, M. Makkee, M. T. Kreutzer, and J. R. van Ommen, *Low-temperature atomic layer deposition delivers more active and stable Pt-based catalysts,* Nanoscale (2017).

[11] M. Argyle and C. Bartholomew, *Heterogeneous Catalyst Deactivation and Regeneration: A Review,* Catalysts 5, 145 (2015).

[12] E. D. Goodman, J. A. Schwalbe, and M. Cargnello, *Mechanistic understanding and the rational design of sinter- resistant heterogeneous catalysts,* ACS Catalysis 7, 7156 (2017).

[13] J. A. Moulijn, A. E. Van Diepen, and F. Kapteijn, *Catalyst deactivation: Is it predictable? What to do?* Applied Catalysis A: General 212, 3 (2001).

[14] Y. Nagai, T. Hirabayashi, K. Dohmae, N. Takagi, T. Minami, H. Shinjoh, and S. Matsumoto, *Sintering inhibition mechanism of platinum supported on ceria-based oxide and Pt-oxide-support interaction,* Journal of Catalysis 242, 103 (2006).

[15] K. Wettergren, F. F. Schweinberger, D. Deiana, C. J. Ridge, A. S. Crampton, M. D. Rötzer, T. W. Hansen, V. P. Zhdanov, U. Heiz, and C. Langhammer, *High sintering resistance of size-selected platinum cluster catalysts by suppressed ostwald ripening,* Nano Letters 14, 5803 (2014).

[16] P. N. Plessow and F. Abild-Pedersen, *Sintering of Pt Nanoparticles via Volatile PtO2: Simulation and Comparison with Experiments,* ACS Catalysis 6, 7098 (2016).

[17] E. Ruckenstein and B. Pulvermacher, *Growth kinetics and the size distributions of supported metal crystallites,* Journal of Catalysis 29, 224 (1973).

[18] P. J. F. Harris, *Growth and structure of supported metal catalyst particles,* International Materials Reviews 40, 97 (1995).

[19] G. Prieto, J. Zečević, H. Friedrich, K. P. De Jong, and P. E. De Jongh, *Towards stable catalysts by controlling collective properties of supported metal nanoparticles,* Nature Materials 12, 34 (2013).

[20] P. Wynblatt and N. A. Gjostein, *Supported metal crystallites,* Progress in Solid State Chemistry 9, 21 (1975).

[21] P. Wynblatt and N. A. Gjostein, *Particle growth in model supported metal catalysts-I. Theory,* Acta Metallurgica 24, 1165 (1976).

[22] Y. F. Chu and E. Ruckenstein, *Behavior of platinum crystallites on carbon substrates,* Surface Science 67, 517 (1977).

[23] D. S. Sholl and R. T. Skodje, *Late-stage coarsening of adlayers by dynamic cluster coalescence,* Physica A: Statistical Mechanics and its Applications 231, 631 (1996).

[24] K. Heinemann and H. Poppa, *Direct observation of small cluster mobility and ripening,* Thin Solid Films 33, 237 (1976).

[25] T. J. Woehl, C. Park, J. E. Evans, I. Arslan, W. D. Ristenpart, and N. D. Browning, *Direct observation of aggregative nanoparticle growth: Kinetic modeling of the size distribution and growth rate,* Nano Letters 14, 373 (2014).

[26] F. Grillo, H. Van Bui, J. A. Moulijn, M. T. Kreutzer, and J. R. Van Ommen, *Understanding and Controlling the Aggregative Growth of Platinum Nanoparticles in Atomic Layer Deposition: An Avenue to Size Selection,* Journal of Physical Chemistry Letters 8, 975 (2017).

[27] F. Wang, V. N. Richards, S. P. Shields, and W. E. Buhro, *Kinetics and mechanisms of aggregative nanocrystal growth,* (2014).

[28] D. V. Talapin, A. L. Rogach, M. Haase, and H. Weller, *Evolution of an ensemble of nanoparticles in a colloidal solution: Theoretical study,* Journal of Physical Chemistry B 105, 12278 (2001).

[29] N. J. J. Johnson, A. Korinek, C. Dong, and F. C. J. M. Van Veggel, *Self-focusing by Ostwald ripening: A strategy for layer-by-layer epitaxial growth on upconverting nanocrystals,* Journal of the American Chemical Society 134, 11068 (2012).

[30] A. La Torre, M. D. C. Giménez-López, M. W. Fay, G. A. Rance, W. A. Solomonsz, T. W. Chamberlain, P. D. Brown, and A. N. Khlobystov, *Assembly, growth, and catalytic activity of gold nanoparticles in hollow carbon nanofibers,* ACS Nano 6, 2000 (2012).

[31] H. Van Bui, F. Grillo, and J. R. van Ommen, *Atomic and molecular layer deposition: off the beaten track,* Chem. Commun. 53, 45 (2017).

[32] F. Grillo, M. T. Kreutzer, and J. R. van Ommen, *Modeling the precursor utilization in atomic layer deposition on nanostructured materials in fluidized bed reactors,* Chemical Engineering Journal 268, 384 (2015).

[33] A. Goulas and J. Ruud van Ommen, *Atomic layer deposition of platinum clusters on titania nanoparticles at atmospheric pressure,* Journal of Materials Chemistry A 1, 4647 (2013).

[34] A. Goulas and J. R. van Ommen, *Scalable production of nanostructured particles using atomic layer deposition,* KONA Powder and Particle Journal 31, 234 (2014).

[35] J. R. van Ommen, D. Kooijman, M. de Niet, M. Talebi, and A. Goulas, *Continuous production of nanostructured particles using spatial atomic layer deposition,* Journal of Vacuum Science & Technology A: Vacuum, Surfaces, and Films 33, 021513 (2015).

[36] S. M. George, *Atomic layer deposition: An overview,* Chemical Reviews 110, 111 (2010).

[37] B. J. O'Neill, D. H. K. Jackson, J. Lee, C. Canlas, P. C. Stair, C. L. Marshall, J. W. Elam, T. F. Kuech, J. A. Dumesic, and G. W. Huber, *Catalyst Design with Atomic Layer Deposition,* ACS Catalysis 5, 1804 (2015).

[38] R. L. Puurunen, *Surface chemistry of atomic layer deposition: A case study for the trimethylaluminum/water process,* Journal of Applied Physics 97 (2005).

[39] H. Kim, H. B. R. Lee, and W. J. Maeng, *Applications of atomic layer deposition to nanofabrication and emerging nanodevices,* (2009).

[40] A. J. M. Mackus, M. J. Weber, N. F. W. Thissen, D. Garcia-Alonso, R. H. J. Vervuurt, S. Assali, A. A. Bol, M. A. Verheijen, and W. M. M. Kessels, *Atomic layer deposition of Pd and Pt nanoparticles for catalysis: on the mechanisms of nanoparticle formation,* Nanotechnology 27, 034001 (2016).

[41] M. B. E. Griffiths, P. J. Pallister, D. J. Mandia, and S. T. Barry, *Atomic Layer Deposition of Gold Metal,* Chemistry of Materials 28, 44 (2016).

[42] N. P. Dasgupta, C. Liu, S. Andrews, F. B. Prinz, and P. Yang, *Atomic layer deposition of platinum catalysts on nanowire surfaces for photoelectrochemical water reduction,* J Am Chem Soc 135, 12932 (2013).

[43] C. Wang, L. Hu, K. Poeppelmeier, P. C. Stair, and L. Marks, *Nucleation and growth process of atomic layer deposition platinum nanoparticles on strontium titanate nanocuboids,* Nanotechnology 28 (2017).

[44] A. M. Lubers, C. L. Muhich, K. M. Anderson, and A. W. Weimer, *Mechanistic studies for depositing highly dispersed Pt nanoparticles on carbon by use of trimethyl(methylcyclopentadienyl)platinum(IV) reactions with O2 and H2O,* Journal of Nanoparticle Research 17 (2015).

[45] S. Sun, G. Zhang, N. Gauquelin, N. Chen, J. Zhou, S. Yang, W. Chen, X. Meng, D. Geng, M. N. Banis, R. Li, S. Ye, S. Knights, G. A. Botton, T. K. Sham, and X. Sun, *Single-atom catalysis using Pt/graphene achieved through atomic layer deposition,* Scientific Reports 3 (2013).

[46] V. Miikkulainen, M. Leskelä, M. Ritala, and R. L. Puurunen, *Crystallinity of inorganic films grown by atomic layer deposition: Overview and general trends,* Journal of Applied Physics 113 (2013).

[47] Z. Zhang and M. G. Lagally, *Atomistic processes in the early stages of thin-film growth,* Science 276, 377 (1997).

[48] J. A. Venables, G. D. T. Spiller, and M. Hanbucken, *Nucleation and growth of thin films,* Reports on Progress in Physics 47, 399 (1984).

[49] A. J. Mackus, M. A. Verheijen, N. Leick, A. A. Bol, and W. M. Kessels, *Influence of oxygen exposure on the nucleation of platinum atomic layer deposition: Consequences for film growth, nanopatterning, and nanoparticle synthesis,* Chemistry of Materials 25, 1905 (2013).

[50] J. Montejano-Carrizales, F. Aguilera-Granja, and J. Morán-López, *Direct Enumeration of the Geometrical Characteristics of Clusters,* Nanostructured Materials 8, 269 (1997).

[51] A. Le Valant, C. Comminges, F. Can, K. Thomas, M. Houalla, and F. Epron, *Platinum Supported Catalysts: Predictive CO and H2 Chemisorption by a Statistical Cuboctahedron Cluster Model,* The Journal of Physical Chemistry C 120, 26374 (2016).

[52] L. Kuipers and R. E. Palmer, *Influence of island mobility on island size distributions in surface growth,* Physical Review B 53, R7646 (1996).

[53] M. Vicanek and N. M. Ghoniem, *The effects of mobility coalescence on the evolution of surface atomic clusters,* Thin Solid Films 207, 90 (1992).

[54] M. J. J. Jak, C. Konstapel, A. van Kreuningen, J. Verhoeven, and J. W. M. Frenken, *Scanning tunnelling microscopy study of the growth of small palladium particles on TiO2(110),* Surface Science 457, 295 (2000).

[55] P. Jensen, *Growth of nanostructures by cluster deposition: Experiments and simple models,* Reviews of Modern Physics 71, 1695 (1999).

[56] G. R. Bell, P. M. Dawson, P. A. Pandey, N. R. Wilson, and P. A. Mulheran, *Size-dependent mobility of gold nano-clusters during growth on chemically modified graphene,* APL Materials 2 (2014).

[57] D. Kandel, *Selection of the scaling solution in a cluster coalescence model,* Physical Review Letters 79, 4238 (1997).

[58] T. Aaltonen, M. Ritala, T. Sajavaara, J. Keinonen, and M. Leskelä, *Atomic layer deposition of platinum thin films,* Chemistry of Materials 15, 1924 (2003).

[59] J. Dendooven, R. K. Ramachandran, E. Solano, M. Kurttepeli, L. Geerts, G. Heremans, J. Rongé, M. M. Minjauw, T. Dobbelaere, K. Devloo-Casier, J. A. Martens, A. Vantomme, S. Bals, G. Portale, A. Coati, and C. Detavernier, *Independent tuning of size and coverage of supported Pt nanoparticles using atomic layer deposition,* Nature Communications 8 (2017).

[60] V. Rontu, A. Selent, V. Zhivonitko, G. Scotti, I. Koptyug, V.-V. Telkki, and S. Franssila, *Efficient catalytic microreactors with atomic layer deposited platinum nanoparticles on oxide support,* Chemistry - A European Journal (2017).

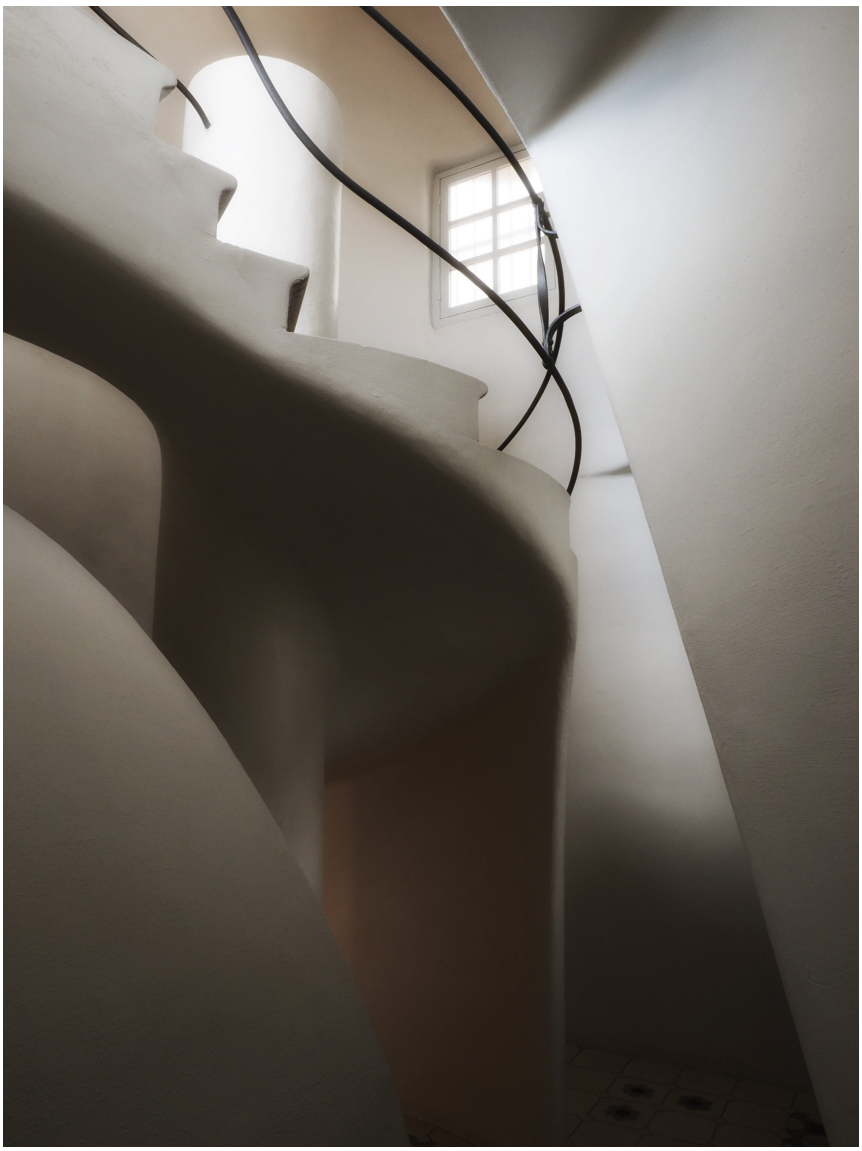

Casa Batlló, Barcelona, Spain 2016.

3

Understanding and Controlling the Aggregative Growth of Platinum Nanoparticles in Atomic Layer deposition: an Avenue to Size Selection

Refutations are seldom final;
in most cases, they are only a prelude to further refinements.

Bertrand, Russell

In this chapter, we present an atomistic understanding of the evolution of the size distribution with temperature and number of cycles in atomic layer deposition (ALD) of Pt nanoparticles (NPs). Atomistic modeling of our experiments teaches that the NPs grow mostly via NP diffusion and coalescence rather than through single-atom processes such as precursor chemisorption, atom attachment, and Ostwald ripening. In particular, our analysis shows that the NPs aggregation takes place during the oxygen half-reaction and that the NP mobility exhibits a size- and temperature-dependent scaling. Finally, we show that -contrary to what has been widely reported- in general, one cannot simply control the NP size by the number of cycles alone. Instead, while the amount of Pt deposited can be precisely controlled over a wide range of temperatures, ALD-like precision over the NP size requires low deposition temperatures (e.g., T<100 °C), when growth is dominated by atom attachment.

Published as: Fabio Grillo, Hao Van Bui, Jacob A. Moulijn, Michiel T. Kreutzer, and J. Ruud van Ommen, Understanding and Controlling the Aggregative Growth of Platinum Nanoparticles in Atomic Layer Deposition: An Avenue to Size Selection, *Journal Physical Chemistry Letters*, 2017, 8 (5), pp 975–983.

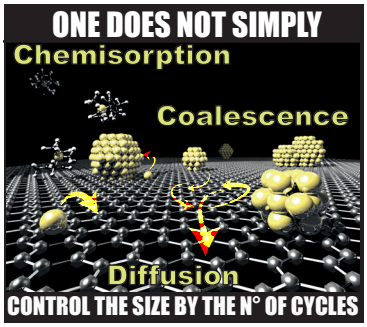

3.1. Introduction

Supported nanoparticles (NPs) play a major role in a wide range of applications from catalysis to electronic, optical, and energy storage devices [1–5]. Scaling materials down to the nanoscale not only maximizes the number of active surface sites, but also brings about unique size-dependent functionalities [3, 6–8]. The latter, however, can only be understood and harnessed through the advent of synthesis routes that enable the deposition of NPs with narrow particle size distributions (PSDs), that is, size-selected NPs [9, 10]. Despite its potential, the scalable synthesis of size-selected NPs on high-surface-area supports, which are relevant to most practical applications, has so far proved elusive [10]. Atomic layer deposition (ALD) is an established thin film deposition technique that has recently seen use in the synthesis of supported NPs with very promising results in terms of control over the NP size [2, 4, 11–14]. By relying on the cyclic repetition of self-limiting gas-solid reactions, ALD boasts digital control and atomic-level precision over the amount of material being deposited [4, 11, 15]. While originally developed for flat substrates, ALD is readily scalable to high-surface-area substrates thanks to its solvent-free and surface-driven nature [4]. Considerable research effort has thus been made to bring the unparalleled atomic-level precision of ALD to the synthesis of supported NPs. Nevertheless, the development of ALD routes for size-selected NPs is currently hampered by a lack of fundamental understanding [4, 16, 17]. The majority of fundamental studies on ALD is, in fact, concerned with the surface chemistry behind the deposition of the atoms of choice on a given substrate, and far less research has been devoted to the understanding of the diffusion phenomena underlying the formation of NPs and the evolution of their PSD [4, 16–21]. As a result, ALD of NPs has been reported with different PSDs and the growth mechanisms leading to these different PSDs are still under debate [1, 2, 4, 12, 14, 17, 20–23].

The understanding of ALD growth is mostly framed in terms of sequential self-limiting chemisorption of ALD precursors leading to a layer-by-layer deposition [21]. However, the nucleation and growth of NPs is bound to be dictated by atomistic processes other than chemisorption such as surface diffusion of adatoms, NP nucleation, diffusion and coalescence, and atom attachment to and detachment from NPs [6, 21, 24–28]. In a seminal work, Mackus et al. [20] argued that, during Pt ALD on oxides, Pt NPs might grow not only due to ALD surface reactions, but also through Ostwald ripening via volatile PtO_2,

i.e., the growth of larger NPs at the expenses of smaller ones through the exchange of single atoms driven by the minimization of the surface energy. Outside the field of ALD, analysis of the PSD has revealed that apart from classical ripening, another mechanism is relevant to the growth of supported NPs: Smoluchowski aggregation [29–31], i.e., NP diffusion and coalescence. Several questions remain, therefore, unanswered: Can we understand NP growth in terms of elementary atomistic processes, and thus identify the governing NP growth mechanisms among layer-by-layer growth due to direct precursor chemisorption, single atom deposition on the substrate followed by attachment to NPs, Ostwald ripening, and NP diffusion and coalescence? And, can we steer the growth so as to achieve size-selection and control the size by simply the number of cycles?

In this chapter, we identify the governing mechanisms behind the nucleation and growth of Pt NPs during ALD. We do so by using the Pt(MeCp)Me_3/O_2 ALD process on bulk quantities of graphene nanoplatelets, which is, as we shall point out later, a model system relevant to several other Pt ALD processes. This platform allowed us to experimentally follow the evolution of the PSD and of the amount of metal deposited during the initial stages of NP growth, i.e., the first 10 ALD cycles. In particular, to shed light on the role of the precursor chemisorption on the NPs nucleation and growth, we probed ex-situ the morphology of the Pt/graphene composites after the first Pt(MeCp)Me_3 and O_2 half-cycles. To further deconvolute the effect of deposition and the growth due to NP sintering, we performed dedicated annealing experiments with the as-synthesized Pt/graphene composites. By modeling the relevant atomistic processes using a rate-equation approach, we could interpret, for the first time, the evolution of the shape of the PSD with the number of ALD cycles and the deposition temperature. Our analysis shows that NPs growth is best described in terms of Smoluchowski aggregation kinetics over a wide range of temperatures, i.e., 80-250 °C, that is, the NPs grow mostly through NP diffusion and coalescence rather than due to single-atom processes such as single-atom attachment/deposition and Ostwald ripening. The story is nuanced, though, as all depends on the cycle number and the deposition temperature: At lower temperatures, growth by single-atom attachment becomes relevant as NPs tend to pin on the substrate, such that the PSD remains narrow. Therefore, we show that, while digital control over the amount of metal being deposited can be achieved over a wide range of temperatures, ALD precision over the NP size is only retained at low deposition temperatures. In other words, contrary to what has been widely claimed [4, 12, 22], in general one cannot precisely control the NP size by simply varying the number of ALD cycles.

3.2. Method

The deposition experiments were carried out in an fluidized bed reactor operated at atmospheric pressure, already described elsewhere [2, 14], via a Pt(MeCp)Me_3/O_2 ALD process on gram-scale batches of graphene nanoplatelets with a specific surface area of 150 $m^2\,g^{-1}$. The latter translated into cycle times of 19-24 min depending on the deposition temperature. In particular, synthetic air (20 wt% O_2) was used as the oxygen source and exposures of 5-10 min were employed to assure the complete removal of organic ligands at all temperatures (see Figure 3.B.10); the Pt(MeCp)Me_3 exposure time was of 4 min; the Pt(MeCp)Me_3 and O_2 exposures were separated by purging steps of 5 min, where nitrogen was used as the purging gas (N_2, 99.999 vol%). Prior to deposition, the graphene powders were treated with ozone for 30 min at 200 °C in order to remove adventitious carbon and activate their

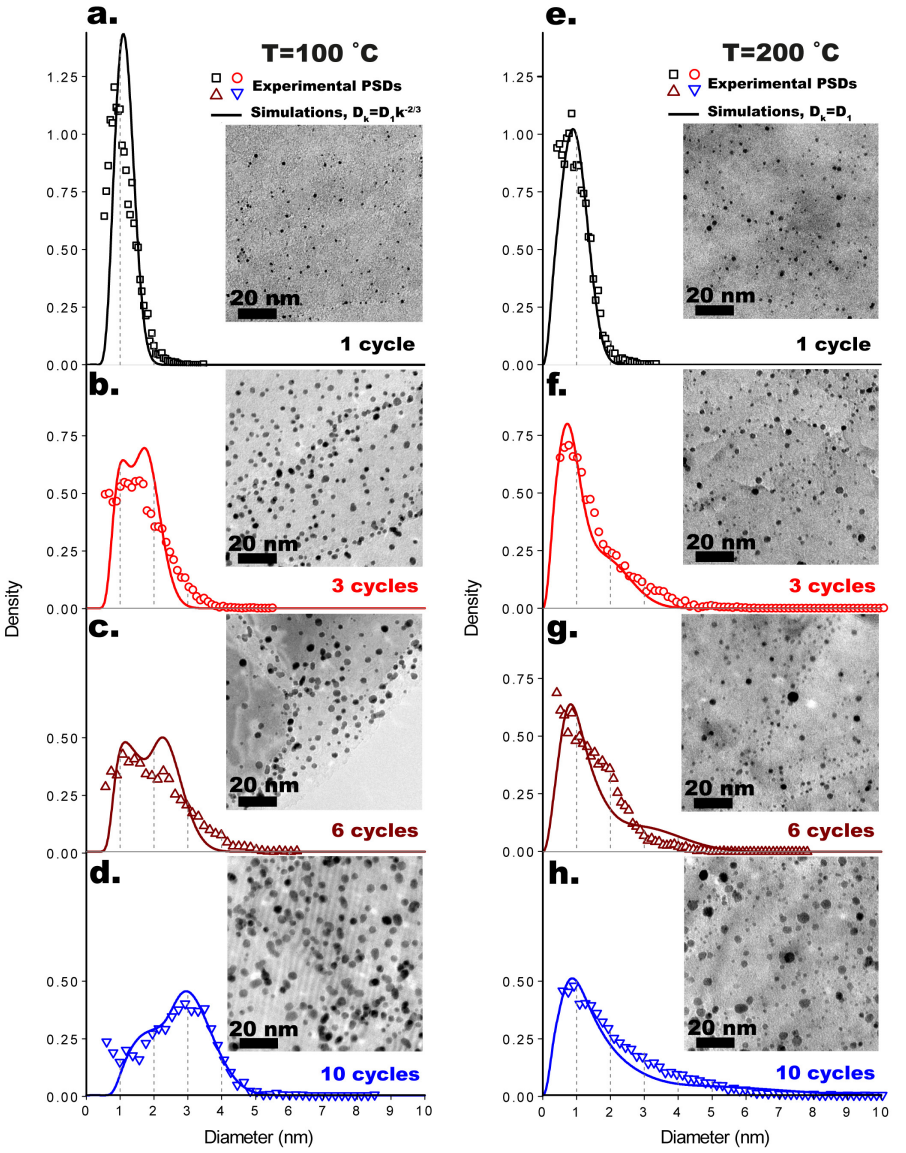

Figure 3.1: Evolution of the experimental and simulated particle size distributions (PSDs) at 100 °C after 1 (a), 3 (b), 6 (c), and 10 (d) cycles, and at 200 °C after 1 (e), 3 (f), 6 (g), and 10 (h) cycles, with a representative TEM micrograph in the respective inset. The PSDs are expressed in terms of probability density function and equivalent projected diameter. Each experimental point corresponds to a bin. The number of bins was calculated by using the Freedman-Diaconis method.

inherently defective surface by incorporating oxygen-containing functional groups for the initial $Pt(MeCp)Me_3$ chemisorption [14, 22, 32]. Annealing experiments were performed

ex-situ both in air and in argon atmospheres at 200 °C and 400 °C for 6, 12, 24, and 48 hours. The Pt/graphene composites were analyzed ex-situ using a suite of characterization techniques including transmission electron microscopy (TEM), high resolution TEM (HRTEM), X-ray photoelectron spectroscopy (XPS), X-ray diffraction (XRD), Raman spectroscopy, thermogravimetric analysis (TGA), and instrumental neutron activation analysis (INAA). The PSDs were obtained by determining the projected area ($\mathcal{A}$) and thus the equivalent projected diameter ($d = \sqrt{\mathcal{A}/4\pi}$) of more than 6000 NPs per sample by means of semi-automatic image analysis of about 10–20 TEM pictures, taken at different magnifications (e.g., 50000x and 100000x) and sample locations. For more experimental details the reader is referred to the Appendix.

3.3. Results and discussion

3.3.1. Experimental results

XPS, XRD, and HRTEM results are consistent with the deposition of metallic and crystalline Pt 3D NPs (see Figure 3.B.2, Figure 3.B.3, and Figure 3.B.8). According to the elemental analysis carried out via INAA, the platinum loading (i.e., Pt atoms per unit area of substrate) varies in an approximately linear fashion with the number of cycles while being virtually temperature-independent in the range of temperatures and ALD cycles considered here, i.e., from 100 °C to 250 °C and from 1 to 10 cycles. Furthermore, the NPs density was estimated to be fairly constant and about 0.0025 nm^{-2} within the temperature range 100-200°C and the cycle range 1-10 (Table S1). Several previous studies on thermal ALD of Pt have reported temperature-dependent growth rates [4, 15, 17, 20, 33]. In particular, thermal ALD of Pt has never been reported for such low temperatures (i.e., T= 80 °C). This is due to the fact that, while the Pt(MeCp)Me_3 chemisorption can be active even at room temperature [17, 34], the oxidation of carbon ligands on non-catalytic surfaces becomes relatively slow below ~ 250 °C at typical ALD conditions, i.e., low oxygen pressures (~ 0.1–1 Torr) and oxygen exposure times on the order of few seconds [4, 15, 17, 20, 33]. Here, instead, we achieved ALD growth at temperatures as low as 80 °C by using oxygen partial pressures on the order of 0.2 bar (~1500 Torr) and oxygen exposure times between 5 and 10 min (Figures 3.B.9 and 3.B.10)). In fact, the combustion kinetics of adsorbed carbon is not only a function of temperature, but also of the partial pressure of the oxidizer [4, 20]. This latter remark emphasizes that in all those ALD processes leading to NP formation based on the combustion of organic ligands, the partial pressure of the oxidizer as well as the exposure time can be more important than the number of cycles, as far as the amount of metal deposited, and thus the average NP size, is concerned.

While the deposition temperature had little to no effect on the Pt loading, it did have a dramatic effect on the evolution of the shape of the PSD with the number of cycles (Figures 3.1). In particular, we observe two different growth regimes, one at low temperatures (i.e., T≤100 °C) and one at high temperatures (i.e., T≥150 °C). The high temperature regime is characterized by broad right-skewed PSDs presenting a persistent peak at about 1 nm followed by a long tail, which shifts towards large sizes as the number of ALD cycles increases. On the other hand, at low temperatures, the PSD remains relatively narrow and increasing the number of cycles results into the gradual disappearance of the peak on the small-size side and the appearance of a new peak towards large sizes, whose position gradually shifts

to the right (Figures 3.1). Surprisingly, low temperatures result in PSDs with larger average diameters (e.g., $\langle d \rangle_{100\,^\circ\mathrm{C}}^{10\ \mathrm{cycles}} = 2.6$ nm and $\langle d \rangle_{200\,^\circ\mathrm{C}}^{10\ \mathrm{cycles}} = 2.0$ nm) that retain relatively low standard deviations (e.g., $\sigma_{100\,^\circ\mathrm{C}}^{10\ \mathrm{cycles}} = 1$ nm and $\sigma_{200\,^\circ\mathrm{C}}^{10\ \mathrm{cycles}} = 1.4$ nm).
The ALD process used here is a representative model system for oxygen-based ALD of Pt NPs in that it reproduced the characteristics of the PSDs reported by different authors for various Pt ALD processes on different substrates and at different temperatures [1, 2, 17, 22]. For example, the features of the high-temperature PSDs can be found in the PSDs reported in the works of: Goulas et al. [2] on the radical-enhanced and atmospheric pressure variant of Pt ALD (250 °C) on TiO_2 nanopowders (1–5 ALD cycles); Sun et al. [22] on the use of Pt ALD (250 °C) for single-atom catalysis (50–150 ALD cycles) on graphene powders; and Mackus et al.[17] on Pt ALD (300 °C) on single-crystal alumina (20–100 ALD cycles). On the other hand, the PSD obtained at low temperature after 10 cycles (T≤100 °C), being narrow and left-skewed, resembles the PSDs reported for plasma-enhanced Pt ALD carried out at room temperature on single-crystal alumina (20–100 ALD cycles) [17]. Clearly, the different growth regimes reported here are an intrinsic characteristic of oxygen-based ALD of Pt NPs.

To resolve the NP formation and growth in finer detail, we studied the morphology of the Pt/graphene composites after the first half-cycle (i.e., Pt(MeCp)Me_3/N_2) as compared to the full cycle (Pt(MeCp)$Me_3/N_2/O_2/N_2$) and the stability of the as-synthesized Pt NPs against prolonged annealing periods at different temperatures. Ex-situ TEM of the Pt/graphene after one half-cycle and one full cycle at 100 °C revealed that the NPs form and grow mostly during the oxidation step (parts a–b of Figure 3.2). This is direct evidence of the fact that, in ALD, NPs can grow via routes other than direct deposition, and thus layer-by-layer growth, at a temperature as low as 100 °C. Subsequent annealing periods in air up to 12 hours at 200 °C resulted in virtually no further NP growth (Figure 3.2d), and only after 24 hours the PSD changed appreciably (parts b–d of Figure 3.2). Annealing of the Pt/graphene obtained after 10 cycles at 100 °C revealed a similar picture, in particular: The composites were relatively stable at 200 °C even after 24 hours in air (Figure 3.B.11). However, annealing periods of more than 6 hours at 400 °C in air resulted in the formation of fractal aggregates of relatively large NPs (d_p ~5–10 nm), consistently with the onset of NP unpinning, diffusion and aggregation above a certain thermal energy threshold.
The fact that the NPs can form and grow at 100 °C upon exposures to oxygen of only 5 min, while remaining virtually stable for 12 hours at 200 °C in the same atmosphere, shows that the aggregation of Pt atoms and thus the NP growth during ALD is induced by the combustion of the organic ligands remaining on the surface after Pt(MeCp)Me_3 chemisorption [35, 36]. Adsorbed organic materials are, in fact, known to suppress the aggregation of supported metals by mediating their mobility [10, 25, 37], especially on graphene surfaces. In addition, combustion reactions catalyzed by the metal itself can evolve heat and gas such as to generate local temperature and pressure fluctuations that can unpin and displace NPs as a whole, thus promoting sintering via NP diffusion and coalescence [38–40], even at temperatures that would not otherwise provide the thermal budget for the onset of mobility. Indeed, the burning of carbon coke adsorbed on commercial catalysts based on oxides-supported Pt is also known to induce metal sintering [38]. Hence, we propose the following NP formation and growth mechanism: The carbon remaining on the surface after the precursor chemisorption suppresses the Pt mobility by providing steric hindrance as well as preferential

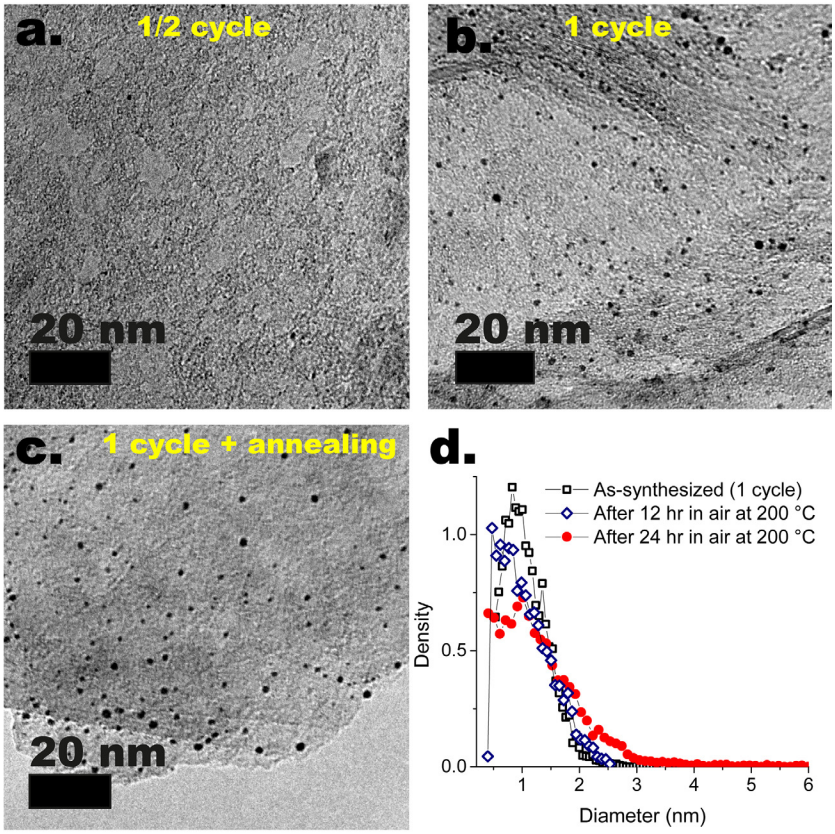

Figure 3.2: (a) Ex-situ TEM of the graphene nanoplatelets after one half-cycle ($Pt(MeCp)Me_3/N_2$) at 100 °C, after one full cycle (b) at 100 °C ($Pt(MeCp)Me_3/N_2/O_2/N_2$), and after one cycle at 100 °C and annealing in air at 200 °C for 24 hours. (d) Particle size distributions of the NPs deposited after one cycle at 100 °C, and before and after annealing in air at 200 °C for 12 and 24 hours.

binding sites for both Pt atoms and NPs; as a result, the removal of carbon promotes the surface diffusion of Pt atoms and thus their aggregation, that is, NP formation; once formed, NPs grow due to further capture of diffusing atoms as well as collision and subsequent coalescence with NPs diffusing as a whole; transient NP mobility is induced by the heat and the gas locally evolved by the combustion reactions that unpin NPs from strong-binding sites.

3.3.2. Model vs Experiments

To identify the governing mechanism behind the different evolution of the PSD at different temperatures, we devised two dynamic models: Model (I) accounts for NP diffusion and coalescence, whereas model (II) accounts for Ostwald ripening. For a qualitative representation of the atomistic processes considered here and their effect on the morphology see Figure 3.3. Furthermore, for a detailed description of the models and their parameters the reader is re-

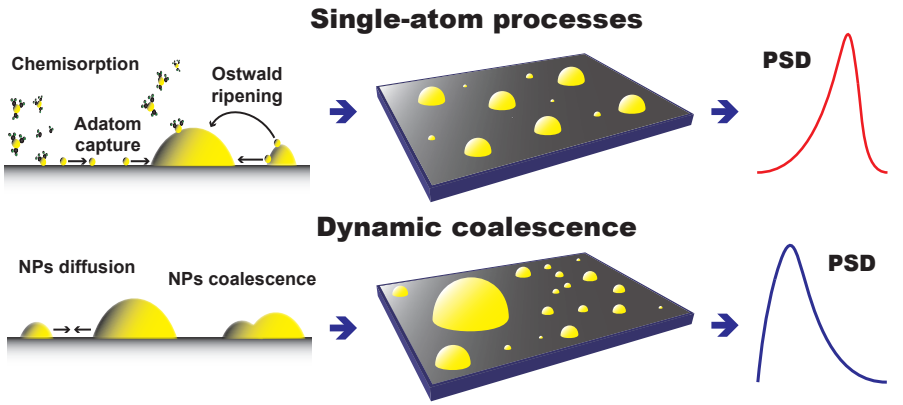

Figure 3.3: Schematic representation of the atomistic processes relevant to ALD of NPs and their effect on morphology, particularly on the shape of the PSD.

ferred to the Appendix 3.A. Both models describe the evolution in time of the population of single atoms and NPs with different sizes. Model (I) is based on Smoluchowski aggregation kinetics [41–43] and allows for: Cyclic generation of single atoms on both the substrate surface and the NPs (deposition); surface diffusion and irreversible aggregation of single atoms; atom attachment to NP (adatom capture); and NP diffusion and coalescence. The NP mobility was assumed to follow a power law of the kind $D_k = D_1(t)k^{-s}$ [30, 31, 42, 44–47], where k is the number of atoms comprising the NP, $D_1(t)$ is the diffusion rate of adatoms, and $s > 0$. The value of the exponent s typically ranges between 0 and 2 depending on the diffusion mechanism and is, in general, a poorly understood function of NP morphology, NP-substrate interaction, reacting atmosphere, and temperature [31, 44, 45]. As such, here it is regarded as a fitting parameter.

Model (II) is a variation of model (I) and allows for: deposition; surface diffusion and aggregation of single atoms; atom attachment to NP; and Ostwald ripening. The thermodynamic driving force for the latter lies in the size-dependent stability of NPs (Gibbs-Thompson effect) [48, 49]. However, in order for Ostwald ripening to take place, several kinetic steps have to be realized: Atom detachment from small NPs, surface diffusion or transport through the vapor phase to larger NPs and subsequent attachment[27, 50, 51]. Each of these steps can be kinetically limited due to large energy barriers. In the case of platinum, the high Pt-Pt bond energy makes the detachment of an atom from Pt NPs an unlikely event [27, 48, 50, 51], especially when Pt does not enjoy a very strong adsorption on the support. For example, Zhou et al. [48] argued that Pt NPs adsorbed on TiO_2 consisting of only few tens of atoms (~0.5-1 nm) are kinetically stable against surface-mediated Ostwald ripening at ALD conditions (at vacuum). A more favorable pathway for Ostwald ripening is the exchange of single atoms in the form of volatile PtO_2 through the vapor phase in the presence of oxidizing atmospheres [20, 27, 50, 51]. Plessow and Abild-Pedersen [50] have recently shown through simulations that gas-phase-mediated ripening can account for the temperature and oxygen pressure dependence of the sintering of Pt NPs supported on alumina and silica at high temperatures (600 °C). On the other hand, they also argued that hardly any sintering via Ostwald ripening is expected to occur up to temperatures of about 400 °C,

even at relatively high oxygen partial pressures (0.1 bar) and for annealing times on the order of several hours. Nonetheless, given that during ALD of Pt, combustion reactions can lead to local temperatures that are considerably higher than the actual deposition temperature, we still consider Ostwald ripening among the possible growth mechanisms. Since gas-phase-mediated ripening has more favorable and less substrate-dependent energetics than surface-mediated ripening, the treatment of Ostwald ripening in model (II) is based on the work of Plessow and Abild-Pedersen [50]. At any rate, this allows us to study the hypothetical effect of Ostwald ripening on the shape of the PSD during ALD of NPs.

The dynamic models allowed us to rule out nucleation and growth scenarios that are

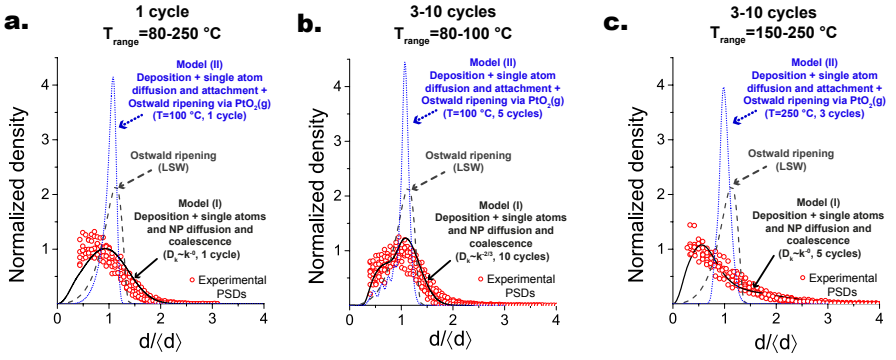

Figure 3.4: Experimental and simulated PSDs rescaled with respect to their respective average diameter and then normalized with respect to their integral. The black solid lines are representative PSDs obtained with model (I), the dark gray dashed line is the classical Lifshitz-Slyozov-Wagner (LSW) PSD for diffusion-limited Ostwald ripening, and the blue dotted lines are representative PSDs obtained with model (II). (a) Experimental PSDs obtained after 1 cycle in the temperature range 80–250 °C, the sum of squared errors (SSE) for model (I), model (II), and the LSW PSD is equal to 3, 131, and 49, respectively. (b) Experimental PSDs obtained in the temperature range 80–100 °C and in the cycle range 3–10, the SSE for model (I), model (II), and the LSW PSD is equal to 9, 182, and 65, respectively. (c) Experimental PSDs obtained in the temperature range 150–250 °C and in the cycle range 3–10, the SSE for model (I), model (II), and the LSW PSD is equal to 3, 157, and 72, respectively.

typically invoked in the literature to describe the growth of NPs in ALD[17, 18, 20, 21]: (1) NP nucleation in the first cycle followed by layer-by-layer growth on preexisting nuclei; (2) deposition on both the substrate and the NPs, single atom diffusion, aggregation, and attachment, i.e., Model (I) letting $s \longrightarrow +\infty$; and (3) deposition on both the substrate and the NPs, single atom diffusion, aggregation, and attachment, and gas-phase-mediated Ostwald ripening, i.e., Model (II). None of these scenarios described the observed PSD evolution (Figures 3.4). In particular, scenario (1) fails to describe the evolution of both the shape of the PSD and the Pt loading (Figure 3.A.3). Scenario (2) is characterized by left-skewed PSDs with a very narrow peak and a clear cut-off on the large-sizes side. In this case, increasing the number of cycles results in a shift of the peak towards larges sizes and increasingly longer tails on the small-sizes side. Furthermore, the cyclic generation of single atoms on the substrate coupled with the absence of an annealing mechanism (e.g., NP diffusion and coalescence, and Ostwald ripening) gives rise to a series of nucleation peaks on the small-sizes side, whose number correlates with the number of cycles (Figure 3.A.4). Interestingly, such feature is observable in the left-skewed and narrow PSDs reported for plasma-enhanced Pt ALD

at room temperature [17]. This points to the fact that at such low temperatures the NPs are stable and effectively pinned on the substrate surface and that ALD growth proceeds, indeed, via single-atom attachment/deposition. Finally, it is worth noting that in scenario (II), each cycle results in an increase in the number of NPs per unit area, which, in the limit of low coverages, eventually saturates to a critical value depending on the ratio between single atoms surface diffusion and generation rates [26].

We also ruled out Ostwald ripening as the dominant growth mechanism as model (II) fails to give a qualitative description of the evolution of the PSD (Figures 3.A.5, 3.A.6 and 3.4), regardless of the temperature used for the simulations. In brief, below 200 °C the addition of Ostwald ripening has little to no effect on the PSDs, which thus overlap with the ones of scenario (2). As expected, the onset of Ostwald ripening at higher temperatures results in the disappearance of the smaller NPs, and thus of the long tails on the small-sizes side of scenario (2). Less trivially, the disappearance of smaller NPs in each cycle is also accompanied by the progressive narrowing ("focusing") of the PSD, which remains nearly symmetric (Figures 3.A.5, 3.A.6, and 3.4c). On the other hand, simulated annealing periods after deposition on the order of tens to hundreds of hours result in the gradual broadening of the PSD ("defocusing"), which eventually approaches its the stationary self-similar form (Figures 3.A.6 and 3.A.7). The latter is slightly more symmetric than the left-skewed PSD predicted by the Lifshitz-Slyozov-Wagner (LSW) theory for diffusion-limited Ostwald ripening [29, 49]. Nevertheless the LSW PSD is a fair approximation and, as such, it is plotted in Figure 3.4 as a reference for the asymptotic PSD in case of Ostwald ripening. The transient focusing of the PSD discussed here is analogous to the behavior of an ensemble of NPs in a colloidal solution undergoing Ostwald ripening in the presence of an excess of monomers that was described by Talapin et al. [49] via Monte Carlo simulations. Johnson et al. [52] exploited the same phenomenon to grow core-shell NPs with very narrow PSDs in a layer-by-layer fashion by employing successive injections of small sacrificial NPs of the shell material to a colloidal solution containing the larger core NPs. Although the focusing of the PSD by Ostwald ripening could inspire the development of analogous NP synthesis routes based on ALD, it clearly cannot account for the PSDs observed here. Finally, the fact that model (II) cannot describe the PSD evolution reinforces the notion that Ostwald ripening of supported noble metals NPs is a slow process that dominates the late stages of growth of large and immobile NPs (i.e., $d_p > 5$ nm) at high temperatures (~ 400–1000 °C) and at long time scales (several hours to years) [25, 27, 30, 51, 53–58],

We could describe the shape of the experimental PSDs and their evolution with the number of cycles and temperature only when allowing for NP diffusion and coalescence, i.e., through model (I) (Figure 3.4). Analysis of the full evolution of the PSD shape (Figure 3.1) revealed that at low deposition temperatures the NP mobility drops with increasing NP-substrate contact area ($D_k \sim k^{-2/3}$), whereas at high temperatures the NP mobility is virtually size-independent ($s \sim 0$). In other words, at low temperatures, upon reaching a critical size, the NPs are effectively pinned on the substrate surface, thus acting as sinks for the mobile NPs that nucleate in their neighborhood, which explains the gradual disappearance of the peak on the small-size side (i.e., the nucleation peak). On the other hand, at high temperatures, since all the diffusing species enjoy the same mobility and approximately the same capture efficiency: New nuclei can form and persist in each cycle, such that the nucleation peak remains in every cycle and the PSD gradually broadens. This picture is also in agreement

with a qualitative assessment of the space-correlation of the NPs in the two different temperature regimes (see Figures 3.1, 3.B.5, 3.B.6, 3.B.7, 3.B.8): At low temperatures the NPs tend to be well-spaced, whereas at high temperatures small NPs can coexist next to large ones and the distribution of the inter-particle distance is qualitatively broad. Finally, we ascribe the temperature-dependent scaling of the NP mobility to the temperature dependence of the combustion rate of carbon ligands: At high temperatures, high combustion rates result in local heat and gas evolution that induces the unpinning of small NPs as well as large ones, whereas at low temperatures, slower combustion kinetics result in temperature and pressure fluctuations of lesser magnitude that can drive the diffusion of only relatively small NPs.

3.3.3. Final remarks and implications

Although our analysis shows that NP diffusion and coalescence is certainly relevant to ALD of Pt NPs, one might expect that the exact size and temperature dependence of the NP mobility depends on the nature of the substrate and on the choice of co-reactant (e.g., O_2 and H_2) [25, 27, 36, 38]. For example, defects and functional groups on the substrate surface can act as strong binding sites or anchoring points for the Pt NPs and are expected to reduce the NP mobility [30], and thus the metal aggregation [36]. In particular, the nature of the defect determines its trapping energy, and thus the temperature at which an NP of a given size has enough thermal energy to unpin [59]. From this perspective, given the autocatalytic nature of combustion reactions, we speculate that there exists a well defined critical deposition temperature for a given substrate and a given oxygen partial pressure at which combustion reactions locally evolve enough heat and gas to unpin small and large NPs alike. In other words, the exact temperature discriminating between growth regimes might differ between substrates, yet two temperature regimes are expected to arise on substrates with different nature, e.g., TiO_2 and graphene nanoplatelets. The considerations put forward so far for oxygen might hold for other co-reactants as they also inherently result in the removal of organic ligands, and thus in local evolution of heat and gas. For example, Lubers et al. [36] have shown that using H_2 instead of O_2 as a co-reactant leads to smaller NPs and a less effective ligands removal. In this case, the latter might have mitigated the NP aggregation due to the mediating effect of the remaining ligands on NP diffusion and a less vigorous heat and gas evolution. However, using H_2 also resulted in significantly lower deposition rates, which alone might account for the smaller NPs. Therefore, the effect of the co-reactant on the evolution of the PSD certainly merits further study.

The inclusion of NP diffusion and coalescence among the NP-growth mechanisms relevant to ALD has important implications for its potential use in the synthesis of supported NPs. One implication is that the deposition temperature can be used to tailor the shape of the PSD and the NPs space-correlation depending on the target application: Narrow PSDs and well-spaced NPs at low temperatures and broad PSDs and particle-distance distributions at high temperatures. A corollary to this is that, in general, one cannot precisely control the NP size by simply varying the number of cycles, as in most instances this would not only result in an increase in the average diameter, but also in a broadening of the PSD. In particular, control over the NP size with ALD-like atomic-level resolution can only be retained when the growth is dominated by single-atom attachment/deposition, that is, when the operating conditions during removal of organic ligands are such that the NPs are virtually immobile.

The second important implication regards the understanding of selective ALD of NPs on

surface defects. For instance, based on the observation of the morphology of graphene after 500–1000 Pt ALD cycles Kim et al. [60] concluded that Pt is predominately deposited on line defects as opposed to basal planes. In light of our results, however, one can explain the same observation by invoking uniform deposition over the entire substrate surface followed by the formation of mobile NPs that, over time, selectively pin onto the line defects, thus depleting the basal planes from ALD-grown material.

3.4. Conclusions

In summary, we studied the evolution of the PSD of Pt NPs in oxygen-based Pt ALD on bulk quantities of graphene nanoplatelets via a joint experimental and modeling approach. While different deposition temperatures resulted in virtually the same amount of deposited metal, the temperature had a dramatic effect on the PSD shape and its evolution with the number of cycles. Low deposition temperatures resulted in narrow PSDs and a mode that gradually shifts towards the large-size side with increasing number of cycles. On the other hand, high deposition temperatures resulted in PSDs presenting a persistent peak in the small-size side and a gradual broadening with increasing number of cycles. Ex-situ TEM of the ALD half-cycles and dedicated annealing experiments show that the NPs form and grow mostly during the oxidation of the carbon ligands, after which they are relatively stable. Both analytical and numerical modeling show that the shape of the PSD and its evolution with temperature and number of cycles are best described in terms of sintering via NP diffusion and coalescence. In particular, the NP mobility was found to exhibit a temperature- and size-dependent scaling. At low temperatures, the NP mobility scales as the inverse of the contact area with the substrate, whereas at high temperatures it is virtually size-independent. As a result, at low temperatures, the NPs effectively pin onto the susbtrate surface once they reach a certain size, which then act as sinks for the small mobile NPs nucleating in their proximity. This explains the gradual disappearance of the peak on the small-size side with increasing number of cycles. At high temperatures, instead, the NP mobility is size-independent, that is, both nucleating NPs and preexisting large NPs enjoy approximately the same capture efficiency, hence the persistent nucleation peak in the PSD and its broadening with the number of cycles. We attribute the temperature-dependent scaling of the NP mobility to the different magnitudes of the local temperature and pressure fluctuations brought about by the combustion of carbon ligands at different temperatures. The insights presented here are relevant not only to ALD of Pt NPs but to ALD of noble-metals NPs in general, as these processes are typically based on the cyclic combustion of organic ligands and NP formation through metal aggregation. Finally, the fundamental insights presented in this letter open up an avenue for the development of ALD routes for the scalable synthesis of size-selected NPs on high-surface-area substrates.

Appendix

3.A. Population Balance Modeling

Here, we first elaborate on the modeling of the deposition process that allows for the diffusion and aggregation of single atoms and NPs (model(I)), and later we describe the modeling of the deposition process that allows for single atoms diffusion and attachment, and gas-phase-mediated ripening of NPs via volatile PtO_2 (model(II)).

Model (I): Deposition and irreversible aggregation by NP diffusion and coalescence

The nucleation and growth of nanoparticles is described by means of the Smoluchowski equation adjusted for compact 3D islands undergoing 2D diffusion and a time-dependent generation term accounting for deposition on both the substrate and the preexisting nanoparticles. The model thus describes the following physical picture:

- In each cycle a certain number of single atoms is generated on both the substrate surface and the preexisting NPs over the time scale τ_{rxn}, which is assumed to vary in the interval from 0 to the cycle time t_{cycle}. The single atoms diffuse over the substrate surface at a rate equal to $D_1(t)$. The meeting of two single atoms leads to the formation of a stable cluster (irreversible growth) or nanoparticle (NP). Once NPs are formed, single atoms can also attach to them (growth due to single-atom attachment). NPs diffuse over the substrate at a rate equal to D_k, where k is the size, i.e., number of atoms comprising the NP. The collision of an NP of size i with a cluster of size j leads to the irreversible and instantaneous formation of a NP of size $i+j$ (diffusion limited aggregation). In particular, only binary collisions are considered (low coverage hypothesis) and single atom detachment from NPs is not treated (no Ostwald ripening).

The model translates into the following population balance:

$$\frac{dn_1}{dt} = g_s(t) - n_1 \sum_{i=1}^{\infty} K_{1i} n_i \tag{3.1}$$

$$\frac{dn_k}{dt} = g_p(t)\left[n_{k-1}(k-1)a_{k-1} - n_k k a_k\right] + \frac{1}{2}\sum_{i+j=k} K_{ij} n_i n_j - n_k \sum_{i=1}^{\infty} K_{ki} n_i \tag{3.2}$$

where n_1 is the population of single atoms on the substrate (at/nm^2), n_k the population of NPs consisting of k atoms, K_{ij} the collision rate between entities of size i and j, a_k is the fraction of surface atoms in an NP of size k (i.e., dispersion), $g_s(t)$ is a time-dependent term accounting for the cyclic generation of mobile atoms on the substrate surface due to ALD reactions expressed in atoms per unit area and time, and, likewise, $g_p(t)$ accounts for

direct deposition on NPs and is expressed in atoms per unit time per number of NP surface atoms (i.e., monolayers per unit time). Without loss of generality K_{ij} can be expressed as [26, 42, 46, 47]:

$$K_{ij} = \sigma_i D_i + \sigma_j D_j \tag{3.3}$$

where σ_i and σ_j are referred to as capture numbers and account for geometric effects on the capture efficiency of species of size i and j, respectively; whereas, D_i and D_j are the 2D diffusion rates of the species i and j, respectively. The capture numbers are a function of the size and the spatial density of the NPs at any given time, and can be estimated from the analytical solution of the 2D diffusion problem in the neighborhood of a diffusing species of arbitrary size. Here, they were estimated in a self-consistent manner as described by Hubartt et al. [47], by solving the following equation at each time step:

$$\sigma_i = \frac{2\pi r_i}{\xi} \frac{K_1(r_i/\xi)}{K_0(r_i/\xi)} \tag{3.4}$$

where r_i is the projected radius of the NP of size i, K_1 and K_0 are the modified Bessel functions of the second kind, and ξ is the diffusion length calculated estimated with the following equation [47]:

$$\xi^{-2} = \sum_{k=1}^{\infty} \sigma_k n_k \tag{3.5}$$

Given the 3D nature of the NPs, the projected diameter d_k ($2r_i$) is let:

$$d_k = \alpha k^{1/3} \tag{3.6}$$

where α is the NP shape factor, which is assumed to be constant over the whole size range. In the case of 3D compact islands undergoing 2D diffusion, the capture numbers are slowly varying functions of time and NPs size, and thus α, and constitute minor logarithmic corrections to the K_{ij} terms [46, 47, 57]. The diffusion rate D_k, on the other hand, can be a strong function of the NP size, and thus have a strong influence on the shape of the PSD. In fact, in the case of pure aggregation, if K_{ij} has the form $\sim (k_i^{-s} + k_j^{-s})$, where $s > 0$, it can be shown that the PSD exhibits self-similarity at long times and that, if rescaled with respect to the average size (number of atoms), it can be reduced to a sole function of the exponent s [43, 61, 62]:

$$f(x = j/j_{mean}) \sim \frac{(1+s)x^s}{\Gamma(1+s)} \exp[-(1+s)x] \tag{3.7}$$

The diffusion rate of 3D NPs has been widely observed to follow, indeed, a power law of the kind $D_k \sim k^{-s}$ [30, 31, 42, 44–47]. For this reason, here we let:

$$D_k = D_1(t) k^{-s} \tag{3.8}$$

where $D_1(t)$ is the diffusion rate of single atoms. However, the value of the exponent s can vary considerably and it is, in general, a poorly understood function of NP morphology, NP-substrate interaction, reacting atmosphere, and temperature. As such, here it is regarded as a fitting parameter. The dispersion a_k has been estimated by assuming the NPs to be metallic NPs with FCC close-packed structures, which is usually the case for supported Pt

NPs, especially on carbon support, as already described elsewhere [14, 63].
The dynamic model (i.e., Eqs. (3.1), (3.2) together with (3.4) and (3.5)) was solved numerically by using an in-house code written and implemented in Matlab. The dynamic model was validated on three different levels: Asymptotic behavior in case of pure aggregation (see Figure 3.A.1), closure of the mass balance, and recovery of linear growth in case of sole deposition on NPs (see Figure 3.A.3b).
The functional form of $g_s(t)$, $g_p(t)$, and $D_1(t)$ is unknown a priori. However, their integral over a cycle time can be related to experimental quantities:

$$G_s = \int_{(n-1)\tau_{cycle}}^{n\tau_{cycle}} g_s(t)dt \tag{3.9}$$

$$G_p = \int_{(n-1)\tau_{cycle}}^{n\tau_{cycle}} g_p(t)dt \tag{3.10}$$

where G_s is the total number of single atoms deposited per unit of substrate area per cycle (at/nm^2/cycle), whereas G_s is the total number of atoms deposited on the NPs per number of NP surface atoms in one cycle (monolayers/cycle). Given this constraint $g_p(t)$ and $g_s(t)$ can assume different functional forms. For example, if we assume the generation term to follow an exponential decay:

$$g_p(t) = \frac{G_p}{\tau_{rxn}} \exp(-t/\tau_{rxn}),\ \tau_{rxn} << \tau_{cycle} \tag{3.11}$$

or assuming a constant generation during the reaction time, we have:

$$g_p(t) = \begin{cases} \dfrac{G_p}{\tau_{rxn}} t, & \text{for } t \le \tau_{rxn} \\ 0, & \text{for } \tau_{rxn} < t < \tau_{cycle} \end{cases} \tag{3.12}$$

$D_1(t)$ is amenable to analogous formulations such as:

$$D_1(t) = \begin{cases} 0, & \text{for } t \le \tau_0 \\ \dfrac{D_0 \tau_{cycle}}{\tau_{cycle} - \tau_0 - \tau_{rxn}} [1 - e^{-(t-\tau_0)/\tau_{rxn}}], & \text{for } \tau_0 < t < \tau_{cycle} \end{cases} \tag{3.13}$$

and:

$$D_1(t) = 2D_0(1 - t/\tau_{cycle}) \tag{3.14}$$

or simply:

$$D_1(t) = \begin{cases} 0, & \text{for } t \le \tau_0 \\ D_0 \dfrac{\tau_{cycle}}{\tau_{cycle} - \tau_0}, & \text{for } \tau_0 < t < \tau_{cycle} \end{cases} \tag{3.15}$$

We studied the effect of several different functional forms for $g_s(t)$, $g_p(t)$, and $D_1(t)$ on the PSD for different values of s. Since for $s \neq 0$ the detailed balance of the single atom population has little to no effect on the shape of the PSD [42], the exact time dependency of $D_1(t)$, $g_s(t)$, and $g_p(t)$ has little to no effect on the simulated PSD within the parameter space explored here, as opposed to the effect of varying s (see Figure 3.A.2). This is due to the dampening effect introduced by the coupling between the different NP populations prescribed by the first two terms in Eq. (3.2) on the fluctuations induced by time-dependent mobility and single-atom generation. Nonetheless, their average values over the cycle duration τ_{cycle} do affect the PSD, in particular:

$$\langle D_1 \rangle = \int_{(n-1)\tau_{cycle}}^{n\tau_{cycle}} D_1(t)dt \tag{3.16}$$

controls the total number of NPs per unit area, that is:

$$\sum_{k=2}^{\infty} n_k = s_p \tag{3.17}$$

whereas G_s and G_p determine the total number of deposited atoms in every p-th cycle, that is:

$$\sum_{k=1}^{\infty} n_k k = G_{tot}(p) \tag{3.18}$$

Accordingly, for each value of s, we varied G_s and G_p so as to match the experimental metal loading evolution, and $\langle D_1 \rangle$ to match the experimental average number of NPs per unit area, which was estimated to be ~0.0025 nm^{-2} in the temperature range 100 – 200°C and the cycle range 1 – 10. By setting G_s equal to the loading after the first cycle (~0.12 nm^{-2}) and G_p equal to the growth per cycle reported for flat substrates [17, 20, 33], expressed in monolayers (~ 0.18 ML), we could reproduce the evolution of the metal loading with the number of cycles over a wide range of $\langle D_1 \rangle$ and s values, and thus PSD shapes, consistently with the experimental observation that different deposition temperatures resulted in the same metal loading and yet different PSDs. The agreement between experimental and simulated PSDs has been quantified in terms of the sum of the squared errors (SSE) after rescaling the PSDs with respect to their respective average diameter, since by doing so the shape factor α cancels out, thus not affecting the agreement evaluation. As the shape factor α could not be estimated experimentally, it was assumed to be 0.35, that is, an NP consisting of 55 atoms has a projected diameter of 1.33 nm, as this value gave the best visual agreement when plotting the PSDs in terms of projected diameter.

In sum, since G_p, G_s, and $\langle D_1 \rangle$ were determined independently, the agreement between simulated and experimental PSDs depended on the sole parameter s, which is then regarded as the fitting parameter of the model. This procedure is analogous to the one employed by Kinosita [64] to study the growth of gold clusters on amorphous carbon, and more recently by Bell et al. [31] to study the size-dependent mobility of gold nano-clusters on chemically modified graphene.

Model (II): Deposition, aggregation by surface diffusion of single atoms and gas-phase-mediated ripening via volatile PtO_2

To explore the effect of gas-phase-mediated Ostwald ripening we modified equation (3.1) and (3.2) to allow for the exchange of Pt atoms via volatile PtO_2(g) driven by the size-dependent stability of NPs (Gibbs-Thompson effect). To understand whether Ostwald ripening can account for the observed PSD evolution, we set the NP mobility to zero, i.e., $D_k = 0$ for $k \neq 1$. This model thus describes the following physical picture:

- In each cycle a certain number of single atoms is generated on both the substrate surface and the preexisting NPs over the time scale τ_{rxn}, which is assumed to vary in the interval from 0 to the cycle time t_{cycle}. The single atoms diffuse over the substrate surface at a rate equal to D_1. The meeting of two single atoms leads to the formation of a cluster or nanoparticle (NP). Once the NPs are formed, single atoms can attach to them (growth due to single-atom attachment). NPs can exchange single atoms in the form of volatile PtO_2 through the gas phase. The NPs are assumed in equilibrium with PtO_2. Since the equilibrium pressure of PtO_2 varies according to the Gibbs-Thompson equation, small particles grow smaller and disappear at expenses of larger ones.

The modeling of the exchange of volatile PtO_2 between Pt NPs is based on the recent work of Plessow and Abild-Pedersen [50], which builds on the seminal work of Wynblatt and Gjostein [27]. In brief, the pressure p_k of PtO_2(g) in equilibrium with an NP of size k (number of atoms) is given by:

$$p_k = p_{O_2} \exp\left(\frac{-\Delta G_{form}(PtO_2) + A_{tot}(k)\gamma_{avg}/k}{k_b T}\right) \tag{3.19}$$

where p_{O_2} is the oxygen pressure, $\Delta G_{form}(PtO_2)$ is the Gibbs energy of formation of PtO_2(g), which is here taken as equal to -1.69 eV [50], $A_{tot}(k)$ is the exposed area of the NP, γ_{avg} the average surface energy of the NP facets, k_b is the Boltzmann constant, and T is the temperature expressed in K. Accordingly, the number of PtO_2(g) molecules striking an NP of size k per unit of time is given by the kinetic theory of gases:

$$J_k A_k = \frac{S}{\sqrt{2\pi m_{PtO_2} k_b T}}(p_b - p_k)A_k \tag{3.20}$$

Where S is the sticking coefficient and p_b is the background pressure or mean-field pressure of PtO_2(g), which is generally different from p_k. In particular, an NP with $p_k = p_b$ neither grows nor shrinks and its radius is typically referred to as the "critical radius". Assuming steady-state and no loss of PtO_2, p_b is given by:

$$p_b = \frac{\sum_k A_k n_k p_k}{\sum A_k n_k} \tag{3.21}$$

where n_k is again the population of NPs of size k (nm^{-2}) For our simulations we have chosen the parameters used by Plessow and Abild-Pedersen [50]. In particular, we have taken

$\gamma_{avg} = \gamma_{111} + \Delta_\gamma$ =130 meV/Å^2 - 55 meV/Å^2, and $S = 1$.
Given that the number of Pt atoms exchanged by an NP of size k with the vapor basin is:

$$\Delta_{atoms}(k) \simeq J_k \mathcal{A}_k \Delta t \tag{3.22}$$

the population balance describing the evolution in time of the PSD consists of the following system of differential equations:

$$\frac{dn_1}{dt} = g_s(t) - n_1 \sum_{i=1}^{\infty} K_{1i} n_i \tag{3.23}$$

$$\frac{dn_2}{dt} = -g_p(t) n_k k a_k + n_1^2 K_{1,1} - n_1 K_{1,k} n_2 + 2 n_2 J_2 \mathcal{A}_2 \tag{3.24}$$

if $p_b - p_k < 0$, then $J_k < 0$ (the NPs shrink) and:

$$\frac{dn_k}{dt} = g_p(t)\left[n_{k-1}(k-1)a_{k-1} - n_k k a_k\right] + n_1(K_{1,k-1}n_{k-1} - K_{1,k}n_k) + (n_k J_k \mathcal{A}_k - n_{k+1} J_{k+1} \mathcal{A}_{k+1}) \tag{3.25}$$

whereas if $p_b - p_k \geq 0$, then $J_k \geq 0$ (the NPs ripen) and:

$$\frac{dn_k}{dt} = g_p(t)\left[n_{k-1}(k-1)a_{k-1} - n_k k a_k\right] + n_1(K_{1,k-1}n_{k-1} - K_{1,k}n_k) + (n_{k-1} J_{k-1} \mathcal{A}_{k-1} - n_k J_k \mathcal{A}_k) \tag{3.26}$$

Lifshitz-Slyozov-Wagner (LSW) PSD

According to Lifshitz-Slyozov-Wagner (LSW) theory, the PSD of an ensemble of particles undergoing diffusion-limited Ostwald ripening approaches the following stationary self-similar PSD [29, 49]:

$$f(r/r_{cr}) = f(u) = (3^4 e/2^{5/3}) u^2 \exp[-1/(1-2u/3)]/[(u+3)^{7/3}(1.5-u)^{11/3}]$$

if $0 < u < 1.5$, otherwise: $f(r/r_{cr}) = 0$, where $r_{cr} = < r >$.

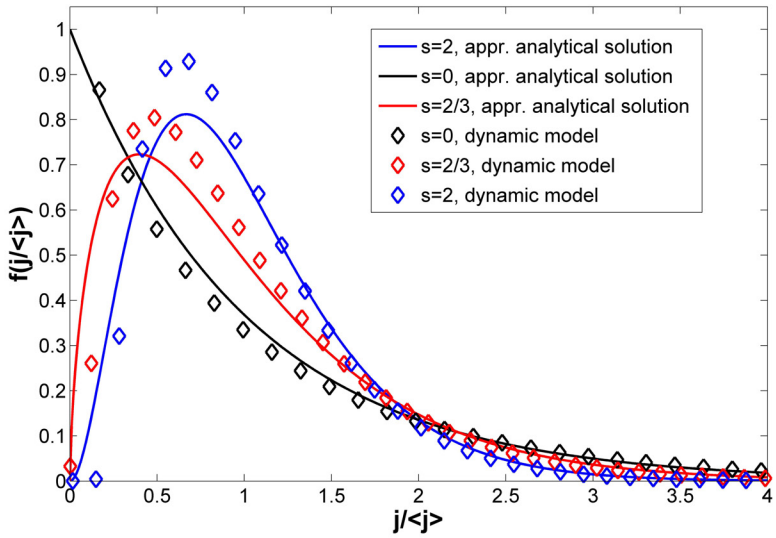

Figure 3.A.1: Long time solution to Eq. (3.2) in the case of pure aggregation ($g_s(t) = 0$ and $g_p(t) = 0$) as compared with the approximate analytical solution (3.7) for different values of s. The numerical solution is in satisfactory agreement with the from approximated solution. In particular, it deviates from it in the same fashion as reported by Sholl and Skodje [43].

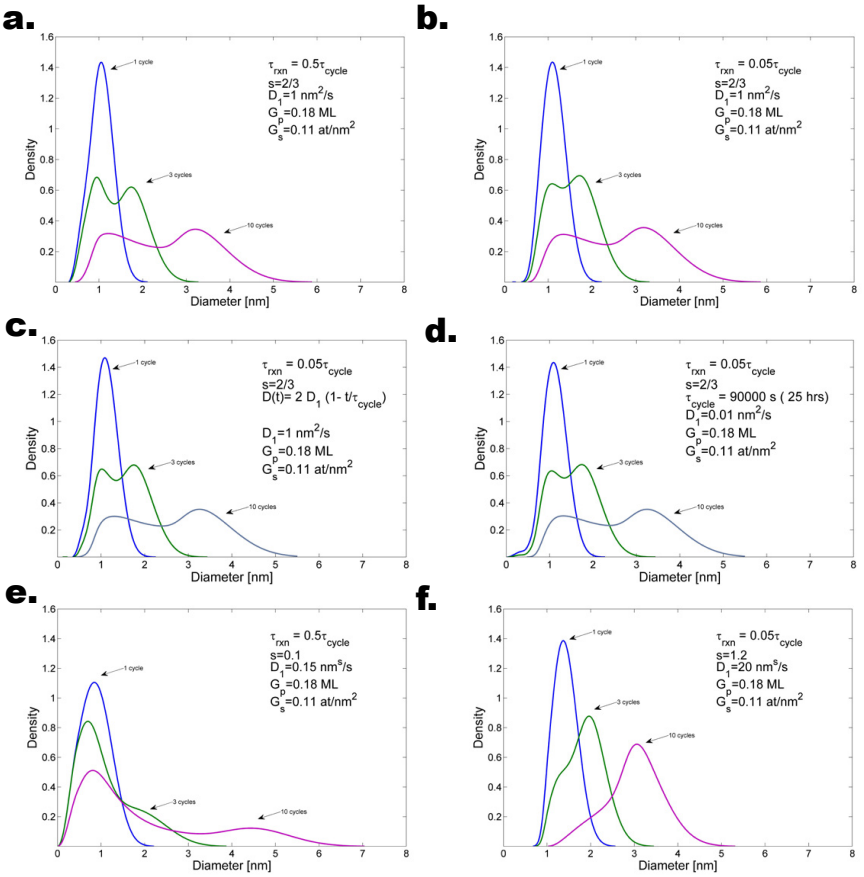

Figure 3.A.2: Simulated PSDs after 1, 3, and 10 cycles for the general case (deposition on both substrate and NPs + aggregation) for different values of s and τ_{rxn} (D_1 was varied to obtain the the same number of NPs in all cases), (τ_{cycle} = 900s, unless specified otherwise). As shown in (a) and (b), a change of one order of magnitude in the value of τ_{rxn} has only a marginal effect on the PSD shape, in that higher values give a slightly higher peak on the small-size side. Furthermore increasing the cycle time by two orders of magnitude while reducing D_1 by two orders of magnitude (d) results in virtually the same PSD as in (b). Changing the functional form of $D_1(t)$ and $g_p(t)$ while keeping the constant the average value over the cycle time also has little to no effect on the PSD, for example (c) shows the case in which $D_1(t)$ varies linearly during the cycle time from a value of 2 nm^2/s to zero as opposed to having a constant value of 1 nm^2/s over the entire cycle time (b). However, changing the value of s from 0.1 (e) to 0.66 (a) and 1.2 (f) has a dramatic qualitative and quantitative effect on the shape of the PSD.

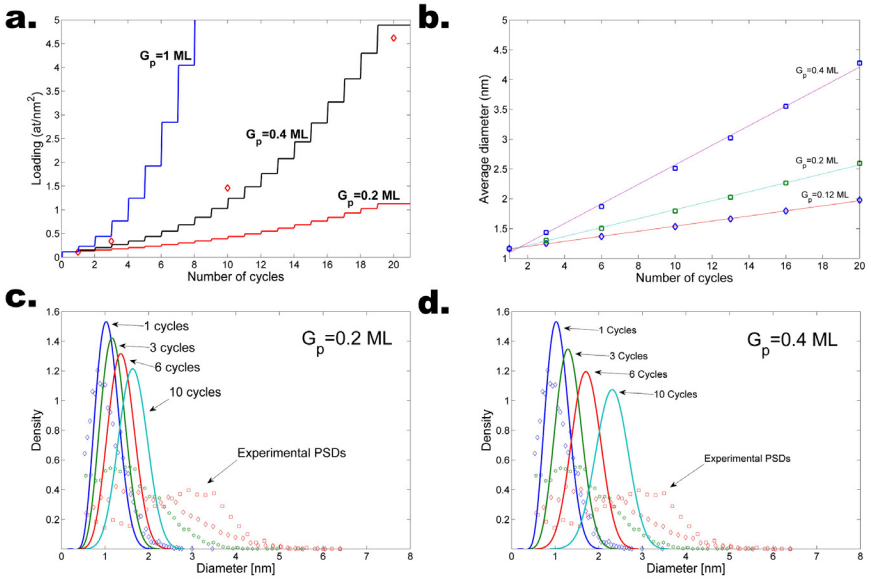

Figure 3.A.3: Simulation results for the case of NP nucleation in the first cycle followed by NP growth due to exclusive deposition on preexisting NPs (no aggregation, i.e., $D_k = 0$, and $G_s = 0$). (a) Simulated metal loading evolution (atoms per unit of substrate surface) for different values of G_p as compared to the experimental values (T=100 °C). (b) Evolution of the average diameter with the number of cycles for different values of G_p. (c) Simulated PSDs after 1, 3, 6, and 10 cycles for a G_p value of 0.2 ML and 0.4 ML (d) as compared with the experimental PSDs for a deposition temperature of 100 °C, ($\tau_{cycle} = 900s$). This scenario cannot give a qualitative description of the experimental PSD evolution. In particular, G_p values of about 0.2 ML, (i.e., the reported growth per cycle on planar Pt surfaces), drastically underestimate the metal loading after 10 cycles as well as the average size. G_p values of about 0.4 ML gives a fairly good fit to the metal evolution from 1 to 10 cycles. However, such a G_p still gives a poor description of the PSD and the average size evolution, apart from being an extremely high value compared to typical reported values for the growth per cycle of Pt ALD. Finally, in this case, it can be easily shown that the metal loading scales with the number of cycles i as $G_s^1(1 + \langle a_k^i \rangle G_p)^{i-1}$, where G_s^1 is the loading after the first cycle and $\langle a_k^i \rangle$ is the average fraction of surface atoms in the NPs at a given cycle.

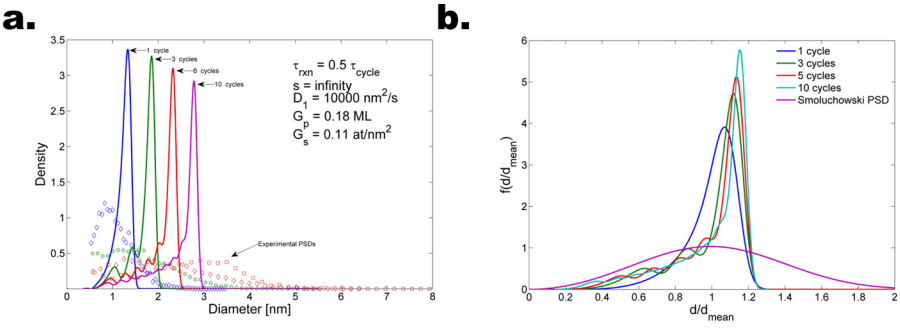

Figure 3.A.4: Simulated PSDs for the growth regime in which single atoms are the only mobile species, that is, $D_k = 0$ for $k \neq 0$. (a) Simulated PSDs after 1, 3, 6, and 10 cycles as opposed to the experimental PSDs for a deposition temperature of 100 °C (D_1 was varied to obtain an NP density of about 0.0025 nm^{-2}). (b) Evolution of the rescaled PSDs with the number of cycles (Smoluchowski PSD for $s = 0$ plotted for reference). ($\tau_{cycle} = 900s$)

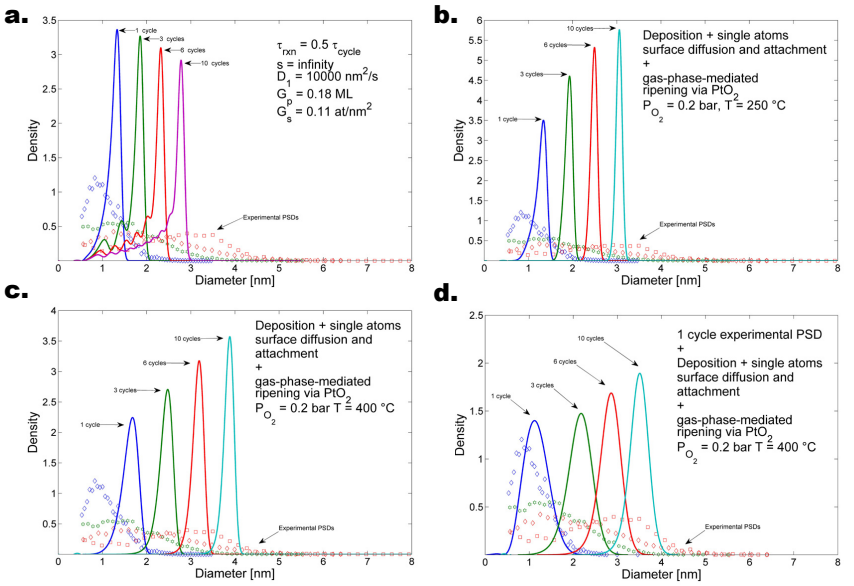

Figure 3.A.5: Simulated PSDs for the growth regime in which NPs can grow via gas-phase-mediated ripening through PtO_2(g), single atom deposition, diffusion and attachment ($D_k = 0$ for $k \neq 0$). (a) Shows the simulated PSDs for T=100 °C and $p_{O_2} = 0.2$ bar, where D_1, G_s, G_p, and τ_{cycle} are the same as in the ones used in the simulation of Figure 3.A.4 (no NP diffusion and coalescence, and no Ostwald ripening). Up to 200 °C, the inclusion of Ostwald ripening has virtually no effect on the predicted PSDs. As compared to the base case (a) increasing the temperature above 200 °C (b) and (c) results in the disappearance of the tail on the small-sizes side and in a focusing (narrowing) of the PSD with increasing number of cycles. (d) Using the experimental right-skewed PSD as the initial condition also results in a focusing of the PSD with increasing number of cycles. Furthermore, the PSD, initially right-skewed, becomes symmetrical and slightly left-skewed.

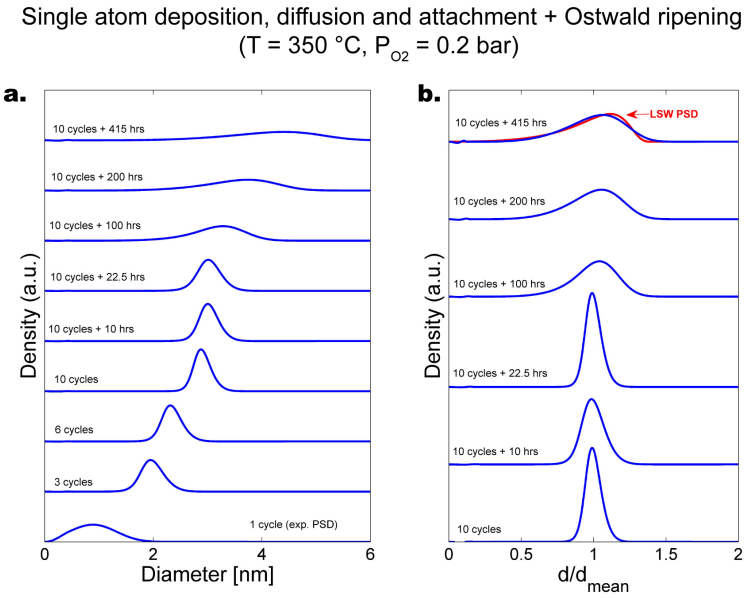

Figure 3.A.6: Simulated PSDs for the growth regime in which NPs can grow via gas-phase-mediated ripening through PtO_2(g), single atom deposition, diffusion and attachment ($D_k = 0$ for $k \neq 0$). D_1, G_s, G_p, and τ_{cycle} are the same as in the ones used in the simulations of figure 3.A.4 and Figure 3.A.5. (a) Shows the evolution of the PSD with the number of cycles and subsequent annealing (no further deposition) using the experimental right-skewed PSD of Figure 3.A.5d as the initial condition. (b) Shows the evolution of the PSD rescaled with respect to the average diameter during the annealing period and thus its approach to the self-similar solution. The latter is fairly close to the stationary PSD predicted by the Lifshitz-Slyozov-Wagner (LSW) theory for diffusion-limited ripening. In particular, the predicted stationary PSD is slightly more symmetric than the LSW PSD. Such discrepancy is ascribable to the fact that LSW theory is based on only the first two terms of the expansion of the Gibbs-Thompson equation, whereas our treatment does not rely on such simplification [30, 49].

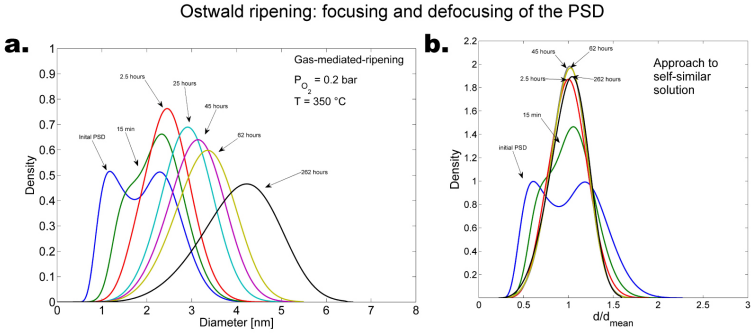

Figure 3.A.7: Simulated evolution of an initially bimodal PSD in case of pure Ostwald ripening (no deposition, no NP diffusion and coalescence). The initial PSD has been obtained by simulating 5 cycles using the model allowing for NP diffusion and coalescence and $s = 0.8$. This simulation shows how Ostwald ripening can give rise to an initial focusing (narrowing) of the PSD followed by a gradual defocusing (broadening) when the initial distribution is broader than the stationary PSD. In other words, Ostwald ripening does not always result into a broadening of the PSD [49].

3.B. Experimental Details and Characterization

The ALD experiments were carried out in a home-built fluidized bed reactor operating at atmospheric pressure as described elsewhere [14]. Briefly, the system consists of a glass column (26 mm in internal diameter and 500 mm in height) placed on top of a single motor Paja PTL 40/40-24 vertical vibration table to assist the fluidization. The graphene nanoplatelets (6-8 nm thick and 12 μm wide, surface area of about 150 $m^2\ g^{-1}$, see Fig. S1 b.) and the trimethyl (methylcyclopentadienyl)platinum(IV) (MeCpPtMe3) precursor were obtained from Strem Chemicals and used as received. Synthetic air (20 wt % oxygen) was used as the oxidizer. The Pt precursor, contained in a stainless steel bubbler, was heated and maintained at 70 °C, whereas the stainless steel tubes connecting the bubbler and the reactor were maintained at 80 °C to avoid precursor condensation. The reactor was heated by an infrared lamp placed parallel to the column with feedback control to maintain a constant temperature during ALD. In each experiment, 0.75 g of graphene powder was used. A gas flow of 0.5 L min-1 was introduced through a distributor plate at the bottom of the reactor column in order to fluidize the powders. Prior to ALD, the powders were dried in air at 120 °C for 1 h. Thereafter, an ozone treatment step at 200 °C for 30 min was applied, which was performed by flowing synthetic air (0.5 L min^{-1}) through an OAS Topzone ozone generator. The ozone-enriched air thus obtained had an ozone content of about 1.5 wt %. The ALD process consisted of sequential exposures of the powders to the Pt precursor (4 min) and synthetic air (5-10 min), separated by a purging step (5 min) using nitrogen as an inert gas (N2, 99.999 vol%).

Raman spectroscopy

The Raman spectra were acquired using a Renishaw inVia Raman microscope equipped with a 514 nm excitation laser. The Pt/graphene powders were immobilized on monocrystalline Si wafers. The Raman peak of Si substrate at 520 cm^{-1} was used as the reference for the Pt/graphene peak position calibration in each measurement. The Raman spectra were measured in air with a 20 mW laser power. The integration time for all Raman spectra was 100 ms. The scanned range was 500-3500 cm^{-1} with intervals of 1.5 cm^{-1}.

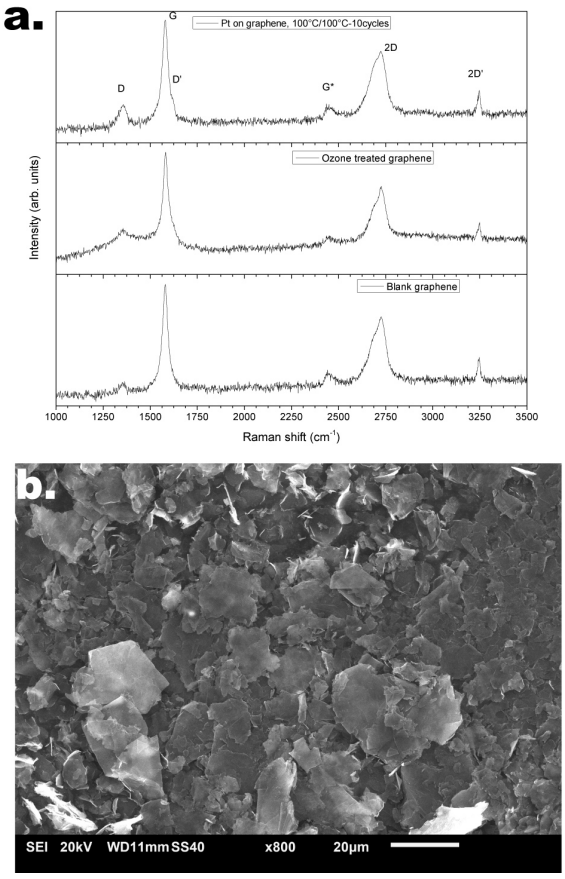

Figure 3.B.1: (a) Raman spectra obtained for blank graphene nanoplatelets, Ozone-treated graphene nanoplatelets, and Ozone-treated graphene nanoplatelets after 10 ALD cycles at 100°C. The spectrum for the blank sample is consistent with few-layer defective graphene. The ozone treatment resulted in a slight increase D peak height, suggesting an increase in the defect density consistent with the incorporation of oxygen-containing species. 10 ALD cycles resulted in the appearance of the D' peak, which is also a signature of the presence of defects, and in the accentuation of the D peak, which might be due to the incorporation of Pt NP. Analogous trends were found for all the deposition temperatures considered here. (b) SEM micrograph of the blank graphene nanoplatelets.

X-ray Photoelectron spectroscopy (XPS)

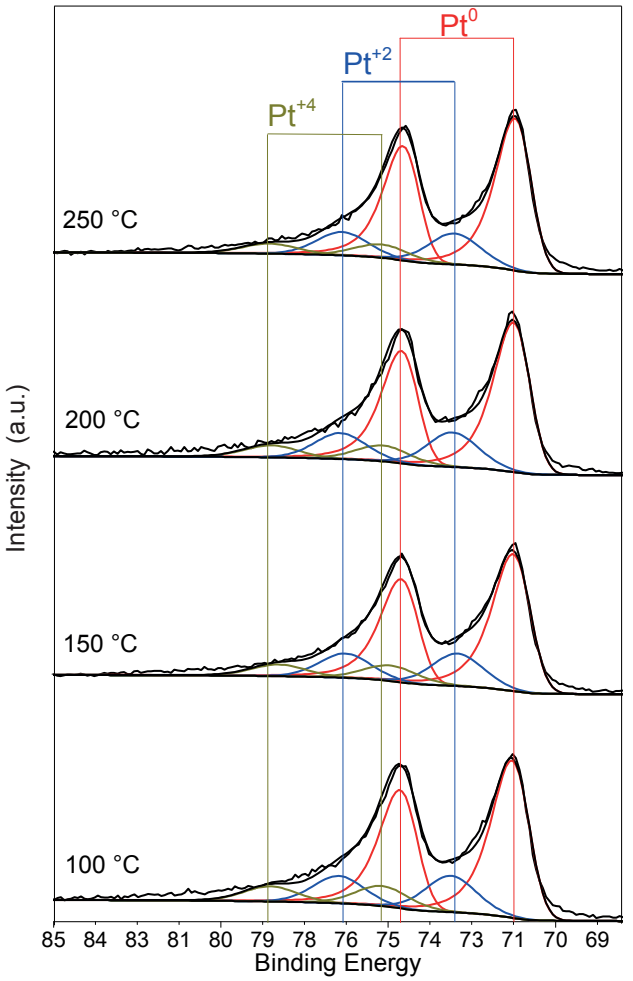

Figure 3.B.2: Pt 4*f* XPS spectra obtained for the Pt deposited on graphene nanoplatelets after 10 ALD cycles at 100 °C, 150 °C, 200 °C, and 250 °C. The binding energies were calibrated using the C1s peak at 284.5 eV as a reference. Before peak fitting, the background was estimated and subtracted by using a Shirley background type. The Pt 4*f* fits were obtained by fixing the separation between $4f_{7/2}$ and $4f_{5/2}$ peaks to the theoretical value of ~ 3.3eV and the ratio between the areas of $4f_{7/2}$ and $4f_{5/2}$ peaks equal to theoretical value of ~ 4/3. The full width at half maximum (FWHM) values were kept constant for all the spectra and equal to about 1.2 eV, 1.8 eV, and 1.9 eV for the Pt^0, Pt^{+2}, and Pt^{+4} peaks, respectively. The spectra were fitted by using 3 doublets, namely, two asymmetric Gaussian-Lorentzian line-shapes with an asymmetric index equal to 0.2 for metallic platinum and two Gaussian-Lorentz line-shapes for both Pt^{+2}, and Pt^{+4}. By doing so, the positions of the Pt $4f_{7/2}$ peaks were found to be ~71, ~73.1 and ~75.2, in agreement with the values reported in literature. Metallic platinum accounted for more than 70% of the atomic concentration of platinum species in all temperature cases. The presence of Pt^{+2} and Pt^{+4} peaks is ascribable to the omnipresent PtO_x species and in particular PtO, Pt(OH), and PtO_2 on the surface of Pt NPs. In particular, Pt^{+2} and Pt^{+4} accounted for about 20% and 10%, respectively, of the deposited platinum.

X-ray Powder Diffraction (XRD)

The Pt/graphene was transferred onto a Si wafer with 300 nm of SiO_2 thermal oxide. This was to eliminate the influence of the substrate (Si) signal in the XRD patterns of the powders. XRD patterns were obtained by a PANalytical X-pert Pro diffractometer with Cu Kα radiation, secondary flat crystal monochromator and X'celerator RTMS Detector system. The angle of interest 2ϑ was measured from 10° to 90° with fine steps of 0.001°.

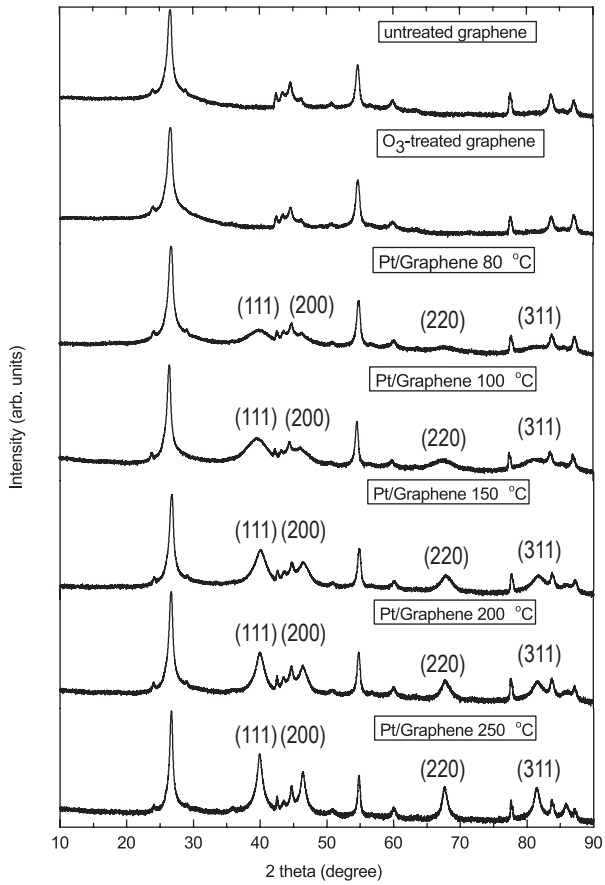

Figure 3.B.3: XRD spectra obtained for untreated graphene nanoplatelets, ozone-treated graphene nanoplatelets, and Pt deposited on ozone-treated graphene nanoplatelets after 10 cycles at 80 °C, 100 °C, 150 °C, 200 °C, and 250 °C. The ozone treatment had little to no effect on the graphene powders crystallinity. The signature of metallic Platinum is present at all deposition temperatures considered here. In particular, the peaks corresponding to metallic platinum consistently sharpens with increasing deposition temperatures, which is consistent with the increased frequency of large NPs (d_p> 5 nm) at deposition temperatures above 100 °C (see Figures 3.B.3, 3.B.5, 3.B.6, 3.B.7).

Transmission Electron Microscopy (TEM) and High Resolution TEM (HRTEM)

As-synthesized Pt/graphene powders were suspended in ethanol and transferred to regular transmission electron microscopy (TEM) grids (3.05 mm in diameter). High resolution TEM (HRTEM) micrographs were obtained using a FEI Titan G2 60-300 transmission electron microscope operated at 300 kV. TEM images were taken at several locations on the grids using a JEOL JEM1400 transmission electron microscope operating at a voltage of 120 kV and a current density of 50 pA cm^{-2}. The images were then analyzed by using the ImageJ software to obtain the PSDs. More than 6000 particles were analyzed for each PSD (see Figure 3.B.4).

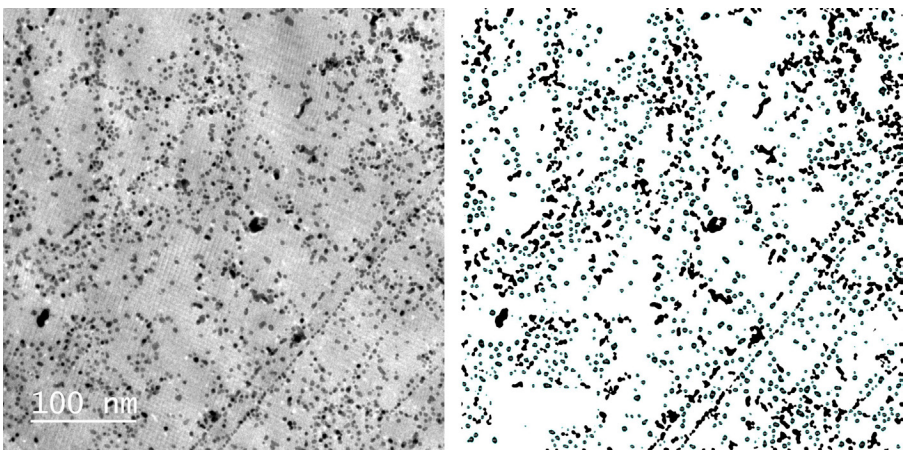

Figure 3.B.4: Example of TEM micrograph before and after image analysis. The image analysis was performed via the software ImageJ in a semi-automatic fashion and consisted of several steps, including, background subtraction, Fast Fourier Transform (FFT) bandpass filtering, thresholding, and segmentation via edge detection. For the particle analysis the edge detection algorithm was allowed to detect objects with circularity between 0.85 and 1 to account for those nanoparticles whose 2D projection was not perfectly circular.

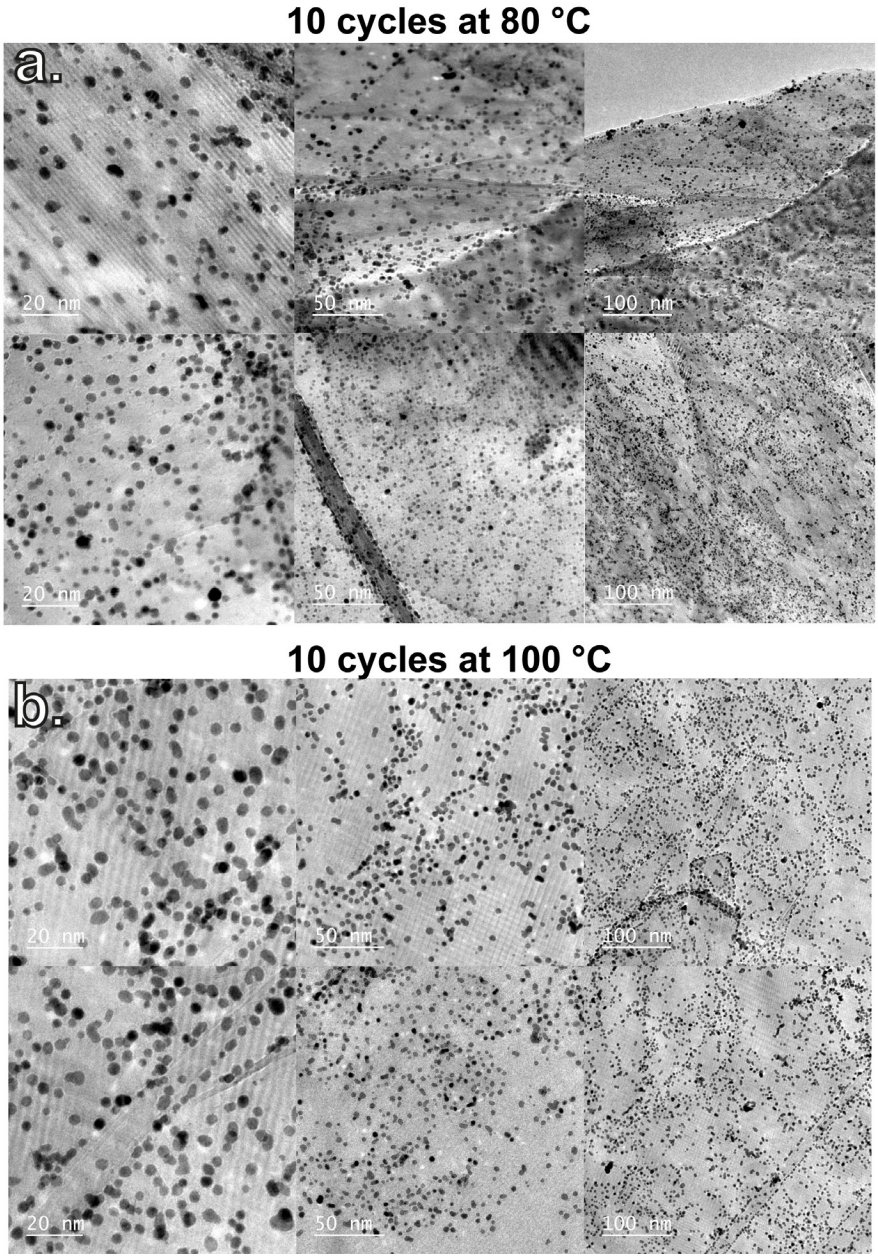

Figure 3.B.5: TEM micrographs of Pt deposited on graphene nanoplatelets after 10 cycles at 80 °C (a) and 100 °C (b), taken at different magnifications.

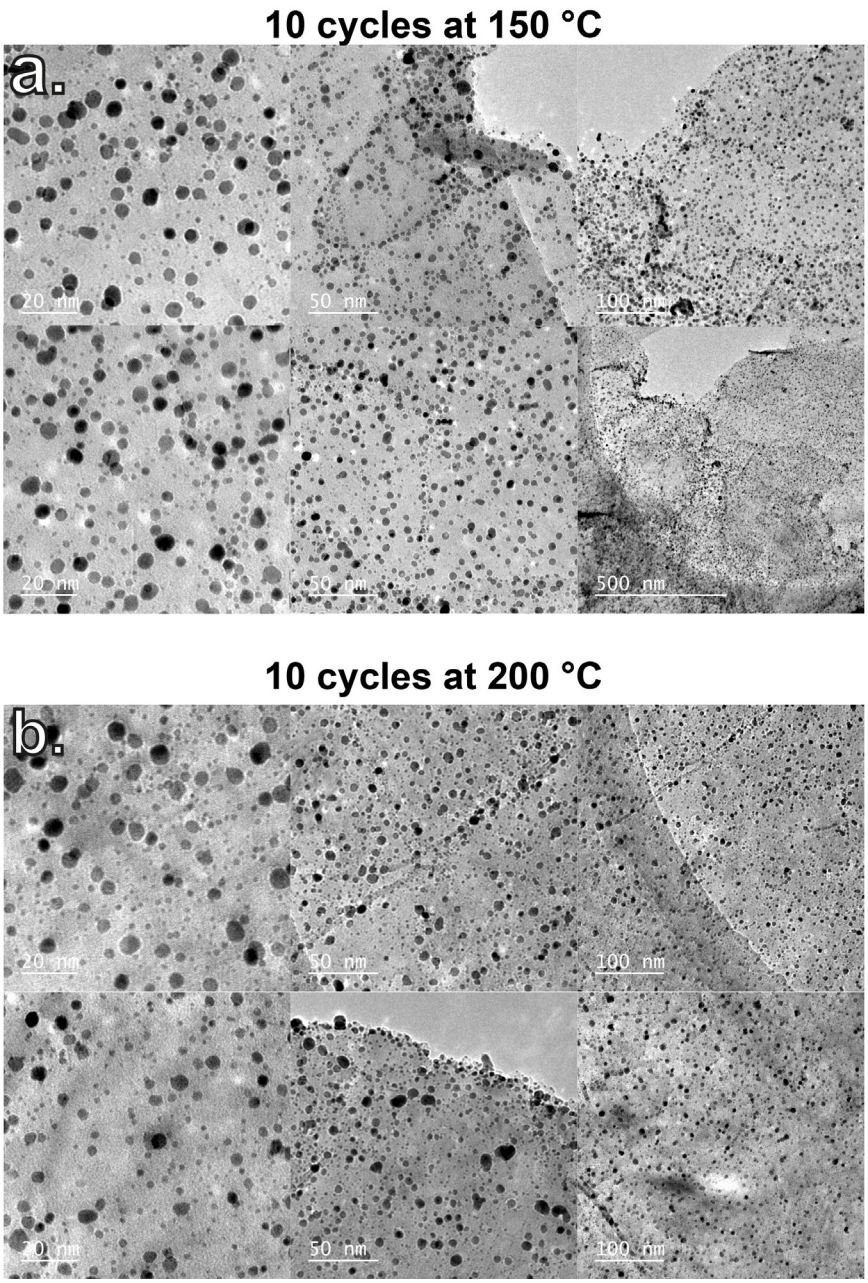

Figure 3.B.6: TEM micrographs of Pt deposited on graphene nanoplatelets after 10 cycles at 150 °C (a) and 200 °C (b), taken at different magnifications.

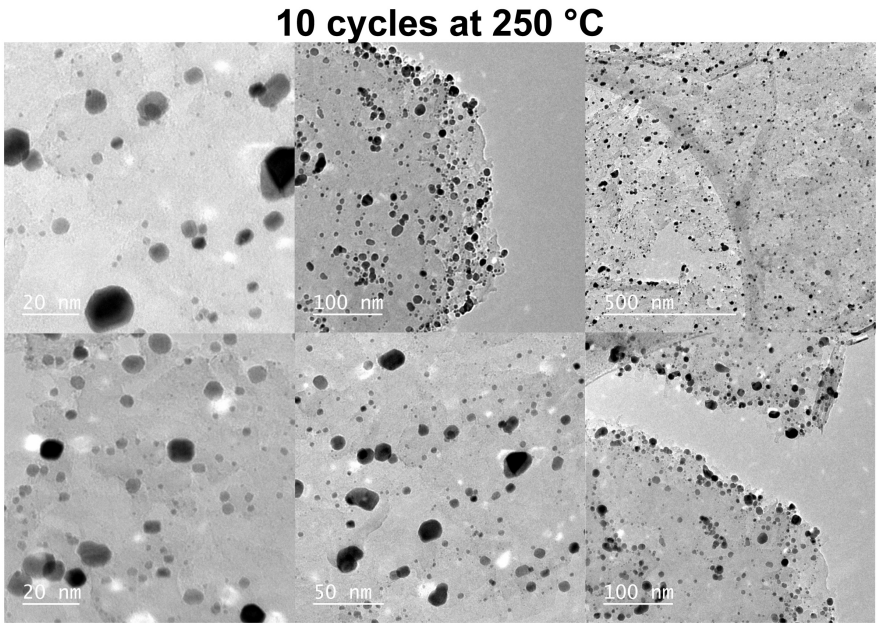

Figure 3.B.7: TEM micrographs of Pt deposited on graphene nanoplatelets after 10 cycles at 250 °C taken at different magnifications.

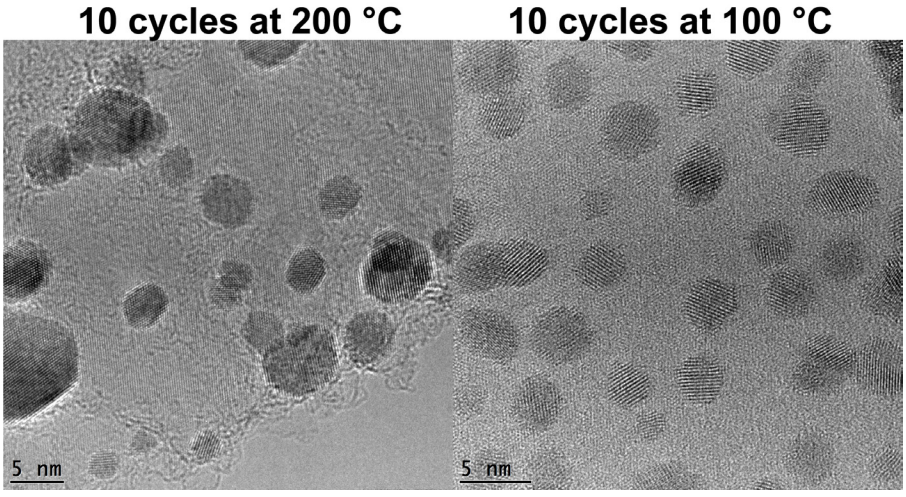

Figure 3.B.8: HRTEMs micrographs of Pt deposited on graphene nanoplatelets after 10 cycles at 200 °C and 100 °C.

	100 °C			150°C			200°C		
N° cycles	1	3	10	1	3	10	1	3	10
Pt loading [wt%]	0.51	1.37	6.00	0.57	1.52	6.07	0.51	1.47	5.87
Pt loading [at/nm^2]	0.12	0.31	1.46	0.13	0.35	1.48	0.12	0.34	1.43
NP density [nm^{-2}]	0.0022	0.0019	0.0028	0.0040	0.0020	0.0025	0.0016	0.0028	0.0031
Mean diameter [nm]	1.1	1.6	2.6	1.0	1.54	2.2	1.2	1.3	2.0
Standard deviation [nm]	0.4	0.7	1	0.4	0.9	1.5	0.6	0.8	1.4

Table 3.B.1: Platinum loading, NP density, and mean diameter and standard deviation after 1,3, and 10 ALD cycles at 100°C, 150°C, and 200°C.

Loading vs PSD

The platinum loading (wt%) was measured via Instrumental Neutron Activation Analysis(INAA). INAA was carried out at the Reactor Institute of Delft (Delft University of Technology). The powders (about 30 mg for each Pt/graphene sample) were loaded into high purity polyethylene capsules. The samples and a standard sample (reference) were then packaged and irradiated in a suitable reactor at a constant neutron flux. All reactors used for neutron activation employed uranium fission, which provides a neutron flux on the order of 1012 cm^{-2} s^{-1}. These neutrons have low kinetic energy, typically less than 0.5 eV. Upon irradiation, a neutron can be absorbed by the target nucleus (i.e., Pt), forming a radioactive nucleus, which carries its own half-life characteristics. The nuclear decay of the radioactive nuclei produce gamma-rays, which are detected by the NAA detectors, from which the Pt loading was determined. For Pt/graphene samples, an average waiting time of 5 days was required to allow the decay of radioactive nuclei. The INAA used in this work allowed detection levels for platinum in the range 101-102 nanograms. The platinum loading after the p-th cycle $G_{tot}(p)$ expressed in terms of at/nm^2 was calculated by using the following expression [14, 15]:

$$G_{tot}(p) = \frac{w_p(N_A/A_r)}{(1-w_p)S} \tag{3.27}$$

where w_p is the weight fraction of Pt in the sample, N_A is the Avogadro constant, A_r is the relative atomic mass of Pt, and S is the surface area per unit weight of the substrate.
The average number of NPs per unit area (NP density) was estimated by assuming the Pt NPs to be metallic close-packed FCC structures. Hence, by geometric construction, the number of atoms N_{atoms} in a Pt NP is given by[65–67]:

$$N_{atoms} = \frac{1}{3}\left[10n^3 - 15n^2 + 11n - 3\right],\ n \geq 1 \tag{3.28}$$

where n is the number of atomic layers making up the NP, where atomic layer is defined such that when, for example, n is equal to 1 the NP consists of a single atom or central site, whereas when n is equal to 2 the the NP consists of a central site fully coordinated by 12 surface atoms, that is an NP of 13 atoms. The diameter of such NP scales linearly with n according to the following formula[65]:

$$d = (2n-1)a/\sqrt{2} \tag{3.29}$$

where a is the lattice constant. Therefore, given the normalized PSD $f_p(d)$, we estimated the NP density s_p, by imposing the following mass balance [14]:

$$s_p \int_{d_{min}}^{d_{max}} f_p(x) N_{atoms}(x) dx = \frac{w_p (N_A / A_r)}{(1 - w_p) S} \tag{3.30}$$

The integral in left-hand side of Eq. (3.30) is the average number of atoms contained in the Pt NPs, which then multiplied by the NP density gives the Pt loading expressed in atoms per unit area, which is given by 3.27 (right-hand side of Eq. (3.30)).

Saturation and Thermogravimetric analysis (TGA)

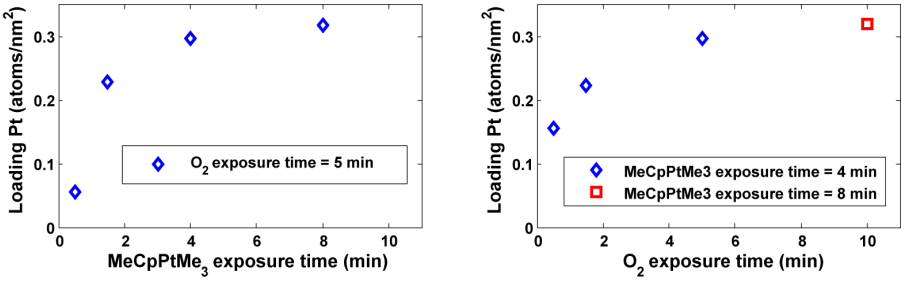

Figure 3.B.9: Saturation curves obtained for Pt ALD at 100 °C after 3 cycles on 0.75 g of graphene nanoplatelets with a surface area of 150 m^2 g^{-1}.

A Mettler Toledo TGA/SDTA 851e thermogravimetric analyzer was used for studying the thermal behavior of the synthesized powders. 3 mg of Pt/graphene was used for each TGA measurement. The TGA curves were recorded while ramping up the powders from 25 to 800 °C with a ramping rate of 5 °C min^{-1} in a synthetic air flow of 100 mL min^{-1}.

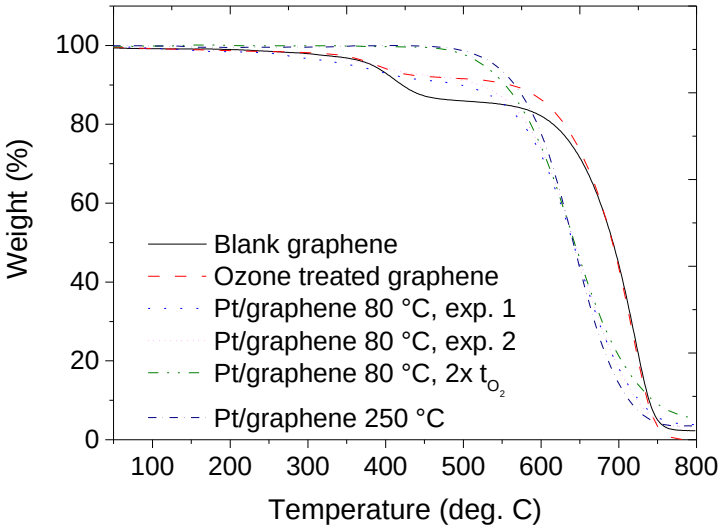

Figure 3.B.10: TGA of untreated graphene nanoplatelets before and after the ozone-treatment, and of the ozone-treated graphene nanoplatelets after: 10 cycles at 80 °C, with the exposure time to synthetic air was fixed to either 5 min (two different experiments) or 10 min, and after 10 cycles at 250 °C with the exposure time to synthetic air fixed to 5 min. The shift to lower temperatures of the onset of mass loss of the Pt/graphene composites as compared with the blank graphene is ascribable to the catalytic nature of Pt towards the combustion of carbon. The decreased mass loss in the 400-500 °C temperature range of the ozone-treated graphene nanoplatelets as compared with the TGA of the untreated shows how the ozone treatment effectively removes most of the adventitious carbon adsorbed on the surface of the graphene. Increasing the exposure time to synthetic air to 10 min in the ALD recipe resulted in a removal of carbon ligands comparable to the one obtained at 250 °C with an exposure time of 5 min. This is ascribable to slower combustion kinetics at low temperatures. Pt/graphene obtained at 150 °C and 200 °C with an oxygen exposure of 5 min exhibited the same weight loss profile as Pt/graphene obtained at 250 °C with the same exposure (not shown). Accordingly, an oxygen exposure time of 10 min and 5 min were chosen for the ALD experiments carried out at low temperatures (i.e., 80 °C and 100 °C) and at high temperatures (i.e., 150 °C, 200 °C, and 250 °C), respectively, to assure the same degree of removal of carbon ligands at both low and high temperatures.

Annealing experiments

The annealing of Pt/graphene was carried out in either air or argon atmosphere. For each experiment, 50-60g of sample was loaded in a ceramic boat. The temperature was ramped up with a ramping rate of 5 °C min^{-1} and maintained at the annealing temperature (200 °C and 400 °C) for different annealing times (6 hours, 12 hours, 24 hours and 48 hours). Hereafter, the samples were collected directly from the oven and cooled down to room temperature in air.

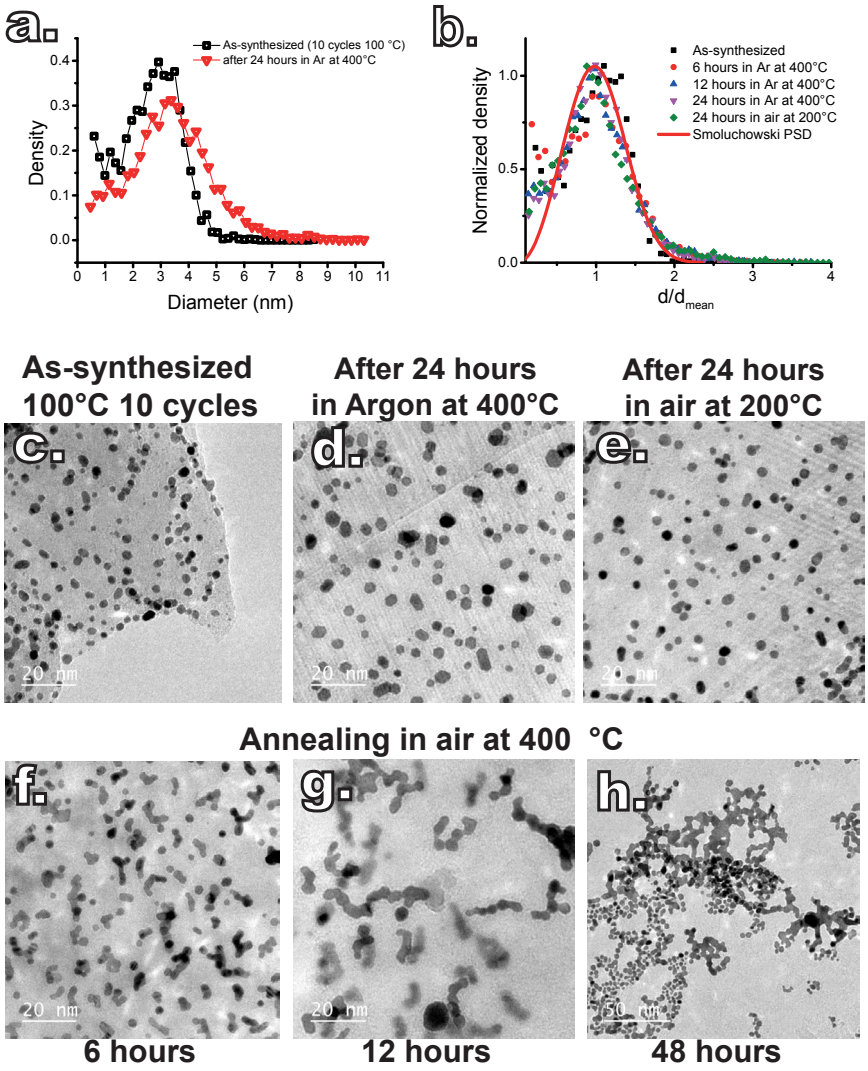

Figure 3.B.11: (a) PSD of the as-synthesized Pt/graphene after 10 cycles at 100°C compared with the PSD after 24 hours of annealing in argon at 400 °C. (b) PSDs of the as-synthesized Pt/graphene after 10 cycles at 100°C and after annealing at different temperatures and in different conditions rescaled with respect to their respective average diameter, compared with the Smoluchowski PSD. (c) TEM micrograph of the graphene nanoplatelets after 10 cycles at 100 °C. (d), (e), (f), (g), and (h) show the as-synthesized Pt/graphene of (c) after different annealing periods at different temperatures and in different atmospheres.

References

[1] J. S. King, A. Wittstock, J. Biener, S. O. Kucheyev, Y. M. Wang, T. F. Baumann, S. K. Giri, A. V. Hamza, M. Baeumer, and S. F. Bent, *Ultralow Loading Pt Nanocatalysts Prepared by Atomic Layer Deposition on Carbon Aerogels,* Nano Lett. 8, 2405 (2008).

[2] A. Goulas and J. Ruud van Ommen, *Atomic layer deposition of platinum clusters on titania nanoparticles at atmospheric pressure,* J. Mater. Chem. A 1, 4647 (2013).

[3] M. Shao, A. Peles, and K. Shoemaker, *Electrocatalysis on Platinum Nanoparticles: Particle Size Effect on Oxygen Reduction Reaction Activity,* Nano Lett. 11, 3714 (2011).

[4] H. V. Bui, F. Grillo, and J. R. van Ommen, *Atomic and molecular layer deposition: off the beaten track,* Chem. Commun. XX, XX (2016).

[5] F. N. Gür, F. W. Schwarz, J. Ye, S. Diez, and T. L. Schmidt, *Toward Self-Assembled Plasmonic Devices: High-Yield Arrangement of Gold Nanoparticles on DNA Origami Templates,* ACS Nano 10, 5374 (2016).

[6] J. Li, Z. Wang, C. Chen, and S. Huang, *Atomic-Scale Observation of Migration and Coalescence of Au Nanoclusters on YSZ Surface by Aberration-Corrected STEM,* Sci. Rep. 4, 5521 (2014).

[7] K. Yamamoto, T. Imaoka, W.-J. Chun, O. Enoki, H. Katoh, M. Takenaga, and A. Sonoi, *Size-specific catalytic activity of platinum clusters enhances oxygen reduction reactions,* Nat. Chem. 1, 397 (2009).

[8] W. Eberhardt, P. Fayet, D. M. Cox, Z. Fu, A. Kaldor, R. Sherwood, and D. Sondericker, *Photoemission from mass-selected monodispersed Pt clusters,* Phys. Rev. Lett. 64, 780 (1990).

[9] K. Wettergren, F. F. Schweinberger, D. Deiana, C. J. Ridge, A. S. Crampton, M. D. Rtözer, T. W. Hansen, V. P. Zhdanov, U. Heiz, and C. Langhammer, *High Sintering Resistance of Size-Selected Platinum Cluster Catalysts by Suppressed Ostwald Ripening,* Nano Lett. 14, 5803 (2014).

[10] B. R. Cuenya and F. Behafarid, *Nanocatalysis: size- and shape-dependent chemisorption and catalytic reactivity,* Surf. Sci. Rep. 70, 135 (2015).

[11] S. M. George, *Atomic Layer Deposition: An Overview,* Chem. Soc. Rev. 110, 111 (2010).

[12] J. Lu, J. W. Elam, and P. C. Stair, *Atomic layer deposition—Sequential self-limiting surface reactions for advanced catalyst "bottom-up" synthesis,* Surf. Sci. Rep. 71, 410 (2016).

[13] B. J. O'Neill, D. H. K. Jackson, J. Lee, C. Canlas, P. C. Stair, C. L. Marshall, J. W. Elam, T. F. Kuech, J. A. Dumesic, and G. W. Huber, *Catalyst Design with Atomic Layer Deposition,* ACS Catal. 5, 1804 (2015).

[14] H. V. Bui, F. Grillo, R. Helmer, A. Goulas, and J. R. van Ommen, *Controlled Growth of Palladium Nanoparticles on Graphene Nanoplatelets via Scalable Atmospheric Pressure Atomic Layer Deposition,* J. Phys. Chem. C 120, 8832 (2016).

[15] R. L. Puurunen, *Surface chemistry of atomic layer deposition: A case study for the trimethylaluminum/water process,* J. Appl. Phys. 97, 121301 (2005).

[16] S. T. Christensen, J. W. Elam, B. Lee, Z. Feng, M. J. Bedzyk, and M. C. Hersam, *Nanoscale Structure and Morphology of Atomic Layer Deposition Platinum on SrTiO 3 (001),* Chem. Mater. 21, 516 (2009).

[17] A. J. M. Mackus, M. J. Weber, N. F. W. Thissen, D. Garcia-Alonso, R. H. J. Vervuurt, S. Assali, A. A. Bol, M. A. Verheijen, and W. M. M. Kessels, *Atomic layer deposition of Pd and Pt nanoparticles for catalysis: on the mechanisms of nanoparticle formation,* Nanotechnology 27, 034001 (2015).

[18] V. Miikkulainen, M. Leskelö, M. Ritala, and R. L. Puurunen, *Crystallinity of inorganic films grown by atomic layer deposition: Overview and general trends,* J. Appl. Phys. 113, 021301 (2013).

[19] M. Knez, *Diffusion phenomena in atomic layer deposition,* Semicond. Sci. Technol. 27, 074001 (2012).

[20] A. J. M. Mackus, M. A. Verheijen, N. Leick, A. A. Bol, and W. M. M. Kessels, *Influence of Oxygen Exposure on the Nucleation of Platinum Atomic Layer Deposition: Consequences for Film Growth, Nanopatterning, and Nanoparticle Synthesis,* Chem. Mater. 25, 1905 (2013).

[21] J. Shi, Z. Li, A. Kvit, S. Krylyuk, A. V. Davydov, and X. Wang, *Electron Microscopy Observation of TiO 2 Nanocrystal Evolution in High-Temperature Atomic Layer Deposition,* Nano Lett. 13, 5727 (2013).

[22] S. Sun, G. Zhang, N. Gauquelin, N. Chen, J. Zhou, S. Yang, W. Chen, X. Meng, D. Geng, M. N. Banis, R. Li, S. Ye, S. Knights, G. A. Botton, T.-K. Sham, and X. Sun, *Single-atom Catalysis Using Pt/Graphene Achieved through Atomic Layer Deposition,* Sci. Rep. 3, 1775 (2013).

[23] M. B. E. Griffiths, P. J. Pallister, D. J. Mandia, and S. T. Barry, *Atomic Layer Deposition of Gold Metal,* Chem. Mater. 28, 44 (2016).

[24] Z. Zhang, *Atomistic Processes in the Early Stages of Thin-Film Growth,* Science 276, 377 (1997).

[25] M. Zinke-Allmang, L. C. Feldman, and M. H. Grabow, *Clustering on surfaces,* Surf. Sci. Rep. 16, 377 (1992).

[26] J. A. Venables, G. D. T. Spiller, and M. Hanbucken, *Nucleation and growth of thin films,* Rep. Prog. Phys. 47, 399 (1984).

[27] P. Wynblatt and N. Gjostein, *Supported metal crystallites,* Prog. Solid State Chem. 9, 21 (1975).

[28] A. L. Torre, M. del Carmen Giménez-López, M. W. Fay, G. A. Rance, W. A. Solomonsz, T. W. Chamberlain, P. D. Brown, and A. N. Khlobystov, *Assembly, Growth, and Catalytic Activity of Gold Nanoparticles in Hollow Carbon Nanofibers,* ACS Nano 6, 2000 (2012).

[29] T. J. Woehl, C. Park, J. E. Evans, I. Arslan, W. D. Ristenpart, and N. D. Browning, *Direct Observation of Aggregative Nanoparticle Growth: Kinetic Modeling of the Size Distribution and Growth Rate,* Nano Lett. 14, 373 (2014).

[30] M. Jak, C. Konstapel, A. van Kreuningen, J. Verhoeven, and J. Frenken, *Scanning tunnelling microscopy study of the growth of small palladium particles on TiO2(110),* Surf. Sci, 457, 295 (2000).

[31] G. R. Bell, P. M. Dawson, P. A. Pandey, N. R. Wilson, and P. A. Mulheran, *Size-dependent mobility of gold nano-clusters during growth on chemically modified graphene,* APL Mater. 2, 012109 (2014).

[32] B. Karasulu, R. Vervuurt, E. Kessels, and A. A. Bol, *Continuous and Ultrathin Platinum Films on Graphene using Atomic Layer Deposition: A Combined Computational and Experimental Study,* Nanoscale XX, XX (2016).

[33] T. Aaltonen, M. Ritala, T. Sajavaara, J. Keinonen, and M. Leskelä, *Atomic Layer Deposition of Platinum Thin Films,* Chem. Mater. 15, 1924 (2003).

[34] S. Takakusagi, K.-i. Fukui, R. Tero, F. Nariyuki, and Y. Iwasawa, *Self-Limiting Growth of Pt Nanoparticles from* MeCpPtMe$_3$ *Adsorbed on* TiO$_2$(110) *Studied by Scanning Tunneling Microscopy,* Phys. Rev. Lett. 91, 066102 (2003).

[35] A. J. M. Mackus, N. Leick, L. Baker, and W. M. M. Kessels, *Catalytic Combustion and Dehydrogenation Reactions during Atomic Layer Deposition of Platinum,* Chem. Mater. 24, 1752 (2012).

[36] A. M. Lubers, C. L. Muhich, K. M. Anderson, and A. W. Weimer, *Mechanistic studies for depositing highly dispersed Pt nanoparticles on carbon by use of trimethyl(methylcyclopentadienyl)platinum(IV) reactions with O2 and H2,* Journal of Nanoparticle Research 17, 179 (2015).

[37] R. Zan, U. Bangert, Q. Ramasse, and K. S. Novoselov, *Interaction of Metals with Suspended Graphene Observed by Transmission Electron Microscopy,* J. Phys. Chem. Lett. 3, 953 (2012).

[38] Y. Chu and E. Ruckenstein, *Behavior of platinum crystallites on carbon substrates,* Surf. Sci. 67, 517 (1977).

[39] V. Rubets and S. Kukushkin, *Determination of migration mechanisms and their influence on the structure of films,* Thin Solid Films 221, 267 (1992).

[40] S. Kukushkin and A. Osipov, *Soliton model of island migration in thin films,* Surf. Sci. 329, 135 (1995).

[41] M. Von Smoluchowski, *Drei vortrage uber diffusion. Brownsche bewegung und koagulation von kolloidteilchen,* Z. Phys. 17, 557 (1916).

[42] M. Vicanek and N. Ghoniem, *The effects of mobility coalescence on the evolution of surface atomic clusters,* Thin Solid Films 207, 90 (1992).

[43] D. S. Sholl and R. T. Skodje, *Late-stage coarsening of adlayers by dynamic cluster coalescence,* Phys. A 231, 631 (1996).

[44] P. Jensen, *Growth of nanostructures by cluster deposition: Experiments and simple models,* Rev. Mod. Phys. 71, 1695 (1999).

[45] K. Winkler, T. Wojciechowski, M. Liszewska, E. Górecka, and M. Fiałkowski, *Morphological changes of gold nanoparticles due to adsorption onto silicon substrate and oxygen plasma treatment,* RSC Adv. 4, 12729 (2014).

[46] Y. A. Kryukov and J. G. Amar, *Effects of cluster diffusion on the island density and size distribution in submonolayer island growth,* Phys. Rev. E 83, 041611 (2011).

[47] B. C. Hubartt, Y. A. Kryukov, and J. G. Amar, *Rate-equation approach to irreversible island growth with cluster diffusion,* Phys. Rev. E 84, 59901 (2011).

[48] Y. Zhou, C. L. Muhich, B. T. Neltner, A. W. Weimer, and C. B. Musgrave, *Growth of Pt Particles on the Anatase TiO2 (101) Surface,* The Journal of Physical Chemistry C 116, 12114 (2012).

[49] D. V. Talapin, A. L. Rogach, M. Haase, and H. Weller, *Evolution of an Ensemble of Nanoparticles in a Colloidal Solution: Theoretical Study,* The Journal of Physical Chemistry B 105, 12278 (2001).

[50] P. N. Plessow and F. Abild-Pedersen, *Sintering of Pt Nanoparticles via Volatile PtO2: Simulation and Comparison with Experiments,* ACS Catalysis 6, 7098 (2016).

[51] P. J. F. Harris, *Growth and structure of supported metal catalyst particles,* Int. Mater. Rev. 40, 97 (1995).

[52] N. J. J. Johnson, A. Korinek, C. Dong, and F. C. J. M. van Veggel, *Self-Focusing by Ostwald Ripening: A Strategy for Layer-by-Layer Epitaxial Growth on Upconverting Nanocrystals,* Journal of the American Chemical Society 134, 11068 (2012), pMID: 22734596.

[53] S. B. Simonsen, I. Chorkendorff, S. Dahl, M. Skoglundh, J. Sehested, and S. Helveg, *Direct Observations of Oxygen-induced Platinum Nanoparticle Ripening Studied by In Situ TEM,* J. Am. Chem. Soc. 132, 7968 (2010).

[54] C. Granqvist, *Size distributions for supported metal catalysts: Coalescence growth versus ostwald ripening,* J. Catal. 42, 477 (1976).

[55] K. Heinemann and H. Poppa, *Direct observation of small cluster mobility and ripening,* Thin Solid Films 33, 237 (1976).

[56] E. Prestat, R. Popescu, H. Blank, R. Schneider, and D. Gerthsen, *Coarsening of Pt nanoparticles on amorphous carbon film,* Surf. Sci. 609, 195 (2013).

[57] E. Ruckenstein, *Growth kinetics and the size distributions of supported metal crystallites,* J. Catal. 29, 224 (1973).

[58] F. Wang, V. N. Richards, S. P. Shields, and W. E. Buhro, *Kinetics and Mechanisms of Aggregative Nanocrystal Growth,* Chem. Mater. 26, 5 (2014).

[59] J. Carrey, J.-L. Maurice, F. Petroff, and A. Vaurès, *Growth of Au clusters on amorphous Al2O3: are small clusters more mobile than atoms?* Surface Science 504, 75 (2002).

[60] K. Kim, H.-B.-R. Lee, R. W. Johnson, J. T. Tanskanen, N. Liu, M.-G. Kim, C. Pang, C. Ahn, S. F. Bent, and Z. Bao, *Selective metal deposition at graphene line defects by atomic layer deposition,* Nat. Commun. 5, 4781 (2014).

[61] D. Kandel, *Selection of the Scaling Solution in a Cluster Coalescence Model,* Phys. Rev. Lett. 79, 4238 (1997).

[62] R. Botet and R. Jullien, *Size distribution of clusters in irreversible kinetic aggregation,* J. Phys. A: Math. Gen. 17, 2517 (1984).

[63] G. Agostini, R. Pellegrini, G. Leofanti, L. Bertinetti, S. Bertarione, E. Groppo, A. Zecchina, and C. Lamberti, *Determination of the Particle Size, Available Surface Area, and Nature of Exposed Sites for Silica-Alumina-Supported Pd Nanoparticles: A Multitechnical Approach,* J. Phys. Chem. C 113, 10485 (2009).

[64] K. Kinosita, *Mobility of small clusters on the substrate surface,* Thin Solid Films 85, 223 (1981).

[65] C. P. Poole, F. J. Jones, and F. J. Owens, *Introduction to Nanotechnology* (John Wiley & Sons, Inc., New York, NY, USA, 2003).

[66] J. Montejano-Carrizales, F. Aguilera-Granja, and J. Morán-López, *Direct Enumeration of the Geometrical Characteristics of Clusters,* Nanostructured Materials 8, 269 (1997).

[67] H.-G. Fritsche and R. Benfield, *Exact analytical formulae for mean coordination numbers in clusters,* Zeitschrift fur Physik D Atoms, Molecules and Clusters 26, 15 (1993).

TU Delft (Aula), The Netherlands 2016.

4

Low-Temperature Atomic Layer Deposition Delivers More Active and Stable Pt-Based Catalysts

We tailored the size distribution of Pt nanoparticles (NPs) on graphene nanoplatelets at a given metal loading by using low-temperature atomic layer deposition carried out in a fluidized bed reactor operated at atmospheric pressure. The Pt NPs deposited at low temperature (100 °C) after 10 cycles were more active and more stable towards the propene oxidation reaction than their high-temperature counterparts. Crucially, the gap in the catalytic performance was retained even after prolonged periods of time (> 24 hours) at reaction temperatures as high as 450 °C. After exposure to such harsh conditions the Pt NPs deposited at 100 °C still retained a size distribution that is narrower than the one of the as-synthesized NPs obtained at 250 °C. The difference in performance correlated with the difference in the number of facet sites as estimated after the catalytic test. Our approach provides not only a viable route for the scalable synthesis of stable supported Pt NPs with tailored size distributions but also a tool for studying the structure-function relationship.

Published as: Hao Van Bui, Fabio Grillo, Sri Sharath Kulkarni, Ronald Bevaart, Nguyen Van Thang, Bart van der Linden, Jacob A. Moulijn, Michiel Makkee, Michiel T. Kreutzer and J. Ruud van Ommen, Low-Temperature Atomic Layer Deposition Delivers More Active and Stable Pt-Based Catalysts, *Nanoscale*, 2017,9, 10802-10810.

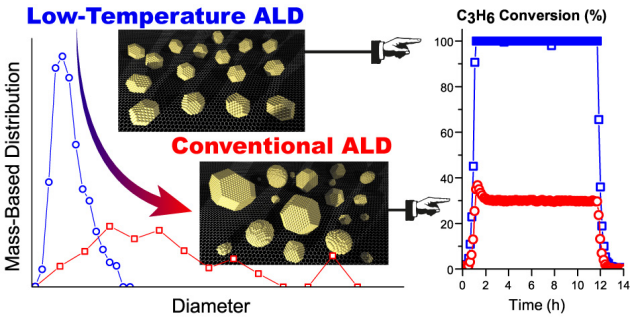

4

4.1. Introduction

Noble metals have always played a pivotal role in catalysis as they boast high activity and selectivity across a wide range of industrially relevant reactions [1–7]. Noble metals have been dispersed on high-surface-area supports as nanoparticles (NPs) to maximize the number of active surface sites [5]. Recently, the advent of nanotechnology has brought new methods and techniques that promise better control over the NP size distribution, such that the relation between NP size and function can be experimentally explored and used in fields beyond conventional catalysis such as microelectronics, and energy storage and conversion [4, 8–12]. Yet, depositing controlled amounts of metal in the form of size-selected NPs, and thus achieving the desired functionality while retaining low metal utilization, remains a challenge, especially on an industrial scale [4, 9, 13]. For example, NPs synthesized via liquid-phase routes based on ligand stabilization typically undergo loss of size-selection upon exposure to reactive environments due to ligand removal and residual solvent decomposition [9]. Furthermore, gas-phase routes for NP size-selection are typically line-of-sight techniques (e.g., pulsed laser deposition, electron beam lithography, and cluster beam deposition) and thus not suitable to high-surface-area substrates [9, 14, 15].

Atomic layer deposition (ALD) is a gas-phase and solvent-free technique that is a promising route for the controlled deposition of NPs, subnanometer clusters, and even single atoms [13, 16–21]. Briefly, the advantage of ALD is that the deposition proceeds stepwise through cyclic self-terminating surface reactions, such that (1) each step can run to completion, even in hard-to-reach places in high-surface-area substrates [14, 16, 19, 20, 22], (2) the amount deposited in each cycle of alternating reactions is tightly controlled, and (3) programming different precursors in sequences of cycles allow for more complex NPs such as bimetallic particles and core/shell and overcoated NPs [17]. In particular, when carried out in fluidized bed reactors (FBRs), ALD lends itself to the deposition of noble metals on bulk quantities of high-surface-area powders with hardly any loss of metal precursors [18, 23, 24]. As a result, ALD has the potential to fabricate supported-noble-metal catalysts reproducibly and on an industrially relevant scale.

Even if the amount deposited is precisely controlled by the self-limiting reactions, control over particle size and stability is more elusive. For example, increasing the number of cycles in thermal ALD of Pt and Pd has been reported to not only vary the average NP size but also broaden the size distribution [21, 25–27]. We have recently described the fate of adsorbed adatoms on supports during ALD, showing that they indeed migrate, form clusters

and sinter [27]. These processes are highly size-dependent (large clusters are less mobile), temperature-dependent (as holds for most sintering processes [1, 2]), and crucially depend also on the extent to which both surface reactions have run to completion. In fact, one can fabricate single-atom catalysts by not running the oxidative removal of precursor ligands to completion. Such a strategy may work for applications where the adsorbed metal atom, surrounded by ligands, is stable. For instance, room-temperature electrocatalytic applications of such strategy have been shown to exhibit limited deactivation [21]. However, exposing such materials to reaction conditions at higher temperatures burns off the ligands and immediately renders these single-atoms mobile, which can then sinter into larger NPs [27]. The crucial outstanding question is whether ALD techniques can produce supported NPs of desirable narrow size distributions that remain stable in catalytic reaction conditions.
Here, we show that Pt nanoparticles deposited by ALD on graphene nanoplatelets (GNP) at low temperatures (100 °C) using a fluidized bed operated at atmospheric pressure not only have a narrow size distributions but are also more stable than their high-temperature counterparts. In particular, high-loading Pt/GNP composites synthesized at low temperature are more active than their high-temperature counterparts. We demonstrate the activity and the stability of the Pt/GNP composites during the propene oxidation reaction at high reaction temperatures (T>200 °C) for prolonged periods of time (> 24 hours). We chose the propene oxidation reaction since it has been widely used as a model reaction for the Pt-catalyzed combustion of volatile organic compounds and, in particular, because it has been shown to be strongly affected by the Pt NP size while being relatively insensitive to the nature of the support [28–32]. The graphene nanoplatelets were chosen because they are a promising support for catalytic applications [33–36]. Moreover, Pt adatoms and nanoparticles tend to migrate and sinter more readily on graphene than on other supports [37–40], such that our system can be considered especially challenging in this respect. Finally, we show that our method, by producing bulk quantities of supported-NPs with narrow size distributions, is also an excellent tool for studying the size-dependent catalytic properties of supported noble metal NPs.

4.2. Experimental

4.2.1. Materials

Graphene nanoplatelets (6–8 nm thick and 15 μm wide, surface area of about 150 m^2g^{-1}) and trimethyl(methylcyclo-pentadienyl)platinum(IV) ($MeCpPtMe_3$) were obtained from Strem Chemicals and used as received.

4.2.2. ALD experiments

The ALD experiments were carried out in a home-built fluidized bed reactor operating at atmospheric pressure as described elsewhere [16, 18]. In brief, the system consists of a glass column (26 mm in internal diameter and 500 mm in height) placed on top of a single motor Paja PTL 40/40–24 vertical vibration table to assist the fluidization. $MeCpPtMe_3$ was used as the Pt and synthetic air (20 wt % oxygen) was used as the oxygen source. The Pt precursor, contained in a stainless steel bubbler, was heated and maintained at 70 °C. The stainless steel tubing connecting the bubbler and the reactor were maintained at 80 °C to avoid precursor condensation. The reactor was heated by an infrared lamp placed parallel

to the column with feedback control to maintain a constant temperature during ALD. In each experiment, 0.75 g of graphene nanoplatelets (GNP) were loaded in the reactor. A gas flow of 0.5 L min^{-1} was introduced through a distributor plate at the bottom of the reactor column in order to fluidize the powders. Prior to ALD, the powders were dried in air at 120 °C for 1 h and then pretreated in ozone-enriched air at 200 °C for 30 min in order to remove adventitious carbon and provide reproducible surface conditions, by flowing synthetic air (0.5 L min^{-1}) through an OAS Topzone ozone generator. The ozone-enriched air had an ozone content of about 1.5 wt%. The ALD process consisted of sequential exposures of the powders to the Pt precursor (4-5 min) and synthetic air (5-10 min), separated by a purging step (5 min) using nitrogen as an inert gas (N_2, 99.999 vol%).

4.2.3. Material characterization

Elemental analysis was carried out by means of instrumental neutron activation analysis (INAA). 30 mg of each as-synthesized sample were loaded into high purity polyethylene capsules. The samples as well as a standard sample (reference) were then packaged and irradiated by a constant neutron flux. The INAA used in this work enables a detection limit in the range of 10–100 nanogram.

A Mettler Toledo TGA/SDTA 851e thermogravimetric analyzer was used for studying the thermal behavior of the synthesized composites. 3 mg of Pt/GNP was used for each TGA measurement. The TGA curves were recorded while ramping up the powders from 25 to 800 °C with a ramping rate of 5 °C min^{-1} in a synthetic air flow of 100 ml min^{-1}.

The morphology of the deposited Pt nanoparticles was investigated by means of transmission electron microscopy (TEM) and high resolution TEM (HRTEM). HRTEM micrographs were obtained using a FEI Titan G2 60–300 transmission electron microscope operated at 300 kV. TEM micrographs were obtained by using a JEOL JEM1400 transmission electron microscope operating at a voltage of 120 kV. As-synthesized composites were suspended in ethanol and transferred to regular transmission electron microscopy grids (3.05 mm in diameter). Number-based particle size distributions were obtained by image analysis of 10-30 TEM micrographs taken at different locations and at different magnifications (e.g., 50k and 100k). The image analysis was carried out by using the ImageJ software. For each sample of the Pt/GNP composites, the equivalent projected diameter ($d = \sqrt{4A_p/\pi}$) of a number of NPs in the range of 2500-7000 was estimated by means of a semiautomatic process involving several steps, including background subtraction, Fast-Fourier-Transform (FFT) band pass filter, treshholding and outline detection. The number-based PSD ($F_1(d)$) was defined in terms of probability density as follows:

$$F_1(d) = \frac{n(d)}{\sum n(d)\Delta d} \tag{4.1}$$

where $n(d)$ is the number of NPs in the size class (bin) d, that is, NPs of size $d \pm \Delta/2$, where Δd is the width of the size class (bin size). The mass-based PSD ($F_3(d)$) was estimated based on $F_1(d)$ assuming that the mass (number of atoms) of an NP scales with d^3 and that the NP shape remains approximately the same across the whole size range:

$$F_3(d) = \frac{F_1(d)d^3}{\sum F_1(d)d^3} \tag{4.2}$$

In particular, we define the span or width of the mass-based distribution as the range of sizes where 80% of the Pt mass lies:

$$\text{PSD span} = d_3(90\%) - d_3(10\%) \tag{4.3}$$

where the diameters $d_3(90\%)$ and $d_3(10\%)$ are defined such that $\sum_0^{d_3(10\%)} F_3 = 0.10$ and $\sum_0^{d_3(90\%)} F_3 = 0.90$, respectively.

4.2.4. Catalytic tests

The catalytic tests of the Pt/GNP composites were carried out by means of a fixed bed reactor coupled with an analysis unit already described elsewhere [41]. In brief, the experimental apparatus consisted of three sections: feed mixing, reactor, and analysis. In each experiment the feed to the reactor consisted of He containing 1000 ppm of propene (C_3H_6) and 1 vol% O_2. The flow rate was mantained at 30 ml/min. The reactor consists of a quartz column 4 mm in diameter and 25 cm in length. The reactor was loaded with 15.4 mg of Pt/GNP composite. To avoid catalyst entrainment, the reactor was first loaded with 50 mg of silicon carbide. The reactor is placed in a furnace capable of withstanding temperatures up to 1000 °C and equipped with a temperature controller. The analysis section connected to the outlet of the reactor was used to monitor the concentration of propene, CO_2, and H_2O. It consisted of a gas chromatograph Chrompack CP 9001, a thermal conductivity detector (TCD), and a flame ionization detector (FID). The apparatus was controlled via a dedicated program run on the Labview software. Prior to the catalytic test, the catalytic bed was exposed to H_2 for 5 min. Each catalytic test consisted of at least two heating and cooling cycles from room temperature to 450 °C with a ramp of 2 °C/min. Pt/GNP composites obtained after 10 ALD cycles at 100 °C and 200 °C were further tested at constant reaction temperatures on the order of 200 °C for about 20 hours. The apparent reaction rate k_{app} ($\text{mol}_{C_3H_6}\ \text{mol}_{Pt}^{-1}\ \text{s}^{-1}$) was calculated from measurements of the C_3H_6 conversion $X_{C_3H_6}$ during the cooling phase of the second heating and cooling cycle of each catalytic test as follows:

$$k_{app} = \frac{QP}{RT} \frac{[C_3H_6]_0 X_{C_3H_6} MW_{Pt}}{m_{cat} y_{Pt}} \tag{4.4}$$

where Q is the overall gas flow rate, P the operating pressure, R the ideal gas constant, T the temperature at the flow controller, $[C_3H_6]_0$ the inital propene concentration, $X_{C_3H_6}$ the propene conversion, m_{cat} the mass of catalyst, y_{Pt} the platinum weight fraction (loading), and MW_{Pt} the platinum molar weight. Finally, our experiments met the Wiesz-Prater and Mears criteria for neglecting the influence of mass transfer limitations (see Appendix).

4.3. Results and discussion

We synthesized several model catalysts consisting of Pt NPs supported on graphene nanoplatelets (Pt/GNP) by using the atmospheric-pressure variant of the $MeCpPtMe_3/O_2$ ALD process described in our previous work [27]. The reader is referred to the latter for a comprehensive characterization of the composites obtainable in the cycle and temperature range used here. In brief, such ALD process, by relying on high oxygen partial pressures (i.e., 0.2 bar) and oxygen exposures on the order of minutes, enables the deposition of metallic Pt NPs at temperatures (e.g., 100 °C) at which conventional ALD would otherwise lead to

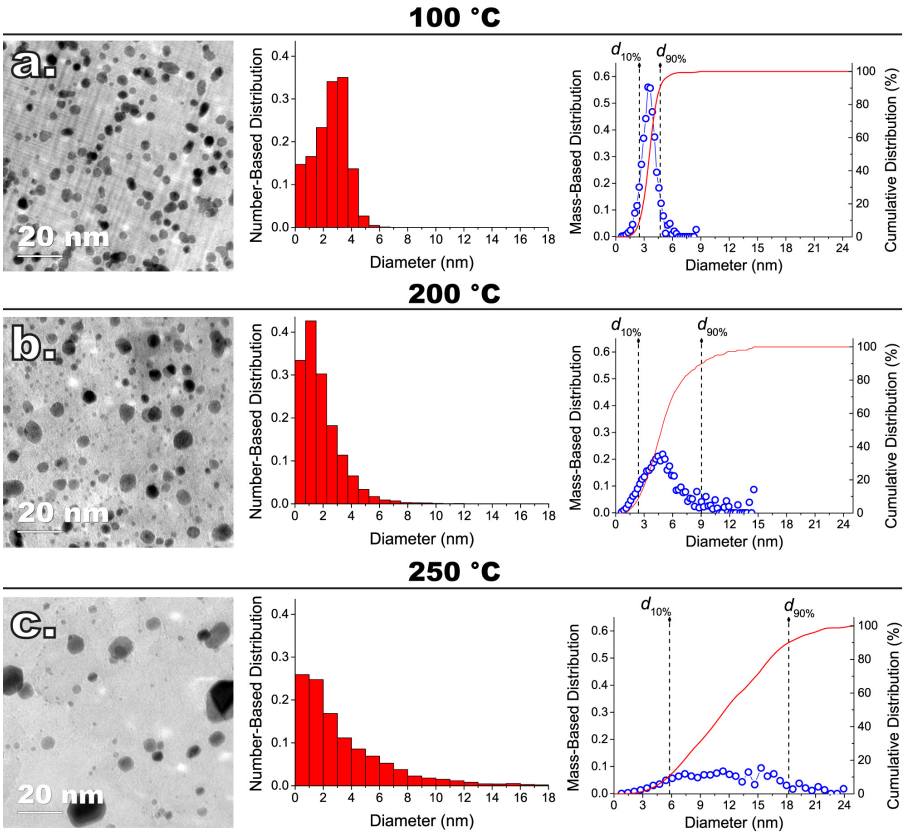

Figure 4.1: Representative TEM images of ALD-grown Pt nanoparticles (NPs) on graphene nanoplatelets (GNP) after 10 cycles at (a) 100 °C, (b) 200 °C, (c) 250 °C, and respective (middle) number-based and (right-hand-side) mass-based size distributions, that is, $F_1(d)$ and $F_3(d)$, respectively. $F_1(d)$ was plotted in the form of histogram by fixing the bin size to about 1 nm in all cases, whereas $F_3(d)$ was plotted in terms of probability density function by calculating the number of bins/points with the Freedman–Diaconis' rule. The platinum loading of the Pt/GNP composites of (a), (b), and (c) was about 6 wt% (~ 48 ng cm^{-2}) in all cases.

negligible deposition without resorting to powerful oxidizers such as ozone and oxygen plasma [18, 25, 42, 43]. The Pt/GNP composites were obtained after 1, 3, and 10 ALD cycles carried out at both 100 °C and 200 °C. In addition, we also carried out 10 ALD cycles at 250 °C to establish a worst case reference for the initial particle size distribution (PSD) span. The same number of cycles resulted in Pt/GNP composites characterized by the same Pt loading and yet different PSDs. The Pt loadings estimated via INAA were 0.5 %wt (~ 4 ng cm^{-2}), 1.5 %wt (~ 12 ng cm^{-2}), and 6 %wt (~ 48 ng cm^{-2}) after 1, 3, and 10 cycles, respectively. As the evolution of the PSD with the number of cycles was already discussed in detail in our previous work [27], here we now elaborate on the evolution with the deposition temperature of the mass-based PSD of the Pt/GNP obtained after 10 cycles (see Figure 4.1), that is, the composites with the highest loading considered here. As we shall point out later, the mass-based PSDs are crucial to the interpretation of the results of the catalytic test. Instead,

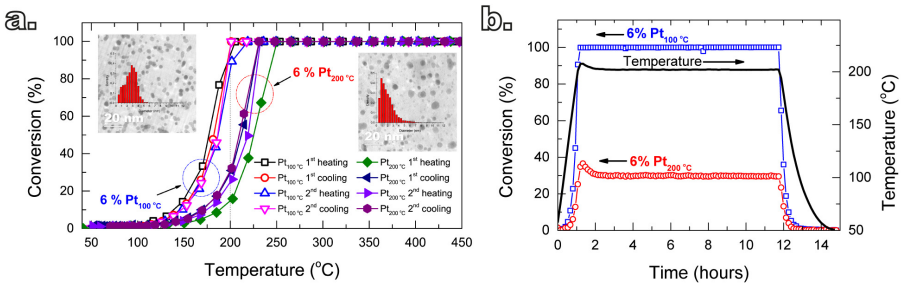

Figure 4.2: Catalytic performance of Pt/GNP obtained after 10 cycles at 100 °C and 200 °C towards propene oxydation. (a) Propene conversion as a function of temperature during two consecutive heating and cooling cycles from room temperature to 450 °C (ramp: 2 °C/min, total time 14 hours). (b) Conversion vs time at a reaction temperature of 200 °C, which was maintained constant for about 11 hours.

4

the PSDs of the Pt/GNP composites obtained after 1 and 3 cycles will be discussed in a later section dedicated to the sintering of the Pt NPs during the catalytic test.

Ten cycles of conventional thermal Pt ALD, that is, ALD carried out at 250 °C [18, 21, 27, 42], gave rise to a very broad right-skewed number-based PSD characterized by a numerous population of small NPs of about 1 nm coexisting next to NPs as large as 24 nm. The analysis of the mass-based PSD shows that, at such conditions, 80% of the platinum mass lies in NPs whose size range spans over more than 12 nm (see Figure 4.1c). Carrying out the same number of cycles below the 250 °C threshold resulted in a dramatic reduction in the metal aggregation. Decreasing the ALD temperature by 50 °C, in fact, brought about a two-fold reduction in the span of the mass-based PSD, which went from about 12 nm to 6 nm (see Figure 4.1b). Further reducing the ALD temperature to 100 °C led to (I) a six-fold decrease in the span of the mass-based PSD, which shrank to about 2 nm, (II) virtually no NPs larger than 6 nm, and (III) a nearly symmetric number- and mass-based PSD (see Figure 4.1a).

We put to test the performance and the stability of the Pt/GNP composites by using propene oxidation as a benchmark reaction. The influence of the ALD temperature on the catalytic performance was investigated by testing the Pt/GNP composites obtained at 100 °C and at 200 °C. The catalytic test consisted of three consecutive steps: (I) two heating/cooling cycles where the temperature of the catalytic bed was increased up to 450 °C and then decreased to room temperature; (II) heating up of the catalytic bed to the temperature at which 100% propene conversion is achieved, which is then maintained for approximately 10 hours, after which the bed is cooled down to room temperature, (III) heating up of the catalytic bed to a temperature at which an intermediate conversion is obtained, which is then maintained for approximately another 10 hours, after which the bed cooled down to room temperature for the last time. The conversion data from the cooling down phase of the second cycle of each step (I) was used to obtain the apparent reaction rate k_{app}, that is, the moles of propene converted per moles of Pt per unit time.

The deposition temperature had little to no effect on the catalytic performance of the composites obtained after 1 and 3 cycles. Furthermore, higher number of cycles, and thus loading, translated into higher conversions at a given temperature, which is in agreement with other reports on the relationship between platinum loading and propene conversion [28–

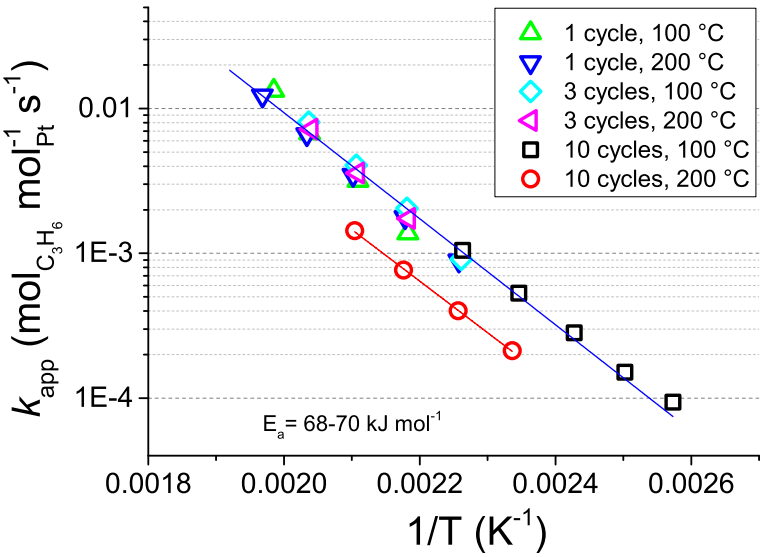

Figure 4.1: Arrhenius plot for k_{app} of propene oxidation over the Pt/GNP composites obtained after 1, 3, and 10 cycles at both 100 °C and 200 °C.

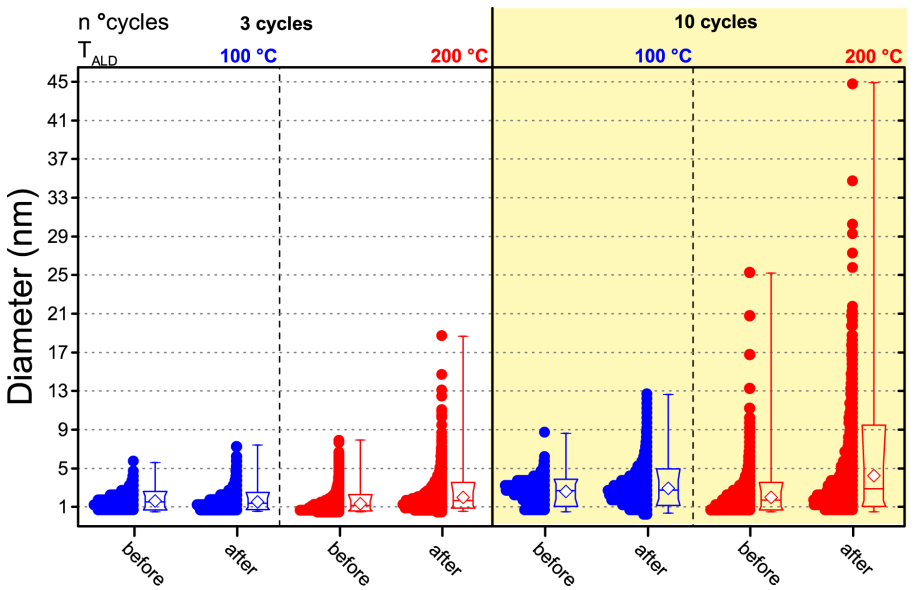

Figure 4.2: Box-and-whisker plots and data overlap of the number-based size distributions of the Pt nanoparticles obtained after 3 and 10 cycles at both 100 °C and 200 °C before and after the catalytic test. The boxes indicate the 10th, 25th, 75th, and 90th percentiles of the population, the whiskers indicate the minimum and the maximum size, and the white diamonds indicate the average size.

32]. On the other hand, despite the same Pt loading, the Pt/GNP composite obtained at low temperature (Pt/GNP/10L) after 10 cycles outperformed its high-temperature counterpart (Pt/GNP/10H). Figure 4.2a shows the catalytic behavior of Pt/GNP/10L and Pt/GNP/10H against temperature cycling in terms of conversion of propene. During the whole duration of the two temperature cycling, which, given the 2 °C/min ramp, amounted to about 14 hours in total, the Pt/GNP/10L composite delivered higher conversions at lower temperatures than the Pt/GNP/10H ($\Delta T_{50\%} \simeq 20$ °C), even after exposure to the reacting environment at temperatures as high as 450 °C. To further test the resilience of the gap in performance, in addition to the two temperature cycling, we exposed the composites to the reacting environment for two consecutive periods of 11 hours each at temperatures in the range of 190-220 °C (see Figure 4..2). As shown in Figure 4.2b, the Pt/GNP/10L composite retains its high activity compared to Pt/GNP/10H, with virtually no deactivation, even when exposed to 200 °C for more than 11 hours.

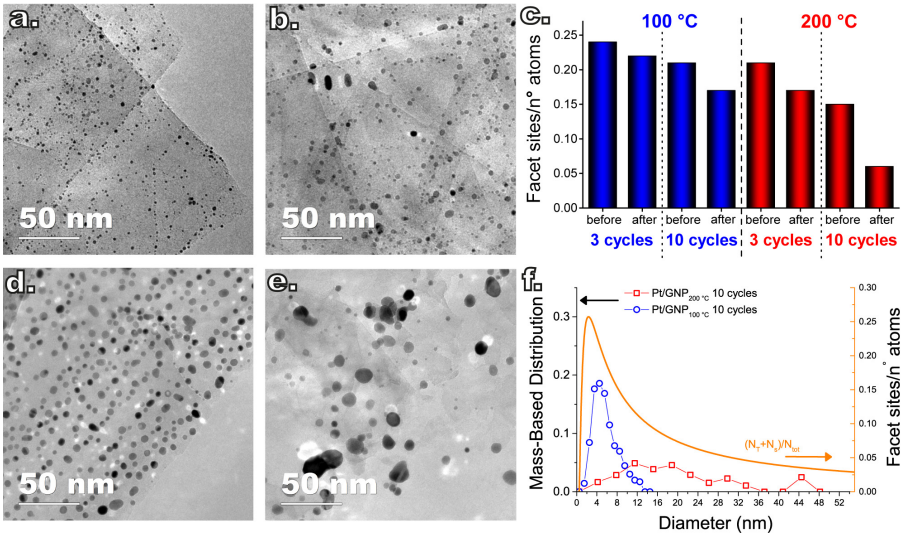

Figure 4.3: TEM micrographs taken after the catalytic test of the Pt/GNP composites obtained after 3 cycles at (a) 100 °C and (b) 200 °C, and after 10 cycles at (d) 100 °C and (e) 200 °C. (c) Number of facet sites, that is, surface sites minus edge and corner sites, divided by the total number of platinum atoms estimated by using the size distributions and assuming the NPs to assume a cubo-octahedral geometry. (f) Mass-based size distributions of the Pt NPs after the catalytic test of the Pt/GNP composites obtained after 10 cycles plotted together with the fraction of facet sites a cubo-octahedral platinum nanoparticle.

To obtain further insights into the reasons behind the gap in activity between Pt/GNP/10L and Pt/GNP/10H, we constructed the Arrhenius plot shown in Figure 4.1 by using the experimental values of the conversion in the range of 2.5-35 % obtained from the cooling part of the second temperature cycle of the catalytic test of Figure 4.2a. By using linear regression we obtained an apparent activation energy of about 68-70 kJ mol^{-1} (16-17 kcal mol^{-1}) for all the composites. This value is within the range of activation energies reported in the literature for propene oxidation over Pt-based catalysts [31]. While the activation energy is approximately the same for all composites, Pt/GNP/10L is still 2.9–2.6 times more active

than its high-temperature counterpart in the temperature range of 125–220 °C, that is, in the conversion range of 0–100 %. Interestingly, the reaction rate per unit mass of platinum at a given temperature was approximately the same for the composites obtained after 1 and 3 cycles and Pt/GNP/10L. Furthermore, the fact that the activation energy is virtually the same for all composites suggests that the gap in performance between Pt/GNP/10L and Pt/GNP/10H arises from a different number of active sites rather than from active sites of different nature.

To understand whether the results of the catalytic test can be interpreted in terms of differences in the PSDs, we also analyzed the composites after the catalytic test since the PSDs obtained after synthesis and prior to the catalytic test are not representative of the state of the catalyst during reaction, as this can induce NP sintering [29]. The Pt NPs in both composites, in fact, did sinter during the catalytic test. Figure 4.2 shows a box-and-whisker plot and data overlap representation of the number-based PSDs of the Pt NPs obtained after 3 and 10 cycles at both 100 °C and 200 °C before and after the catalytic test (see also Figure 4.3 a–b and Figure 4.3 d–e for representative TEM micrographs of the composites after the catalytic test). While both the low-temperature and the high-temperature composites did sinter, the low-temperature composites retained a narrow PSD compared to their high-temperature counterparts. In particular, the catalytic test resulted in virtually no change in the average NP size and the span of the number-based PSD of the low-temperature composite obtained after 3 cycles, whereas its high-temperature counterpart saw a twofold increase in the PSD span and in the average size as well as the appearance of a long tail on the large-size side. Analogously, while the Pt/GNP/10L composite saw a slight increase in the PSD span and in the average size, the Pt/GNP/10H composite saw a three-fold increase in the PSD span and in the average size, and the appearance of a long tail on the large-size side.

Despite the sintering, the Pt/GNP/10L (Figure 4.3d) still retained a homogeneous spatial and size distribution. On the other hand, the NPs in the Pt/GNP/10H composite (Figure 4.3e) sintered dramatically, giving rise to a considerable reduction in NP density (~ 94 %), loss of spatial homogeneity, the formation of aggregates of NPs as well as of individual NPs as large as 45 nm. While the span of the mass-based PSD of the NPs in the Pt/GNP/10L composite increased to about 6 nm from an initial value of 2 nm, the Pt/GNP/200 composite saw a more than five-fold increase in the same span, which went from 6 nm to more than 32 nm (see Figure 4.3f). It is worth noting that the span of the mass-based PSD of the Pt/GNP/10L composite after the catalytic test, and thus exposure to temperatures as high as 450 °C for prolonged periods of time, is still two times smaller than the span of the PSD of the as-synthesized NPs deposited at 250 °C (see Figure 4.3c and Figure 4.1c). Finally, the fact that such a drastic difference between the PSDs before and after the catalytic test was not reflected in an appreciable loss of activity during the long phases of the catalytic test (see Figure 4..2 and Figure 4.2) suggests that NP sintering took place only in the very beginning of the test.

To gain further insights into the different sintering and catalytic behaviours of the Pt/GNP composites we devised a series of computer simulations of the sintering process and a geometrical model for the catalytic activity of the NPs. To model the evolution of the PSDs due to sintering, we used the rate-equation approach already described in our previous work [27]. This model was used here to model the evolution of the PSDs of the as-synthesized Pt/GNP composites due to both gas-phase-mediated Ostwald ripening and NP diffusion

and coalescence. The purpose of the simulations was to give a qualitative description of the effect of different initial PSDs at a given metal loading on the sintering process and not to reproduce the exact PSDs after the catalytic test.

The resistance to sintering of the low-temperature composites and the different effect of the temperature during the synthesis and the catalytic test can arise from a number of reasons. The tendency of an ensemble of NPs to sinter depends, in fact, not only on the temperature but also on the shape of the initial PSD, the reaction environment, and the presence of carbonaceous species adsorbed on the catalyst surface [1, 2, 27, 44–46]. The initially narrow PSD of the Pt NPs synthesized at low temperature can effectively suppress sintering due to Ostwald ripening, given that the driving force of such mechanism lies in the PSD span [44]. Furthermore, the PSD of the Pt/GNP/10L NPs was not only narrow but also symmetric, whereas the Pt/GNP/10H composite had a large number of small NPs coexisting next to large ones. Sintering simulations using the experimental PSDs of both the Pt/GNP/10L and the Pt/GNP/10H composites as the initial condition clearly show that the latter sinters much faster than the former (see Figure 4..5) both in conditions that promote Ostwald ripening and in conditions in which the ensemble sinters via simultaneous Ostwald ripening and NP diffusion and coalescence. However, while we could achieve a qualitative description of the different stability of the low- and high-temperature composites, given a set of simulation parameters, we could not reproduce the exact discrepancy between the composites. The presence of large particles (d> 5 nm) in the high-temperature composites before the catalytic test might explain such a discrepancy if such NPs are more mobile than smaller ones upon exposure to the reacting mixture. Yet, at this moment, we do not have enough evidence to substantiate such mechanism. Finally, we argue that the effect of temperature during synthesis is more severe than it is during the catalytic test since the former relies on the cyclic combustion of the organic ligands remaining after the precursor chemisorption, and this process promotes sintering via NP diffusion and coalescence [27].

The geometrical model for describing the catalytic activity of an ensemble of Pt NPs builds on both the already available body of literature on the structure sensitivity of Pt-catalyzed propene oxidation and the evidence presented here. It has already been shown that the reaction rate per unit of mass of platinum is approximately the same across catalysts characterized by relatively low loadings (~ 1 wt%) and different NP sizes [31], which is in agreement with our results for Pt/GNP/10L and the Pt/GNP composites obtained after 1 and 3 cycles. Since larger NPs have lower dispersions, that is, surface sites vs total number of atoms, the reaction rates per unit area of platinum, often referred to as turnover frequencies (TOF), are higher for larger NPs. As a result, there is a general agreement on the size dependence of the catalytic activity of Pt NPs towards the combustion of hydrocarbons, and in particular of propene: the surface of large NPs is more active than the one of small NPs [28–32, 47]. Such size dependence has been attributed to the fact that large NPs exhibit weaker Pt-O bonding, given that loosely bound oxygen is more active towards the oxidation of hydrocarbons [28, 30, 31, 47]. However, while this simple picture is in agreement with most of our results, it still cannot explain the gap in performance between Pt/GNP/10L and Pt/GNP/10H. Hence, we propose a simple geometrical model that can account for all the observed results. We assume that oxygen is strongly bound to the atoms sitting at the corners and the edges of the exposed facets of an NP, which are thus not active towards propene oxidation [9, 31]. Instead, the number of moles of propene converted per unit time

is assumed to be directly proportional to the number of facet sites and thus:

$$k_{app} \propto N_F/N_{tot} = D_F \tag{4.5}$$

where N_F and N_{tot} are the number of facet sites and the total number of atoms in a NP, respectively, and D_F is the contribution of facet sites to the total metal dispersion, that is to say, the metal dispersion excluding corner and edge sites (see Figure 4.3f). Clearly, we are neglecting the possible role of metal-support interactions and electronic finite-size effects. Nevertheless, it has already been shown that metal-support interactions have little to no effect on the Pt-catalyzed oxidation of propene across a wide range of supports [28–32]. Furthermore, Li et al. [7] argued that not only quantum-size effects are unlikely to play a role in the catalytic properties of Pt NPs but also that the electronic properties of Pt clusters as small as 1.6 nm (147 atoms) already approach the single crystal limit. To describe the evolution of the fraction of facet sites with size we assumed the Pt NPs to take a cuboctahedral geometry, which is already been shown to mimic the evolution of the surface sites of the most stable clusters of Pt over a wide range of sizes [7, 48]. Hence, we can express D_F as a function of the NP size [49, 50] as follows:

$$D_F(v) = \frac{N_T + N_S}{N_{tot}} = \frac{18(v-1)^2 + 12(v-1)(v-2)}{10v^3 + 15v^2 + 11v + 3} \tag{4.6}$$

where N_T and N_S are the number of atoms in triangular and square facets, respectively, v is the shell number or cluster order, which depends linearly on the NP size d as follows [50]:

$$(2v+1)a/\sqrt{2} = d,\ v > 0 \tag{4.7}$$

where a is the lattice constant. Since the number of atoms in an NP scales as d^3, the D_F of an ensemble of NPs characterized by a number-based PSD $F_1(d)$ and a mass-based PSD $F_3(d)$ is simply:

$$\bar{D}_F = \frac{\sum_0^\infty F_1(d) d^3 D_F(d)}{\sum_0^\infty F_1(d) d^3} = \sum_0^\infty F_3(d) D_F(d) \tag{4.8}$$

By using Eq. (4.8) and the experimental mass-based PSDs before and after the catalytic test we could estimate the ratio between the number of facet sites and the total number of platinum atoms in the Pt/GNP composites (see Figure 4.3 c). Moreover, Eq. (4.8) was also used to calculate the fraction of facet sites of the simulated PSDs (see Figure 4..4). Indeed, the Pt/GNP composites obtained after 3 cycles and the Pt/GNP/10L composite have about the same fraction of facet sites, which is in agreement with their having virtually the same reaction rate per unit of mass of platinum. Crucially, the Pt/GNP/10H composite has about 63% less facet sites than the other composites, which is in agreement with the Pt/GNP/10L being about 2.9–2.6 times more active than Pt/GNP/10H (see Figure 4.1, Figure4.3 c and Figure 4.3f). Finally, sintering simulations of the Pt NPs obtained for a low number of cycles and thus low loadings, show that the fraction of facet sites remains fairly constant even after the NPs ensemble has lost more than 90 % of the initial number of NPs and the dispersion has dropped by more than 2-3 times and the surface-averaged diameter, that is the equivalent diameter obtained from CO and H_2 chemisorption, has increased by the same figure (see Figure 4..4). This is again in agreement with the fact that the catalyst with low loadings and

different NP size exhibit approximately the same reaction rate per unit mass of platinum. The reason why the fraction of facet sites of an ensemble of NPs remains fairly constant at low coverages, regardless of the average size, is that the fraction of facet sites is a non-linear function of the Pt NP size (see Figure 4.3 f) that approaches zero for small NPs and has a maximum at about 2.5 nm after which it decreases and then steadily levels off at large sizes. Clearly, there exists an infinite number of mass-based PSDs that, once multiplied by $D_F(d)$ and integrated (see Eq. (4.8)), lead to the same fraction of facet sites and thus the same reaction rate per unit mass of platinum. However, at relatively high loadings (large average sizes), broad right-skewed mass-based PSDs, such as the one of the Pt/GNP/10H composite after the catalytic test, fall under the descending side of $D_F(d)$ and thus lead to small facet sites fractions.

4.4. Conclusions

In conclusion, we have demonstrated that, compared to conventional Pt ALD, low-temperature ALD enables the synthesis of supported Pt nanoparticles that have (I) narrow size distributions, (II) higher activity at high metal loadings, and (III) higher stability at a given Pt loading. Crucially, the gap in performance between the low-temperature composite obtained after 10 cycles and its high-temperature counterpart towards propene oxidation was retained even after prolonged period of times (>24 hours) at temperatures as high as 450 °C. Furthermore, the Pt NPs synthesized at 100 °C, once exposed to such harsh conditions, retained a size distribution that is narrower than the one of the Pt NPs synthesized at 250 °C. Hence, the temperature history is more important than the absolute temperature to which the Pt NPs are exposed. The difference in catalytic activity was attributed to different fractions of surface active sites, as corroborated by a simple geometrical model based on the analysis of the size distributions after the catalytic test. Our analysis emphasizes that when the reaction happens mostly on the facets of the NPs, dispersion and average size are poor descriptors of the catalytic performance. Instead, one should take into account the whole size distribution to make meaningful comparisons. The ability to tailor the size distribution of NPs at a given metal loading coupled with the analysis of the performance presented here exemplifies how ALD can be used as a tool for elucidating the relationship between size and functionality in NP-based materials. Such advantages, demonstrated here by using graphene nanoplatelets, can find application in the study and the optimization of the activity, selectivity, and stability of carbon-supported Pt NPs for fuel cells electrodes. Finally, we anticipate that the use of high oxygen partial pressure can push the lower temperature limit of thermal ALD of noble metals on other carbon supports way below 100 °C, that is, the lowest ALD temperature explored here. Yet, whether the advantages of our approach can be extended to oxide supports merits further study.

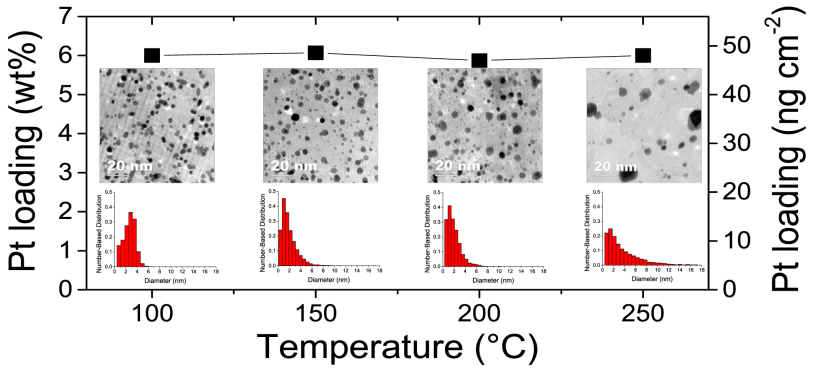

Figure 4..1: Platinum loading vs deposition temperature after 10 ALD cycles and respective size distributions and representative TEM micrographs.

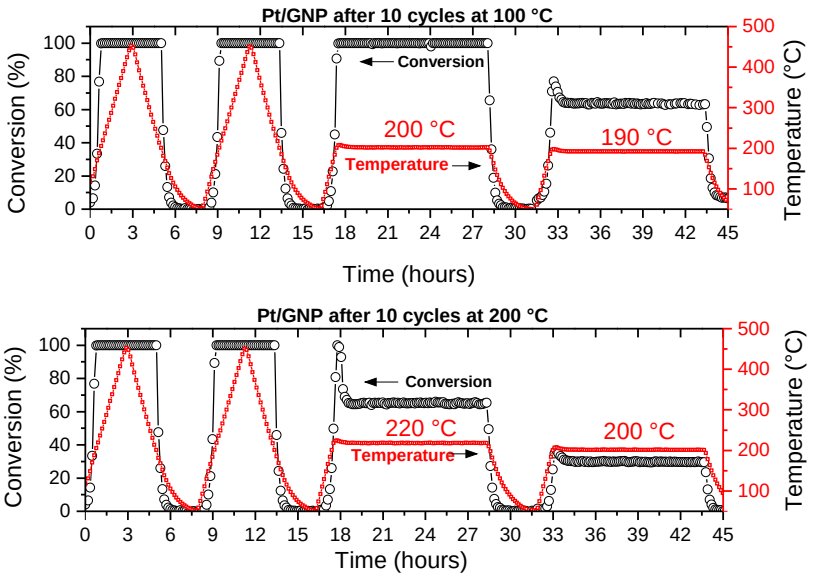

Figure 4..2: Extended results of the catalytic test plotted as propene conversion and temperature vs time obtained for (upper part) Pt/GNP/100 and Pt/GNP/200 (bottom).

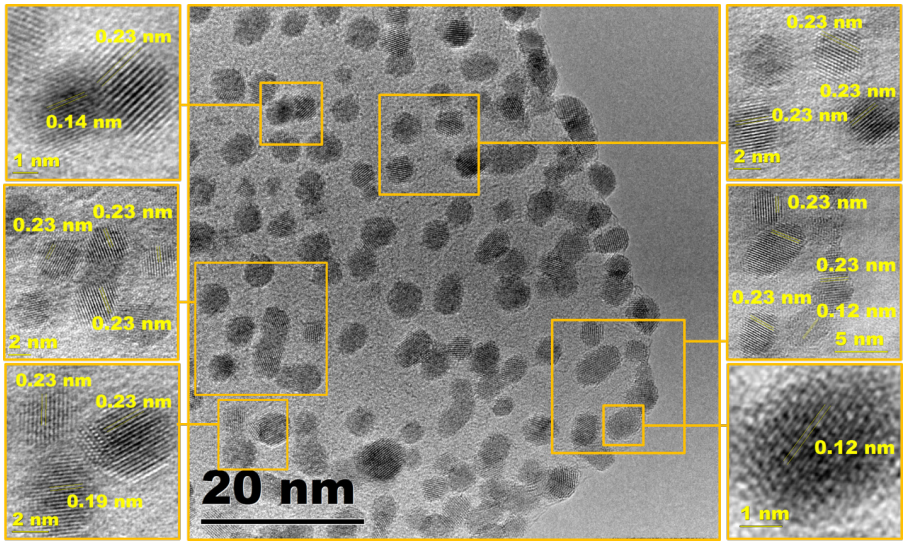

Figure 4..3: HRTEM image of the as-synthesized Pt/GNP/100 (center). The satellite images are zoomed-in views highlighting the crystalline structure and lattice constants of Pt NPs.

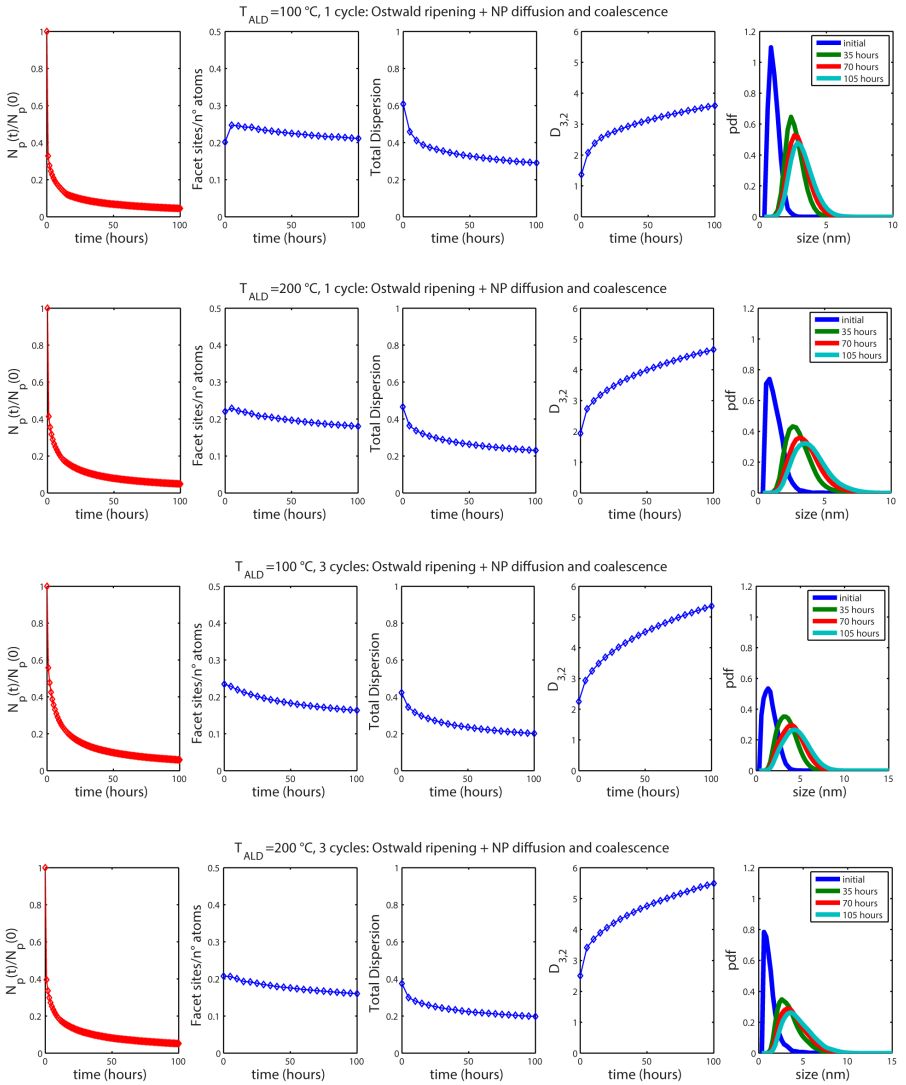

Figure 4..4: Simulation results of the sintering of Pt nanoparticles via simultaneous gas-phase-mediated Ostwald ripening and nanoparticle diffusion and coalescence. The initial conditions of the simulations were the experimental particle size distributions and nanoparticle density of the as-synthesized composites obtained after 1 and 3 cycles at both 100 °C and 200 °C. The parameters used for each simulation were: T=350 °C, p_{O_2}=152 torr, $D_k = D_1 k^{-0.1}$ (where D_k is the mobility of a nanoparticle of size k, that is the number of atoms comprising the nanoparticle) and D_1=0.01 nm^2 s^{-1}. From left to right, the plots show the evolution of: the number of nanoparticles per unit area normalized to to the initial value; the total number of facet sites divided by the total number of atoms; the total dispersion, that is the total number of surface atoms divided by the total number of atoms; the surface-averaged diameter of the ensemble; and the number-based particle size distribution.

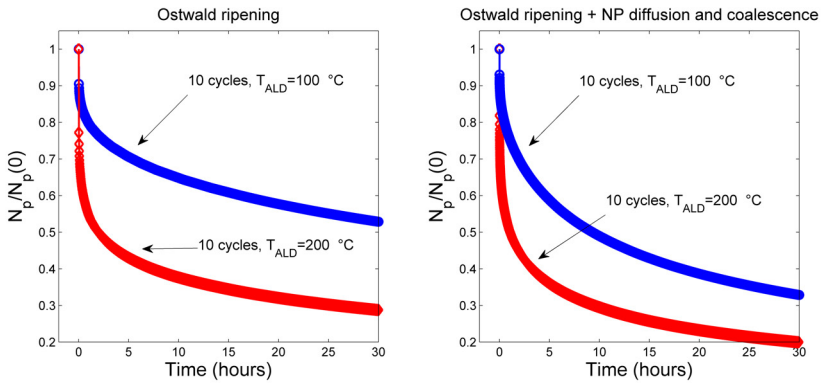

Figure 4..5: Simulation results of the sintering of Pt nanoparticles via gas-phase-mediated Ostwald ripening and nanoparticle diffusion and coalescence. The initial conditions of the simulations were the experimental particle size distributions and nanoparticle density of the as-synthesized composites obtained after 10 cycles at both 100 °C and 200 °C. The y-axis indicates number of nanoparticles per unit area normalized to the initial value. (T=350 °C, p_{O_2}=152 torr) and nanoparticle diffusion and coalescence ($D_k = D_1 k^{-2/3}$, D_1=0.1 nm^2 s^{-1}).

4

Evaluation of the impact of mass-transfer limitations

In order to rule out possible mass transfer limitations we used the Wiesz-Prater criterion for internal mass transfer limitation:

$$C_{WP} = \frac{r_{obs} \varrho_p R^2}{D_{eff} C_s} << 1$$

and the Mears criterion for external mass transfer limitations.

$$C_M = \frac{r_{obs} \varrho_b R}{k_c C_s} << 1$$

Where r_{obs} is the observed reaction rate expressed in mol gcat^{-1}s^{-1}, ϱ_p is the density of the catalyst particles, R is the volume-based radius of the catalyst particles, D_{eff} is the diffusion coefficient of the reactant within the catalyst particles, C_s is either concentration of reactant at outer surface of the catalyst particle for the Wiesz-Prater criterion or the concentration of reactant at the inlet of the reactor for the Mears criterion, ϱ_p is the bulk density of the catalyst and, k_c is the external mass transfer coefficient. ϱ_b varies in the range of 0.03-0.1 g/cm^3 as reported by the supplier (Strem Chemicals) and it was thus approximated to an average value of 65 kg/m^3. The volume-based radius was measured by means of a LS Beckman Coulter Particle Size Analyzer and it was found to be about 18.35 μm. The density of the catalyst particle was estimated as follows:

$$\varrho_p = \varrho_{graphite} (1 - \epsilon_p) \sim 86 \text{ kg/m}^3$$

Where $\varrho_{graphite}$ is the density of graphite, which is about 2160 kg/m^3, and ϵ_p is the void fraction of the catalyst particle. The latter is assumed to be consisting of agglomerated

graphene nanoplatelets, in other wordsϵ_p is the void fraction of the graphene nanoplatelets agglomerates. ϵ_p, in turn, was estimated as follows:

$$\epsilon_p = 1 - \frac{\left(\varrho_b / \varrho_{graphite}\right)}{(1 - \epsilon_{bed})} \sim 0.96$$

Here, $(1 - \epsilon_{bed})$, that is, the packing density of the catalytic bed, was assumed to be about 0.3 (close random packing for ellipsoids). Such a high value of the void fraction for the graphene nanoplatelets agglomerates (ϵ_p>0.9) is consistent with typical values reported for agglomerates of nanostructured powders such as agglomerates of nanoparticles (0.95-0.99). Given the high porosity of the graphene nanoparticle agglomerates, D_{eff} was assumed to be about 10^{-5} m^2/s, that is the typical value of the diffusion coefficient of a gas undergoing molecular diffusion at atmospheric pressure and room temperature (conservative estimate). Given the low Reynolds number (~0.01, using average values for the viscosity and the density of helium in the temperature range of 100-450 °C and a superficial velocity of 0.04 m/s), we made a conservative estimate of k_c by approximating the Sherwood number to 2 (stagnant flow around a sphere). By doing so we found a k_c of about 5 m/s. By using the aforementioned figures and calculating r_obs based on the maximum and the minimum value of k_app reported in this work, we obtain:

$$C_{WP} \sim 10^{-5} - 10^{-6} << 1$$

$$C_M \sim 10^{-6} - 10^{-1} << 1$$

Hence, we conclude that the influence of mass transfer on our results is negligible.

References

[1] P. Wynblatt and N. Gjostein, *Supported metal crystallites,* Prog. Solid State Chem. 9, 21 (1975).

[2] P. J. F. Harris, *Growth and structure of supported metal catalyst particles,* Int. Mater. Rev. 40, 97 (1995).

[3] J. A. Farmer and C. T. Campbell, *Ceria Maintains Smaller Metal Catalyst Particles by Strong Metal-Support Bonding,* Science 329, 933 (2010).

[4] S. Guo and E. Wang, *Noble metal nanomaterials: Controllable synthesis and application in fuel cells and analytical sensors,* Nano Today 6, 240 (2011).

[5] B. R. Cuenya, *Synthesis and catalytic properties of metal nanoparticles: Size, shape, support, composition, and oxidation state effects,* Thin Solid Films 518, 3127 (2010).

[6] H. Gandhi, G. Graham, and R. McCabe, *Automotive exhaust catalysis,* Journal of Catalysis 216, 433 (2003), 40th Anniversary Commemorative Issue.

[7] L. Li, A. H. Larsen, N. A. Romero, V. A. Morozov, C. Glinsvad, F. Abild-Pedersen, J. Greeley, K. W. Jacobsen, and J. K. Nørskov, *Investigation of Catalytic Finite-Size-Effects of Platinum Metal Clusters,* The Journal of Physical Chemistry Letters 4, 222 (2013), pMID: 26291235.

[8] K. Yamamoto, T. Imaoka, W.-J. Chun, O. Enoki, H. Katoh, M. Takenaga, and A. Sonoi, *Size-specific catalytic activity of platinum clusters enhances oxygen reduction reactions,* Nat. Chem. 1, 397 (2009).

[9] B. R. Cuenya and F. Behafarid, *Nanocatalysis: size- and shape-dependent chemisorption and catalytic reactivity,* Surf. Sci. Rep. 70, 135 (2015).

[10] N. Satoh, T. Nakashima, K. Kamikura, and K. Yamamoto, *Quantum size effect in TiO2 nanoparticles prepared by finely controlled metal assembly on dendrimer templates,* Nat. Nanotechnol. 3, 106 (2008).

[11] H. Ye and R. M. Crooks, *Electrocatalytic O 2 Reduction at Glassy Carbon Electrodes Modified with Dendrimer-Encapsulated Pt Nanoparticles,* J. Am. Chem. Soc. 127, 4930 (2005).

[12] F. N. Gür, F. W. Schwarz, J. Ye, S. Diez, and T. L. Schmidt, *Toward Self-Assembled Plasmonic Devices: High-Yield Arrangement of Gold Nanoparticles on DNA Origami Templates,* ACS Nano 10, 5374 (2016).

[13] S. Vajda, M. J. Pellin, J. P. Greeley, C. L. Marshall, L. A. Curtiss, G. A. Ballentine, J. W. Elam, S. Catillon-Mucherie, P. C. Redfern, F. Mehmood, and P. Zapol, *Subnanometre platinum clusters as highly active and selective catalysts for the oxidative dehydrogenation of propane,* Nature Materials 8, 213 (2009).

[14] C. Detavernier, J. Dendooven, S. Pulinthanathu Sree, K. F. Ludwig, and J. A. Martens, *Tailoring nanoporous materials by atomic layer deposition,* Chem. Soc. Rev. 40, 5242 (2011).

[15] D. Longrie, D. Deduytsche, and C. Detavernier, *Reactor concepts for atomic layer deposition on agitated particles: A review,* Journal of Vacuum Science & Technology A: Vacuum, Surfaces, and Films 32, 010802 (2014).

[16] H. Van Bui, F. Grillo, and J. R. van Ommen, *Atomic and molecular layer deposition: off the beaten track,* Chem. Commun. 53, 45 (2017).

[17] B. J. O'Neill, D. H. K. Jackson, J. Lee, C. Canlas, P. C. Stair, C. L. Marshall, J. W. Elam, T. F. Kuech, J. A. Dumesic, and G. W. Huber, *Catalyst Design with Atomic Layer Deposition,* ACS Catalysis 5, 1804 (2015).

[18] A. Goulas and J. R. van Ommen, *Atomic layer deposition of platinum clusters on titania nanoparticles at atmospheric pressure,* Journal of Materials Chemistry A 1, 4647 (2013).

[19] S. M. George, *Atomic Layer Deposition: An Overview,* Chem. Soc. Rev. 110, 111 (2010).

[20] R. L. Puurunen, *Surface chemistry of atomic layer deposition: A case study for the trimethylaluminum/water process,* J. Appl. Phys. 97, 121301 (2005).

[21] S. Sun, G. Zhang, N. Gauquelin, N. Chen, J. Zhou, S. Yang, W. Chen, X. Meng, D. Geng, M. N. Banis, R. Li, S. Ye, S. Knights, G. A. Botton, T.-K. Sham, and X. Sun, *Single-atom Catalysis Using Pt/Graphene Achieved through Atomic Layer Deposition,* Sci. Rep. 3, 1775 (2013).

[22] V. Miikkulainen, M. Leskelä, M. Ritala, and R. L. Puurunen, *Crystallinity of inorganic films grown by atomic layer deposition: Overview and general trends,* J. Appl. Phys. 113, 021301 (2013).

[23] F. Grillo, M. T. Kreutzer, and J. R. van Ommen, *Modeling the precursor utilization in atomic layer deposition on nanostructured materials in fluidized bed reactors,* Chemical Engineering Journal 268, 384 (2015).

[24] D. M. King, J. A. S. II, X. Liang, L. F. Hakim, and A. W. Weimer, *Atomic layer deposition on particles using a fluidized bed reactor with in situ mass spectrometry,* Surface and Coatings Technology 201, 9163 (2007), euro {CVD} 1616th European Conference on Chemical Vapor Deposition.

[25] A. J. M. Mackus, M. J. Weber, N. F. W. Thissen, D. Garcia-Alonso, R. H. J. Vervuurt, S. Assali, A. A. Bol, M. A. Verheijen, and W. M. M. Kessels, *Atomic layer deposition of Pd and Pt nanoparticles for catalysis: on the mechanisms of nanoparticle formation,* Nanotechnology 27, 034001 (2015).

[26] H. V. Bui, F. Grillo, R. Helmer, A. Goulas, and J. R. van Ommen, *Controlled Growth of Palladium Nanoparticles on Graphene Nanoplatelets via Scalable Atmospheric Pressure Atomic Layer Deposition,* J. Phys. Chem. C 120, 8832 (2016).

[27] F. Grillo, H. Van Bui, J. A. Moulijn, M. T. Kreutzer, and J. R. van Ommen, *Understanding and Controlling the Aggregative Growth of Platinum Nanoparticles in Atomic Layer Deposition: An Avenue to Size Selection,* The Journal of Physical Chemistry Letters 8, 975 (2017), pMID: 28178779.

[28] S. Benard, M. Ousmane, L. Retailleau, A. Boreave, P. Vernoux, and A.-F. Giroir-Fendler, *Catalytic removal of propene and toluene in air over noble metal catalystThis article is one of a selection of papers published in this Special Issue on Biological Air Treatment.* Canadian Journal of Civil Engineering 36, 1935 (2009).

[29] P. Denton, A. Giroir-Fendler, H. Praliaud, and M. Primet, *Role of the Nature of the Support (Alumina or Silica), of the Support Porosity, and of the Pt Dispersion in the Selective Reduction of NO by C3H6 under Lean-Burn Conditions,* Journal of Catalysis 189, 410 (2000).

[30] L. Liotta, *Catalytic oxidation of volatile organic compounds on supported noble metals,* Applied Catalysis B: Environmental 100, 403 (2010).

[31] L. M. Carballo and E. E. Wolf, *Crystallite size effects during the catalytic oxidation of propylene on Ptγ-Al2O3,* Journal of Catalysis 53, 366 (1978).

[32] P. Marécot, A. Fakche, B. Kellali, G. Mabilon, P. Prigent, and J. Barbier, *Propane and propene oxidation over platinum and palladium on alumina: Effects of chloride and water,* Applied Catalysis B: Environmental 3, 283 (1994).

[33] N. Zhang, Y. Zhang, and Y.-J. Xu, *Recent Progress on Graphene-Based Photocatalysts: Current Status and Future Perspectives,* Nanoscale 4, 5792 (2012).

[34] C. Huang, C. Li, and G. Shi, *Graphene Based Catalysts,* Energy Environ. Sci. 5, 8848 (2012).

[35] S. Navalon, A. Dhakshinamoorthy, M. Alvaro, and H. Garcia, *Carbocatalysis by Graphene-Based Materials,* Chem. Rev. 114, 6179 (2014).

[36] B. F. Machado and P. Serp, *Graphene-Based Materials for Catalysis,* Catal. Sci. Technol. 2, 54 (2012).

[37] H. D. Ozaydin, H. Sahin, R. T. Senger, and F. M. Peeters, *Formation and diffusion characteristics of Pt clusters on Graphene, 1H-MoS2and 1T-TaS2,* Annalen der Physik 526, 423 (2014).

[38] C. Feng, J. Wang, Y. Cheng, P. He, and K. M. Liew, *Diffusion mechanism of platinum nanoclusters on well-aligned carbon nanotubes,* RSC Adv. 4, 60711 (2014).

[39] E. Lamas and P. Balbuena, *Adsorbate effects on structure and shape of supported nanoclusters: A molecular dynamics study,* The Journal of Physical Chemistry B 107, 11682 (2003).

[40] J. Chen and K.-Y. Chan, *Size-dependent mobility of platinum cluster on a graphite surface,* Molecular Simulation 31, 527 (2005).

[41] S. Sartipi, H. Jansma, D. Bosma, B. Boshuizen, M. Makkee, J. Gascon, and F. Kapteijn, *Six-flow operations for catalyst development in Fischer-Tropsch synthesis: Bridging the gap between high-throughput experimentation and extensive product evaluation,* Review of Scientific Instruments 84, 124101 (2013).

[42] A. J. M. Mackus, M. A. Verheijen, N. Leick, A. A. Bol, and W. M. M. Kessels, *Influence of Oxygen Exposure on the Nucleation of Platinum Atomic Layer Deposition: Consequences for Film Growth, Nanopatterning, and Nanoparticle Synthesis,* Chem. Mater. 25, 1905 (2013).

[43] T. Aaltonen, M. Ritala, T. Sajavaara, J. Keinonen, and M. Leskelä, *Atomic Layer Deposition of Platinum Thin Films,* Chem. Mater. 15, 1924 (2003).

[44] K. Wettergren, F. F. Schweinberger, D. Deiana, C. J. Ridge, A. S. Crampton, M. D. Rtözer, T. W. Hansen, V. P. Zhdanov, U. Heiz, and C. Langhammer, *High Sintering Resistance of Size-Selected Platinum Cluster Catalysts by Suppressed Ostwald Ripening,* Nano Lett. 14, 5803 (2014).

[45] Y. Chu and E. Ruckenstein, *Behavior of platinum crystallites on carbon substrates,* Surf. Sci. 67, 517 (1977).

[46] K.-J. Hu, S. R. Plant, P. R. Ellis, C. M. Brown, P. T. Bishop, and R. E. Palmer, *Atomic Resolution Observation of a Size-Dependent Change in the Ripening Modes of Mass-Selected Au Nanoclusters Involved in CO Oxidation,* Journal of the American Chemical Society 137, 15161 (2015).

[47] N. Radic, B. Grbic, and A. Terlecki-Baricevic, *Kinetics of deep oxidation of n-hexane and toluene over Pt/Al2O3 catalysts: Platinum crystallite size effect,* Applied Catalysis B: Environmental 50, 153 (2004).

[48] A. Le Valant, C. Comminges, F. Can, K. Thomas, M. Houalla, and F. Epron, *Platinum Supported Catalysts: Predictive CO and H2 Chemisorption by a Statistical Cuboctahedron Cluster Model,* The Journal of Physical Chemistry C 120, 26374 (2016).

[49] J. Montejano-Carrizales, F. Aguilera-Granja, and J. Morán-López, *{DIRECT} {ENUMERATION} {OF} {THE} {GEOMETRICAL} {CHARACTERISTICS} {OF} {CLUSTERS},* Nanostructured Materials 8, 269 (1997).

[50] C. P. Poole, F. J. Jones, and F. J. Owens, *Introduction to Nanotechnology* (John Wiley & Sons, Inc., New York, NY, USA, 2003).

Dublin, Ireland 2016.

5

From Single Atoms to Nanoparticles: Autocatalysis and Metal Aggregation in Atomic Layer Deposition of Pt on TiO_2 Nanopowder

We present a fundamental understanding of the interplay between ligand-removal kinetics and metal aggregation during the formation of platinum nanoparticles (NPs) in atomic layer deposition of Pt on TiO_2 nanopowder using $MeCpPtMe_3$ as the precursor and O_2 as the co-reactant. We followed the growth from single atoms to NPs as a function of the oxygen exposure (P_{O_2} x time). We could model the kinetics by accounting for the autocatalytic combustion of the precursor ligands via a variant of the Finke-Watzky two-step model. We find that even at relatively high oxygen exposures (< 120 mbar s) little to no Pt is deposited after the first cycle and that most of the Pt is atomically dispersed. Increasing the oxygen exposure above 120 mbar s results in a rapid increase in the Pt loading, which saturates at exposures » 120 mbar s. The deposition of more Pt inevitably leads to the formation of NPs that can be as large as 6 nm. Crucially, high P_{O_2} (≥ 5 mbar) hinders the metal aggregation, thus leading to narrow particle size distributions. Our results show that ALD of Pt NPs is reproducible across small and large surface areas if the precursor ligands are removed at high P_{O_2}.

Published as: Fabio Grillo, Hao Van Bui, Damiano La Zara, Antonius A. I. Aarnink, Alexey Y. Kovalgin, Patricia Kooyman, Michiel T. Kreutzer, and J. Ruud van Ommen, From Single Atoms to Nanoparticles: Autocatalysis and Metal Aggregation in Atomic Layer Deposition of Pt on TiO_2 Nanopowder, *Small*, accepted for publication.

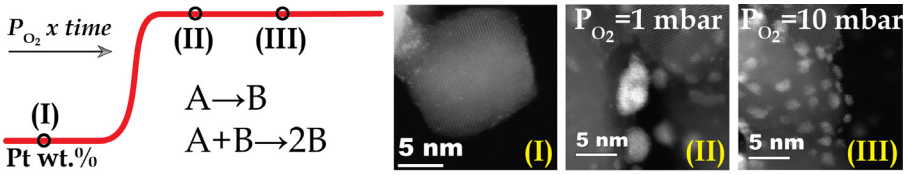

5.1. Introduction

Most industrial catalysts have consisted of nanoparticles (NPs) dispersed on high-surface-area supports since the early days of catalysis [1–8]. Yet, obtaining supported NPs with a narrow particle size distribution (PSD) in a controlled and scalable fashion remains a challenge: it is, in fact, one of the main research goals of modern nanoscience [7, 9–19]. Narrow PSDs are crucial to practical applications not only because NPs exhibit size-dependent properties, but also because they are often associated with a higher resistance to sintering and thus higher stability [17, 20–22]. The main obstacle towards narrow PSDs lies in the lack of fundamental understanding of the mechanisms behind the formation of NPs on supports [7, 9, 11, 23]: "catalysts are currently prepared rather than synthesized" [23]. Supported NPs are typically obtained via the aggregation of monomers or single atoms released by the decomposition of precursor molecules, which can be induced by reaction with one or more co-reactants, or simply by heat-treatment [1, 9, 11, 12]. It follows that the rational synthesis of NPs with tailored PSDs requires an understanding of the interplay between precursor conversion and monomer aggregation.

Atomic layer deposition (ALD) is a well-established thin film deposition tecnique that promises to bring the precision of nanotechnology to catalyst synthesis [18, 19, 23–25]. In ALD, the synthesis starts with precursor molecules chemisorbing on the surface of the support via self-limiting gas-solid reactions: less than a monolayer is deposited in each reaction step [24, 26–28]. Depending on the precursor of choice, the support is then exposed to a suitable co-reactant so that the precursor ligands are removed and more precursor can chemisorb in the next reaction step. By repeating this sequence in a cyclic fashion, depending on the affinity between the ALD-grown material and the support, one can grow thin films, NPs, and even single atoms with submonolayer precision [18, 19, 24–31]. Crucially, in virtue of being a surface-driven and solvent-less technique, ALD circumvents several shortcomings of conventional liquid-phase and gas-phase techniques in that: (I) it is not a line-of-sight tecnique and is thus suitable for high-surface-area supports such as powders [24, 32, 33]; (II) does not suffer from the mass-transfer limitations inherent to liquid-phase processes and it is thus less prone to lead to inhomogeneous deposition [18, 24, 25, 33]; (III) NP nucleation takes place on the support surface only, that is, secondary homogeneous nucleation is inherently suppressed [18, 25]; (IV) does not require separation steps and yields catalysts with little to no impurities [22, 24, 25].

Although ALD of thin films on flat substrates is a mature technology, ALD of NPs on high-surface-area supports is still poorly understood [19, 24, 34, 35]. For example, ALD of platinum NPs results in very different PSDs depending on the reaction conditions, reactor configuration, and nature of the support [19, 24, 30, 31, 34, 36–43]. Mackus et al. [44] argued that in Pt ALD the NP size depends on the oxygen exposure during the ligand-removal step because the presence of oxygen affects the mobility of Pt species and thus the aggregation of

atoms into NPs, which in turn can catalyze combustion reactions. Yet, while the reaction atmosphere can certainly affect the NP by mediating the aggregation process [7, 8, 19, 21, 45], the oxygen exposure also determines the extent of the ligand-removal and thus the amount of Pt deposited in each cycle, which alone directly affects the NP size. In fact, the role of the extent of the ALD reactions in ALD of NPs is typically overlooked, especially in studies concerning flat substrates [34]. Also, it is not clear whether the understanding gained by studying ALD on flat substrates is directly applicable to ALD on high-surface-area supports [24, 34, 40]. Typically, ALD on high-surface-area supports results in NPs larger than 1 nm, even after only few ALD cycles [19, 24, 31, 34, 36, 42], whereas achieving the same size in ALD on flat substrates can require as many as 50 cycles [34]. This discrepancy might be due to the prolonged precursor dosing times used in ALD on high-surface-area supports [24, 34], which might exacerbate NP sintering or result in undesired precursor decomposition. However, in our recent work, we showed that even in ALD on high-surface-area supports NPs mostly form and grow during the ligand-removal step rather than during the precursor dosing [19]. This is also in agreement with the recent findings of Dendooven et al. [41]. Hence, the outstanding questions are: (1) what is the interplay between the kinetics of the ligand-removal step and that of the metal aggregation? And, in particular, is ALD of NPs reproducible across small and large surface areas in terms of loading and PSD? (2) Which operating conditions suppress metal aggregation, thus resulting in narrow PSDs?
We present a study designed to answer the above questions for ALD of Pt NPs on TiO_2 nanopowders using $Me_3MeCpPt$ as the precursor and O_2 as the co-reactant for the ligand-removal step. To understand the interplay between ligand-removal and metal aggregation, we followed the growth from single atoms to NPs, at a given number of cycles, as a function of the oxygen exposure via elemental analysis and electron microscopy, and in particular via high angle annular dark field (HAADF) imaging. We explored a parameter space encompassing oxygen partial pressures and exposures times that are relevant to both vacuum reactors for flat substrates and reactors for large batches of high-surface-area substrates [24, 26, 31, 34, 36, 44, 46, 47]: [0.1 mbar - 1 bar x 20 s - 600 s]. We show that the extent of ligand-removal and thus the amount of material deposited as a function of the oxygen exposure follows a sigmoidal curve, which is consistent with the autocatalytic nature of combustion reactions. In particular, we find that exposure values typically used in ALD on flat substrates lie in the "incubation" region of the parameter space: little to no Pt is being deposited after the first cycle as a result of incomplete removal of the precursor ligands after the oxygen exposure. Finally, we show that high oxygen partial pressures ($\geq$ 5 mbar) result in narrow and symmetric PSDs, whereas low pressures result in broad PSDs with a long tails towards the large-size side.

5.2. Results and discussion

We begin by examining the effect of the oxygen exposure on the ligand-removal kinetics in terms of the evolution of the Pt loading. First, we focus on results concerning Pt ALD on minute amounts of TiO_2 nanopowder supported on TEM grids that was carried out in vacuum reactors designed for flat substrates. This particular setting allowed us to carry out ALD on supports with a high specific-surface-area such as TiO_2 nanopowder while keeping the total surface area within values that are relevant to ALD on flat substrates ($\sim 10^{-3}$-10^{2} cm^2). By doing so, we avoided the prolonged precursor exposure times that are typically

associated with ALD on high-surface-area supports such as powders [24, 26, 34]. As we will point out later, this aspect is crucial for ruling out the long precursor exposures as the leading cause of the widely reported formation of large NPs on high-surface-area substrates even after a few ALD cycles [34]. After discussing the effect of the oxygen exposure on the ligand-removal kinetics, we will discuss how the oxygen exposure affects the metal aggregation and thus the PSD of the NPs. We will then show how the partial pressure affects the broadness of the PSD. Finally, we will discuss the reproducibility and scalability of the process by comparing the results obtained using vacuum reactors on small surface areas with those obtained using a fluidized bed reactor operated at atmospheric pressure on large areas ($\simeq$75 m^2).

5.2.1. Ligand-removal kinetics from the evolution of the Pt loading

As shown in Figure 5.C.1, the amount of platinum measured after 5 ALD cycles as a function of the oxygen exposure (oxygen pressure x time) exhibits a sigmoidal or S-shaped curve. At low oxygen exposures the Pt/Ti ratio remains virtually constant at about 2.4 wt%. After a critical oxygen exposure, or "incubation phase", the Pt/Ti ratio rapidly increases and then saturates at about 12 wt%. In particular, for an oxygen pressure of 1 mbar, the Pt/Ti ratio approaches saturation only after exposures of several minutes, whereas for an oxygen pressure of 0.133 mbar (100 mTorr) the Pt/Ti ratio remains close to the incubation value even after exposures as long as 10 minutes. Since the Pt/Ti ratio at saturation is five times the one in the incubation phase, we infer that in the experiments performed using low oxygen exposures, $MeCpPtMe_3$ chemisorption, and thus Pt deposition, took place only in the first ALD cycle.

After the first cycle, the deposition of platinum can stop because of (1) an ineffective removal of the carbonaceous layer forming upon $MeCpPtMe_3$ chemisorption and (2) the lack of active surface oxygen [44, 46–48]. This is because $MeCpPtMe_3$ chemisorption proceeds through combustion-like surface reactions that consume surface oxygen and that produce a carbonaceous layer that hinders further $MeCpPtMe_3$ adsorption. Indeed, ex-situ X-ray photoelectron spectroscopy (XPS) shows that using low oxygen exposures result in a partial reduction of the TiO_2 surface in concomitance with the deposition of small amounts of platinum (see Figure 5.2). Even after exposure to ambient conditions, the surface of the Pt/TiO_2 composites obtained after 5 ALD cycles using oxygen exposures of 1 mbar x 20 s presented ~ 14 at.% Ti^{3+} and ~ 3 at.% Ti^{2+}, whereas the same number of cycles performed using an oxygen exposure of 5 mbar x 300 s resulted in a surface concentration of Ti^{3+} and Ti^{2+} of ~ 7 at.% and $\lesssim$ 1 at.%, respectively. Intermediate oxygen exposures resulted in intermediate degrees of reduction of the TiO_2 surface (see Figure 5.A.XPS). In other words, high oxygen exposures effectively re-oxidize the TiO_2 surface that is periodically reduced by $MeCpPtMe_3$, thus providing the surface oxygen for the onset of $MeCpPtMe_3$ chemisorption, which would otherwise take place only during the first $MeCpPtMe_3$ exposure. Furthermore, the hypothesis that low oxygen exposures are ineffective in combusting the carbonaceous layer formed upon the first $MeCpPtMe_3$ pulse is also substantiated by the fact that the platinum deposited using low oxygen exposures is mostly atomically dispersed (see the first panel of Figure 5.3). Adsorbed carbon can in fact prevent the diffusion and aggregation of adatoms and thus the formation of nanoparticles (NPs) [9, 19, 49, 50].

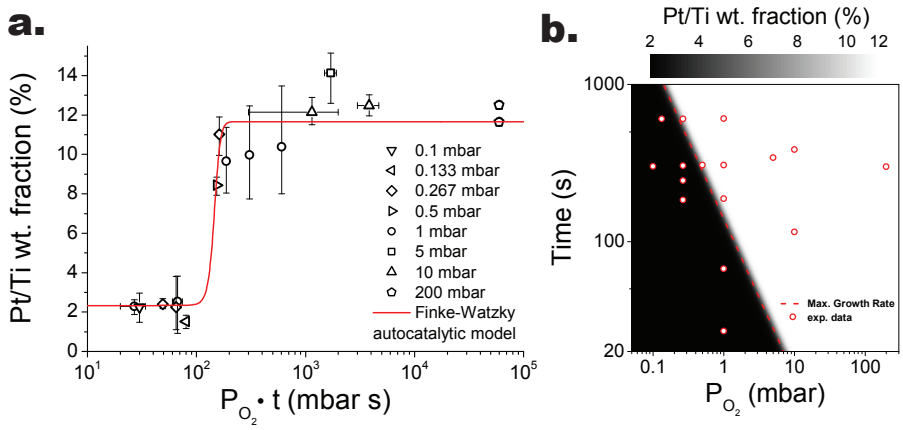

Figure 5.1: Evolution of the platinum loading with oxygen partial pressure and exposure time after 5 cycles expressed in terms of Pt/Ti weight fraction. (a) Experimental loading and Finke-Watzky two-step model (R^2 ~0.92). The vertical error bars indicate the estimated 95% confidence intervals. The horizontal error bars indicate the minimum exposure, calculated as the target pressure times the time during which the pressure is kept constant, and the maximum exposure, calculated as the target pressure times the total duration of the oxygen exposure, that is the time spanning the opening of the reaction chamber to the oxygen flow and the moment at which the reaction chamber has reached the base pressure. (b) 2D representation of Pt loading vs the parameter space obtained with the fitted Finke-Watzky two-step model. The dashed line indicates the locus of the maximum growth rate, i.e., the exposure at which 50% of the maximum loading is attained.

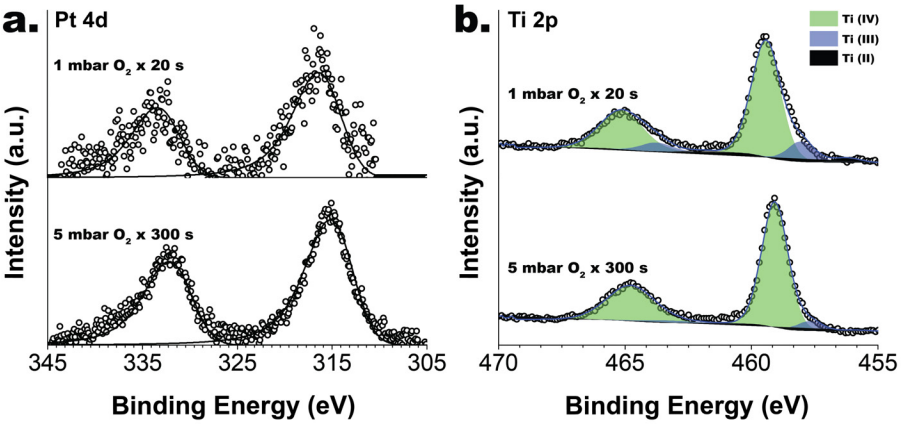

Figure 5.2: (a) Pt 4d and (b) Ti 2p ex-situ XPS spectra of the Pt/TiO_2 composites obtained after 5 ALD cycles using different oxygen exposures.

We argue that the sigmoidal trend exhibited by the amount of platinum as a function of the oxygen exposure arises from the autocatalytic nature of the combustion of the carbon ligands remaining after the $MeCpPtMe_3$ chemisorption. Chemical systems, and especially combustion systems, often exhibit sigmoidal kinetic curves if their kinetics involves a positive chemical feedback or, in other words, if their kinetics is autocatalytic: the concentration of a reaction product increases the rate of its own production [51, 52]. A common chem-

ical feedback in combustion kinetics, and possibly the simplest, is given by the so-called quadratic autocatalysis: $A + B \rightarrow 2B$. The term "quadratic" arises from the fact that, if the initial concentration of B is close to zero, the reaction rate is $\sim [A](1-[A]) = [A] - [A]^2$. This means that A is consumed at an initial small rate that, increases over time, reaches a maximum, and then decreases again, such that the extent of reaction as a function of time is a sigmoid. Interestingly, sigmoidal curves often also describe the decomposition kinetics of metal precursors during the liquid-based synthesis of metal nanoparticles [11, 13, 53–57]. In fact, Finke and Watzky (F-W) [53, 56, 58] proposed in 1997 a physical model based on quadratic autocatalysis for the formation of iridium nanoclusters. Despite its simplicity, the F-W model has since found application in the description of a broad range of nucleation and growth phenomena [53]. The F-W model is based on two pseudoelementary reaction steps: slow and continuous nucleation ($A \xrightarrow{r_1} B$), followed by fast autocatalytic growth ($A + B \xrightarrow{r_2} 2B$) [53]. Here, we adapt the F-W two-step model to describe the kinetics of the cyclic combustion of the precursor ligands during the oxygen exposure, and thus the evolution of Pt/Ti ratio after 5 ALD cycles.

The combustion reactions underlying the removal of the precursor ligands during the oxygen exposure can comprise a large number of individual steps [44, 47, 48]. We reduce such sets of reactions to two pseudo-elementary steps by assuming that all the individual elementary reactions can be grouped into two characteristics "time scale bands" [51]. We therefore describe the ligand-removal kinetics in terms of the following two pseudo-elementary steps: (1) slow combustion reaction of the carbon ligands A, producing gaseous products and surface species B (nucleation step of the F-W model); (2) fast autocatalytic reaction betwen A and B resulting in the production of $2B$ and more gaseous products (autocatalytic step of the F-W model). Several surface chemistries can give rise to kinetics of this kind. Although resolving the exact surface chemistry is beyond the scope of this work, we discuss here three possible mechanisms.

At the beginning of the oxygen exposure, the oxygen molecules will mostly react with the carbonaceous layer, as this can effectively shield the TiO_2 surface as well as the Pt atoms. The oxidation of adsorbed carbon in the absence of an oxidation catalyst is known to be a slow reaction [19, 44, 48]. Nonetheless, the slow combustion of the carbonaceous layer $C_{(s)}$ also results in the gradual reduction of the adsorbed platinum, which can in turn catalyze the combustion of more carbon ligands [44, 47, 48]:

$$\mathrm{Pt(C)} \xrightarrow{O_2} \mathrm{Pt} + \mathrm{C}_{(g)}$$

$$\mathrm{Pt(C)} + \mathrm{Pt} \xrightarrow{O_2} 2\,\mathrm{Pt} + \mathrm{C}_{(g)}$$

where Pt(C) is the platinum precursor in its chemisorbed state and $C_{(g)}$ indicates volatile combustion products (e.g., CO_x, $C_xO_yH_z$, H_2O). In fact, platinum typically catalyzes combustion reactions by dissociating O_2 into more active oxygen radicals ($O_2 \longrightarrow 2O^{\bullet}$). Yet, the ability of Pt to dissociate O_2 manifests itself only when the Pt is aggregated in fairly large (2-3 nm) and faceted NPs [22, 59]. Also, the catalytic reach of the Pt NPs is likely to be limited to the carbon ligands in their neighborhood, unless, of course, they can migrate over the TiO_2 surface. Indeed, the local evolution of gas and heat arising from reactions catalyzed by the NPs can promote NP diffusion and coalescence [19].

Analogously, also TiO_{2-x} surface sites, which are exposed by the slow combustion of the

carbonaceous layer, can give rise to an autocatalytic behaviour. As the slow combustion of the carbonaceous layer exposes the underlying surface, O_2 molecules can react with Ti^{3+} and Ti^{2+} sites producing superoxide radical groups [60], which in turn can lead to the combustion of more adsorbed carbon:

$$C_{(s)} \xrightarrow{O_2} S + C_{(g)}$$
$$C_{(s)} + S \xrightarrow{O_2} 2\,S + C_{(g)}$$

Another mechanism that is consistent with the F-W model is suggested by the fact that the slow non-catalyzed combustion of the carbonaceous layer can still lead to the formation of free radicals $C^{\bullet}_{(s)}$ such as organic hydroperoxides [61]. If these radicals react in an autocatalytic fashion with the remaining adsorbed carbon then we can write:

$$C_{(s)} \xrightarrow{O_2} C^{\bullet}_{(s)} + C_{(g)}$$
$$C_{(s)} + C^{\bullet}_{(s)} \xrightarrow{O_2} 2\,C^{\bullet}_{(s)} + C_{(g)}$$

At any rate, all of the above scenarios translate into the same differential equation:

$$\frac{d\vartheta_c}{dt} = k_1\vartheta_c + k_2\vartheta_c(1-\vartheta_c),\ k_1 = k_1^0 P_{O_2}^m \text{ and } k_2 = k_2^0 P_{O_2}^n \tag{5.1}$$

where ϑ_c is the surface coverage of adsorbed carbon, P_{O_2} is the oxygen partial pressure, and k_1^0, k_2^0, m, n are reaction constants and the reaction orders of the two pseudoelementary reaction steps, respectively. Equation 5.1 allows us to describe the ligand-removal kinetics as a function of the oxygen exposure. If we also assume that: (1) the amount of platinum that can be deposited in each cycle is proportional to $(1-\vartheta_c)$; (2) the extent of the ligand-removal step and thus ϑ_c is the same in each cycle; and (3) the maximum loading scales linearly with the number of cycles within the first 5 ALD cycles, then the Pt/Ti weight ratio is:

$$\mathcal{M}_{Pt}/\mathcal{M}_{Ti}(P_{O_2}, t)_5 = m_5 \simeq m_1[1+4(1-\vartheta_c)] \tag{5.2}$$

where m_1 is Pt/Ti weight ratio after the first cycle. It follows that:

$$m_5(P_{O_2}, t) = \frac{m_1\left[5 + \frac{k_2-4k_1}{k_1}e^{-t(k_1+k_2)}\right]}{1+\frac{k_2}{k_1}e^{-t(k_1+k_2)}} \tag{5.3}$$

By assuming that the two pseudo-elementary reaction steps are first order reactions with respect to the oxygen partial pressure (m=n=1), we obtain a reasonable description of the data ($R^2 \simeq 0.92$) with only two parameters: k_1^0 and k_2^0. We find that the time scales of the two pseudo-elementary steps are well separated: $k_2^0/k_1^0 \sim 4\cdot 10^6 \gg 1$, where $k_2^0 \sim 0.1\ \text{mbar}^{-1}\ \text{s}^{-1}$. Figure 5.C.1b shows a 2D representation of the Pt/Ti ratio as a function of the oxygen partial pressure and exposure time obtained with the F-W two-step model. This model allows us to give a rigorous definition to the upper boundary of the induction phase (black region in Figure 5.C.1b). We define the upper boundary of the induction phase as the oxygen exposure $(P_{O_2}\cdot t)$ at which the acceleration of the reaction rate is maximum [53]:

$$(P_{O_2}\cdot t)_{\text{induction}} = \frac{\ln\left[\frac{k_2^0}{k_1^0}(2-\sqrt{3})\right]}{k_1^0+k_2^0} = 119 \pm 15\ \text{mbar}\cdot\text{s} \tag{5.4}$$

5

In other words, oxygen pressures as high as 1 mbar would result in little to no combustion of the ligands even after 2 minutes of oxygen exposure. The main conclusion that can be drawn from this analysis is that a wide cross-section of the literature on ALD of Pt NPs on oxides is likely based on experiments where the ligand-removal step was not carried out to completion. In fact, a large number of studies are based on ALD experiments carried out with oxygen pressures ≤ 1 mbar and exposure times ≤ 60 s [18, 30, 34, 39, 41, 44].

5.2.2. Effect of the oxygen exposure on the size distribution

Electron microscopy shows that the oxygen exposure determines not only the Pt loading but also the degree of metal aggregation. Figure 5.3 shows HAADF-STEM and TEM images of the morphology of the Pt/TiO_2 composites obtained after 5 cycles at different oxygen exposure times and at an oxygen pressure of 1 mbar. The Z-contrast of the HAADF-STEM images clearly shows that the Pt deposited within the incubation phase (1 mbar x 20 s) remains mostly atomically dispersed. Not running the ligand-removal step to completion is therefore a viable avenue to fabricate supported single atoms. In fact, we argue that Sun et al. [39] could deposit single atoms (and NPs) on graphene sheets because of the short short oxygen exposures (2 s) and low oxygen pressures (< 1 mbar) they used. On the other hand, long exposure times (≥ 180 s), and thus higher Pt loadings, result in the formation of NPs that can be as large as 6 nm even after only 5 cycles. These numbers clearly indicate that the NPs form and grow via diffusive aggregation rather than by layer-by-layer growth. Also, this clearly demonstrates that the formation of large NPs after a few ALD cycles on high-surface-area substrates is not necessarily due to a long precursor dosing [34]. Finally, while single atoms and clusters of two or three atoms are still present in the composites obtained with long oxygen exposures (see Figure 5.3), most of the Pt is contained in NPs (≥ 1 nm).

Although high oxygen exposures (> 120 mbar s) resulted in about the same Pt/Ti ratio (≃ 12 wt%), irrespective of the oxygen pressure, the degree of the metal aggregation was a strong function of the oxygen pressure. Figure 5.4 shows TEM images of the Pt/TiO_2 composites obtained after 5 cycles using different oxygen partial pressures. An oxygen pressure of 0.1 mbar resulted in no visible NPs even when using oxygen exposure times of 300 s. At higher pressures (0.27-10 mbar) and long oxygen exposures (300-600 s) the Pt forms into NPs whose size range depends on the oxygen pressure. Interestingly, oxygen pressures below 5 mbar result in few and mostly large NPs (≥ 2 nm), whereas oxygen pressures ≥ 5 mbar result in a high density of small NPs ~ 1 nm. Figure 5.5 quantifies this difference by showing the PSDs and the average number density of the NPs on composites with about the same Pt loading as a function of the oxygen pressure. Clearly, high oxygen pressures result in narrow PSDs, whereas low oxygen pressures result in broad and right-skewed PSDs. To investigate this further we also carried out 10 cycles using 10 mbar of oxygen. As shown in Figure 5.6, after 10 cycles the NPs are still small and well-dispersed and PSD remains narrow while shifting towards large-size side.

Interestingly, the PSDs obtained at high oxygen pressures are consistent with a recent report on Pt ALD on TiO_2 (flat substrate) using oxygen plasma at 300 °C as the oxidizer [43]. In fact, also Rontu et al. [43] report the formation of NPs of 1-2 nm after 5 ALD cycles. It is reasonable to assume that the oxygen plasma used by Rontu et al. [43] insured the complete combustion of the carbon-ligands. This reinforces our conclusion that NPs > 1 nm can

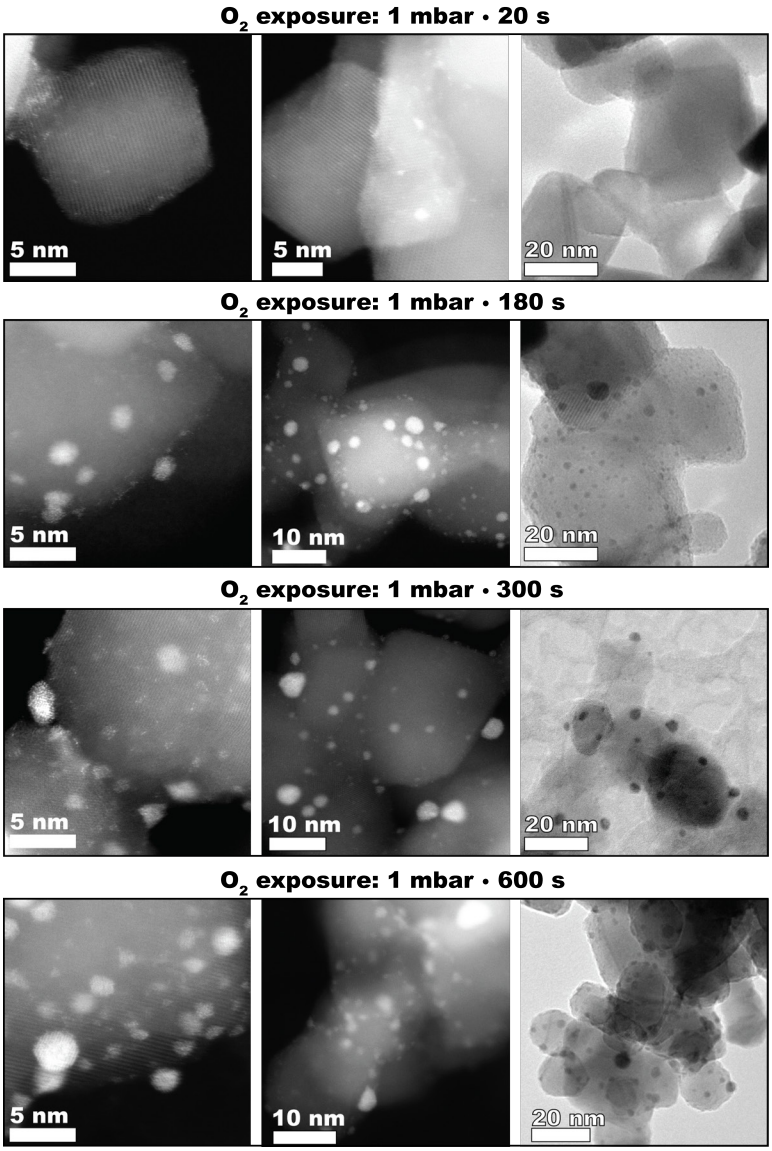

Figure 5.3: Representative HAADF and TEM images of the morphology of the Pt/TiO_2 composites after 5 cycles using different oxygen exposure times. The oxygen pressure in the ligand-removal step was 1 mbar and the exposure time of $Me_3MeCpPt$ was 5 s in all cases.

emerge even after only few ALD cycles provided that the carbon ligands are removed and that atom diffusion is active. Also, the fact that a strong oxidizer such as oxygen plasma led to narrow PSDs offers a clue into the NP growth mechanism.

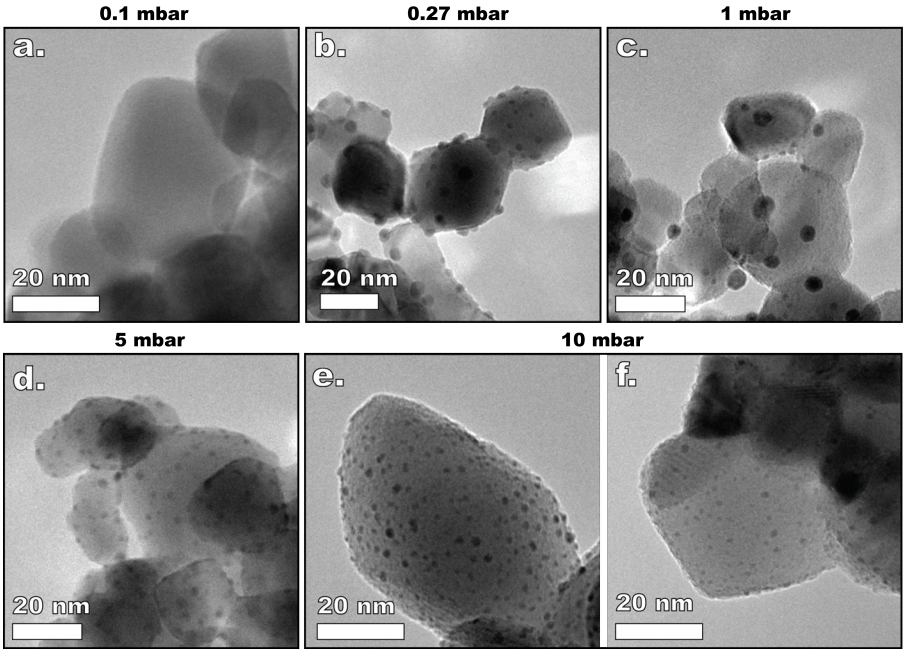

Figure 5.4: Representative TEM images of the morphology of the Pt/TiO_2 composites after 5 cycles using different oxygen pressures. The oxygen exposure time in the ligand-removal step was of 600 s for (b) and about 300 s for (a), (c), (d), (e), and (f). The exposure time of $Me_3MeCpPt$ was 5 s in all cases.

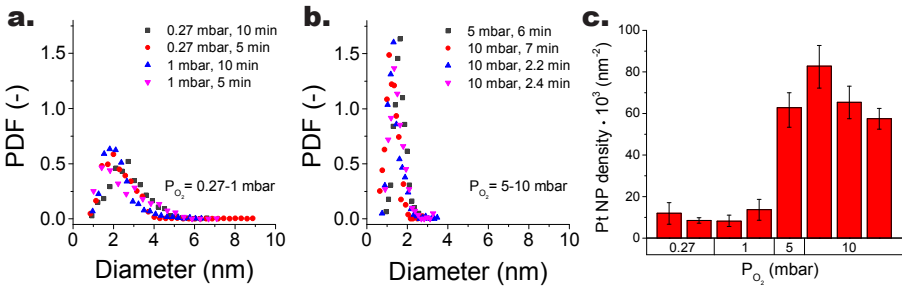

Figure 5.5: Particle size distribution (PSDs) after 5 cycles at low (a) and high (b) oxygen pressure and at different exposure times. The PSDs are expressed in terms of probability density function, and the number of bins was estimated by using the Freedman-Diaconis rule. (c) Average number of NPs per unit area (density) as a function of oxygen pressure estimated from the PSDs and the platinum loading approximating the NPs to hemisperical caps (the error bars indicate 95% confidence intervals).

5.2.3. On the mechanisms of nanoparticle formation and growth

There are at least two possible phenomena that can account for the different degree of metal aggregation observed at different oxygen pressures: (1) increased adhesion energy between the Pt NPs and TiO_2 at high oxygen partial pressures due to the formation of a stable interfacial oxide that acts as an anchoring point; and (2) pressure-dependent competition

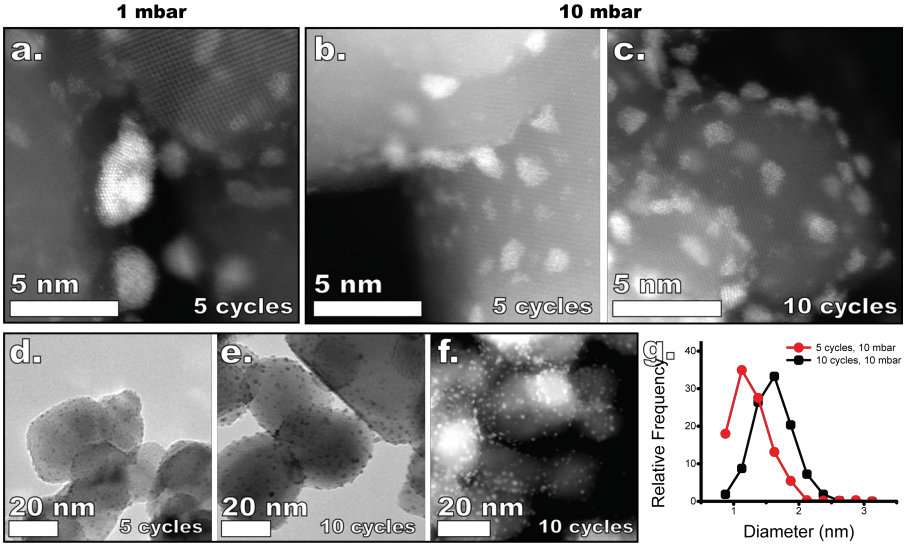

Figure 5.6: Morphology of the Pt/TiO_2 composites at low and high oxygen partial pressure. HAADF images of the composites after 5 cycles using an oxygen pressure of 1 mbar (a) and of 10 mbar (b). HAADF image of the composite after 10 cycles using an oxygen pressure of 10 mbar (c). TEM images of the composites after 5 (d) and 10 (e) cycles using an oxygen pressure of 10 mbar. (f) HAADF image of the composite after 10 cycles using an oxygen pressure of 10 mbar. (g) Particle size distributions of the Pt NPs after 5 and 10 cycles using an oxygen exposure of 10 mbar.

between direct ligand combustion, autocatalytic surface growth, and diffusive aggregation. The interaction between Pt and TiO_2 has been widely studied [62]. Yet, most of the research concerned with the stability of Pt overlayers has been devoted to the understanding of what is referred to as the strong metal-support interaction (SMSI) [62–64] under highly reducing conditions, that is, at high temperature and ultra-high vacuum. Far less research has been devoted to the stability of Pt on TiO_2 under oxidizing conditions and relatively low temperatures (300 °C). Nonetheless, it is well known in catalysis that noble metal NPs supported on oxides can be stabilized via a mild oxygen treatment. In particular, Solano et al. [65] have recently shown that the formation of a PtO_2 shell around Pt NPs upon exposure to oxygen is crucial to their stability against coarsening: The onset of coarsening is retarded at higher oxygen partial pressures, as these stabilize the PtO_2 shell. In general, the adhesion energy between a metal such as Pt and an oxide increases with the density of surface oxygen atoms on the oxide surface [66], which in turn is a function of the oxygen partial pressure. Nagai et al. [67] have shown that the sintering of Pt in oxidizing conditions can be inhibited as a result of an increase of the electron density of oxygen in the support, which result in strong Pt-oxide-support interactions. It has also been proposed that oxygen spillover from the support to noble metal NPs can prevent NP agglomeration by introducing short-range interparticle repulsion forces [68, 69]. High oxygen partial pressures, by increasing the surface density of surface oxygen, could therefore increase the the Pt/TiO_2 adhesion energy and promote interparticle repulsion via enhanced oxygen spillover.

Another possibility is that the kinetics of the combustion the ligands affects the way the

NP form and grow. For example, at low oxygen pressure the rate of ligand combustion, and thus the formation of mobile Pt atoms, is very low. As a result, the nucleation rate of Pt NPs will be very low, that is, at the beginning only a few NPs form. Yet, if the NPs can catalyze the combustion of more ligands and thus the formation of more mobile Pt atoms, the few nucleated NPs can undergo rapid autocatalytic surface growth, thus suppressing the formation of more NPs. While the NPs will likely catalyze the combustion of carbon ligands only in their neighborhood, the local evolution of gas and heat can promote NP mobility [19, 70], thus enlarging the effective catalytic reach of the growing NPs. Indeed, Pt NPs have been reported to undergo diffusion and coalescence upon heat treatment [62, 71]. On the other hand, at high oxygen pressure, the non-catalytic combustion of the organic ligands (first step of the F-W model) can be fast enough to generate a high concentration of mobile Pt atoms in a short time, which would then lead to the nucleation of a large number of small NPs. A similar mechanism involving a competition between autocatalytic surface growth and diffusive agglomeration was also invoked by Aiken et al. [13] to explain the effect of hydrogen concentration on the PSD of colloidal Rh NPs synthesized by reducing a Rh precursor in the liquid-phase.

5

5.2.4. Reproducibility across small and large surface areas

Finally, Figure 5.7 shows that ALD of Pt NPs is reproducible across small ($\lesssim 10^{-3}$ cm^2) and large (~ 75 m^2) surface areas, as well as reactor configurations, provided that the ligand-removal step is carried out at high oxygen partial pressure (≥ 5 mbar). Remarkably, the size range is virtually unaffected by the fact that the large-surface-area experiments required precursor exposure times as long as 12 min whereas the small-surface-area experiments were carried out with a precursor exposure of 5 s (the oxygen exposure time was of ~ 300 s in all cases). This further validates the hypothesis that the formation and growth of NPs during ALD is mostly determined by the operating conditions during the ligand-removal step [19].

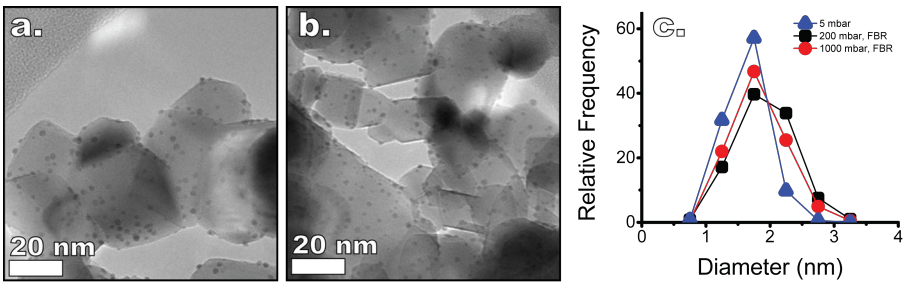

Figure 5.7: TEM images of the Pt/TiO_2 composites obtained using a custom made vacuum reactor for flat substrates using an oxygen pressure of 5 mbar (a) and using a fluidized bed reactor operating at an oxygen pressure of 200 mbar (b). Particle size distributions of the Pt NPs obtained in the vacuum reactor for flat substrates and of those obtained using the fluidized bed reactor (c). In all cases the oxygen exposure time was about 300 s.

5.3. Final remarks and outlook

The status of the surface of the TiO_2 nanopowder and, in particular, its degree of reduction clearly plays a crucial role on the Pt stability as well as on the $Me_3MeCpPt$ chemisorption.

Here, we have shown that the TiO_2 surface is partially reduced during the $Me_3MeCpPt$ chemisorption and oxidized during the oxygen exposure. Oxygen molecules can oxidize the TiO_x surface during or after the carbonaceous layer is combusted. Yet, we could not directly resolve the exact dynamics of the evolution of the removal of the carbonaceous layer and of the TiO_2 surface chemistry. This would in fact require *in operando* or, at least, *in-situ* surface techniques. The same is true for verifying the formation of a PtO_2 shell around the Pt NPs during the oxygen exposure and its dependence with the oxygen partial pressure. These aspects certainly merit further study. Furthermore, here we did not explore the effect of surface modifications prior to ALD. Previous studies have already shown that tailored surface pretreatments can be instrumental not only to the onset of precursor chemisorption but also to the mitigation of metal aggregation [29, 30, 72, 73]. While the initial state of the surface of the support is crucial for the whole ALD process, our results also emphasize how the sequential exposure to different reacting environments induces periodic changes in the metal-support interaction, whose nature and extent are a strong function of the operating conditions. Understanding how the reaction atmosphere affects the overlayer stability during each ALD step is crucial to the devising of ALD schemes that enable deposition while retaining minimal metal aggregation. Finally, as the operating conditions can affect not only the size of the NPs but also their surface chemistry, further studies should be dedicated to the effect of the deposition conditions on the catalytic performance of the as-synthesized supported Pt NPs.

5.4. Conclusions

We have established that:

- $Me_3MeCpPt/O_2$ ALD of Pt NPs on TiO_2 nanopowders is reproducible across small and large surface areas in terms of Pt loading, provided that the ligand-removal step is carried out with oxygen exposures above a critical threshold (~ 120 mbar s). This is because the extent of ligand-removal as a function of the oxygen exposure follows a sigmoidal profile characterized by an "incubation" region at low oxygen exposures (≤ 120 mbar s). The latter result in negligible deposition after the first cycle. In particular, after 5 ALD cycles, the Pt remains mostly atomically dispersed over the TiO_2 surface, which remains partially reduced as a result of $Me_3MeCpPt$ chemisorption. This shows that single-atom catalysts can indeed be fabricated with ALD by not running the ligand-removal step to completion. On the other hand, oxygen exposures > 120 mbar s lead to (1) an increase in the Pt loading, which saturates at high oxygen exposures, indicating the complete removal of precursor ligands, and (2) the progressive oxidation of the TiO_2 surface. The higher Pt loading at high oxygen exposures result in the formation of NPs > 2 nm even after only 5 ALD cycles. This is the case regardless of the reactor configuration and the total surface area. In particular, oxygen pressures typically accessible in vacuum reactors for flat substrates (e.g., 0.1-1 mbar) translate into exposure times on the order of several minutes for the ligands-removal step to reach saturation. Since Pt ALD is often carried using oxygen exposure times on the order of tens of seconds at most, we argue that most studies reporting on Pt NPs on oxides performed in vacuum reactors for flat substrates are based on experiments where the ligand-removal step was not run to completion. This

can explain why the size of the NPs grown by Pt ALD on flat substrates is often reported to be lower than the size of NPs grown by Pt ALD on powders, which is usually performed using oxygen exposures on the order of minutes. Finally, the ligand-removal kinetics is well described by a variant of the Finke-Watzky allowing for the autocatalytic combustion of the carbon ligands.

- While the metal loading is reproducible across different surface areas, provided that the oxygen exposure is » 120 mbar s, the PSD is a strong function of the oxygen partial pressure. At oxygen pressures ≤ 1 mbar the PSDs are broad and right-skewed (1-6 nm after 5 cycles), whereas at oxygen pressures ≥ 5 mbar the PSDs are narrow and symmetric (1-3 nm after 5 cycle). As a result, the number of NPs per unit area is significantly higher at higher pressures. This suggests that high oxygen partial pressures suppress the diffusive aggregation of Pt NPs by (1) promoting the formation of a PtO_2 shell that anchors the NPs to the TiO_2 surface and (2) promoting the rapid combustion the carbon ligands, and thus the generation of a large number of mobile Pt atoms in a short period of time, which in turn results in the burst nucleation of many small NPs.

In conclusion, we have shown that understanding how the operating conditions during the ligand-removal step affect surface chemistry and metal aggregation is crucial for achieving the synthesis of supported NPs with narrow PSDs in a reproducible and scalable fashion. This is true for all ALD-routes for supported NPs that rely on the cyclic removal of precursor ligands. Also, our results are of relevance to the emerging field of area-selective ALD as we clearly show that, while the growth might be kinetically suppressed by a slow ligand-removal step, single atoms are still deposited during the first precursor exposure. Nonetheless, this aspect, while detrimental to area-selective ALD, can still be exploited for the synthesis of single-site catalysts.

5.5. Experimental section

5.5.1. Materials

The metal precursor trimethyl(methylcyclo-pentadienyl)platinum(IV) ($MeCpPtMe_3$, 99%) was obtained from Strem Chemicals and used as received. The nanopowders used as the substrate consisted of Aeroxide P-25 titanium dioxide particles (TiO_2, 99.5% purity) received from Evonik (average size: 21 nm, surface area 50 $m^2\ g^{-1}$). The nanopowders were supported on QUANTIFOIL® (R 1.2/1.3 type, 3.05 mm in diameter) aluminum grids for transmission electron microscopy (TEM). The TEM grids were loaded with TiO_2 nanopowder by drop-casting a solution prepared by crashing the powder in an agate mortar in ethanol. The same dispersion was used for all the TEM grids.

5.5.2. ALD experiments

ALD of Pt in vacuum reactors for flat substrates. The majority of the ALD experiments, that is the ones concerning oxygen partial pressures of 0.1, 0.5, 1, 5, and 10 mbar, was performed in a custom-built single-wafer hot-wall ALD reactor already described elsewhere [74–76]. The reactor chamber was 25 cm^3 in volume and was loaded via a loadlock system, which was instrumental in maintaining the reactor at high vacuum (base pressure ~ $2{\cdot}10^{-7}$ mbar).

In each experiment, a TEM grid loaded with TiO_2 nanopowder was placed on a dummy silicon wafer, which was then loaded into the ALD reactor. An order of magnitude estimate of the upper bound of the total TiO_2 surface present in each experiment can be obtained by assuming that the TiO_2 particles occupy 10% of the volume of the cylinder having a height of 100 nm and a diameter equal to the one of the TEM grid (3.05 mm) [77]: $0.1\pi R^2 h \varrho_{TiO_2} S_{BET} \simeq 10^{-3}$ cm^2, where S_{BET} is the surface area per unit mass of the TiO_2 nanopowder and ϱ_{TiO_2} is the density of TiO_2. Such surface area is about 5 orders of magnitude lower than the one of the 4-inch wafer ($\sim$ 80 cm^2) on which the TEM grid is placed. The bubbler containing $MeCpPtMe_3$ was kept at 70 °C via a heating jacket. The vapor pressure at this temperature was measured to be 1.9 mbar. The line connecting the bubbler to the reaction chamber was kept at 80 °C. All the deposition experiments were carried out at 300 °C. Each ALD cycle consisted of the following steps: (I) 5 s of $MeCpPtMe_3$ precursor dosing; (II) a pump down period long enough such that a base pressure of $5 \cdot 10^{-6}$ mbar is reached (pump); (III) 10 s of N_2 purge (50 sccm); (IV) pump; (V) O_2 exposure (50 sccm), (VI) pump; (VII) 30 s of N_2 purge; and (VIII) pump. The time required to pump down the chamber after each oxygen exposure as well as the time required to reach the target pressure varied depending on the target oxygen pressure. The former increased from ~2 to 120 s and the latter increased from ~2 to 55 s upon increasing the target pressure from 0.1 to 10 mbar. Once reached, the target pressure was kept constant for the designated exposure time, which varied in the range 20-600 s. The series of experiments at 100 and 200 mtorr (0.133 and 0.267 mbar) of oxygen were carried out in a FlexAL® ALD system following an analogous procedure.

ALD of Pt on gram-scale batches of TiO_2 nanopowders. These ALD experiments were carried out in a custom-built fluidized bed reactor operating at atmospheric pressure already described elsewhere [19, 22, 78]. The Pt precursor, contained in a stainless steel bubbler, was heated and kept at 70 °C by a heating jacket controlled by a PDI controller. The stainless steel line connecting the bubbler and the reactor was kept at 80 °C to avoid the precursor condensation. The reactor was heated via an infrared lamp placed parallel to the column. The temperature was measured by a thermocouple inserted in the powder bed and controlled by a PDI controller. In each experiment, 1.5 g of TiO_2 were loaded into the reactor. The powder waw fluidized by means of a gas flow 0.5 L min^{-1}. Prior to ALD, the powder was dried in air at 120 °C for 1 h and then pretreated in pure oxygen at 300 °C for 5 min. The ALD process consisted of sequential exposures of the powders to the Pt precursor (8-12 min) and synthetic air or pure oxygen (5 min), separated by a purging step (10-15 min) using nitrogen as an inert gas (N_2, 99.999 vol%).

5.5.3. Characterization

The morphology of the Pt/TiO_2 composites was investigated by means of transmission electron microscopy (TEM) and high angle annular dark field scanning transmission electron microscopy (HAADF-STEM). STEM-BF and HAADF transmission electron microscopy images were recorded using a JEOL JEM-ARM200F double Cs-corrected TEM equipped with a FEG, a STEM unit and an HAADF detector, operated at 200 kV. TEM micrographs were obtained using a JEOL JEM1400 transmission electron microscope equipped with a JED-2300 Analysis Station for Energy-dispersive X-ray spectroscopy (EDS) and operating at

120 kV. Number-based particle size distributions of the ALD-grown Pt NPs were obtained by image analysis of 10-30 TEM micrographs taken at different locations and at different magnifications (e.g., 50k and 100k). For each sample the equivalent projected diameter ($d = \sqrt{4A_p/\pi}$) of 600-1000 Pt NPs was measured manually using the software ImageJ. For all the experiments carried out on TiO_2 nanopowders supported on TEM grids, the elemental analysis was carried out via EDS and X-ray photoelectron spectroscopy (XPS). XPS measurements were performed via a K-alpha Thermo Fisher Scientific spectrometer (see Figure 5.A.XPS). Elemental analysis of the samples obtained with the fluidized bed reactor was carried out via inductively coupled plasma optical emission spectrometry (ICP-OES) using a Perkin Elmer Optima 3000 DV optical emission spectrometer. The Pt/Ti ratio was obtained via EDS by acquiring about 20 spectra at different locations on the TEM grid and at different magnifications (see Figures 5.B.EDS spectra). The 95% confidence intervals were estimated by bootstrap sampling using the Matlab function "bootci" with 10000 iterations. To confirm the validity of this method, 3 samples obtained with the fluidized bed reactor were characterized by both ICP-OES and EDS. The two methods are found to be in reasonable agreement (see Supplementary Information).

Appendix

5.A. XPS

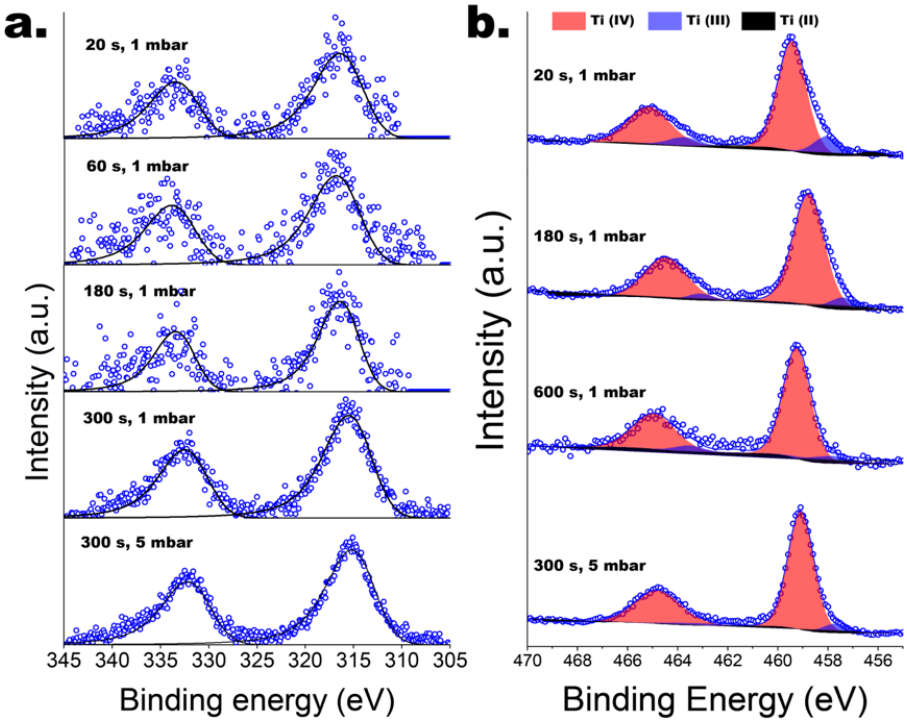

Figure 5.A.1: Ex-situ high-resolution X-ray photoelectron spectra of the 4d Pt (a) and 2p Ti (b) signal.

5.B. EDS spectra

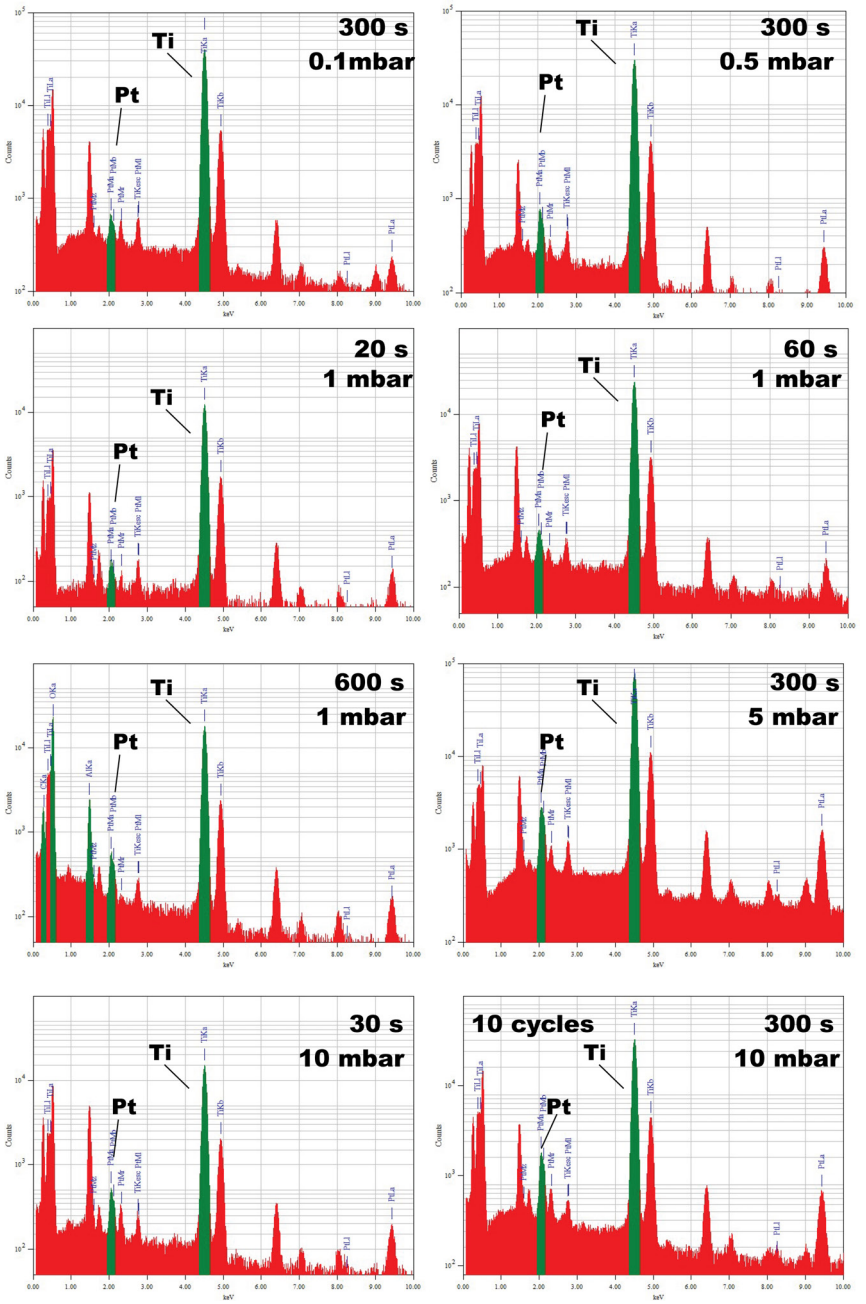

Figure 5.B.1: Representative EDS spectra concerning Pt/TiO_2 obtained after 5 cycles unless otherwise specified.

5.C. EDS vs ICP

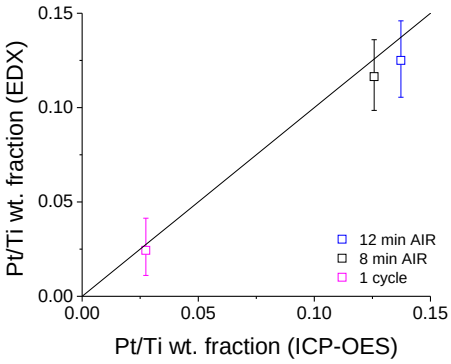

Figure 5.C.1: Pt/Ti wt% ratio of samples obtained with the fludized bed reactor described here as measured by inductively coupled plasma optical emission spectrometry (ICP-OES) and energy-dispersive X-ray spectroscopy (EDX). EDX was performed on Pt/TiO_2 composites dispersed on Al TEM grids, and ICP-OES was performed on mg-batches of the same Pt/TiO_2 composites.

References

[1] J. Moulijn, M. Makkee, and A. Van Diepen, *Chemical process technology*, 2nd ed. (Wiley, 2013) p. 566.

[2] J. K. Norskov, F. Studt, F. Abild-Pedersen, and T. Bligaard, *Introduction to Microfabrication* (2010) pp. 1–13.

[3] R. Schlögl, *Heterogeneous catalysis,* Angewandte Chemie - International Edition 54, 3465 (2015).

[4] C. H. Bartholomew and R. J. Farrauto, *Fundamentals of Industrial Catalytic Processes: Second Edition* (2010) pp. 1–966.

[5] S. B. A. Hamid and R. Schlögl, *The Impact of Nanoscience in Heterogeneous Catalysis,* The Nano-Micro Interface: Bridging the Micro and Nano Worlds: Second Edition 2-2, 405 (2015).

[6] B. C. Gates, G. W. Huber, C. L. Marshall, P. N. Ross, J. Siirola, and Y. Wang, *Catalysts for Emerging Energy Applications,* MRS Bulletin 33, 429 (2008).

[7] P. J. F. Harris, *Growth and structure of supported metal catalyst particles,* International Materials Reviews 40, 97 (1995).

[8] P. Wynblatt and N. A. Gjostein, *Supported metal crystallites,* Progress in Solid State Chemistry 9, 21 (1975).

[9] B. Roldan Cuenya and F. Behafarid, *Nanocatalysis: Size- and shape-dependent chemisorption and catalytic reactivity,* Surface Science Reports 70, 135 (2015).

[10] M. A. Watzky, E. E. Finney, and R. G. Finke, *Transition-metal nanocluster size vs formation time and the catalytically effective nucleus number: A mechanism-based treatment,* Journal of the American Chemical Society 130, 11959 (2008).

[11] J. E. Mondloch, E. Bayram, and R. G. Finke, *A review of the kinetics and mechanisms of formation of supported-nanoparticle heterogeneous catalysts,* Journal of Molecular Catalysis A: Chemical 355, 1 (2012).

[12] S. S. I. Baker C.C. Pradhan A., *Encyclopedia of nanoscience and nanotechnology* (CRC Press, Boca Raton, 2004) pp. 449–473.

[13] J. D. Aiken and R. G. Finke, *Nanocluster formation synthetic, kinetic, and mechanistic studies. The detection of, and the methods to avoid, hydrogen mass-transfer limitations in the synthesis of polyoxoanion- and tetrabutylammonium-stabilized, near- monodisperse 40 ± 6 Å Rh(0) nanocl,* Journal of the American Chemical Society 120, 9545 (1998).

[14] K. An and G. A. Somorjai, *Size and Shape Control of Metal Nanoparticles for Reaction Selectivity in Catalysis,* ChemCatChem 4, 1512 (2012).

[15] S. Mozaffari, W. Li, C. Thompson, S. A. Ivanov, S. Seifert, B. Lee, L. Kovarik, and A. M. Karim, *Colloidal nanoparticle size control: Experimental and kinetic modeling investigation of the ligand-metal binding role in controlling the nucleation and growth kinetics,* Nanoscale (2017).

[16] H. Brune, *Microscopic view of epitaxial metal growth: nucleation and aggregation,* Surface Science Reports 31, 125 (1998).

[17] K. Wettergren, F. F. Schweinberger, D. Deiana, C. J. Ridge, A. S. Crampton, M. D. Rötzer, T. W. Hansen, V. P. Zhdanov, U. Heiz, and C. Langhammer, *High sintering resistance of size-selected platinum cluster catalysts by suppressed ostwald ripening,* Nano Letters 14, 5803 (2014).

[18] J. Lu, J. W. Elam, and P. C. Stair, *Atomic layer deposition - Sequential self-limiting surface reactions for advanced catalyst "bottom-up" synthesis,* Surface Science Reports 71, 410 (2016).

[19] F. Grillo, H. Van Bui, J. A. Moulijn, M. T. Kreutzer, and J. R. Van Ommen, *Understanding and Controlling the Aggregative Growth of Platinum Nanoparticles in Atomic Layer Deposition: An Avenue to Size Selection,* Journal of Physical Chemistry Letters 8, 975 (2017).

[20] E. E. Finney and R. G. Finke, *Catalyst Sintering Kinetics Data: Is There a Minimal Chemical Mechanism Underlying Kinetics Previously Fit by Empirical Power-Law Expressions - And if So, What Are Its Implications?* Industrial and Engineering Chemistry Research 56, 10271 (2017).

[21] E. D. Goodman, J. A. Schwalbe, and M. Cargnello, *Mechanistic understanding and the rational design of sinter- resistant heterogeneous catalysts,* ACS Catalysis 7, 7156 (2017).

[22] H. Van Bui, F. Grillo, S. S. Kulkarni, R. Bevaart, N. Van Thang, B. van der Linden, J. A. Moulijn, M. Makkee, M. T. Kreutzer, and J. R. van Ommen, *Low-temperature atomic layer deposition delivers more active and stable Pt-based catalysts,* Nanoscale (2017).

[23] R. Schlögl and S. B. Abd Hamid, *Nanocatalysis: Mature science revisited of something really new?* Angewandte Chemie - International Edition 43, 1628 (2004).

[24] H. Van Bui, F. Grillo, and J. R. van Ommen, *Atomic and molecular layer deposition: off the beaten track,* Chem. Commun. 53, 45 (2017).

[25] B. J. O'Neill, D. H. K. Jackson, J. Lee, C. Canlas, P. C. Stair, C. L. Marshall, J. W. Elam, T. F. Kuech, J. A. Dumesic, and G. W. Huber, *Catalyst Design with Atomic Layer Deposition,* ACS Catalysis 5, 1804 (2015).

[26] R. L. Puurunen, *Surface chemistry of atomic layer deposition: A case study for the trimethylaluminum/water process,* Journal of Applied Physics 97 (2005).

[27] S. M. George, *Atomic layer deposition: An overview,* Chemical Reviews 110, 111 (2010).

[28] V. Miikkulainen, M. Leskelä, M. Ritala, and R. L. Puurunen, *Crystallinity of inorganic films grown by atomic layer deposition: Overview and general trends,* Journal of Applied Physics 113 (2013).

[29] H. Yan, H. Cheng, H. Yi, Y. Lin, T. Yao, C. Wang, J. Li, S. Wei, and J. Lu, *Single-Atom Pd1/Graphene Catalyst Achieved by Atomic Layer Deposition: Remarkable Performance in Selective Hydrogenation of 1,3-Butadiene,* Journal of the American Chemical Society 137, 10484 (2015).

[30] H. Yan, Y. Lin, H. Wu, W. Zhang, Z. Sun, H. Cheng, W. Liu, C. Wang, J. Li, X. Huang, T. Yao, J. Yang, S. Wei, and J. Lu, *Bottom-up precise synthesis of stable platinum dimers on graphene,* Nature Communications 8 (2017).

[31] A. Goulas and J. Ruud van Ommen, *Atomic layer deposition of platinum clusters on titania nanoparticles at atmospheric pressure,* Journal of Materials Chemistry A 1, 4647 (2013).

[32] D. Longrie, D. Deduytsche, and C. Detavernier, *Reactor concepts for atomic layer deposition on agitated particles: A review,* Journal of Vacuum Science & Technology A: Vacuum, Surfaces, and Films 32, 010802 (2014).

[33] F. Grillo, M. T. Kreutzer, and J. R. van Ommen, *Modeling the precursor utilization in atomic layer deposition on nanostructured materials in fluidized bed reactors,* Chemical Engineering Journal 268, 384 (2015).

[34] A. J. M. Mackus, M. J. Weber, N. F. W. Thissen, D. Garcia-Alonso, R. H. J. Vervuurt, S. Assali, A. A. Bol, M. A. Verheijen, and W. M. M. Kessels, *Atomic layer deposition of Pd and Pt nanoparticles for catalysis: on the mechanisms of nanoparticle formation,* Nanotechnology 27, 034001 (2016).

[35] J. Shi, Z. Li, A. Kvit, S. Krylyuk, A. V. Davydov, and X. Wang, *Electron microscopy observation of TiO2 nanocrystal evolution in high-temperature atomic layer deposition,* Nano Letters 13, 5727 (2013).

[36] A. M. Lubers, C. L. Muhich, K. M. Anderson, and A. W. Weimer, *Mechanistic studies for depositing highly dispersed Pt nanoparticles on carbon by use of trimethyl(methylcyclopentadienyl)platinum(IV) reactions with O2 and H2,* Journal of Nanoparticle Research 17 (2015).

[37] S. T. Christensen, J. W. Elam, F. A. Rabuffetti, Q. Ma, S. J. Weigand, B. Lee, S. Seifert, P. C. Stair, K. R. Poeppelmeier, M. C. Hersam, and M. J. Bedzyk, *Controlled growth of platinum nanoparticles on strontium titanate nanocubes by atomic layer deposition,* Small 5, 750 (2009).

[38] C. Wang, L. Hu, K. Poeppelmeier, P. C. Stair, and L. Marks, *Nucleation and growth process of atomic layer deposition platinum nanoparticles on strontium titanate nanocuboids,* Nanotechnology 28 (2017).

[39] S. Sun, G. Zhang, N. Gauquelin, N. Chen, J. Zhou, S. Yang, W. Chen, X. Meng, D. Geng, M. N. Banis, R. Li, S. Ye, S. Knights, G. A. Botton, T. K. Sham, and X. Sun, *Single-atom catalysis using Pt/graphene achieved through atomic layer deposition,* Scientific Reports 3 (2013).

[40] X. Liang, Y. Zhou, J. Li, and A. W. Weimer, *Reaction mechanism studies for platinum nanoparticle growth by atomic layer deposition,* Journal of Nanoparticle Research 13, 3781 (2011).

[41] J. Dendooven, R. K. Ramachandran, E. Solano, M. Kurttepeli, L. Geerts, G. Heremans, J. Rongé, M. M. Minjauw, T. Dobbelaere, K. Devloo-Casier, J. A. Martens, A. Vantomme, S. Bals, G. Portale, A. Coati, and C. Detavernier, *Independent tuning of size and coverage of supported Pt nanoparticles using atomic layer deposition,* Nature Communications 8 (2017).

[42] N. P. Dasgupta, C. Liu, S. Andrews, F. B. Prinz, and P. Yang, *Atomic layer deposition of platinum catalysts on nanowire surfaces for photoelectrochemical water reduction,* J Am Chem Soc 135, 12932 (2013).

[43] V. Rontu, A. Selent, V. Zhivonitko, G. Scotti, I. Koptyug, V.-V. Telkki, and S. Franssila, *Efficient catalytic microreactors with atomic layer deposited platinum nanoparticles on oxide support,* Chemistry - A European Journal (2017).

[44] A. J. Mackus, M. A. Verheijen, N. Leick, A. A. Bol, and W. M. Kessels, *Influence of oxygen exposure on the nucleation of platinum atomic layer deposition: Consequences for film growth, nanopatterning, and nanoparticle synthesis,* Chemistry of Materials 25, 1905 (2013).

[45] P. N. Plessow and F. Abild-Pedersen, *Sintering of Pt Nanoparticles via Volatile PtO2: Simulation and Comparison with Experiments,* ACS Catalysis 6, 7098 (2016).

[46] Y. Zhou, D. M. King, X. Liang, J. Li, and A. W. Weimer, *Optimal preparation of Pt/TiO2 photocatalysts using atomic layer deposition,* Applied Catalysis B: Environmental 101, 54 (2010).

[47] T. Aaltonen, M. Ritala, T. Sajavaara, J. Keinonen, and M. Leskelä, *Atomic layer deposition of platinum thin films,* Chemistry of Materials 15, 1924 (2003).

[48] A. J. M. Mackus, N. Leick, L. Baker, and W. M. M. Kessels, *Catalytic combustion and dehydrogenation reactions during atomic layer deposition of platinum,* Chemistry of Materials 24, 1752 (2012).

[49] M. Zinke-Allmang, L. C. Feldman, and M. H. Grabow, *Clustering on surfaces,* Surface Science Reports 16, 377 (1992).

[50] R. Zan, U. Bangert, Q. Ramasse, and K. S. Novoselov, *Interaction of metals with suspended graphene observed by transmission electron microscopy,* Journal of Physical Chemistry Letters 3, 953 (2012).

[51] S. K. Scott, *Chapter 5 Global behaviour in the oxidation of hydrogen, carbon monoxide and simple hydrocarbons,* in *Low-Temperature Combustion and Autoignition*, Vol. Volume 35, edited by M. J. P. B. T. C. C. Kinetics (Elsevier, 1997) pp. 439–544.

[52] I. R. Epstein and J. A. Pojman, *An introduction to nonlinear chemical dynamics: Oscillations, Waves, Patterns, and Chaos* (1998) pp. 1–408.

[53] L. Bentea, M. A. Watzky, and R. G. Finke, *Sigmoidal Nucleation and Growth Curves Across Nature Fit by the Finke-Watzky Model of Slow Continuous Nucleation and Autocatalytic Growth: Explicit Formulas for the Lag and Growth Times Plus Other Key Insights,* Journal of Physical Chemistry C 121, 5302 (2017).

[54] F. Wang, V. N. Richards, S. P. Shields, and W. E. Buhro, *Kinetics and mechanisms of aggregative nanocrystal growth,* (2014).

[55] P. N. Njoki, J. Luo, M. M. Kamundi, S. Lim, and C. J. Zhong, *Aggregative growth in the size-controlled growth of monodispersed gold nanoparticles,* Langmuir 26, 13622 (2010).

[56] E. E. Finney and R. G. Finke, *Fitting and interpreting transition-metal nanocluster formation and other sigmoidal-appearing kinetic data: A more thorough testing of dispersive kinetic vs chemical-mechanism-based equations and treatments for 4-step type kinetic data,* Chemistry of Materials 21, 4468 (2009).

[57] E. E. Finney and R. G. Finke, *Nanocluster nucleation and growth kinetic and mechanistic studies: A review emphasizing transition-metal nanoclusters,* Journal of Colloid and Interface Science 317, 351 (2008).

[58] M. A. Watzky and R. G. Finke, *Transition metal nanocluster formation kinetic and mechanistic studies. A new mechanism when hydrogen is the reductant: Slow, continuous nucleation and fast autocatalytic surface growth,* Journal of the American Chemical Society 119, 10382 (1997).

[59] M. Shao, A. Peles, and K. Shoemaker, *Electrocatalysis on platinum nanoparticles: Particle size effect on oxygen reduction reaction activity,* Nano Letters 11, 3714 (2011).

[60] D. N. Pei, L. Gong, A. Y. Zhang, X. Zhang, J. J. Chen, Y. Mu, and H. Q. Yu, *Defective titanium dioxide single crystals exposed by high-energy {001} facets for efficient oxygen reduction,* Nature Communications 6 (2015).

[61] R. W. Walker and C. Morley, *Chapter 1 Basic chemistry of combustion,* in *Low-Temperature Combustion and Autoignition*, Vol. Volume 35, edited by M. J. P. B. T. C. C. Kinetics (Elsevier, 1997) pp. 1–124.

[62] U. Diebold, *The surface science of titanium dioxide,* Surface Science Reports 48, 53 (2003).

[63] S. Zhang, P. N. Plessow, J. J. Willis, S. Dai, M. Xu, G. W. Graham, M. Cargnello, F. Abild-Pedersen, and X. Pan, *Dynamical observation and detailed description of catalysts under strong metal-support interaction,* Nano Letters 16, 4528 (2016).

[64] F. Pesty, H. P. Steinrück, and T. E. Madey, *Thermal stability of Pt films on TiO2(110): evidence for encapsulation,* Surface Science 339, 83 (1995).

[65] E. Solano, J. Dendooven, R. K. Ramachandran, K. Van de Kerckhove, T. Dobbelaere, D. Hermida-Merino, and C. Detavernier, *Key role of surface oxidation and reduction processes in the coarsening of Pt nanoparticles,* Nanoscale (2017).

[66] C. T. Campbell and Z. Mao, *Chemical Potential of Metal Atoms in Supported Nanoparticles: Dependence upon Particle Size and Support,* ACS Catalysis , 8460 (2017).

[67] Y. Nagai, T. Hirabayashi, K. Dohmae, N. Takagi, T. Minami, H. Shinjoh, and S. Matsumoto, *Sintering inhibition mechanism of platinum supported on ceria-based oxide and Pt-oxide-support interaction,* Journal of Catalysis 242, 103 (2006).

[68] I. V. Yentekakis, G. Goula, P. Panagiotopoulou, S. Kampouri, M. J. Taylor, G. Kyriakou, and R. M. Lambert, *Stabilization of catalyst particles against sintering on oxide supports with high oxygen ion lability exemplified by Ir-catalyzed decomposition of N2O,* Applied Catalysis B: Environmental 192, 357 (2016).

[69] I. V. Yentekakis, G. Goula, S. Kampouri, I. Betsi-Argyropoulou, P. Panagiotopoulou, M. J. Taylor, G. Kyriakou, and R. M. Lambert, *Ir-Catalysed Nitrous oxide (N2O) Decomposition: Effect of Ir Particle Size and Metal-Support Interactions,* (2017).

[70] Y. F. Chu and E. Ruckenstein, *Behavior of platinum crystallites on carbon substrates,* Surface Science 67, 517 (1977).

[71] F. Behafarid and B. R. Cuenya, *Coarsening phenomena of metal nanoparticles and the influence of the support pre-treatment: Pt/TiO2(110),* Surface Science 606, 908 (2012).

[72] J. Pyeon, C. Cho, S.-H. Baek, C.-Y. Kang, J.-S. Kim, D. Jeong, and S. Kim, *Control of the initial growth in atomic layer deposition of Pt films by surface pretreatment,* Nanotechnology 26 (2015).

[73] T. Gong, L. Qin, W. Zhang, H. Wan, J. Lu, and H. Feng, *Activated carbon supported palladium nanoparticle catalysts synthesized by atomic layer deposition: Genesis and evolution of nanoparticles and tuning the particle size,* Journal of Physical Chemistry C 119, 11544 (2015).

[74] A. Y. Kovalgin, M. Yang, S. Banerjee, R. O. Apaydin, A. A. Aarnink, S. Kinge, and R. A. Wolters, *Hot-Wire Assisted ALD: A Study Powered by In Situ Spectroscopic Ellipsometry,* Advanced Materials Interfaces 4 (2017).

[75] H. Van Bui, A. Y. Kovalgin, A. A. I. Aarnink, and R. A. M. Wolters, *Hot-Wire Generated Atomic Hydrogen and its Impact on Thermal ALD in TiCl4/NH3 System,* ECS Journal of Solid State Science and Technology 2, P149 (2013).

[76] S. Bystrova, a. a. I. Aarnink, J. Holleman, and R. a. M. Wolters, *Atomic Layer Deposition of W[sub 1.5]N Barrier Films for Cu Metallization,* Journal of The Electrochemical Society 152, G522 (2005).

[77] M. Weinmann, *Chemical Processing of Ceramics, Second Edition,* (2005).

[78] R. Beetstra, U. Lafont, J. Nijenhuis, E. M. Kelder, and J. R. Van Ommen, *Atmospheric pressure process for coating particles using atomic layer deposition,* Chemical Vapor Deposition 15, 227 (2009).

Reggia di Caserta, Italy 2016.

6

Self-Organized Growth of TiO_2 Anatase Nanorods on Graphene Nanoplatelets by Atomic Layer Deposition

Understanding the spontaneous organization of atoms on well-defined surfaces promises to enable control over the shape and size of supported nanostructures. Atomic layer deposition (ALD) boasts atomic-scale control in the synthesis of thin films and nanoparticles (NPs). Yet, control over the shape of ALD-grown nanostructures remains virtually unexplored. Here, we report on the bottom-up formation of both linear and V-shaped anatase TiO_2 nanorods on gram-scale batches of graphene nanoplatelets via $TiCl_4/H_2O$ ALD carried out at 300 °C. Nanorods as large as 200 nm form after only 5 ALD cycles, indicating that diffusive aggregation rather than layer-by-layer growth is behind the nanorod formation. High resolution transmission electron microscopy revealed that the nanorods form via the oriented attachment of NPs. In particular, the substrate played a crucial role in that the lattices of the TiO_2 nanorods and graphene nanoplatelets were in rotational alignment as a result of lattice matching. Increasing the precursor exposure time induced a transition from NPs to NP chains to nanorods and ultimately to large and symmetric NPs. Crucially, the evolution of the shape of the deposited nanostructures took place at saturation conditions.

Submitted as: Fabio Grillo, Damiano La Zara, Paul Mulder, Michiel T. Kreutzer, and J. Ruud van Ommen, Self-Organized Growth of TiO_2 Anatase Nanorods on Graphene Nanoplatelets by Atomic Layer Deposition.

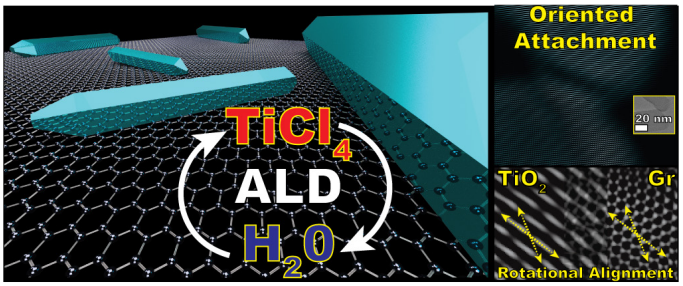

6.1. Introduction

The notion that the properties of matter depend upon the size, the shape, and the arrangement of its most minute constituents dates all the way to the fifth century BC with the atomistic philosophers Leucippus and Democritus [1–3]. Yet, it is only since the advent of modern nanotechnology that the principle of imparting function to matter by tuning its structure at the nanoscale started being explored and harnessed. As a rule, the properties of a material become size- and shape-dependent when its size approaches the nanoscale [4–10]. It has therefore become clear that composite materials consisting of nanostructured constituents of controlled composition, shape, and size can emerge as a new class of materials with far-reaching applications [4–6, 8, 11–15]. However, the smallest scale at which current fabrication methods can directly manipulate matter is reaching a fundamental limit [16]. Nonetheless, another pathway promises to expand the reach of nanotechnology: the autonomous ordering of atoms on well-defined surfaces [16, 17]. In particular, understanding the self-ordering phenomena behind the alignment of inorganic materials on the surface of 2D materials, such as graphene, promises to open up new avenues for the fabrication of functional nanocomposites [16–18].

Atomic layer deposition (ALD) is a gas-phase bottom-up technique based on cyclic sequences of self-limiting reactions that bring about the deposition of less than a monolayer per cycle[19–22]. It has already established itself as the method of choice for the layer-by-layer deposition of conformal thin films in applications that require atomic-level precision [22]. While mostly developed for flat substrates, ALD is also scalable to high-surface-area substrates, which are relevant for a variety of applications in fields spanning catalysis, energy storage and conversion, and medicine [20, 23–34]. Given its unparalleled precision and scale-up potential, considerable research effort has been put in expanding its capability to the deposition of nanostructures other than thin films such as nanoparticles (NPs) [20, 24, 25, 35–39]. However, the formation and growth of NPs is mediated not only by ALD surface chemistry but also by non-equilibrium phenomena such as adatom and NP diffusion and aggregation [35, 40]. Since such mechanisms are a strong function of reaction conditions and adlayer-support interactions, control over the NP size can be achieved only under certain system-dependent conditions [35, 38, 39]. Nonetheless, if properly understood, unconventional growth pathways can expand the range of nanostructures that can be synthesized by ALD [40, 41]. After achieving control over the NP size, the natural next step in the advancement of ALD of NPs is the synthesis of shape-controlled NPs and, in particular, of

1D nanocrystals such as nanorods.

Inspired by a recent finding of Shi et al. [42], Wen and He [43] posed the question: "Can oriented-attachment be an efficient growth mechanism for the synthesis of 1D nanocrystals via atomic layer deposition?" Oriented attachment (OA) is a non-classical growth mechanism, mostly observed in the liquid phase, that involves the self-organization of particles or crystallites that migrate, align, and then fuse along a preferential crystallographic orientation, such that the resulting crystal grows in an asymmetric fashion [44–46]. Although still poorly understood, a growing body of evidence suggests that OA dominates the solution-based growth not only of important nanomaterials but also of minerals in biogenic and geological environments [44, 47–49]. For this reason, De Yoreo et al. [47] argued that a rational exploitation of OA can bring about significant advances in the design and the synthesis of nanomaterials. Along these lines, Shi et al. [42] have shown that high-temperature (≥600 °C) ALD of TiO_2 can indeed be used to grow nanorods via a mechanism that the authors argued to be a vapor-phase variant of OA. In fact, in contrast to OA of individual crystals that align and fuse, they proposed that the nanorods grow at the expense of an amorphous layer encapsulating the lateral facets, which migrates and attaches onto the facets exposed to the gas-phase [42]. Yet, despite its relevance, this process yielded nanorods only on substrates presenting highly-confined submicrometer-sized spaces, such as deep Si nanowires forests, and after a large number of cycles (≥75). Furthermore, the nanorods were found to grow along an out-of-plane direction on a TiO_x wetting layer without any heteroepitaxial alignment with the underlying substrate. While Shi et al. [42] showed that in principle OA can be exploited to synthesize 1D nanocrystals via ALD, several questions of both practical and fundamental nature remain unanswered: (1) Since OA transcends the layer-by-layer model of ALD, what is the interplay between the self-limiting behaviour of ALD reactions and the atomistic processes behind the formation of nanorods? And, in particular, can the nanorod size still be controlled by the number of cycles? (2) Can the substrate promote OA during ALD? For example, a variety of nanostructures are known to self-align on 2D materials in an attempt to minimize the interfacial-energy [18, 50–52]. (3) Is the process scalable to bulk quantities of 2D materials such as graphene nanoplatelets?

Here, we report on the bottom-up formation of anatase nanorods via oriented attachment on gram-scale batches of graphene nanoplatelets at temperatures as low as 300 °C via $TiCl_4/H_2O$ ALD. We show that nanorods as large as 200 nm can form even after only 5 cycles, indicating that the growth is dominated by diffusive aggregation. The number of cycles affects mostly the number rather than the size of the nanorods. Statistical analysis of the shape of the nanostructures at different reactant dosing reveals a competitive process between growth pathways leading to either symmetric growth, and thus NPs, or asymmetric growth, and thus nanorods. In particular, the population of the different observed nanostructures is a non-linear function of the exposure time of $TiCl_4$ and H_2O even at saturation conditions. Finally, transmission electron microscopy provides direct evidence not only of oriented attachment of individual TiO_2 nanocrystals but also of an in-plane lattice alignment between TiO_2 and graphene nanoplatelets.

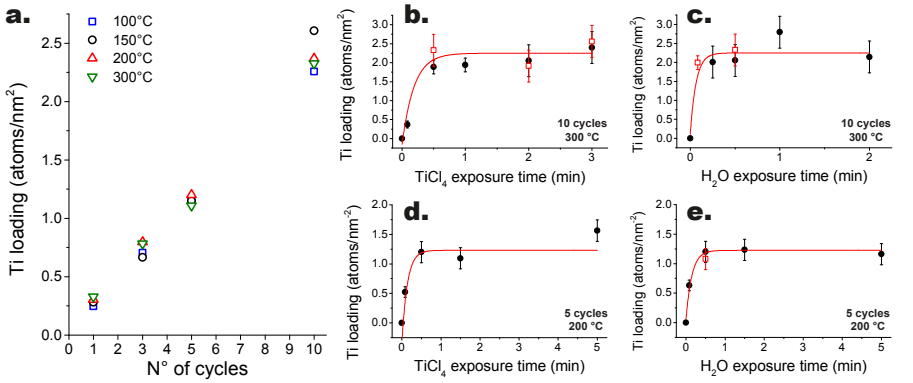

Figure 6.1: Self-limiting behavior of the surface chemistry of the ALD reactions. Evolution of the amount of titanium deposited (i.e., the loading) with the number of ALD cycles at different temperatures (a). Evolution of the Ti loading with the exposure time of $TiCl_4$ (b) and H_2O (c) at 300°C after 10 cycles. The loading indicated by the red open squares and by black circles of (b) and (c) were obtained by having the $TiCl_4$ bubbler at 0°C and 30°C, respectively. Evolution of the Ti loading with the exposure time of $TiCl_4$ (d) and H_2O (e) at 200°C after 5 cycles. The loading indicated by the red open square of (e) was obtained by having the H_2O bubbler at 80°C. Unless otherwise specified all the experiments were carried out with the $TiCl_4$ and H_2O bubbler kept at 30°C. The vapor pressure of $TiCl_4$ is ~2.5 Torr at 0°C and ~14.6 Torr at 30°C, whereas H_2O has a vapor pressure of ~31.8 Torr at 30°C and of ~355.1 Torr at 80°C [53]. The error bars indicate 95% confidence intervals.

6.2. Results and discussion

6.2.1. Self-limiting behavior

The hallmark of ALD is its self-limiting nature [19, 20]. We tested whether TiO_2 can be grown in a self-limiting fashion on gram-scale batches of graphene nanoplatelets by following the amount of deposited Ti as a function of the exposure time and the partial pressure of the precursors: $TiCl_4$ and H_2O (see Figure 6.1). The evolution of the Ti loading (at nm^{-2}) as a function of precursor exposure time shows that the surface reactions saturate after an exposure of about 30 s of $TiCl_4$ and 15 s of H_2O. This is true at different temperatures (200°C and 300°C), number of cycles (i.e., 5 and 10), and precursor partial pressures (see Figure 6.1 b-e). In particular, past the saturation point, the Ti loading remains fairly constant within a time window of several minutes. In addition, the value of the Ti loading at saturation after 10 cycles is ~2.3 at nm^{-2}, which is about two times the saturation value after 5 cycles. In fact, exposure times of 30 s for the exposure of both precursors resulted in a linear increase of the Ti loading with the number of cycles in the cycle range 1-10 and in the temperature range 100-300°C. If we consider that a monolayer of anatase exposing {100} facets has a Ti density of ~16.7 at nm^{-2}, a growth per cycle (GPC) of ~0.23 Ti at nm^{-2} translates into ~1.4% of a monolayer per cycle. This GPC is about ten times lower than the steady-state GPC (i.e., in the limit of large number of cycles) typically reported for $TiCl_4/H_2O$ ALD, which is in the range of 10-15% of a monolayer per cycle [54–56]. Such low GPC is consistent with the low reactivity of graphitic surfaces, which, lacking dangling bonds, induce what is referred to as substrate-inhibited ALD growth [19]. Nonetheless, ALD growth can still start from the very first cycle because, in contrast to ideal graphene or perfect graphitic surfaces, the surface of graphene nanoplatelets used here is inherently defective, and as such can be

activated by the incorporation of oxygen-containing species during the ozone pretreatment step [35, 57, 58].

6.2.2. Effect of deposition temperature on crystallinity, morphology, and chemical state

While the deposition temperature had virtually no effect on the amount of deposited Ti, it did affect the crystallinity, the morphology, and the chemical state of the ALD-grown TiO_x. The XPS spectra of the composites obtained after 10 cycles in the temperature range 100-300 °C reveal that the Ti atoms are mostly in the Ti^{4+} state, with a small fraction being in the Ti^{3+} state (see Figure 6..1). In particular, the fraction of the latter decreases from about 10% at 100 °C to less than 4% at 300 °C. The Ti^{3+} contribution to the Ti2p spectra is probably due to the presence of non-stoichiometric TiO_2. This is corroborated by the shift towards lower binding energies of the peak associated with the Ti-O bonds in the O1s region with increasing deposition temperature, which is known to be correlated with a reduction in the concentration of oxygen vacancies [59, 60]. The deposition of non-stoichiometric TiO_2 at low temperature is also consistent with the absence of the signature of cristallinity in the XRD patterns of the composites obtained at temperatures below 200 °C (see Figure 6..1). On the other hand, a clear signature of the presence of anatase TiO_2 is evident for the composites obtained at 200 °C and 300 °C. In particular, the peaks associated with the anatase structure were narrower for the composites obtained at 300 °C, indicating the formation of larger crystallites at higher temperature.

The transition from amorphous TiO_x to anatase TiO_2 with increasing temperature is also reflected in the evolution of the morphology of the composites as revealed by TEM analysis (see Figure 6..2). At 100 °C the TiO_x appears in the form of irregularly shaped 2D flakes (Figure 6..2a). On the other hand, at 200 °C, while 2D flakes are still visible, a fraction of the ALD-grown TiO_2 forms into distinct crystallites with sharp corners (Figure 6..2b). Crucially, at 300 °C the 2D flakes are no longer present, instead, the same amount of TiO_2 is concentrated in nanostructures ranging from individual and agglomerated nanoparticles (NPs) to either linear nanorods or v-shaped nanorods (see Figure 6..2c, Figure 6.1, and Figure 6.4). To test whether the formation of nanorods is simply triggered by an increase in temperature, we annealead at 300 °C the composites obtained after 10 cycles at 100 °C and 200 °C for two hours (≃the average duration of 10 cycles) in synthetic air and in $N_2 + H_2O$, respectively. In particular, we annealed the composites in the same reactor where all the ALD experiments were performed. After annealing, the morphology did change in that 2D flakes were no longer present and most of the TiO_2 formed into percolated NPs, however, no nanorods were observed (see Figure 6..5). This suggests that the sequential nature of ALD, and thus the timing of each precursor exposure, is crucial for the formation of nanorods.

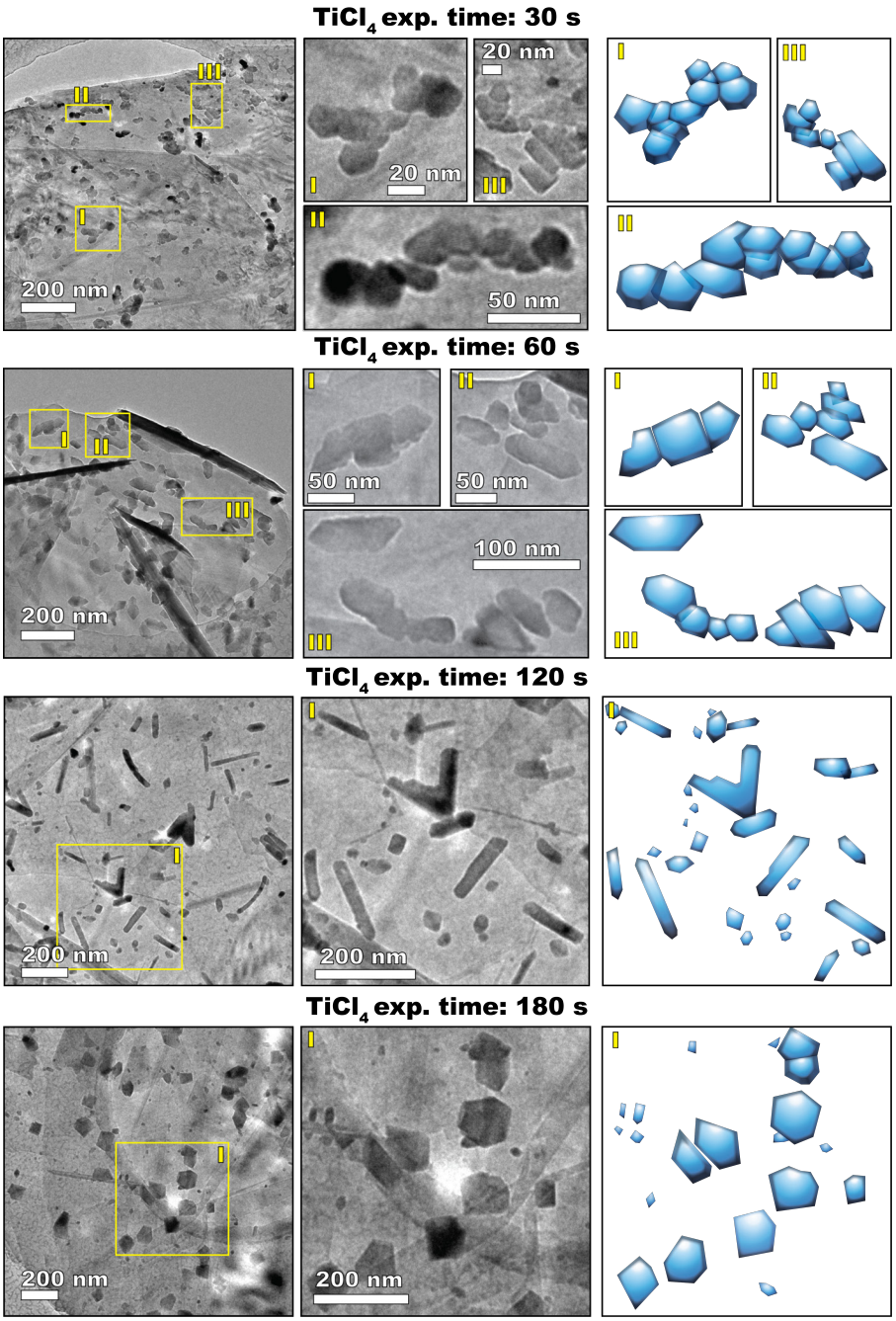

Figure 6.1: Effect of the $TiCl_4$ exposure time on the morphology of the TiO_2 nanostructures grown at 300 °C after 10 ALD cycles (the water exposure time was of 30 s in all cases). The images in the first two columns are TEM micrographs, whereas the third column contains schematic representations of the morphology of the observed nanostructures.

6.2.3. Effect of precursor exposure time on the morphology and unfolding of asymmetric growth

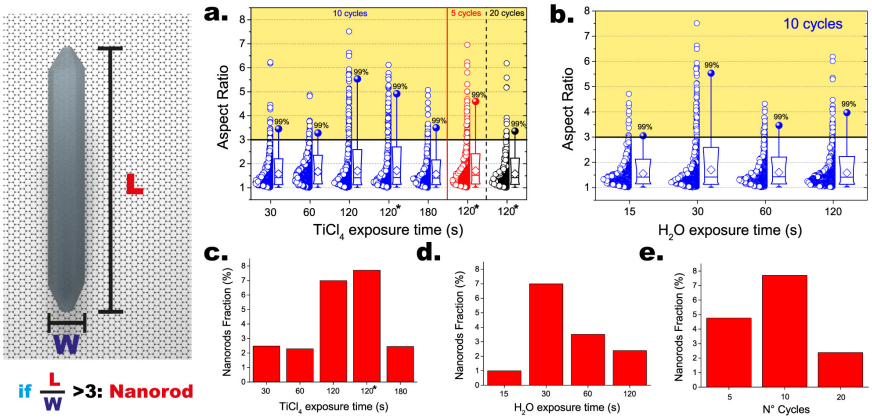

Figure 6.2: Summary of the statistical analysis of the shape of the nanostructures obtained with ALD at 300 °C. Box plots and data overlap of the evolution of the aspect ratio as a function of the $TiCl_4$ and H_2O exposure time (a) and (b). The boxes indicates the 10th, 25th, 75th, and 90th percentiles of the population, the full circle indicates the maximum, the white diamonds indicate the average, and the horizontal blue line in the box indicates the median. Evolution of the average fraction of nanorods, that is the number of nanorods divided by the total number of observed nanostructures, as a function of $TiCl_4$ (c) and H_2O (d) exposure time, and of the number of cycles (e). The asterisks indicate that the experiments were carried out with the $TiCl_4$ bubbler kept at 30 °C, otherwise all the data was obtained with experiments in which the $TiCl_4$ and H_2O bubbler were kept at 0 °C and 30 °C respectively.

The precursor exposure time had a dramatic effect on the morphology of the ALD-grown TiO_2. Figure 6.1 shows the evolution of the morphology of the TiO_2 nanostructures deposited after 10 cycles at 300 °C with varying $TiCl_4$ exposure times in the range 30-180 s. Strikingly, while the morphology varies considerably within such range of exposures, the Ti loading remains virtually the same (see Figure 6.1 and Figure 6.1). This means that prolonged $TiCl_4$ exposures affect the growth process by exacerbating the effect of diffusion phenomena rather than by the addition of more TiO_2.

$TiCl_4$ exposures of 30 s resulted in the formation of a large number of both round and asymmetric NPs of about 20 nm in size that are mostly clustered in elongated chain-like agglomerates. Sporadically, also nanorods with sharp facets were observed (see also Figure 6..2c). Image analysis shows that about 50% of the nanostructures have an aspect ratio (AR) ranging from 1.5 to 6 and that the nanorods ($AR \geq 3$ & $C \leq \pi/4$) account for about 2.5 % of the total population (see Figure 6.2a).

Increasing the $TiCl_4$ exposure time to 60 s resulted in a larger fraction of elongated structures having an aspect ratio between 1.5 and 3. In this case, the nanostructures are less irregular and more symmetric with respect to their major axis. TEM images clearly show that such structures mostly consist of few individual NPs that are partially aligned and fused. In fact, the average size of the asymmetric NPs doubled compared to the previous case (see Figure 6..3). This indicates that longer exposures promoted the diffusion and coalescence of the individual NPs. Furthermore, although the fraction of nanorods was comparable to the

previous case, the number of structures having an aspect ratio of about 2 and sharp lateral edges increased.
Crucially, $TiCl_4$ exposures of 120 s resulted in the formation of a significantly higher number of both linear and V-shaped nanorods presenting sharp lateral facets (see also Figure 6.4). In particular, the length of the nanorods was distributed in the range 50-500 nm, whereas the width ranged from ~10 to 60 nm. Interestingly, the average nanorod width is about equal to the average NP size (~20 nm), which is consistent with the NPs being the building blocks of the nanorods. In this case, the fraction of nanorods accounted for ~7-8% of the all population. It is worth noting that the fraction of nanorods is calculated on a number basis: total number of nanorods divided by the total number of observed nanostructures. On a weight basis, however, nanorods would account for a fraction of TiO_2 much larger than 8%. In the first approximation, if we assume that all the TiO_2 is distributed in NPs and nanorods, and that the average nanorod weight is equal to average NP weight times the average nanorod AR (~5), then the nanorods account for about 30% of the total TiO_2 mass.

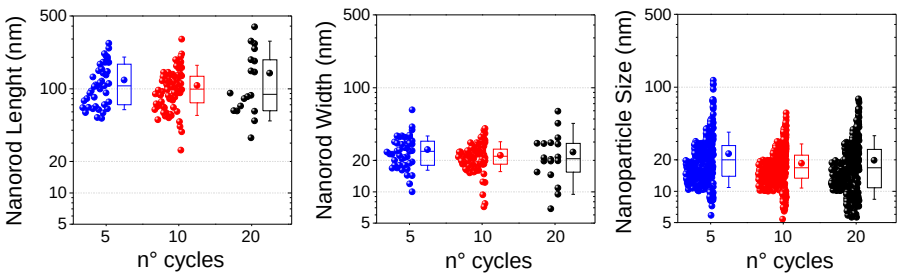

Figure 6.3: Box plots and data overlap of the evolution of the length and width of the nanorods, and of the size of the nanoparticles with the number of cycles (pulse sequence: 2 min/5 min/30 s/5 min). The boxes indicates the 10th, 25th, 75th, and 90th percentiles of the population, the full circle indicates the maximum, the white diamonds indicate the average, and the horizontal blue line in the box indicates the median.

$TiCl_4$ exposures of 180 s suppressed the formation of nanorods and, instead, promoted the growth of large and nearly symmetric NPs. In fact, the fraction of symmetric NPs with a diameter larger than 40 nm increased at the expenses of the nanorod fraction (see also Figure 6..3). Therefore, there exists an optimum in the $TiCl_4$ exposure time that promotes asymmetric growth and thus maximizes the fraction of nanorods. Interestingly, varying the H_2O exposure time affected the morphology in a similar fashion, with 30 s of H_2O exposure being the optimal time for nanorods formation when using $TiCl_4$ exposures of 120 s (see Figure 6..4 and Figure 6.2d). In addition, varying the number of cycles also resulted in an evolution of the relative fraction of nanorods exhibiting an optimum (see Figure 6.2e). In particular, an increase in the number of cycles from 5 to 10 resulted in an increase in the nanorod fraction, while the nanorod and NP size remained virtually unaffected. On the other hand, increasing the number of cycles from 10 to 20 not only decreased the fraction of nanorods but also broadened the size distribution of both nanorods and asymmetric NPs (see Figure 6.3 and Figure 6..3). As we will point out later, the existence of an optimum and the evolution of the size of the different nanostructures can be explained in terms of a competition between diffusion phenomena leading to either symmetric or asymmetric growth in concomitance with the nucleation of new NPs in each cycle as a result

of deposition.

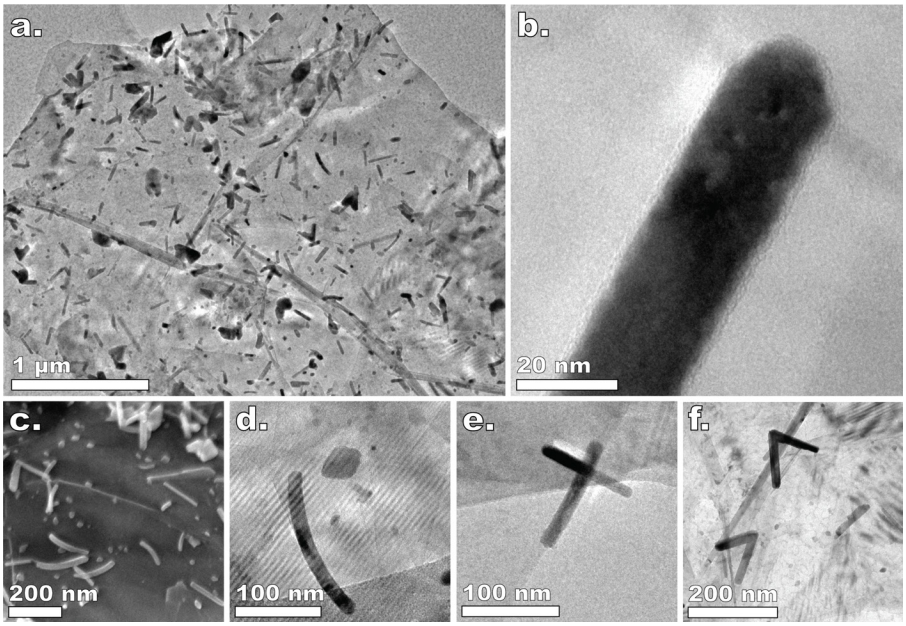

Figure 6.4: TEM micrograph of a graphene nanoplatelet after 10 ALD cycles carried out at 300 °C using the pulsing sequence: 2 min/5 min/30 s/5 min (a). TEM micrograph of the tip of a nanorod encapsulated by an amorphous layer (b). FESEM micrograph of the TiO_2/graphene composites obtained after 10 cycles at 300 °C (c) using the same pulsing sequence as in (a). Selection of TEM micrographs of nanorods of peculiar morphology: curved nanorod (d), nanorod aligned with the edge of the nanoplatelet (e), and v-shaped nanorods (f).

The transition from individual NPs to nanorods with varying $TiCl_4$ exposure time presented in Figure 6.1 bears a striking resemblance to the solution growth of Pt_3 Fe nanorods from nanoparticle building blocks via oriented attachment observed by Liao et al. [49]. By using real-time TEM they could monitor the spontaneous formation of nanorods in a solution containing Pt and Fe precursors that undergo reduction upon electron beam illumination. In particular, they observed three distinct stages. In the first stage, a large number of small NPs nucleate upon precursor reduction. These NPs grow by parallel atom attachment and NP coalescence until they reach a critical size. In this stage, coalescing NPs relax in spherical shapes. In the second stage, colliding NPs form into NP chains that do not coalesce into spherical NPs. When most NPs form into NP chains, these can in turn undergo end-to-end attachment and form longer chains. In the third stage, polycrystalline chains can straighten and form into single crystal nanorods via the alignment and mass redistribution between the individual NPs within the chain. The similarities between the evolution of the morphology with $TiCl_4$ exposure time revealed by ex-situ TEM (Figure 6.1) and the mechanism observed by Liao et al. [49] in real time suggest that an analogous three-stage process is likely to be behind the formation of TiO_2 nanorods during ALD on graphene nanoplatelets. Yet, it must be noted that the latter is considerably more complex than the growth of Pt_3 Fe nanorods in solution in that: the nucleation of TiO_2 NPs is heterogeneous; the diffusion

of TiO_x species and of NPs takes place over a surface, that is, in 2D; new material is added cyclically to the system, rather than being added all at once at the beginning of the process; TiO_2 is deposited in each cycle on both the substrate and the preexisting nanostructures; both the reaction environment and the surface chemistry change periodically as a result of the pulsing sequence and of the surface reactions. Before discussing how the mechanism unveiled by Liao et al. [49] can explain our results if the above aspects are taken into account, we first present the results of the HRTEM analysis substantiating the role of oriented attachment and of the substrate in the growth mechanism.

6.2.4. HRTEM analysis: oriented attachment, heteroepitaxial alignment, and the effect of the substrate

Figure 6.5a shows two distinct single-crystal nanorods attached at one extremity exhibiting a perfect alignment along {011} facets as shown by FFT analysis. Another example of oriented attachment is given in Figure 6..6l, which shows a small TiO_2 NP attached to one end of a nanorod with a perfect lattice alignment. This is direct evidence that the TiO_2 NPs can indeed undergo oriented attachment during ALD on graphene nanoplatelets. More evidence is also shown in Figure 6.5f where a single-crystal nanorod, whose width is bound by atomically smooth {011} facets for about 3/4 of its length, is attached to a distinct NP, which is again aligned along {011} facets, as highlighted in the insert (I). The nanorod fused to an NP of Figure 6.5f is also consistent with the mechanism revealed by Liao et al. [49], where individual NPs, NP chains, and nanorods first undergo end-to-end oriented attachment and then form into straight single-crystal nanorods via mass redistribution. The fact that the nanorods are bound by {011} is no surprise as they exhibit the lowest surface energy among the anatase crystal facets [61]. This is also consistent with the findings of Shi et al. [62]. The driving force for oriented attachment is in fact the reduction of the total surface energy [63]. Another indirect evidence of oriented attachment lies in the presence of curved nanorods (see Figure 6.1 and 6.4c-d). This is because Zhang et al. [64] have shown that nanorods forming in solutions via oriented attachment of small anatase NPs exposing {011} facets, such as the ones formed during ALD as shown in Figure 6.5b, bend in order to lower their energy.

The lattice mismatch and the poor chemical affinity between graphitic surfaces and oxides such as TiO_2 entail high interfacial energies [18, 65]. The minimization of the latter can drive not only the transition from 2D flakes to NPs and nanorods but also the in-plane alignment between the crystal lattices of TiO_2 and graphene. Indeed, HRTEM images and their Fourier transforms clearly show that the lattices of the TiO_2 nanorods and graphene nanoplatelets are rotationally aligned (see Figure 6.5c-e and Figure 6..6 a-h). For example, the {013} and {011} facets of the nanorod in Figure 6.5c are perfectly aligned with the zig-zag and armchair directions of the graphitic lattice, respectively (see inserts (I) and (II) of Figure 6.5c-d). Heteroepitaxial alignment is known to be driven by lattice matching [17, 18, 66–68]. In fact, we find that the TiO_2 facets that are aligned with carbon hexagon minimize the lattice mismatch. For the nanorod in Figure 6.5c, the interplanar spacing of {033} and {017} facets is about the length of one carbon hexagon (lattice mismatch ≃0.8% and ≃0.4%, respectively), whereas the spacing between {013} and {020} is about the distance between two carbon atoms in the carbon hexagon (lattice mismatch ≃12% and ≃10%, respectively).

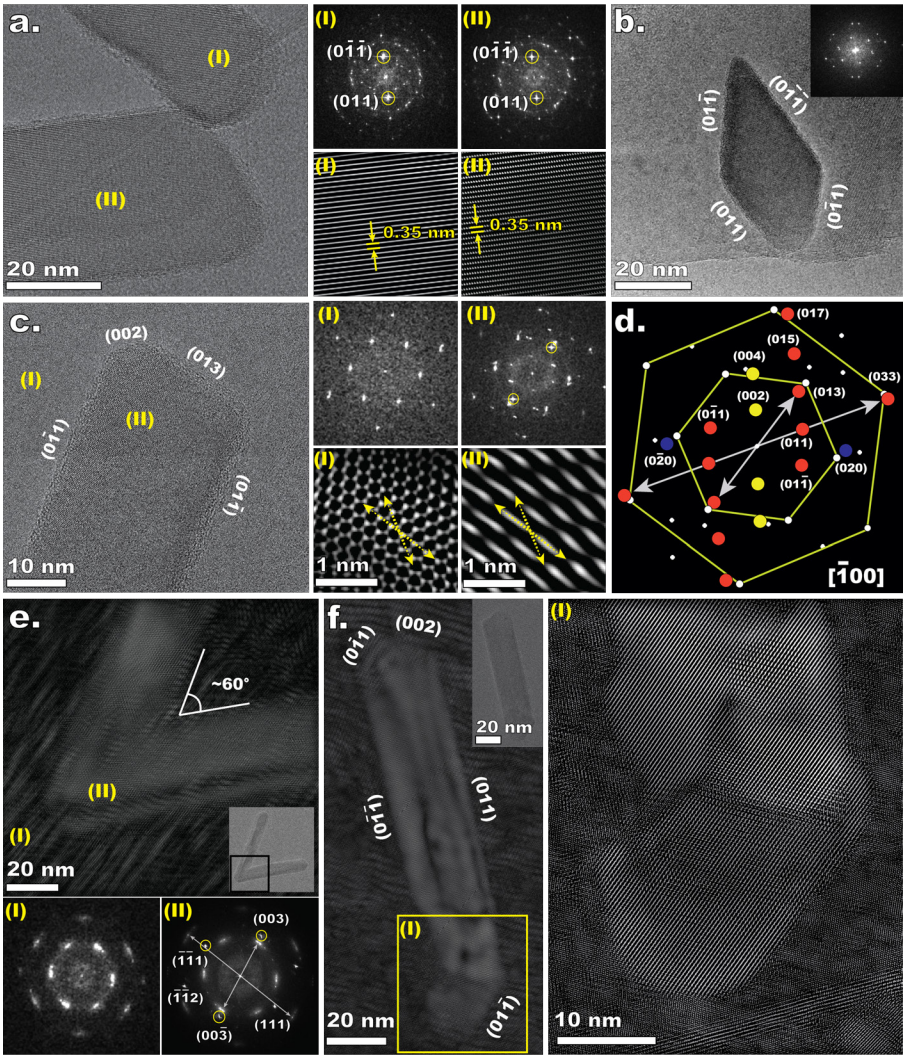

Figure 6.5: (a) High resolution transmission electron microscopy (HRTEM) micrograph of two nanorods undergoing oriented attachment, Fast-fourier-transform (FFT) patterns of the indicated areas, and inverse FFT images obtained by singling out the frequencies associated with the {011} facets. (b) Representative HRTEM micrograph of a TiO_2 nanoparticle exhibiting the tetragonal dipyramidal structure, characteristic of anatase crystals, exposing {011} facets. (c) HRTEM micrograph of a supported nanorod, FFT patters of the indicated areas, and inverse FFT (IFFT) images obtained by singling out the frequencies associated with the lattice of graphene (I) and of TiO_2 (II). (d) Analysis of the FFT pattern of the area indicated as (II), highlighting the heteroepitaxial alignment between TiO_2 and graphene nanoplatelet. (e) HRTEM image and corresponding IFFT of a V-shaped nanorod, and FFT patterns of the corresponding indicated areas. The IFFT was obtained by singling out the FFT patterns associated with the lattice of both TiO_2 and graphene nanoplatelet. (e) HRTEM image and corresponding IFFT of a nanorod with an irregular bottom tip (f). The insert highlights the incorporation by oriented attachment of a distinct crystallite at the bottom of the nanorod. The IFFT was obtained as in.

An atomic-scale rotational alignment between adsorbates and substrate often translates into

a preferential alignment between the adsorbates, especially if they are 1D nanostructures such as nanorods [18, 50]. Indeed, we found that the orientation of the nanorods exhibits a 12-fold symmetry, in other words, the angle between the major axis of two nanorods lying on the same graphene nanoplatelet is always a multiple of 30° (see Figure 6..7). This is a clear indication that the substrate has an active role in mediating the directional growth of the deposited TiO_2 into nanorods. We conclude that during ALD TiO_x species and individual NPs diffuse and aggregate in an asymmetric fashion so that the TiO_2 crystals grow in the direction that minimizes the interfacial energy. A diffusion field that exhibits a 12-fold symmetry can explain, among other things, the formation of V-shaped nanorods with an internal angle of about 60° or 30° as the ones shown in Figure 6.4f, Figure 6.5e, and Figure S7. Finally, also the edges of the graphene nanoplatelets can impart directionality to the growth process, as they act as impassable boundaries for diffusing species as well as for growing crystals. For example, Figure 6..6i shows a TiO_2 crystalline NP whose lattice sharply terminates in correspondence of the edge of the graphene nanoplatelet. Analogously, edges can act as a template for the directional growth of nanorods, as shown in in Figure 6.4e.

6.2.5. Growth Mechanism

In light of the results of our analysis and, in particular, of the following two observations: (i) non-linear dependence of the nanorod fraction on the exposure time of both precursors and the number of cycles, and (II) rotational alignment between the lattices of TiO_2 and graphene nanoplatelets driven by lattice matching; we propose the following growth mechanism (see Figure 6.6). In each cycle, TiO_x species form on both the graphene nanoplatelets and the already-deposited TiO_2 as a result of ALD surface reactions. During the first cycles, TiO_x species diffuse and form into anatase NPs to minimize the interfacial energy. Once formed, the NPs can grow by capturing diffusing TiO_x species or by undergoing diffusion and coalescence with neighboring NPs. In particular, the NPs will tend to diffuse and grow in accord with the symmetry of the lattice of the underlying graphene. Before reaching a critical size, two colliding NPs can coalesce into a symmetric NP. With increasing number of cycles, the deposition of more TiO_2 leads to an increase in the number of NPs, which in turn increases the chances of two NPs undergoing diffusive aggregation. Upon reaching a certain size the coalescence step slows down (the characteristic time for the coalescence of two spherical NPs scales with R^4) [69]. As the NPs and the NP population grows in size, the NPs start coming in contact without coalescing, and thus forming NP chains. In particular, NPs in close proximity can align and undergo oriented attachment. Alternatively, NPs can come in contact forming irregular polycrystalline chains. Given enough time and at the right conditions (e.g., $TiCl_4$ or H_2O atmosphere), NP chains can form into single-crystal nanorods via alignment and mass redistribution between the individual NPs within the chain. Furthermore, oriented attachment of NPs can still lead to steps or gaps along the lateral sides of the forming nanorod, if the NPs are of different size or if their centers of mass are not aligned (see Figure 6.6). In this case, a straight nanorod can form via preferential attachment of migrating TiO_x species to the steps in the lateral facets. In the limit of long times, however, NP chains and nanorods will inevitably tend to relax into the most stable shape, that is, the tetragonal bipyramidal shape [45, 46, 63]. There are, therefore, three processes in series that are all mediated by TiO_2 mobility: NP aggregation into NP chains, NP relaxation into nanorods, and relaxation of nanorods into symmetric bipyramidal NPs.

It follows that, if both $TiCl_4$ and H_2O promote the mobility of TiO_2, there will be an optimal exposure time that maximizes the formation of nanorods. Indeed, the chemical environment, and especially the presence of water, is known to affect the mobility of TiO_2 species as well as the tendency of TiO_2 nanocrystals to undergo oriented attachment [45, 70]. Also, with increasing the number of cycles, large and irregular structures can form as new NPs attach to preexisting nanostructures and growing neighboring nanostructures come into contact with each other. Since the time scale associated with the relaxation of a polycristalline chains into nanorods will likely increase with chain length and complexity, the fraction of nanorods is bound to decrease after a critical number of cycles. Finally, this picture implies that the optimal exposure time varies from cycle to cycle, since the time scales associated with the diffusive process leading to the formation of nanorods depend on the TiO_2 coverage and the size of the nanostructures. This particular insight paves the way for an optimization of the process aimed at maximizing the nanorod fraction.

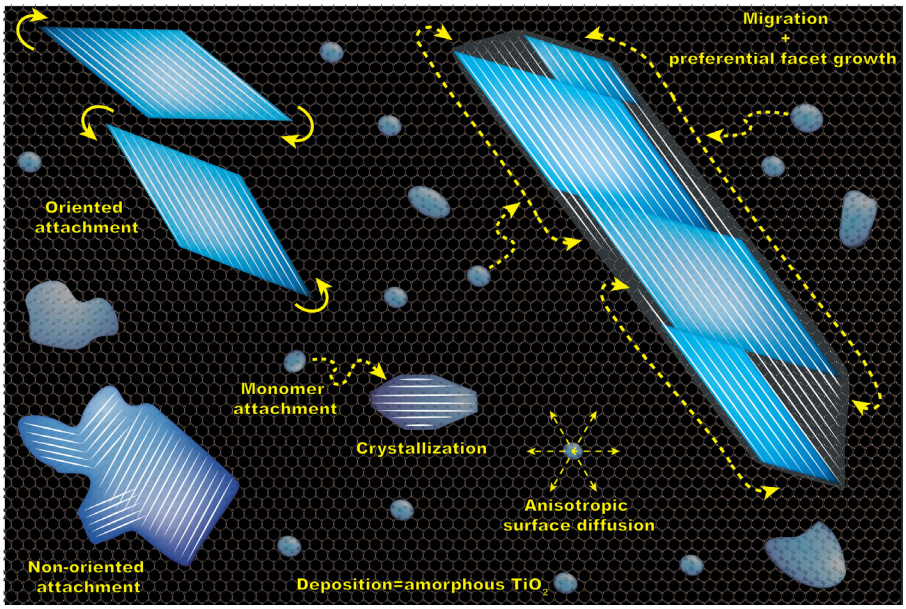

Figure 6.6: Schematic representations of the proposed mechanisms for the formation and growth of the observed nanostructures.

6.3. Conclusions

We have demonstrated the use of ALD as a route for the bottom-up synthesis of TiO_2 nanorods on gram-scale batches of graphene nanoplatelets. By varying the deposition temperature from 100 °C to 300 °C, we could tune the morphology of the ALD-grown TiO_2 from amorphous flakes to crystalline anatase nanoparticles and nanorods, while retaining the same TiO_2 loading. Nanorods > 200 nm in length could be obtained even after only 5 cycles, indicating that the growth is dominated by diffusive aggregation rather than by a layer-by-layer mechanism. In particular, complex structures such as V-shaped and

curved nanorods were observed. The asymmetric growth of the nanoparticles, and thus the formation of nanorods, was induced by modulating the exposure time of the precursors: $TiCl_4$ and H_2O. Prolonged annealing experiments show that the sequential nature of the ALD process is crucial for the nanorods formation. Statistical analysis of the evolution of the shape and the relative number of different nanostructures formed at different exposure times revealed a competition between growth pathways leading to either asymmetric or symmetric growth. In particular, the number of nanorods is a non-linear function of the exposure time of the precursors and of the number of cycles: there exists an optimum. The number of cycles mostly affects the relative number of the nanorods rather their size. High-resolution transmission electron microscopy revealed that the TiO_2 nanocrystals can undergo oriented attachment and that the width of the nanorods is bound by {011} facets. Crucially, analysis of the relative lattice orientation clearly shows an in-plane rotational alignment between the lattices of the TiO_2 nanocrystals and graphene nanoplatelets. Hence, the minimization of the interfacial energy by lattice-matching is considered to be among the major driving forces for the diffusive aggregation underlying the nanorod formation and growth. The insights presented here are also relevant to ALD of other oxides that are known to form nanorods such as vanadium oxide and zinc oxide. We hope that our work will motivate future studies on the exploitation of non-classical growth pathways for the synthesis nanostructures with controlled size and shape via ALD. In particular, we believe that fundamental studies on the role of the substrate in mediating the self-organization of forming nanocrystals can expand the capabilities of ALD and other synthesis methods, especially with regard to nanostructures supported on 2D materials.

6.4. Experimental

6.4.1. Materials

Graphene nanoplatelets (6-8 nm thick and 15 m wide, and a surface area of about 150 $m^2\ g^{-1}$) and the Ti precursor, titanium tetrachloride ($TiCl_4$), were obtained from Strem Chemicals and used as received. Demineralized water was used as the co-reactant. Both precursors were contained in stainless steel bubblers.

6.4.2. ALD experiments

The ALD experiments were carried out in a home-built fluidized bed reactor operated at atmospheric pressure already described elsewhere[35, 71]. The reactor consists of a glass column (2.6 cm in internal diameter and 50 cm in height), placed on top of a double-motor vibration table (Paja PTL 40/40-24) to assist the fluidization process. The titanium precursor ($TiCl_4$) was kept either at 30 °C or at 0 ° C by means of an ice bath to investigate the influence of the vapor pressure on the Ti loading and the morphology of the ALD-grown TiO_2 nanostructures. The co-reactant (H_2O) was kept either at 30 °C or 80 °C by means of an heating tape wrapped around the bubbler. The precursors were delivered to the reactor by flowing N_2 -the carrier gas- through the bubblers. The reactor was connected to three separate gas lines: two for the precursor delivery and one for the purging gas. The reactor was heated by an infrared lamp parallel to the glass column with a PID controller to maintain the desired temperature, i.e., 100 °C, 150 °C, 200 °C or 300 °C. An ALD cycle consisted of sequential exposures of $TiCl_4$ (5 s - 5 min) and H_2O (5 s-5 min), separated

by N_2 (99.999 vol.%) purging steps (5-10 min). In each experiment, 0.75 g of graphene nanopowder was loaded in the reactor. Prior to the deposition, the nanopowder was dried over night at 120 °C. An optimized gas flow of 0.8 NL min^{-1} was used to achieve uniform fluidization of the nanopowder at all times. To remove adventitious carbon and activate the inherently defective surface of the graphene nanoplatelets, the nanopowder was pretreated in-situ with ozone-enriched air obtained by flowing synthetic air (20 wt.% O_2) through an ozone generator (Certizon Ozonizer C200, O_3 output of 200 mg/h) prior to each ALD experiment. After the pretreatment and before the ALD experiment, the reactor was purged with N_2 for 30 min.

6.4.3. Material characterization

The morphology of the TiO_2/graphene composites was investigated via transmission electron microscopy (TEM), scanning electron microscopy (SEM), and high-resolution transmission electron microscopy (HRTEM). The as-synthesized TiO_2/graphene composites were suspended in ethanol and transferred to regular TEM grids of 3.05 mm in diameter. Such grids were then used for all the microscopes. TEM images were taken using a JEOL JEM1400 transmission electron microscope operating at a voltage of 120 kV. The images were then analysed by using the software Imagej to determine the size and shape of the TiO_2 nanostructures. For each sample, 900-1000 nanostructures were characterized by measuring the following descriptors: perimeter (P), area (A), aspect ratio of the fitted ellipse (AR), and circularity: $4\pi A/P^2$ (C). On account of these parameters, the analyzed structures were grouped into three different categories: nanoparticles (NPs), asymmetric nanoparticles (ANPs) and nanorods (NRs). NPs are defined as nanostructures with C $\geq \pi/4 \simeq 0.785$ (an object with P and A such that C$\geq \pi/4$ cannot be approximated by a rectangle). The NP size was then determined by calculating the equivalent projected diameter: $d_{NP} = \sqrt{4A/\pi}$. NRs are defined as nanostructures having AR$\geq$ 3. The length and the width of the nanorods are then defined as the height and the base of the equivalent rectangle having the same P and A. ANPs are structures that fall in neither of the previous groups, that is, structures characterized either by AR $\leq$ 3 and C$\leq \pi/4$ or AR $\geq$ 3 and C$\geq \pi/4$. SEM images were obtained by using a JEOL JSM-840 scanning electron microscope with a LaB6 source at a voltage of 40 kV. HRTEM micrographs were taken using a FEI Cs corrected cubed Titan operating at 300 kV. Crystallographic analysis (determination of lattice spacing, crystal orientation, exposed facets, etc.) was carried out by analyzing the Fast-Fourier-Transform of the HRTEM images with the aid of the software CrysTBox [72, 73] and jems V4.

The crystal structure of the composites was analysed by X-ray owder diffraction (XRD). The composites were transferred onto a Si wafer coated with 300 nm of SiO_2 to remove the influence of the Si signal in the XRD patterns. The diffractograms were obtained by a PANalytical X-pert Pro diffractometer with Cu Kα radiation, secondary flat crystal monochromator and X'celerator RTMS Detector system. The angle of interest 2ϑ was measured from 10° to 80° with steps of 0.001°.

The chemical state and the composition of the composites was investigate by X-ray photoelectron (XPS) carried out with a ThermoFisher K-Alpha system using Al Kα radiation with photon energy of 1486.7 eV. The composites were immobilized on a carbon tape placed on a Si wafer. XPS scans were acquired using a 200 μm spot size, 55 eV pass energy and 0.1 eV/step with charge neutralization. The XPS spectra were fitted with the CasaXPS software.

Elemental analysis was carried out by means of inductively coupled plasma optical emission spectrometry (ICP-OES) and instrumental neutron activation analysis (INAA). The two techniques gave comparable Ti loadings. For ICP-OES, approximately 25 mg of powder were destructed in a solution containing 4.5 mL HCl (30%), 1.5 mL HNO_3 (65%) and 1 mL HF (40%) using a microwave (Multiwave PRO). The destruction time in the microwave was 180 min at maximum power. After destruction the samples were diluted with 50 mL with Milli-Q water and then analysed with a PerkinElmer Optima 4300 DV optical emission spectrometer. For INAA, around 25 mg of powder were loaded into high purity polyethylene capsules. The samples as well as a reference sample and an empty capsule were then sealed together in polyethylene foil, packed in an irradiation container and irradiated by a constant neutron flux. INAA has a detection limit in the range of 10-100 ng. The measurements were performed for 1 hour after an appropriate time in order to let the nuclides decay. Then, the results were interpreted by a UNIX-based computer system, which converts all the information, e.g., peak area and energies, in terms of Ti weight fraction (wt.%). The Ti loading (L) was expressed in terms of at nm^{-2} by using the following equation [19, 35]:

$$L = \frac{x_{\mathrm{Ti}} N_A / \mathrm{MW}_{\mathrm{Ti}}}{(1 - x_{\mathrm{Ti}}) S}$$

where x is the wt.% of Ti in the powder sample, N_A is Avogadro's number, $\mathrm{MW}_{\mathrm{Ti}}$ is the molecular weight of titanium, and S is the surface area of the graphene nanoplatelets.

Appendix

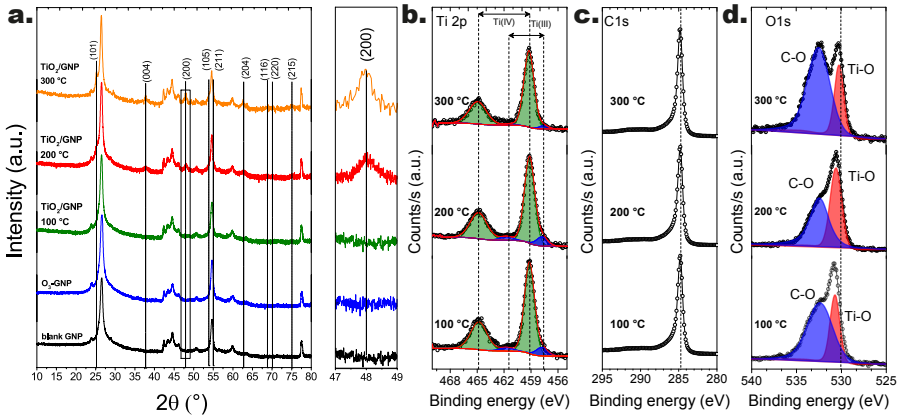

Figure 6..1: X-ray Powder Diffraction (XRD) spectra (a) and X-ray photoelectron spectroscopy (XPS) spectra (b-d) of the TiO_2 graphene composites obtained after 10 cycles at different temperatures. In particular, (b) shows the XPS spectra of the Ti2p region, (c) shows the spectra of the C1s region, and (d) shows the spectra of the O1s regions. All the experiments were carried out by following the pulsing sequence: 30 s $TiCl_4$/ 5 min N_2 purge / 30 s H_2O/5 min N_2 purge.

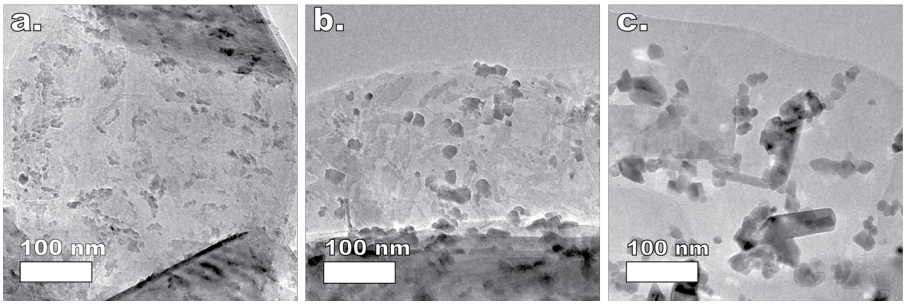

Figure 6..2: Effect of the deposition temperature on the morphology of the ALD-grown TiO_2. Representative TEM images of the TiO_2/Graphene composites obtained after 10 cycles at 100, 200, and 300 °C. All the experiments were carried out by following the pulsing sequence: 30 s $TiCl_4$/ 5 min N_2 purge / 30 s H_2O/5 min N_2 purge.

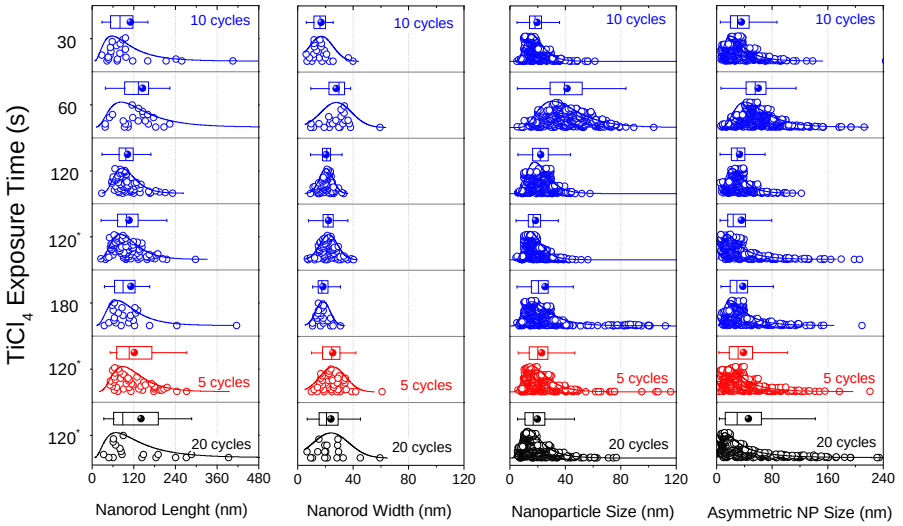

Figure 6..3: Size distributions: nanoparticles, nanorods, asymmetric nanoparticles

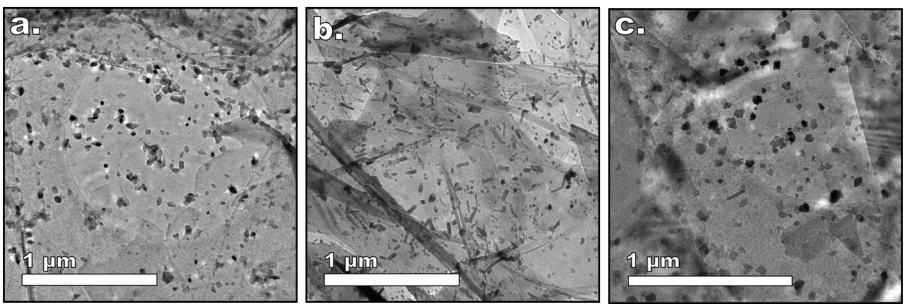

Figure 6..4: Effect of the water exposure on the morphology of the ALD-grown TiO_2 at 300 °C. Representative TEM images of the TiO_2/Graphene composites obtained after 10 cycles using a water exposure time of 15 s (a), 30 s (b), and 2 min (c).

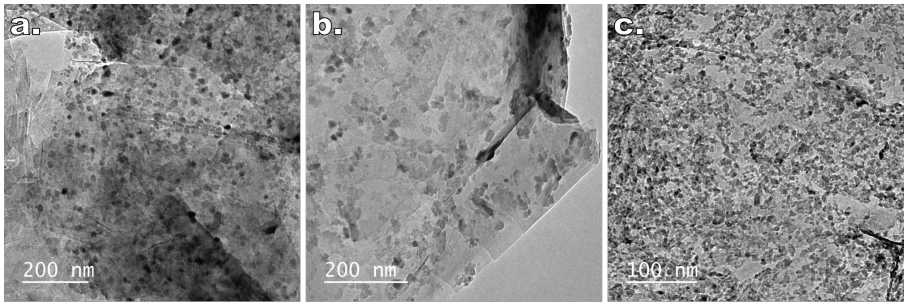

Figure 6..5: Effect of 2 hours of annealing at 300 °C in N_2 + H_2O (a-b) and synthetic air (c) on the morphology of the TiO_2/graphene composites obtained after 10 ALD cycles carried out at 200 °C (a and b) and 100 °C (c). Tha ALD cycles were carried out by following the pulsing sequence: 30 s $TiCl_4$/ 5 min N_2 purge / 30 s H_2O/5 min N_2 purge.

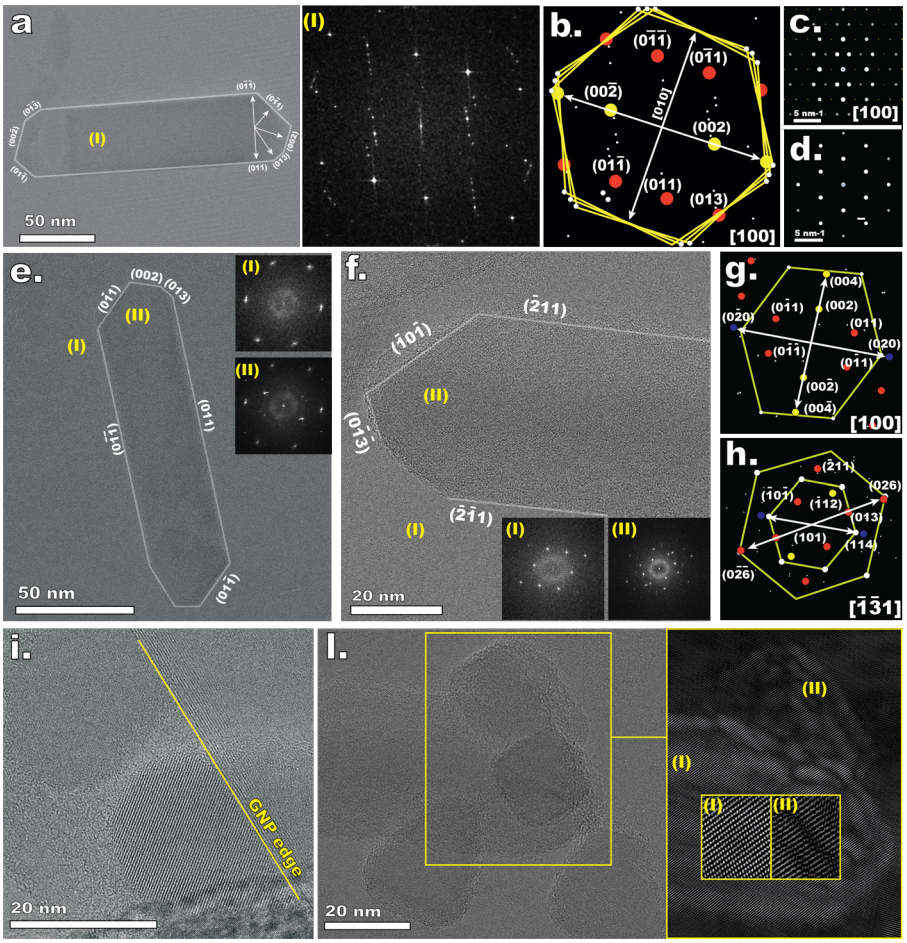

Figure 6..6: High resolution transmission electron microscopy (HRTEM) analysis of TiO_2 nanostructures deposited after 10 cycles at 300 °C. HRTEM image of a nanorod and its Fast-Fourier-Transform (a). Analysis of the FFT of the HRTEM image shown in (a), highlighting the alignment between the TiO_2 lattice and the one of the underlying graphene nanoplatelets (b). Simulated electron diffraction patterns of anatase TiO_2 (c) and graphene (d). HRTEM images of nanorods (e and f) and FFT images of selected areas of the graphene surface (I) and of the (II) nanorods. (g) and (h) show the analysis of the FFT spectra of images (e) and (f), respectively. HRTEM image of a TiO_2 crystal pinned on the edge of a graphene nanoplatelet (i). HRTEM image of the back of a nanorod and few TiO_2 nanoparticles (l). The insert highlights the oriented attachment of one nanoparticle to the nanorod. The insert was obtained by inverting the FFT of image (l) after singling out the pattern associated with the TiO_2 lattice. All the experiments were carried out by following the pulsing sequence: 2 min $TiCl_4$/ 5 min N_2 purge / 30 s H_2O/5 min N_2 purge.

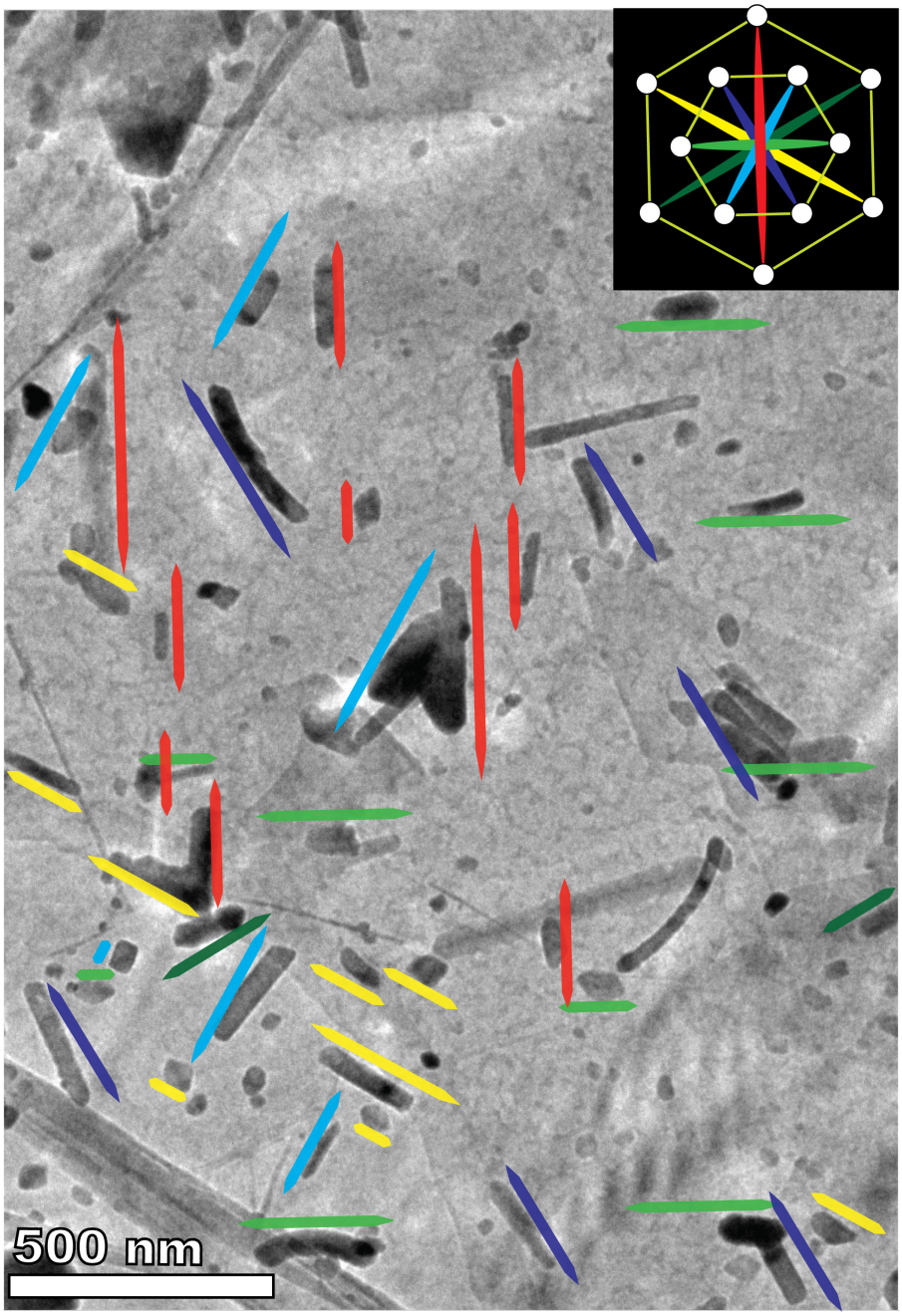

Figure 6..7: TEM image highlighting the alignment of the nanorods.

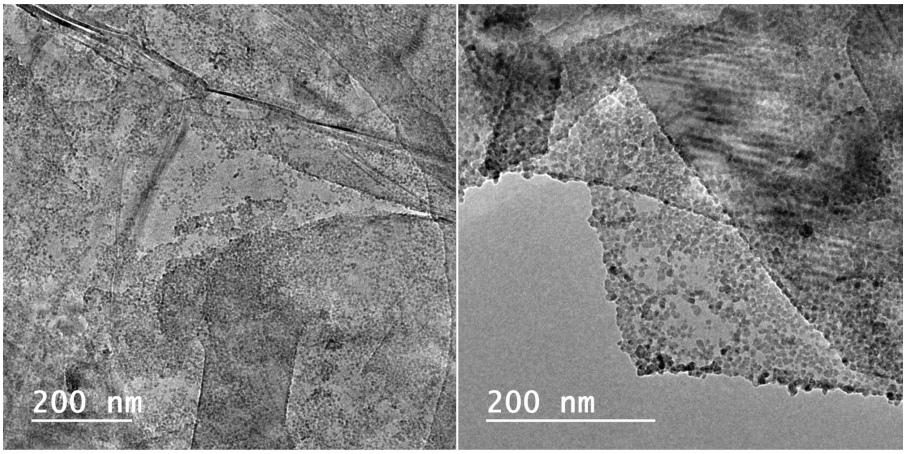

Figure 6..8: Representative TEM images of the TiO_2/Graphene composite obtained after 10 ALD cycles carried out at 300 °C using titanium tetraisopropoxide (TTIP) instead of $TiCl_4$ as the titanium precursor. The ALD experiment was carried out by following the pulsing sequence: 2 min TTIP/ 5 min N_2 purge / 30 s H_2O/5 min N_2 purge.

References

[1] B. Russell, *A History of Western Philosophy* (Routledge, 1946).

[2] S. Berryman, *Ancient Atomism,* in *The Stanford Encyclopedia of Philosophy*, edited by E. N. Zalta (Metaphysics Research Lab, Stanford University, 2016) winter 201 ed.

[3] S. Connor, *Living by Numbers: In Defence of Quantity* (Reaktion Books, 2016).

[4] C. P. Poole and F. Owens, *Introduction to nanotechnology* (John Wiley & Sons, Inc., New York, NY, USA, 2003) pp. xii, 388 p.

[5] Q. Z. Qian, A. Boxman, and U. Chowdhry, *Nanotechnology in the chemical industry - Opportunities and challenges,* Journal of Nanoparticle Research 5, 567 (2003).

[6] S. S. I. Baker C.C. Pradhan A., *Encyclopedia of nanoscience and nanotechnology* (CRC Press, Boca Raton, 2004) pp. 449–473.

[7] A. Albanese, P. S. Tang, and W. C. W. Chan, *The effect of nanoparticle size, shape, and surface chemistry on biological systems.* Annual review of biomedical engineering 14, 1 (2012).

[8] B. R. Cuenya, *Synthesis and catalytic properties of metal nanoparticles: Size, shape, support, composition, and oxidation state effects,* Thin Solid Films 518, 3127 (2010).

[9] L. Li, A. H. Larsen, N. A. Romero, V. A. Morozov, C. Glinsvad, F. Abild-Pedersen, J. Greeley, K. W. Jacobsen, and J. K. Nørskov, *Investigation of catalytic finite-size-effects of platinum metal clusters,* Journal of Physical Chemistry Letters 4, 222 (2013).

[10] A. R. Tao, S. Habas, and P. Yang, *Shape control of colloidal metal nanocrystals,* Small 4, 310 (2008).

[11] R. P. Feynman, *The pleasure of finding things out*, edited by J. Robbins (Perseus Books, Cambridge, MA, 2000).

[12] M. J. Stevens, *How shape affects microtubule and nanoparticle assembly,* Science 343, 981 (2014).

[13] D. Yohan and B. D. Chithrani, *Applications of nanoparticles in nanomedicine,* Journal of Biomedical Nanotechnology 10, 2371 (2014).

[14] F. Sanchez and K. Sobolev, *Nanotechnology in concrete - A review,* Construction and Building Materials 24, 2060 (2010).

[15] H. N. Cheng, K. T. Klasson, T. Asakura, and Q. Wu, *Nanotechnology in agriculture,* in *ACS Symposium Series*, Vol. 1224 (2016) pp. 233–242.

[16] J. V. Barth, G. Costantini, and K. Kern, *Engineering atomic and molecular nanostructures at surfaces,* Nature 437, 671 (2005).

[17] W. C. Lee, K. Kim, J. Park, J. Koo, H. Y. Jeong, H. Lee, D. A. Weitz, A. Zettl, and S. Takeuchi, *Graphene-templated directional growth of an inorganic nanowire,* Nature Nanotechnology 10, 423 (2015).

[18] J. Yang, K. Kim, Y. Lee, K. Kim, W. C. Lee, and J. Park, *Self-organized growth and self-assembly of nanostructures on 2D materials,* FlatChem 5, 50 (2017).

[19] R. L. Puurunen, *Surface chemistry of atomic layer deposition: A case study for the trimethylaluminum/water process,* Journal of Applied Physics 97 (2005).

[20] H. Van Bui, F. Grillo, and J. R. van Ommen, *Atomic and molecular layer deposition: off the beaten track,* Chem. Commun. 53, 45 (2017).

[21] S. M. George, *Atomic layer deposition: An overview,* Chemical Reviews 110, 111 (2010).

[22] E. Ahvenniemi, A. R. Akbashev, S. Ali, M. Bechelany, M. Berdova, S. Boyadjiev, D. C. Cameron, R. Chen, M. Chubarov, V. Cremers, A. Devi, V. Drozd, L. Elnikova, G. Gottardi, K. Grigoras, D. M. Hausmann, C. S. Hwang, S.-H. Jen, T. Kallio, J. Kanervo, I. Khmelnitskiy, D. H. Kim, L. Klibanov, Y. Koshtyal, A. O. I. Krause, J. Kuhs, I. Kärkkänen, M.-L. Kääriäinen, T. Kääriäinen, L. Lamagna, A. A. Łapicki, M. Leskelä, H. Lipsanen, J. Lyytinen, A. Malkov, A. Malygin, A. Mennad, C. Militzer, J. Molarius, M. Norek, Ç. Özgit-Akgün, M. Panov, H. Pedersen, F. Piallat, G. Popov, R. L. Puurunen, G. Rampelberg, R. H. A. Ras, E. Rauwel, F. Roozeboom, T. Sajavaara, H. Salami, H. Savin, N. Schneider, T. E. Seidel, J. Sundqvist, D. B. Suyatin, T. Törndahl, J. R. van Ommen, C. Wiemer, O. M. E. Ylivaara, and O. Yurkevich, *Review Article: Recommended reading list of early publications on atomic layer deposition—Outcome of the "Virtual Project on the History of ALD",* Journal of Vacuum Science & Technology A: Vacuum, Surfaces, and Films 35, 010801 (2017).

[23] F. Grillo, M. T. Kreutzer, and J. R. van Ommen, *Modeling the precursor utilization in atomic layer deposition on nanostructured materials in fluidized bed reactors,* Chemical Engineering Journal 268, 384 (2015).

[24] J. Lu, J. W. Elam, and P. C. Stair, *Atomic layer deposition - Sequential self-limiting surface reactions for advanced catalyst "bottom-up" synthesis,* Surface Science Reports 71, 410 (2016).

[25] B. J. O'Neill, D. H. K. Jackson, J. Lee, C. Canlas, P. C. Stair, C. L. Marshall, J. W. Elam, T. F. Kuech, J. A. Dumesic, and G. W. Huber, *Catalyst Design with Atomic Layer Deposition,* ACS Catalysis 5, 1804 (2015).

[26] C. Marichy, M. Bechelany, and N. Pinna, *Atomic layer deposition of nanostructured materials for energy and environmental applications,* Advanced Materials 24, 1017 (2012).

[27] D. Longrie, D. Deduytsche, and C. Detavernier, *Reactor concepts for atomic layer deposition on agitated particles: A review,* Journal of Vacuum Science & Technology A: Vacuum, Surfaces, and Films 32, 010802 (2014).

[28] D. M. King, X. Liang, and A. W. Weimer, *Functionalization of fine particles using atomic and molecular layer deposition,* Powder Technology 221, 13 (2012).

[29] D. M. King, J. A. Spencer, X. Liang, L. F. Hakim, and A. W. Weimer, *Atomic layer deposition on particles using a fluidized bed reactor with in situ mass spectrometry,* Surface and Coatings Technology 201, 9163 (2007).

[30] L. F. Hakim, J. Blackson, S. M. George, and A. W. Weimer, *Nanocoating Individual Silica Nanoparticles by Atomic Layer Deposition in a Fluidized Bed Reactor,* Chemical Vapor Deposition 11, 420 (2005).

[31] J. R. van Ommen, D. Kooijman, M. de Niet, M. Talebi, and A. Goulas, *Continuous production of nanostructured particles using spatial atomic layer deposition,* Journal of Vacuum Science & Technology A: Vacuum, Surfaces, and Films 33, 021513 (2015).

[32] J. A. McCormick, B. L. Cloutier, A. W. Weimer, and S. M. George, *Rotary reactor for atomic layer deposition on large quantities of nanoparticles,* Journal of Vacuum Science & Technology A: Vacuum, Surfaces, and Films 25, 67 (2007).

[33] C. L. Duan, X. Liu, B. Shan, and R. Chen, *Fluidized bed coupled rotary reactor for nanoparticles coating via atomic layer deposition,* Review of Scientific Instruments 86 (2015).

[34] T. O. Kääriäinen, M. Kemell, M. Vehkamäki, M. L. Kääriäinen, A. Correia, H. A. Santos, L. M. Bimbo, J. Hirvonen, P. Hoppu, S. M. George, D. C. Cameron, M. Ritala, and M. Leskelä, *Surface modification of acetaminophen particles by atomic layer deposition,* International Journal of Pharmaceutics 525, 160 (2017).

[35] F. Grillo, H. Van Bui, J. A. Moulijn, M. T. Kreutzer, and J. R. Van Ommen, *Understanding and Controlling the Aggregative Growth of Platinum Nanoparticles in Atomic Layer Deposition: An Avenue to Size Selection,* Journal of Physical Chemistry Letters 8, 975 (2017).

[36] A. Goulas and J. Ruud van Ommen, *Atomic layer deposition of platinum clusters on titania nanoparticles at atmospheric pressure,* Journal of Materials Chemistry A 1, 4647 (2013).

[37] A. M. Lubers, C. L. Muhich, K. M. Anderson, and A. W. Weimer, *Mechanistic studies for depositing highly dispersed Pt nanoparticles on carbon by use of trimethyl(methylcyclopentadienyl)platinum(IV) reactions with O2 and H2,* Journal of Nanoparticle Research 17 (2015).

[38] A. J. M. Mackus, M. J. Weber, N. F. W. Thissen, D. Garcia-Alonso, R. H. J. Vervuurt, S. Assali, A. A. Bol, M. A. Verheijen, and W. M. M. Kessels, *Atomic layer deposition of Pd and Pt nanoparticles for catalysis: on the mechanisms of nanoparticle formation,* Nanotechnology 27, 034001 (2016).

[39] J. Dendooven, R. K. Ramachandran, E. Solano, M. Kurttepeli, L. Geerts, G. Heremans, J. Rongé, M. M. Minjauw, T. Dobbelaere, K. Devloo-Casier, J. A. Martens, A. Vantomme, S. Bals, G. Portale, A. Coati, and C. Detavernier, *Independent tuning of size and coverage of supported Pt nanoparticles using atomic layer deposition,* Nature Communications 8 (2017).

[40] M. Knez, *Diffusion phenomena in atomic layer deposition,* Semiconductor Science and Technology 27 (2012).

[41] J. Shi, Z. Li, A. Kvit, S. Krylyuk, A. V. Davydov, and X. Wang, *Electron microscopy observation of TiO2 nanocrystal evolution in high-temperature atomic layer deposition,* Nano Letters 13, 5727 (2013).

[42] J. Shi, Z. Li, A. Kvit, S. Krylyuk, A. V. Davydov, and X. Wang, *Electron microscopy observation of TiO2 nanocrystal evolution in high-temperature atomic layer deposition,* Nano Letters 13, 5727 (2013).

[43] K. Wen and W. He, *Can oriented-attachment be an efficient growth mechanism for the synthesis of 1D nanocrystals via atomic layer deposition?* Nanotechnology 26, 382001 (2015).

[44] R. L. Penn, *Imperfect Oriented Attachment: Dislocation Generation in Defect-Free Nanocrystals,* Science 281, 969 (1998).

[45] V. K. Ivanov, P. P. Fedorov, A. Y. Baranchikov, and V. V. Osiko, *Oriented attachment of particles: 100 years of investigations of non-classical crystal growth,* Russian Chemical Reviews 83, 1204 (2014).

[46] W. He, K. Wen, and Y. Niu, *Introduction to Oriented-Attachment Growth Mechanism,* in *Nanocrystals from Oriented-Attachment for Energy Applications* (Springer International Publishing, Cham, 2018) pp. 1–13.

[47] J. J. De Yoreo, P. U. Gilbert, N. A. Sommerdijk, R. L. Penn, S. Whitelam, D. Joester, H. Zhang, J. D. Rimer, A. Navrotsky, J. F. Banfield, A. F. Wallace, F. M. Michel, F. C. Meldrum, H. Cölfen, and P. M. Dove, *Crystallization by particle attachment in synthetic, biogenic, and geologic environments,* Science 349 (2015).

[48] J. Zhang, F. Huang, and Z. Lin, *Progress of nanocrystalline growth kinetics based on oriented attachment,* Nanoscale 2, 18 (2010).

[49] H. G. Liao, L. Cui, S. Whitelam, and H. Zheng, *Real-time imaging of Pt3Fe nanorod growth in solution,* Science 336, 1011 (2012).

[50] W. C. Lee, K. Kim, J. Park, J. Koo, H. Y. Jeong, H. Lee, D. A. Weitz, A. Zettl, and S. Takeuchi, *Graphene-templated directional growth of an inorganic nanowire,* Nature Nanotechnology 10, 423 (2015).

[51] Z. Luo, L. A. Somers, Y. Dan, T. Ly, N. J. Kybert, E. J. Mele, and A. T. C. Johnson, *Size-selective nanoparticle growth on few-layer graphene films,* Nano Letters 10, 777 (2010).

[52] E. Evans, O. Bahl, and J. Thomas, *The decoration of, and epitaxial growth of gold on, graphite surfaces,* Carbon 5, 587 (1967).

[53] C. L. Yaws and M. A. Satyro, *The Yaws Handbook of Vapor Pressure* (2015) pp. 1–314.

[54] M. Ritala, M. Leskelä, E. Nykänen, P. Soininen, and L. Niinistö, *Growth of titanium dioxide thin films by atomic layer epitaxy,* Thin Solid Films 225, 288 (1993).

[55] M. Ritala, M. Leskel¯i, L.-S. Johansson, and L. Niinist6, *Atomic force microscopy study of titanium dioxide thin films grown by atomic layer epitaxy,* Thin Solid Films 228, 32 (1993).

[56] R. L. Puurunen, T. Sajavaara, E. Santala, V. Miikkulainen, T. Saukkonen, M. Laitinen, and M. Leskelä, *Controlling the Crystallinity and Roughness of Atomic Layer Deposited Titanium Dioxide Films,* Journal of Nanoscience and Nanotechnology 11, 8101 (2011).

[57] S. Sun, G. Zhang, N. Gauquelin, N. Chen, J. Zhou, S. Yang, W. Chen, X. Meng, D. Geng, M. N. Banis, R. Li, S. Ye, S. Knights, G. A. Botton, T. K. Sham, and X. Sun, *Single-atom catalysis using Pt/graphene achieved through atomic layer deposition,* Scientific Reports 3 (2013).

[58] B. Karasulu, R. H. J. Vervuurt, W. M. M. Kessels, and A. A. Bol, *Continuous and ultrathin platinum films on graphene using atomic layer deposition: a combined computational and experimental study,* Nanoscale 8, 19829 (2016).

[59] A. K. Rumaiz, B. Ali, A. Ceylan, M. Boggs, T. Beebe, and S. Ismat Shah, *Experimental studies on vacancy induced ferromagnetism in undoped TiO2,* Solid State Communications 144, 334 (2007).

[60] B. Santara, P. K. Giri, K. Imakita, and M. Fujii, *Evidence of oxygen vacancy induced room temperature ferromagnetism in solvothermally synthesized undoped TiO2 nanoribbons,* Nanoscale 5, 5476 (2013).

[61] W. Chen, Q. Kuang, Q. Wang, and Z. Xie, *Engineering a high energy surface of anatase TiO2 crystals towards enhanced performance for energy conversion and environmental applications,* RSC Advances 5, 20396 (2015).

[62] J. Shi, Z. Li, A. Kvit, S. Krylyuk, A. V. Davydov, and X. Wang, *Electron microscopy observation of TiO2 nanocrystal evolution in high-temperature atomic layer deposition,* Nano Letters 13, 5727 (2013).

[63] K. Wen and W. He, *Can oriented-attachment be an efficient growth mechanism for the synthesis of 1D nanocrystals via atomic layer deposition?* Nanotechnology 26, 382001 (2015).

[64] H. Zhang, M. P. Finnegan, and J. F. Banfield, *Titania nanorods curve to lower their energy.* Nanoscale 5, 6742 (2013).

[65] W. Li, F. Wang, Y. Liu, J. Wang, J. Yang, L. Zhang, A. a. Elzatahry, D. Al-Dahyan, Y. Xia, and D. Zhao, *General strategy to synthesize uniform mesoporous TiO2/Graphene/Mesoporous TiO2 sandwich-like nanosheets for highly reversible lithium storage,* Nano Letters 15, 2186 (2015).

[66] Y. Shi, W. Zhou, A.-Y. Lu, W. Fang, Y.-H. Lee, A. L. Hsu, S. M. Kim, K. K. Kim, H. Y. Yang, L.-J. Li, J.-C. Idrobo, and J. Kong, *van der Waals Epitaxy of MoS2 Layers Using Graphene as Growth Templates.* Nano letters 12, 2784 (2012).

[67] Y. J. Hong, J. W. Yang, W. H. Lee, R. S. Ruoff, K. S. Kim, and T. Fukui, *Van der Waals Epitaxial Double Heterostructure: InAs/Single-Layer Graphene/InAs,* Advanced Materials 25, 6847 (2013).

[68] W. Dang, H. Peng, H. Li, P. Wang, and Z. Liu, *Epitaxial heterostructures of ultrathin topological insulator nanoplate and graphene,* Nano Letters 10, 2870 (2010).

[69] P. Wynblatt and N. A. Gjostein, *Supported metal crystallites,* Progress in Solid State Chemistry 9, 21 (1975).

[70] M. Raju, A. C. T. Van Duin, and K. A. Fichthorn, *Mechanisms of oriented attachment of TiO2 nanocrystals in vacuum and humid environments: Reactive molecular dynamics,* Nano Letters 14, 1836 (2014).

[71] H. Van Bui, F. Grillo, S. S. Kulkarni, R. Bevaart, N. Van Thang, B. van der Linden, J. A. Moulijn, M. Makkee, M. T. Kreutzer, and J. R. van Ommen, *Low-temperature atomic layer deposition delivers more active and stable Pt-based catalysts,* Nanoscale (2017).

[72] M. Klinger and A. Jäger, *Crystallographic Tool Box (CrysTBox): automated tools for transmission electron microscopists and crystallographers,* Journal of Applied Crystallography 48, 2012 (2015).

[73] M. Klinger, *More features, more tools, more CrysTBox,* Journal of Applied Crystallography 50, 1226 (2017).

Notre-Dame de Fourvière, Lyon, France 2017.

7

Transport phenomena and Precursor Utilization in Atomic Layer Deposition on Nanostructured Powders Performed in Fluidized Bed Reactors

In this chapter, we present a multiscale dynamic model as a means of understanding and optimizing the precursor utilization during atomic layer deposition (ALD) on nanoparticles and micron-sized nano-porous particles in fluidized bed reactors. We used as case study the deposition of alumina using trimethylaluminum and water on both, titania nanoparticles and micron-sized nano-porous γ-alumina particles under low (~1 mbar) and atmospheric pressure. In doing so, we assess the effect of the precursor transport, from the inlet of the reactor to the particles active surface, on the precursor utilization efficiency. Our results show that, at proper operating conditions, fast ALD reaction kinetics enables the saturation of the particles surface area with hardly any loss of precursors. Finally, simple scaling rules for the optimization of the precursor utilization are proposed.

Published as: Fabio Grillo, Michiel T. Kreutzer, J. Ruud van Ommen, Modeling the precursor utilization in atomic layer deposition on nanostructured materials in fluidized bed reactors, *Chemical Engineering Journal*, 384-398 (268), 2015.

7.1. Introduction

Atomic layer deposition (ALD) carried out in fluidized bed reactors (FBRs) is a promising technique for coating and decorating nanostructured materials such as nanoparticles and micron-sized nano-porous particles [1–4]. Such technology boasts the potential for attaining production schemes relevant to the industrial scale, thanks to the inherent scalability of FBRs, while retaining the capability of ALD to tune surfaces at the nanoscale [2–7]. In a foreseeable future, such potential could boost the application of nanostructured materials in fields such as the production of improved catalysts and enhanced materials for fuel cells and batteries. [1–3, 5, 8–12]. However, the economic and environmental feasibility of the scale-up of such process strongly depends on the efficiency with which the ALD precursors are used, as they represent a major operating cost and may be harmful for the environment [6].

ALD is a technology derived from chemical vapor deposition that enables the deposition of conformal and pinhole-free films on both flat and high aspect-ratio substrates with a precision down to the atomic level [5, 13]. In ALD the film thickness is controlled in a digital fashion by dividing the deposition process into cycles. Each cycle consists of a sequence of precursor exposures interposed by purging or evacuation steps. During a precursor exposure, a certain amount of material, usually a submonolayer, is deposited via self-saturating surface reactions. The purging steps are crucial to the thickness control, as they prevent the undesired material deposition arising from gas-phase reactions between two subsequent precursors and reaction by-products. The number of precursors used in each cycle and thus the number of exposures depends on the material to be deposited. Most ALD systems are binary and thus each cycle comprises of two precursor exposures referred to as half-reactions and two purging steps [5, 13, 14]. Although such technique has been mostly applied in the semiconductor industry to the coating of flat substrates, the sequential steps of ALD can be readily applied to the coating of particle-substrates in FBRs. In fact, ALD cycles can be performed in a FBR by properly modulating the composition of the fluidizing gas used for suspending the particle-substrate in a fluid-like state [6, 11].

Gas fluidization of micron-sized particles has already been successfully employed in several industrial fields such as chemical synthesis, drying and coating technology [15]. Therefore, the expertise developed for such particles can be readily applied to ALD on micron-sized nano-porous particles. On the other hand, gas fluidization of nanopowders is a relatively new field, mostly limited to the lab-scale. Nevertheless, it is proving to be one of the best available technology for dispersing and processing large quantities of nanoparticles [7, 16]. Notwithstanding the small size of the primary particles, nanopowders can indeed be fluidized as they form micron-sized highly porous agglomerates [7, 17, 18]. Upon fluidization a dynamic equilibrium between breaking and cohesive forces determines the properties of the nanoparticle agglomerates and thus their fluidization behaviour [17, 19]. Despite the tendency of nanoparticles to agglomerate during fluidization, several experimental studies have proven that the coating of individual nanoparticles via ALD in FBRs is indeed possible [1, 5, 11]. Finally, even if more research has to be devoted to its implementation in an industrial scale, ALD in FBRs is a technologically viable route for tailoring the surface of bulk quantities of nanoparticles and nano-porous micron-sized particles.

A comprehensive assessment of the economic and environmental feasibility of ALD in FBRs in an industrial scale is not yet available. Nonetheless, residual gas analysis (RGA) via in situ mass spectrometry has shown that the use of FBRs, at low pressures, enables high

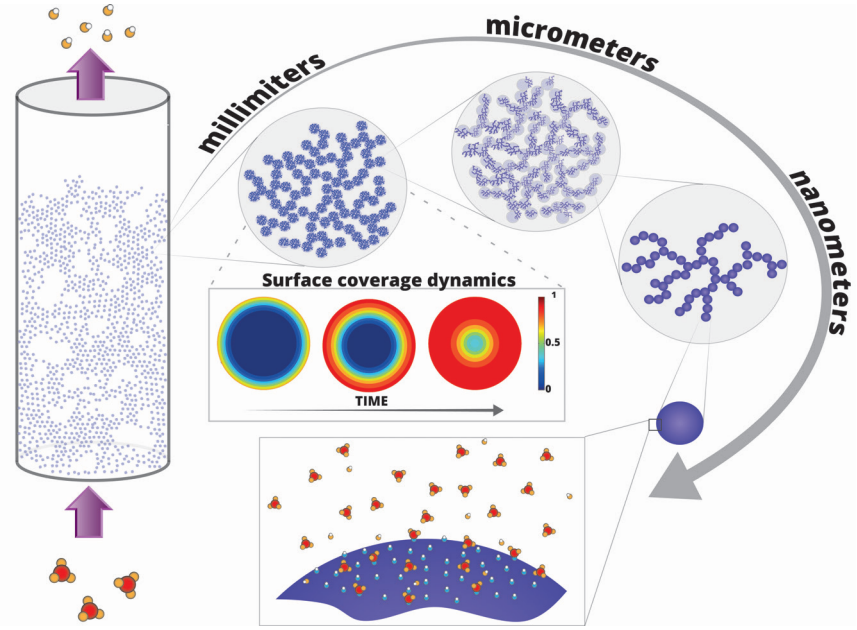

Figure 7.1: Schematic representation of ALD on nanopowders performed in FBRs.

precursor utilization efficiency at relatively high surface conversion over a broad spectrum of particle-substrates and ALD chemistries [6]. This intrinsic high efficiency has been ascribed to the fact that the high degree of mixing, achievable in fluidized beds, coupled with the high surface area given by the particles, reduces the probability that a precursor molecule will not react with an active site before exiting the reactor [1, 6, 8]. Nevertheless, a thorough dynamic analysis of the governing processes that play a role in determining the precursor utilization efficiency has not yet been carried out.

The objective of this work is to characterize the dynamics of ALD on nanoparticles and micron-sized nano-porous particles in FBRs. To that end, we develop a multiscale reactor model capable of capturing the interplay between the typically fast ALD reaction kinetics and the transport of the precursor, from the inlet of the reactor to the particles active surface. In doing so, we investigate the influence of pressure, reactor height, average bubble size and internal structure of both nanoparticle agglomerates and micron-sized nano-porous particles on the precursor utilization efficiency. In particular, we will study the process at both reduced and atmospheric pressure. Both processes have their own advantages and drawbacks [6, 11]. Working at atmospheric pressure is more attractive from a scale-up standpoint, whereas operating at reduced pressure might result in a more efficient process and a better product quality. Therefore, this study is also meant to further clarify the differences between the two approaches in terms of precursor utilization efficiency.". Therefore, this study is also meant to further clarify the differences between the two approaches in terms of precursor utilization efficiency.

The trimethylaluminum (TMA) and water (H_2O) ALD process has been chosen as the base

for the case study as it is the most studied and employed ALD system [5, 13, 14]. Degussa P-25 Titania (TiO_2) nanoparticles and Sasol puralox micron-sized nano-porous γ-alumina (γ-Al_2O_3) particles were selected as the particle substrate as they are among the most used supports for heterogeneous catalysis, and because they both exhibit bubbling fluidization behaviour. The latter enables the study of the effect of the quality of the gas-solid contact from a worst-case scenario perspective, as opposed to particle-substrates that exhibit homogeneous fluidization.

7.2. Multiscale modeling

In this section, we first present a generic model, including transients and a hierarchical, multiscale description of diffusion in nanoparticle agglomerates. Subsequently, we simplify this model by dropping the transients and collapsing the multiscale diffusion model to a shrinking core. In both models, we consistently selected the most cautions description of the process, such that the outcome of the model in terms of precursor utilization efficiency is conservative.

Most ALD chemistries are designed to be very reactive, with fast kinetics, such that most ALD processes in the semiconductor industry are mass-transfer limited [20–23]. The TMA/H_2O system is no exception. Nevertheless, in ALD on nanoparticles in FBRs, given the good gas-solid contact achievable in such reactors [6, 15] and the highly open structure of nanoparticle agglomerates [7, 17, 18, 24, 25], both mass transfer and surface reactions might be equally rate-limiting in determining the deposition dynamics, especially at reduced pressure where the diffusion process is fast. For this reason, for ALD on nanoparticles in FBRs, the dynamics of both the TMA and H_2O exposures are modeled by coupling a multiscale precursor transport model with a detailed description of the adsorption kinetics and surface coverage dynamics. The latter is based on the kinetic model for TMA/H_2O ALD recently developed by Travis et al. [26–28] from absolute reaction theory, which we will briefly describe later. This kinetic model has the advantage that it uses no empirical or simulation-based sticking coefficients to describe ALD dynamics, as often done in other approaches [29–31]. For ALD on micron-sized nano-porous particles in FBRs, however, we simplify the description of the precursor transport and reaction within the particles to a shrinking-core model [15, 22, 32], because of the considerable diffusion limitations introduced by the internal structure of such particles.

7.2.1. ALD on nanoparticles in FBRs

Precursor transport model at the reactor scale

The model for the precursor transport in a bubbling bed of nanoparticle agglomerates, at the reactor scale (see Fig. 7.1), consists of a system of unsteady-state mole balances based on the following assumptions:

- The bubbling bed of nanoparticle agglomerates consists of two phases: an emulsion phase, which in turn consists of interstitial gas and nanoparticle agglomerates, and bubble phase that is assumed to be without solid particles.

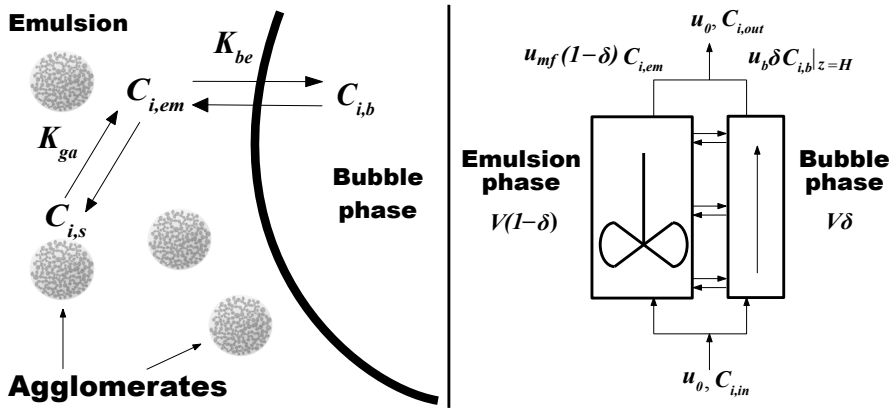

Figure 7.1: Representation of the reactor model at the reactor scale.

- The gas entering the reactor is distributed over the two phases according to the two-phase theory [15, 33]. Therefore, the emulsion phase is assumed to be in the minimum fluidization conditions and all the remaining gas flows through the bed as bubbles.
- The bubble properties are not a function of the reactor height H; instead, the bubbles are characterized by the average bubble size d_b and rising velocity u_b.
- The emulsion phase is totally backmixed, whereas the bubble phase is in plug flow regime. The whole FBR is assumed to operate in isothermal conditions.
- The agglomerates are assumed to be spherical particles with fixed average diameter d_{ag} and porosity ϵ_{ag}.
- The two phases exchange chemical species through convection and diffusion and the overall effect can be described through the lumped interphase mass transfer coefficient K_{be}.
- In the emulsion phase, the mass transfer between interstial gas and outer surface of nanoparticle agglomerates can be described through the mass transfer coefficient K_{ga}.
- In each exposure the precursor (TMA or H_2O) is diluted in nitrogen (N_2), which acts as both the carrier and main fluidization gas.

Before describing the mole balances in some detail, we briefly comment on the conservative assumptions on which the reactor model is based.

The two-phase theory tends to overestimate the amount of gas flowing through the bed as bubbles depending on the particles properties [15, 36]. To the best of our knowledge, no quantitative studies on the bubble phase fraction in bubbling beds of nanoparticles have yet been carried out. Hence, the prediction of the two-phase theory is taken here as a conservative estimation with regard to the quality of the gas-solid contact. For analogous reasons, we do not take into account the bubble growth and we study instead the effect of

Mole balances at the reactor scale
For the bubble phase:
$\frac{\partial C_{i,b}}{\partial t} + u_b \frac{\partial C_{i,b}}{\partial z} = -K_{be}\left(C_{i,b} - C_{i,em}\right)$
Boundary conditions:
$C_{i,b}\vert_{z=0} = C_{i,in},\ C_{i,b}\vert_{t_b=0} = 0$
For the emulsion phase:
$\frac{dC_{i,em}}{dt} = \frac{u_{mf}}{H\epsilon_{mf}}\left(C_{i,in} - C_{i,em}\right) + + \frac{K_{be}\delta}{H\epsilon_{mf}(1-\delta)}\int_0^H \left(C_{i,b} - C_{i,em}\right) dz - -K_{ga}\frac{6(1-\epsilon_{mf})}{\epsilon_{mf} d_{ag}}\left(C_{i,em} - C_{i,s}\right)$
Initial condition:
$C_{i,em}\vert_{t=0} = 0$
Correlations for parameters estimation[15, 33–35]
Flow distribution at the inlet:
$u_0 = \delta u_b + (1-\delta) u_{mf}$
Bed voidage ϵ_{fb}:
$\epsilon_{fb} = \delta + (1-\delta)\,\epsilon_{mf}$
Bubble rising velocity:
$u_b = u_0 - u_{mf} + 0.711\sqrt{g d_b}$
Interphase mass transfer coefficient:
$K_{be} = \frac{6}{d_b}\left[\frac{u_{mf}}{3} + \left(\frac{4 D_i \epsilon_{mf} u_b}{\pi d_b}\right)^{0.5}\right]$
Bubbles volumetric fraction:
$\delta = \frac{u - u_{mf}}{u_b - u_{mf}}$
Mass transfer coefficient in the emulsion phase:
$K_{ga} = \frac{D_i}{d_{ag}}\left[2 + a\left(1 - \epsilon_{mf}\right)\mathrm{Re}^b \mathrm{Sc}^{1/3}\right] \sim \frac{2D_i}{d_{ag}}$
Diffusion coefficient D_i:
Hirschfelder, Bird and Spotz method

Table 7.1: Precursor model at the reactor scale and correlations for parameters estimation.

the average bubble properties (u_b and d_b) on the precursor utilization efficiency.

Analogous conservative considerations hold for neglecting the presence of solids in the bubble phase. In fact, the bubbles in a FBR of nanoparticles are likely to contain small agglomerates, which could considerably enhance the gas-solid mass transfer given their highly porous and reactive nature during ALD [15]. Furthermore, this model does not take into account freeboard and distributor effects, which in turn can enhance the gas-solid mass transfer [15, 36].

The backmixing assumption for the solids is fairly reasonable for bubbling beds with bed height to bed diameter ratio H/d_t from 0.1 to 4 [37]. Nevertheless, bubbling beds of

nanoparticles usually show segregation of solids caused by the presence of larger agglomerates, mainly formed during the storage and transport of the nanopowder [7, 38]. This inconvenience is usually overcome by drying and sieving the nanopowder so as to remove larger agglomerates ($d_{ag} > 500\ \mu m$). Moreover, solid segregation during ALD can be drastically reduced by means of assisting methods such as stirring, vibration or the use of microjets [6, 7]. Given the aforementioned considerations and the low bed expansion of a fluidized bed of Degussa P-25 TiO_2 nanoparticles ($H/H_0 < 2$) [38], the agglomerates can be considered to be backmixed for initial bed height to bed diameter $H_0/d_t < 2$. Finally, the interstitial gas is not only backmixed due to the solids recirculation but also because it continuously exchanges chemical species with the particles. Therefore, the backmixing assumption for the emulsion phase is not just conservative but takes into account the actual bed hydrodynamics during ALD.

We now describe the mole balances derived on the basis of the aforementioned assumptions. The precursor transport model at the reactor scale consists of the mole balances for the i-th chemical species written for both the bubble and emulsion phase, accompanied by their respective boundary conditions, given in Table 7.1. The correlations used for the estimation of model parameters such as the volumetric bubble fraction δ, the bubble velocity u_b, the mass transfer coefficients K_{be} and K_{ga}, and the diffusion coefficients D_i are also given in Table 7.1. The volumetric bubble fraction as well as the flow distribution at the inlet and the bed voidage, arise from a material balance at the inlet of the reactor based on the two-phase theory. The other parameters, namely, the minimum fluidization velocity u_{mf}, the corresponding void fraction ϵ_{mf}, the expanded bed height H and the average nanoparticle agglomerate diameter d_{ag} are estimated from data available in the literature, whereas the average bubble diameter d_b is treated as an adjustable parameter.

The chemical species considered here are: TMA, H_2O, CH_4 and N_2. The TMA half-reaction is modeled by setting the inlet concentrations of all the chemical species equal to zero, except for TMA and N_2, whose concentrations are set equal to $C_{\mathrm{TMA},in}$ and $C_{\mathrm{N_2},in}$, respectively. The same goes for the H_2O exposure, with the inlet concentration of TMA and H_2O set equal to zero and $C_{\mathrm{H_2O},in}$, respectively. The mole balances for the bubble phase and the emulsion phase are written in terms of the concentrations: $C_{i,in}$ at the inlet, $C_{i,b}$ in the bubble phase, $C_{i,em}$ in the emulsion phase and $C_{i,s}$ at the outer surface of the nanoparticle agglomerates.

The left-hand-side of the bubble phase mole balance is the sum of the convective and transient term, whereas the right-hand-side arises from the interphase mass transfer. The left-hand-side of the emulsion phase mole balance is the transient term, whereas the right-hand-side is the sum of three terms: in/out, interphase and emulsion-gas-to-agglomerates mass transfer. The interphase mass transfer coefficient K_{be} is estimated from the correlation of Sit and Grace [34] for bubbling bed reactors. This correlation has been selected as it has proven to give the best available predictions of interphase mass transfer coefficients in three-dimensional bubbling bed reactors and it takes into account both diffusive and convective contributions [36]. The mass transfer coefficient in the emulsion phase is usually predicted by using a Frössling-like equation [15, 36] (see Table 7.1). In our case, the Reynolds

and Schmidt numbers are relatively small and the Sherwood number tends toward the minimum theoretical value of 2. For this reason, we have taken a conservative estimation of the mass transfer coefficient in the emulsion phase by assuming Sh = 2.

Precursor transport model at the nanoparticle-agglomerate scale

The description of the precursor transport at the nanoparticle-agglomerate scale is closely related to the multi-level porous structure of the nanoparticle agglomerates formed during the fluidization process. For this reason, before presenting the precursor transport model, we briefly describe the model of the nanoparticle agglomerates internal structure on which the transport model is based.

In a fluidized bed of nanoparticles, primary particles are arranged in chain-like structures of 200-300 nm in size, referred to as aggregates, formed by either agglomeration, due to interparticle forces (London-van der Waals), or sintering during the manufacturing process. Aggregates coalesce into larger and more compact spherical or ellipsoidal agglomerates of 1-100 μm in size called simple agglomerates. Finally, the latter further agglomerate into open structures of 200-600 μm in size called complex agglomerates [7, 17, 18, 39]. The structure of such nanoparticle agglomerates has been commonly described in terms of fractal geometry [7, 16]. De Martín et al. [24, 25] have recently shown how Degussa P-25 TiO_2 nanoparticle agglomerates, formed upon gas fluidization, can be described as multifractal objects by means of three fractal dimensions. According to this description, the density of aggregates, simple and complex agglomerates scale as:

$$\varrho_j = \varrho_{j-1} k_j \left(\frac{d_j}{d_{j-1}} \right)^{D_{f,j}-3}, j = \begin{cases} 0. \text{ primary particle} \\ 1. \text{ aggregate} \\ 2. \text{ simple agglomerate} \\ 3. \text{ complex agglomerate} \end{cases} \tag{7.1}$$

where k_j is the pre-factor, $D_{f,j}$ the fractal dimension and d_j the size of the j-th agglomerate level.

By following such description and assuming the following typical average properties for each agglomerate level: $d_0 = 21$ nm, $d_1 = 260$ nm, $d_2 = 30\,\mu$m, $d_3 = 300\,\mu$m and $\varrho_0 = 4000$ kg/m^3 [7, 24, 25], we model the Degussa P-25 TiO_2 nanoparticle agglomerates as porous media characterized by a three-level hierarchical structure. Hence, the densities of the three levels, estimated using Eq. 7.1, are:

$$\varrho_1 = 415 \text{ kg/m}^3,\ \varrho_2 = 204 \text{ kg/m}^3,\ \varrho_3 = 47 \text{ kg/m}^3 \tag{7.2}$$

which translate into the total porosities ϵ_i:

$$\epsilon_1 = 0.90,\ \epsilon_2 = 0.95,\ \epsilon_3 = 0.99 \tag{7.3}$$

and the effective porosities $\epsilon_{i,k}$, that is the porosity of the i-th level with respect to the k-th level assuming the latter to be non-porous:

$$\epsilon_{2,1} = 0.51,\ \epsilon_{3,2} = 0.77 \tag{7.4}$$

Such porosities are consistent with the multi-stage agglomeration described by Yao et al. [17]. In particular, a total porosity of the aggregates ϵ_1 of 0.90 is consistent with open chain-like structures, whereas an effective porosity $\epsilon_{2,1}$ of 0.51 is consistent with the high compaction between aggregates within the simple agglomerates and an effective porosity $\epsilon_{3,2}$ of 0.77 is consistent with the looser compaction between simple agglomerates within complex agglomerates. Hence, in analogy with bidispersed catalysts made by pelletizing

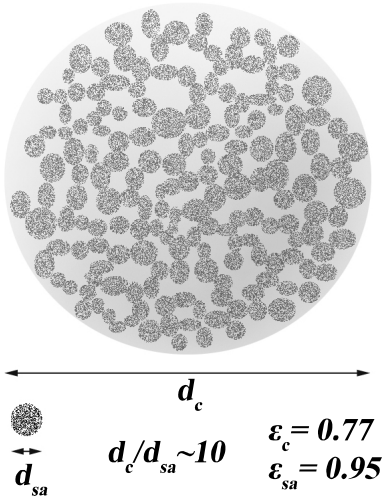

Figure 7.2: Schematic representation of a nanoparticle agglomerate.

porous primary particles, the nanoparticle agglomerates are envisioned as bidispersed porous particles formed by the assembly of simple agglomerates. Therefore, in this simplified picture, the precursor diffusion takes place in two levels: the complex-agglomerate level, characterized by the porosity ϵ_c=$\epsilon_{3,2}$= 0.77, and the simple agglomerate level, characterized by the porosity ϵ_{sa}=$\epsilon_{2,0}$= 0.95 (see Fig. 7.2). To model the diffusion within the two levels we assume the void space at the larger level, i.e. between simple agglomerates, to consist of cylindrical pores that go from the outside of the complex agglomerates to the their center. These long cylindrical pores are then connected to the smaller level which in turn consist of cylindrical pores that go from the outside of simple agglomerates to their center. Hence the void space within the nanoparticle agglomerates is characterized by two average pore diameters: λ_c for the complex agglomerate level and λ_{sa} for the simple agglomerate level. The equivalent cylindrical pore diameter in an assembly of spherical particles can be estimated as [40]:

$$\lambda = \frac{2\,\epsilon\,d_p}{3(1-\epsilon)} \tag{7.5}$$

In our case, given the high voidage in both levels, we make a conservative estimation of the pore sizes by approximating λ to the particle diameter d_p. Thus, we obtain

$$\lambda_c \sim d_2 = 30\,\mu\text{m} \tag{7.6}$$

for the complex agglomerate level, and:

$$\lambda_{sa} \sim \frac{d_1 + d_0}{2} = 140.5 \text{ nm} \tag{7.7}$$

for the simple agglomerates level. Given the great difference between the two average pore diameters, the diffusion regime in the two levels may differ depending on the Knudsen number, and thus on the operating pressure. The Knudsen number is defined as:

$$\text{Kn}_k = \frac{l}{\lambda} \tag{7.8}$$

where l is the mean free path of a precursor molecule. For large Knudsen numbers (Kn >> 1), the interactions between molecules and pore walls control the diffusion process rather than the collisions between molecules, and the diffusion regime is referred to as Knudsen regime, as opposed to the hydrodynamic or Fickian regime at low Knudsen numbers (Kn << 1). The molecules mean free path can be estimated as:

$$l = \frac{k_B T}{\pi \sqrt{2} \sigma^2 P} \tag{7.9}$$

where k_B is the Boltzmann constant, T is the temperature, σ the molecule collision diameter and P the pressure. In this work, two cases will be examined, one at atmospheric pressure (1.013 bar) and one at low pressure (1 mbar). Assuming a deposition temperature of 500 K and a TMA collision diameter of 0.5465 nm[1] (with water analogous results are obtained), at atmospheric pressure the Knudsen number has the following values:

$$\text{Kn}_c = 1.7 \cdot 10^{-3}, \ \text{Kn}_{sa} = 0.37 \tag{7.10}$$

Thus, in the complex-agglomerate level the diffusion process can be described in Fickian terms, whereas in the simple agglomerates level both Knudsen and Fickian diffusion contribute to the diffusion process since the Knudsen number is close to one. The latter condition is referred to as transition regime. At 1 mbar the Knudsen number assumes the following values:

$$\text{Kn}_c = 1.73, \ \text{Kn}_{sa} = 370.35 \tag{7.11}$$

therefore, in this case the complex-agglomerate level is characterized by the transition regime, whereas in the simple agglomerates level the Knudsen regime is fully developed. In light of these considerations, we describe the diffusion within the nanoparticle agglomerates by defining effective diffusion coefficients for the two pressure cases and the two agglomerate levels. The effective diffusion coefficient for the i-th chemical species and k-th level can be defined as:

$$D_{i,k} = \frac{\epsilon_k}{\tau_k} D_i \tag{7.12}$$

for the hydrodynamic regime[2];

$$D_{i,k} = \frac{\epsilon_k}{\tau_k} D_{i,K}|_{\lambda_k} \tag{7.13}$$

[1] The collision diameter has been estimated from the TMA molal volume at normal boiling point [35].
[2] The diffusion coefficient D_i has been estimated by using the modified Hirschfelder, Bird and Spotz method [35].

for the Knudsen regime and

$$D_{i,k} = \frac{\epsilon_k}{\tau_k}\left[\frac{1}{D_i} + \frac{1}{D_{i,K}|_{\lambda_k}}\right]^{-1} \tag{7.14}$$

for the transition regime [41], where $D_{i,K}|_{\lambda_k}$ is estimated as [42]:

$$D_{i,K}|_{\lambda_k} = 48.5\lambda_k\sqrt{\frac{T}{M_i}} \tag{7.15}$$

and the tortuosity τ_k is approximated as $1/\epsilon_k$ [43].

Since the mathematical treating of diffusion and reaction in bidispersed porous media is not straightforward, we further simplify the problem by tailoring the mathematical model to the two pressure cases considered here. This is done by comparing the diffusion time scales in the two agglomerate levels in both pressure cases:

$$\frac{\tau_{sa}}{\tau_c} = \frac{R_{sa}^2}{R_c^2}\frac{D_{TMA,c}}{D_{TMA,sa}} = \begin{cases} 1.5\cdot 10^{-2}, & P = 1.013\,\text{bar} \\ 1.21, & P = 1\,\text{mbar} \end{cases} \tag{7.16}$$

Since at atmospheric pressure the diffusion time scale in the simple agglomerates level is roughly two orders of magnitude greater than in the complex agglomerate level, we neglect the diffusion limitations in the simple agglomerates level and model the diffusion and reaction by treating the agglomerates as mono-dispersed porous media characterized by the porosity ϵ_{ag}=ϵ_3= 0.99 and the effective diffusion coefficient of the complex agglomerate level $D_{i,c}$. On the other hand, at 1 mbar the two diffusion time scales have roughly the same order of magnitude. For this reason, we treat the nanoparticle agglomerates as bidispersed porous particles and model the diffusion and reaction by means of a dynamic version of the particle-pellet model [44, 45]. In this model, the simple agglomerates are treated as uniformly distributed point sinks at the larger level and the strength of the sink term is calculated from a reaction-diffusion balance over a spherical simple agglomerate. Such approximations can be used to describe the diffusion process as long as the concentration profiles in the complex-agglomerate level are relatively flat, which is likely to be the case at low pressure but not at atmospheric pressure as will be discussed later.

To summarize, the precursor transport model at the nanoparticle-agglomerate level is based on the following assumptions:

- The nanoparticles agglomerates are spherical particles of average diameter d_c, formed by spherical sub agglomerates of average diameter d_{sa}. The dynamic nature of the agglomerates is not taken into account, therefore the precursor transport is treated from a worst-scenario perspective.

- At atmospheric pressure, as far as the diffusion is concerned, the agglomerates act as mono-dispersed porous media characterized by the porosity ϵ_{ag} and the effective diffusion coefficient $D_{i,c}$.

- At 1 mbar, with regard to the diffusion, the agglomerates act as bi-dispersed porous media characterized by the porosities ϵ_{sa} and ϵ_c, and the effective diffusion coefficients $D_{i,c}$ and $D_{i,sa}$. The concentration profiles in the sub agglomerates are symmetrical and the simple agglomerates can be assumed to act as uniformly distributed point sinks.

- The precursor is present in diluted concentrations and the convective terms in the mole balances can be neglected.

- The nanoparticle agglomerates are in isothermal conditions.

The resulting mole balances, accompanied by their respective boundary conditions, are listed in Table 7.2. For the case at atmospheric pressure, the mathematical model consists of one parabolic partial differential equation describing the evolution in time of the precursor concentration $C_{i,ag}$ along the radial coordinate r_c, accompanied by a set of boundary conditions. In particular, the zero flux condition at the center of the agglomerates due to symmetry and a Robin boundary condition for the flux at outer surface of the agglomerate ($r_c = R_c$), which couples the model at the nanoparticle-agglomerate level with the model at the reactor scale. The generation term g_i is a function of the surface coverage, precursor concentration and active surface to volume ratio as it will be described later.

For the case at 1 mbar, the mathematical model consists of two coupled partial differential equations describing the evolution in time of both the precursor concentration at the complex-agglomerate level $C_{i,c}$ along the radial coordinate r_c, and the precursor concentration at the simple agglomerate level $C_{i,sa}$ along both the radial coordinates r_{sa} and r_c. The boundary conditions for the complex-agglomerate level are analogous to those for the agglomerate level in the previous case. For the simple agglomerate level, the assumption of symmetrical concentration profiles translates into the Dirichlet boundary condition $C_{i,sa} = C_{i,c}$ at the outer surface of each simple agglomerate along the radial coordinate r_c.

Adsorption kinetics and surface coverage dynamics

A number of authors have developed several ALD reactor models aimed at understanding the ALD dynamics on both flat and high aspect-ratio substrates [29–31]. These models strongly depend on the use of proper ALD kinetics, whereas only empirical or simulation-based sticking coefficients are available. Travis et al. [26–28] have recently shown how realistic ALD reaction and growth surface dynamics models can be derived from first principles, which, coupled with a proper precursor transport model, provides a valuable tool for dynamic optimization of ALD processes. For this reason, the adsorption kinetics and the surface coverage dynamics used in the present work is based on the work of Travis et al. Here we briefly describe the adsorption kinetics and surface coverage dynamics model implemented in our precursor transport model; for further details the reader is referred to Travis et al. [26–28].

In each half-reaction (TMA and H_2O) the adsorption kinetics and surface coverage dynamics model assumes the particles surface to consist of adsorbed methyl groups (Me), hydroxyl

Mole balance for the case at atmospheric pressure

$$\epsilon_{ag}\frac{\partial C_{i,ag}}{\partial t} = \frac{D_{i,c}}{r_c^2}\frac{\partial}{\partial r_c}\left(r_c^2\frac{\partial C_{i,ag}}{\partial r_c}\right) + g_i$$

$$B.C. = \begin{cases} \frac{\partial C_{i,ag}}{\partial r_c}|_{r_c=0} = 0 \\ -D_{i,c}\frac{\partial C_{i,ag}}{\partial r_c}|_{r_c=R_c} = K_{ga}(C_{i,s} - C_{i,em}) \\ C_i^s = C_i^{ag}|_{r_c=R_c} \\ C_{i,ag}|_{t=0} = 0 \end{cases}$$

Mole balances for the case at 1 mbar

For the complex agglomerate level:

$$\epsilon_c\frac{\partial C_{i,c}}{\partial t} = \frac{D_{i,c}}{r_c^2}\frac{\partial}{\partial r_c}\left(r_c^2\frac{\partial C_{i,c}}{\partial r_c}\right) - \frac{3(1-\epsilon_c)}{r_{sa}}D_{i,sa}\left(\frac{\partial C_{i,sa}}{\partial r_{sa}}\right)_{r_{sa}=R_{sa}}$$

For the simple agglomerate level ($[0, R_c]$x$[0, R_{sa}]$):

$$\epsilon_{sa}\frac{\partial C_{i,sa}}{\partial t} = \frac{D_{i,sa}}{r_{sa}^2}\frac{\partial}{\partial r_{sa}}\left(r_{sa}^2\frac{\partial C_{i,sa}}{\partial r_{sa}}\right) + g_i$$

$$B.C. = \begin{cases} \frac{\partial C_{i,c}}{\partial r_c}|_{r_c=0} = \frac{\partial C_{i,sa}}{\partial r_{sa}}|_{r_{sa}=0} = 0 \\ -D_{i,c}\frac{\partial C_{i,c}}{\partial r_c}|_{r_c=R_c} = K_{ga}\left(C_i^s - C_i^{em}\right) \\ C_i^s = C_{i,sa}|_{r_c=R_c} \\ C_{i,sa}|_{r_{sa}=R_{sa}} = C_{i,c} \\ C_{i,sa}|_{t=0} = C_{i,c}|_{t=0} = 0 \end{cases}$$

Table 7.2: Precursor transport model at the nanoparticle-agglomerate scale

groups (OH) and oxygen bridges (O). We thus define the following surface coverages:

$$\vartheta_{\mathrm{Me}} = \frac{[\mathrm{Me}]}{[\widehat{\mathrm{Me}}]},\ \vartheta_{\mathrm{OH}} = \frac{[\mathrm{OH}]}{[\widehat{\mathrm{OH}}]} \tag{7.17}$$

where [Me] and [OH] are the surface concentrations of methyl and hydroxyl groups, respectively, whereas $[\widehat{\mathrm{Me}}]$ and $[\widehat{\mathrm{OH}}]$ are their maximum values based on steric hindrance considerations [26].

The surface coverage dynamics depends on the rate of the gas-solid reactions taking place during each half-reaction. ALD precursors can chemisorb onto the surface with three mechanisms: ligand exchange, association and dissociation [5, 13, 14]. Several experimental and theoretical studies [28, 46–49] suggest how during the TMA half-reaction, aluminum atoms are mostly deposited through ligand exchange between TMA molecules and hydroxyl groups, and association/dissociation reactions start to play a role only in the deposition on low hydroxylated surfaces. Furthermore, the growth per cycle (GPC) – the amount of material deposited per each cycle – reported in the literature for both low and fully hydroxylated surfaces is consistent with the termination of chemisorption reactions by steric hindrance

between methyl groups [13]. By assuming the particle surface to be fairly hydroxylated at the beginning of each TMA half-reaction, the ligand exchange chemisorption reaction between TMA molecules and hydroxyl groups is considered to be the main surface reaction. Moreover, the adsorbed methyl groups are allowed to react with neighboring hydroxyl groups [13, 26, 27]. The surface reactions are assumed to reach saturation once the methyl surface concentration has reached the maximum concentration allowed by steric hindrance.

During the water half-reaction, water molecules react with the adsorbed methyl groups, through ligand exchange chemisorption, releasing methane and restoring surface hydroxyl groups and the reaction is terminated by the depletion of surface methyl groups [5, 13, 26, 27, 46, 48, 50].

The chemisorption reactions are modeled through the following reaction rates expressed per unit area per unit time derived by Travis et al. from absolute reaction theory [26–28]:

$$\nu_1 = \nu_r(C_{TMA}, \vartheta_{OH}),\ \nu_2 = \nu_2(C_{\mathrm{H_2O}}, \vartheta_{OH})\ ,\ \nu_3 = \nu_3(C_{\mathrm{H_2O}}, \vartheta_{OH}) \tag{7.18}$$

where ν_1 is used to model the reaction between TMA molecules and hydroxyl groups during the TMA half-reaction, whereas ν_2 and ν_3 are used to model the reactions between H_2O and methyl groups during the H_2O half-reaction. The subsequent reaction between adsorbed methyl groups and neighbouring hydroxyl groups, taking place right after the TMA chemisorption, is modeled by assuming that on a fully hydroxylated surface ($\vartheta_{\mathrm{OH}} \sim 1$) the methyl groups will further react with two neighboring hydroxyl groups generating oxygen bridges and releasing methane, whereas on a surface with a low concentration of hydroxyl groups ($\vartheta_{\mathrm{OH}} \sim 0$) the methyl groups will not react any further [26]. The resulting surface species balances and generation terms for the precursor transport model are given in Table 7.3. It is worth noting that the generation terms have different definitions depending on the pressure case due to the precursor transport model formulation at the nanoparticle-agglomerate scale. In fact, the active surface to volume ratio S_p/V_k is referred to the complex agglomerate level for the case at atmospheric pressure and to the simple agglomerate level for the case at 1 mbar.

Time scales

In order to obtain further insight into the process dynamics and guide the interpretation of the simulation results, we will now discuss the time scales characterizing ALD on nanoparticles in FBRs. We distinguish three groups of time scales according to the physical or chemical process to which they are related, i.e. precursor transport, chemisorption reactions and surface coverage dynamics.

With regard to the precursor transport we can identify six time scales (Eqs. 7.19 and Eqs. 7.20): the average gas residence time in the emulsion phase τ_{em}, the gas residence time in the bubble phase τ_b, the interphase mass transfer time scale τ_{int}, the emulsion gas to agglomerates mass transfer time scale τ_{ga}, the complex agglomerate diffusion time scale τ_c and the simple agglomerate diffusion time scale τ_{sa}.

$$\tau_{em} = \frac{H(1-\delta)}{u_{mf}},\ \tau_b = \frac{H}{u_b},\ \tau_{int} = \frac{1}{K_{be}} \tag{7.19}$$

Surface coverage dynamics [26, 27]
$[\widehat{\mathrm{Me}}]\frac{\partial \vartheta_{\mathrm{Me}}}{\partial t} = (2-2\vartheta_{\mathrm{OH}})(1-\vartheta_{\mathrm{Me}})\nu_1 - (1-\vartheta_{\mathrm{OH}})\nu_2 - \vartheta_{\mathrm{OH}}\nu_3$
$[\widehat{\mathrm{OH}}]\frac{\partial \vartheta_{\mathrm{OH}}}{\partial t} = -(1+2\vartheta_{\mathrm{OH}})(1-\vartheta_{\mathrm{Me}})\nu_1 + (1-\vartheta_{\mathrm{OH}})\nu_2 + \vartheta_{\mathrm{OH}}\nu_3$
Initial conditions:
TMA half-reaction: $\begin{cases}\vartheta_{\mathrm{Me}}\vert_{t=0} = 0\\ \vartheta_{\mathrm{OH}}\vert_{t=0} = \vartheta^0_{\mathrm{OH}}\end{cases}$ — H_2O half-reaction: $\begin{cases}\vartheta_{\mathrm{Me}}\vert_{t=0} = 1\\ \vartheta_{\mathrm{OH}}\vert_{t=0} = 0\end{cases}$
Generation terms
$g_{TMA} = -(1-\vartheta_{\mathrm{Me}})\nu_1 \frac{S_p}{V_k} 10^{18}/N_{avo}$
$g_{\mathrm{H_2O}} = [-(1-\vartheta_{\mathrm{OH}})\nu_2 - \vartheta_{\mathrm{OH}}\nu_3]\frac{S_p}{V_k} 10^{18}/N_{avo}$
$g_{CH_4} = [(1+2\vartheta_{\mathrm{OH}})(1-\vartheta_{\mathrm{Me}})\nu_1 + (1-\vartheta_{\mathrm{OH}})\nu_2 + \vartheta_{\mathrm{OH}}\nu_3]\frac{S_p}{V_k} 10^{18}/N_{avo}$
$\begin{cases}k = c,\ P{=}1.013\ \text{bar}\\ k = sa,\ P{=}1\ \text{mbar}\end{cases}$

Table 7.3: Adsorption kinetics and surface coverage dynamics

$$\tau_{ga} = \frac{R_c}{K_{ga}},\ \tau_c = \frac{R_c^2}{D_{i,c}},\ \tau_{sa} = \frac{R_{sa}^2}{D_{i,sa}} \tag{7.20}$$

One can estimate the order of magnitude of the reaction time scale during the pulsing time by defining an average reaction rate coefficient $\langle \nu'_k \rangle$ as:

$$\langle \nu'_k \rangle = \frac{\tilde{g}_{i,k}}{C_i}\ \ [1/s] \tag{7.21}$$

where $\tilde{g}_{i,k}$ is the linearised[3] generation term with respect to precursor concentration C_i, estimated at $\vartheta_{\mathrm{Me}} = 0.5$ and $\vartheta_{\mathrm{OH}} = \vartheta^0_{\mathrm{OH}}/2$. Thus, we can define the chemisorption reaction time scale as:

$$\tau_{i,rxn} = 1/\langle \nu'_k \rangle \tag{7.22}$$

Furthermore, we compare the order of magnitude of the reaction time scale to the internal diffusion time scale by defining an equivalent Thiele modulus ϕ^*_k based on the average value

[3] The linear approximation gives good estimates of $g_{i,k}$ only at low precursor concentrations. Nevertheless, in the next sections it will be highlighted how the precursor concentration is indeed close to zero for most of the pulsing time.

of the reaction rate coefficient:

$$\phi_k^* = R_k \sqrt{\frac{\langle \nu_k' \rangle}{D_{i,k}}}, \begin{cases} k = c, \ P = 1.013 \text{ bar} \\ k = sa, \ P = 1 \text{ mbar} \end{cases} \tag{7.23}$$

The relevant time scale of the surface coverage dynamics is the saturation time τ_{sat}, which is

Precursor transport and reaction time scales [s]					
	1.013 bar	1 mbar		1.013 bar	1 mbar
τ_{em}	0.91	0.91	τ_b	0.42	0.42
τ_{int}	$5 \cdot 10^{-2}$	$2.6 \cdot 10^{-3}$	τ_{ga}	$9.34 \cdot 10^{-4}$	$9.25 \cdot 10^{-7}$
τ_c	$1.6 \cdot 10^{-3}$	$1.15 \cdot 10^{-5}$	τ_{sa}	$2.43 \cdot 10^{-5}$	$1.39 \cdot 10^{-5}$
τ_{rxn}	$2.5 \cdot 10^{-5}$	$5.7 \cdot 10^{-6}$	ϕ_k^*	8	1.56

Table 7.4: Time scales and Thiele modulus for the TMA half-reaction at 1.013 bar and 1 mbar, for a batch of 22 g of Degussa P-25 TiO_2 nanoparticles, estimated by using the parameters given in Table 7.5.

$S_{BET}[\frac{m^2}{g}]$	$\varrho_b[\frac{kg}{m^3}]$	$u_{mf}[\frac{cm}{s}]$	$u[\frac{cm}{s}]$	ϵ_{mf} [-]	H_0/d_t [-]
50	130	5[38]	7	0.5	1
d_t[cm]	H/H_0	M_{TiO_2} [g]	$T[K]$	d_b [cm]	ϑ_{OH}^0 [-]
6	1.7[38]	22.05	500	1	0.47

Table 7.5: Simulation parameters for ALD on nanoparticles

the time needed for the surface coverage to span over its whole range of values. For example, for the TMA half-reaction, τ_{sat} is the time needed for the methyl groups surface coverage ϑ_{Me} to go from its initial value, say $\vartheta_{Me} = 0$, to its maximum value $\vartheta_{Me} = 1$. However, τ_{sat} strongly depends on the precursor utilization efficiency, which, in turn, is a function of the operating parameters. Nevertheless, we can refer to the minimum saturation τ_{sat}^{min}, which is the saturation time assuming complete uptake of the precursor, estimated as:

$$\tau_{sat}^{min} = \frac{\left(\varrho_b S_{BET} n_{max}\right)\left[\left(H_0/d_t\right) d_t\right]}{u_0 C_{i,in}} \tag{7.24}$$

where ϱ_b is the bulk density of the nanopowder, S_{BET} is the Brunauer—Emmett—Teller (BET) surface area per unit mass of the particles, n_{max} is the maximum number of precursor molecules that can chemisorb onto the surface expressed in mol/m^2, u_0 is the superficial velocity at the inlet of the reactor and $C_{i,in}$ is the inlet precursor concentration. The minimum saturation time typically ranges from minutes to hours depending on the operating conditions and reactor scale. For example, for the TMA half-reaction on a small batch of Degussa P-25 titania nanoparticles (see Table 7.5 for the values of S_{BET}, ϱ_b, (H_0/d_t), d_t and u_0), by assuming the maximum surface concentration of aluminum atoms after saturation to be

4.8 nm^{-2} [51], the minimum saturation time ranges within the following values depending on the TMA partial pressure at the reactor inlet $P_{TMA,in}$:

$$\tau_{sat}^{min} \in [18\ s, 5\ \text{hours}] \text{ for } P_{TMA,in} \in [0.1, 100]\ \text{mbar} \tag{7.25}$$

Given the substrate properties ($\varrho_b S_{BET} n_{max}$) and the initial bed height H_0, the minimum saturation time can in principle be reduced by increasing either the superficial velocity or the inlet precursor concentration. However, the former has an upper limit set by powder elutriation issues [7] and the latter is often limited by the precursor delivery system. ALD precursors are typically liquid or solids which are fed to the FBR by either direct vaporization or through bubblers [6, 11], and in each case the inlet precursor concentration is limited by the precursor volatility and thermal stability.

Equation (7.24) suggests that the minimum saturation time can be decoupled from the scale of the reactor, and thereby the amount of material to be coated, by keeping the bed height fixed and increasing the reactor diameter. Once H_0 and u_0 are optimized to obtain proper fluidization of the nanopowder and $C_{i,in}$ is set by the precursor delivery system, the minimum saturation time does not depend on the reactor diameter d_t, which can be scaled up in order to process the desired amount of material ($\propto d_t^2$) without further increase in operating time.

It is worth noting that for ALD in FBRs on nanoparticles or other high-surface-area substrates, the minimum saturation time can be several orders of magnitude greater than the average reactor residence time. For instance, if we define the latter as:

$$\langle \tau \rangle = \left(\frac{1}{\tau_b} + \frac{1}{\tau_{em}} \right)^{-1} \left[\delta + (1-\delta)\, \epsilon_{mf} \right] = \frac{H\, \epsilon_{fb}}{u_0} \tag{7.26}$$

and by recalling Eq. (7.24), the minimum saturation time to the average reactor residence time ratio can be expressed as:

$$\frac{\tau_{sat}^{min}}{\langle \tau \rangle} = \frac{\varrho_b S_{BET} n_{max}}{C_{i,in}} \left(\frac{H}{H_0}\, \epsilon_{fb} \right)^{-1} \tag{7.27}$$

For a bubbling bed, the term in parenthesis is typically of the order of one, since $\epsilon_{fb} < 1$ and usually $H/H_0 \leq 2$ [15], whereas the ratio between the concentration of active sites in the bed and the inlet precursor concentration $\left(\varrho_b S_{BET} n_{max}\right) / C_{i,in}$ can be much greater than one. For example, for the parameters for Degussa P-25 titania nanoparticles from Table 7.5, the saturation time to gas residence time for the TMA half-reaction at atmospheric pressure ranges within the following values:

$$\tau_{sat}^{min} / \langle \tau \rangle \in \left[3 \cdot 10^5, 320 \right] \text{ for } P_{TMA,in} \in [0.1, 100]\ \text{mbar} \tag{7.28}$$

This implies that the number of precursor molecules entering the reactor is usually much smaller than the number of molecules that can chemisorb onto the particles surface for most of the pulsing time. This is an indication that in ALD on high-surface-area particles high precursor utilization efficiencies can indeed be achieved given the large number of possible

collisions between precursor molecules and active sites during most of the pulsing time. Furthermore, the decoupling between the reactor dynamics ($\langle\tau\rangle$) and the surface coverage dynamics (τ_{sat}^{min}) facilitates the control of the process.

Table 7.4 gives the values of the time scales and Thiele modulus characterizing the TMA half-reaction (analogous results are obtained for the H_2O half-reaction) at both atmospheric pressure and 1 mbar for a batch of 22 g of Degussa P-25 titania nanoparticles. In both cases, the average residence time in both the emulsion and bubble phase is from one to several orders of magnitude greater than the mass transfer and reaction time scales, notwithstanding the small batch of nanoparticles considered here. In particular, at atmospheric pressure the reaction is faster than the diffusion in the complex agglomerate level and in the emulsion phase the deposition process is likely to be limited by both external and internal mass transfer since:

$$\tau_{ga} \simeq \tau_c >> \tau_{sa} > \tau_{rxn}$$

On the other hand, at 1 mbar, the reaction time scale is comparable with the diffusion time scale in the simple agglomerates level, which, in turn is comparable with the diffusion time scale in the complex agglomerate level and both are about one order of magnitude greater than the time scale of the external mass transfer in the emulsion phase. Overall, all the mass transfer time scales are smaller at 1 mbar and the largest time scale in both cases is the time scale of the interphase mass transfer (for $d_b = 1$ cm).

Finally, the reaction is faster than the precursor transport for both pressures considered here, and the greater time scales related to the precursor transport are the residence times τ_{em} and τ_b, and thereby $\langle\tau\rangle$. As the $\langle\tau\rangle$ is much smaller than the minimum saturation time, as previously argued, both the surface coverage and the precursor concentration within the reactor will evolve in a quasi-steady state regime for most of the pulsing time. In particular, we expect three periods in each half-reaction: a short initial transient whose duration is proportional to $\langle\tau\rangle$, during which the precursor concentration in the reactor approaches a quasi-steady state concentration (~ 0); a subsequent quasi-steady state period, whose duration is of the order of magnitude of τ_{sat}^{min}, during which the surface coverage slowly increases; and a final transient starting in proximity of the surface saturation, when the reaction slows down considerably, during which the precursor concentration in the reactor approaches the inlet concentration in a period of time proportional to $\langle\tau\rangle$.

7.2.2. ALD on nano-porous micron-sized particles in FBRs

We now modify our model slightly to describe a closely related process i.e. ALD on micron-sized nano-porous particles in FBRs. Such substrates are usually high-surface area mesoporous media with average pore diameter in a typical range of 5-15 nm and internal porosity $\epsilon_p = 0.5 - 0.6$. The dynamic model can be readily applied to such particles by treating them as porous media characterized by the porosity ϵ_p, the average pore diameter λ_p and the effective diffusion coefficient $D_{i,p}$. The latter can be estimated by using Eq. (7.12), (7.13) or (7.14), depending on the diffusion regime. However, in this case, the internal structure of such particles allows us to simplify the model and obtain an analytical expression for the precursor utilization efficiency. The diffusion of precursor molecules within such particles is mostly driven by Knudsen diffusion, which given the pore size, results in an equivalent Thiele

modulus $\phi_p^* >> 1$, in both the TMA and H_2O half-reactions. As a result, in this type of substrates, the ALD reactions are likely to proceed along the particle radius in sharp reaction fronts [21] and the description of diffusion and reaction within the particles reduces to the solution of a Stephan problem. In particular, we tailor the shrinking core model [15, 32] to ALD on nano-porous micron-sized particles in FBRs. If we assume the time scale of the reaction front advancement to be much greater than the residence time in both emulsion and bubble phase, we can rewrite the mole balances for emulsion and bubble phase given in Table 7.1 in a quasi-steady regime fashion:

$$u_b \frac{\partial C_{i,b}}{\partial z} = K_{be}\left(C_{i,em} - C_{i,b}\right) \tag{7.29}$$

$$\begin{aligned} u_{mf}(1-\delta)(C_{i,in} - C_{i,em}) + \\ + K_{be}\delta \int_0^H \left(C_{i,b} - C_{i,em}\right) dz - \\ - K_{gp} \frac{6\left(1-\epsilon_{mf}\right)(1-\delta)H}{d_p} (C_{i,em} - C_{i,s}) = 0 \end{aligned} \tag{7.30}$$

whereas the mole balance at the particle scale, assuming the particles to be spherical, can be written as [15, 32]:

$$\frac{d}{dr}\left(r^2 \frac{dC_{i,p}}{dr}\right) = 0, \quad r_{rf} < r < R_p \tag{7.31}$$

$$B.C. = \begin{cases} C_{i,p} = 0, & r = r_{rf} \\ C_{i,p} = C_{i,s}, & r = R_p \end{cases} \tag{7.32}$$

where r_{rf} is the position of the reaction front ($0 < r_{rf} < R_p$) and $C_{i,s}$ is the precursor concentration at the outer surface of the particle. Eq. (7.31) can be solved analytically, so as to derive an expression for the molar flux at the reaction front:

$$J|_{r=r_{rf}} = \frac{D_{i,p} C_{i,s}}{r_{rf} - r_{rf}^2 / R_p} \tag{7.33}$$

where $D_{i,p}$ is the effective diffusion coefficient of the precursor in the particle. Therefore the amount of precursor consumed by the reaction at any given time can be written as:

$$J|_{r=r_{rf}} 4\pi r_{rf}^2 n_p = \frac{D_{i,p} C_{i,s}}{r_{rf} - r_{rf}^2 / R_p} 4\pi r_{rf}^2 \frac{S_p^{ext}}{4\pi R_p^2} = \frac{D_{i,p} C_i r_{rf}}{(R_p - r_{rf}) R_p} S_p^{ext} \tag{7.34}$$

where n_p is the number of particles and S_p^{ext} is the total external surface of the particles. Hence, the mole balance at the outer surface of the particles can be written as:

$$K_{gp}(C_{i,em} - C_{i,s}) = \frac{D_{i,p} C_{i,s} r_{rf}}{\left(R_p - r_{rf}\right) R_p} \tag{7.35}$$

The advance of the reaction front can be described through the active sites balance:

$$\frac{d}{dt}\left(V_1^p (S_p^{tot}/V_p) n_{max}\right) = 4\pi r_{rf}^2 J|_{r=r_{rf}} \tag{7.36}$$

where V_1^p is the volume of a single particle, (S_p^{tot}/V_p) the surface area per unit of volume of particle and n_{max} is again the maximum number of precursor molecules that can chemisorb on the particle surface expressed in mol/m^2.

Letting:

$$f = r_{rf}/R_p, \;\; \alpha = \frac{R_p^2 \tilde{u}}{3(1-\epsilon_0) H_0 D_{i,p}}, \;\; \beta = \frac{\tilde{u} R_p}{3(1-\epsilon_0) H_0 K_{gp}} \tag{7.37}$$

and

$$\tilde{t} = \frac{t}{\tau_{sat}^{min}} \tag{7.38}$$

where:

$$\tilde{u} = u_{mf}(1-\delta) + u_b \delta \left[1 - \exp(-HK_{be}/u_b)\right] \tag{7.39}$$

and ϵ_0 is the initial bed voidage. Equations (7.29) and (7.30) can be solved analytically to express the concentration of the precursor in both phases as a function of the reaction front f as:

$$C_{i,b} = C_{i,em} + (C_{i,in} - C_{i,em})\left[1 - \exp(-HK_{be}/u_b)\right] \tag{7.40}$$

$$C_{i,em} = \frac{C_{i,in}}{1+\beta}\left[\beta + \frac{\alpha(1-f)}{f(1+\beta)+\alpha(1-f)}\right] \tag{7.41}$$

whereas the evolution of the reaction front f as a function of time is derived by integrating Eq. (7.36):

$$\tilde{t} = \frac{u_0}{\tilde{u}}\left[(1+\beta-\alpha)(1-f^3) + \frac{3}{2}\alpha(1-f^2)\right] \tag{7.42}$$

Since the saturation of the surface corresponds to $f = 0$ the saturation time can be derived from Eq. (7.42) as:

$$\tau_{sat} = \tau_{min}^{sat}\left[\frac{u_0}{\tilde{u}} + \frac{R_p^2 u_0}{6(1-\epsilon_0) H_0 D_{i,p}} + \frac{u_0 R_p}{3(1-\epsilon_0) H_0 K_{gp}}\right] \tag{7.43}$$

where:

$$\frac{u_0}{\tilde{u}} = \frac{1}{1 - \frac{u_b \delta}{u_0}\exp(-HK_{be}/u_b)} \tag{7.44}$$

Therefore, if we define the efficiency of the process η as the deviation of the saturation time from its minimum value we arrive to the analytical expression:

$$\eta = \frac{1}{\frac{1}{1-\frac{u_b \delta}{u_0}\exp(-HK_{be}/u_b)} + \frac{u_0 R_p}{3(1-\epsilon_0) H_0 K_{gp}} + \frac{u_0 R_p^2}{6(1-\epsilon_0) H_0 D_{i,p}}} \tag{7.45}$$

The three terms in the denominator of Eq. (7.45) arise from the mass transfer limitations at the bubble, emulsion and particle scale respectively. The first term in the denominator is usually greater than one and tends to one for tall reactors or very fast mass transfer exchange rates between bubble and emulsion phase. The last two terms tend to zero when the residence time in the reactor is greater than the time scale of the emulsion-gas-to-particle mass transfer and internal diffusion respectively.

7.3. Simulation results and discussion

7.3.1. ALD on nanoparticles in FBRs

In this section we present and discuss the simulation results obtained for ALD on nanoparticles in FBRs. The mathematical model, consisting of the equations given in Table 7.1, 7.2 and 7.3, has been reduced to a system of ordinary differential equations via finite difference schemes and thus solved numerically in Matlab.

Several simulations have been carried out for different reactor sizes and, in particular, for lab-scale reactors, where the lowest efficiencies are expected, given the short residence times experienced by the precursors. Table 7.5 gives the parameters used for the simulation of both TMA and H_2O half-reactions for a small batch of TiO_2 nanoparticles.

A sensitivity analysis suggests that the superficial velocity in the emulsion phase, and thus the minimum fluidization velocity u_{mf}, has virtually no effect on the precursor uptake in the emulsion phase and the surface coverage dynamics. However, u_{mf} does have an influence on the overall dynamics and thus on the precursor utilization efficiency, by affecting the precursor transport time scales in the bubble phase τ_b and τ_{int}. Furthermore, to the best of our knowledge the minimum fluidization conditions of Degussa P-25 TiO_2 nanopowder at 1 mbar without assisting methods have never been reported. In light of these considerations, we will first show the simulation results obtained for the atmospheric pressure case, for which the minimum fluidization velocity is known, then discuss the surface coverage dynamics at reduced pressure assuming the same fluidization conditions and finally present a detailed discussion on the effect of pressure and minimum fluidization velocity on the precursor utilization efficiency.

We will now discuss the simulated residual gas analysis (RGA) for the TMA and H_2O half-reactions, i.e. the evolution in time of the outlet concentration of TMA, H_2O and CH_4 as well as the cumulative amount of produced CH_4 normalized to the amount of converted precursor (see Fig. 7.1). For example, for the TMA pulse the nondimensional cumulative CH_4 is defined as:

$$\int_0^{\tau_{sat}} \frac{C_{CH_4,out}}{C_{TMA,in} - C_{TMA,out}} dt \tag{7.46}$$

whereas the outlet concentration $C_{i,out}$ is defined as weighted average of the concentration in each of the phases:

$$C_{i,out} = \frac{u_{mf}(1-\delta) C_{i,em} + u_b \delta C_{i,b}|_{z=H}}{u_0} \tag{7.47}$$

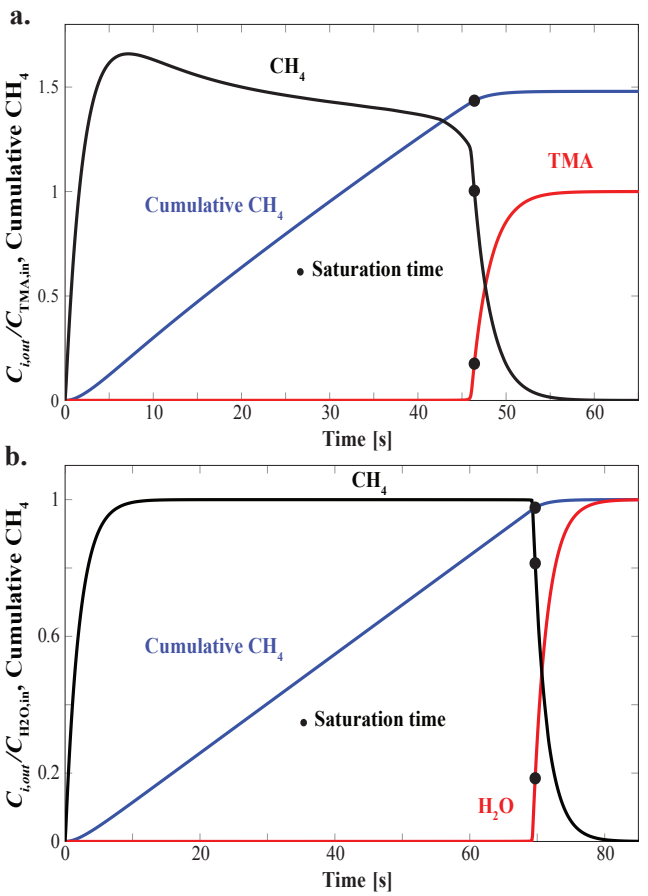

Figure 7.1: Simulated RGAs for the TMA (a.) and H_2O (b.) half-reaction at atmospheric pressure.

In most cases, e.g. for the parameters set given in Table 7.5, the simulated RGAs exhibit the same behavior at both atmospheric pressure and 1 mbar (not shown). Therefore, we will first describe the RGA for the atmospheric pressure case and then discuss the differences between the two pressure cases with emphasis on the precursor utilization efficiency.

According to the simulated RGAs (see Fig. 7.1), the outlet concentration of the reaction byproduct (CH_4) starts increasing as soon as the precursors (TMA or H_2O) are fed into the reactor, whereas the outlet precursor concentration stays close to zero for most of the pulsing time. The shape of the outlet CH_4 concentration curve reflects the three distinct periods of the precursor pulse anticipated in section 2.1.4, with two transients: one at the beginning of the pulse and the other in proximity of the surface saturation, both of the duration of a few $\langle\tau\rangle$; and a plateau region which spans over a time close to τ_{sat}^{min}. The normalized cumulative CH_4 curve follows the same three regions behavior and in this case the quasi-steady state region is characterized by an approximately constant slope of the curve for a period of the

order of magnitude of τ_{sat}^{min}. The final value of such curve gives information about surface state after each half-reaction. For instance, after the TMA half-reaction this value is close to 1.5, that is three methyl groups are released as methane for every two TMA molecules that chemisorb onto the surface, which is consistent with an aluminum to methyl groups ratio on the surface of 2/3 reported in literature for temperatures around 500 K [46, 47]. The different stoichiometry in the two half-reactions results in different CH_4 to precursor ratios during the quasi-steady-state period. On the one hand, since the amount of methane released during the TMA half-reaction is assumed to depend on the surface hydroxyl groups concentration, the outlet methane to inlet TMA ratio varies slightly during the quasi-steady state period according to the current surface state. On the other one hand, since we have assumed that each water molecule reacts with one methyl group with subsequent release of one methane molecule the outlet methane to inlet H_2O ratio is equal to 1 for the whole quasi-steady state period of the H_2O half-reaction. Finally, the fluidized bed of nanoparticles agglomerates acts as an adsorbing column notwithstanding the backmixing in the emulsion phase and the relatively short gas residence time of the simulated lab-scale FBR. In analogy with an adsorption column, the outlet precursor concentration resembles a breakthrough curve, characterized by a sudden breakthrough right before the saturation time. Experimental RGAs reported by King et al. [1, 6] also show a nearly linear curve for the cumulative CH_4, and a steep breakthrough of the TMA concentration.

The main differences between the two pressure cases lie in the sensitivity of the precursor utilization efficiency to the residence time in the bubble phase τ_b and the way the primary particles within the nanoparticle agglomerates are exposed to the precursors depending on their radial position. Figure 7.2a shows the evolution in time of the methyl groups surface coverage profiles within the agglomerates at different times for atmospheric pressure. The advance of the reaction within the agglomerates is limited by the diffusion in the complex agglomerate level. The concentration profiles (not shown) are congruent with the surface coverage profiles, which slowly advance towards the center of the agglomerates with the pulsing time. For this reason, if the ALD process is operated in a non-saturating regime, each cycle would result in an inhomogeneous product. Of course, this analysis assumes that the particles that make up the agglomerates are themselves not mobile. If, however, the time scale of the break-up and rearrangement of the agglomerates is smaller than the diffusion time, such rearrangement will help to suppress concentration gradients and level out the surface coverage within the agglomerates. Finally, notwithstanding the diffusion limitation at the complex agglomerate level, the molar flux to the agglomerates is still high enough to consume virtually all the precursor in the emulsion phase before the reaction front reaches the center of the agglomerate.

At 1 mbar the diffusion in the complex agglomerate level acts in concert with the diffusion in the simple agglomerate level. Since both diffusion processes are relatively fast, the concentration profiles in the complex agglomerate level are flat. As a result, the surface coverage in the simple agglomerates located in proximity of the outer surface and the center of the complex agglomerates are almost equal. In turn, the surface coverage within the simple agglomerates increases almost at the same rate regardless of the simple agglomerate radius (see Fig. 7.2b). Therefore, at 1 mbar the diffusion within the nanoparticle agglomerates

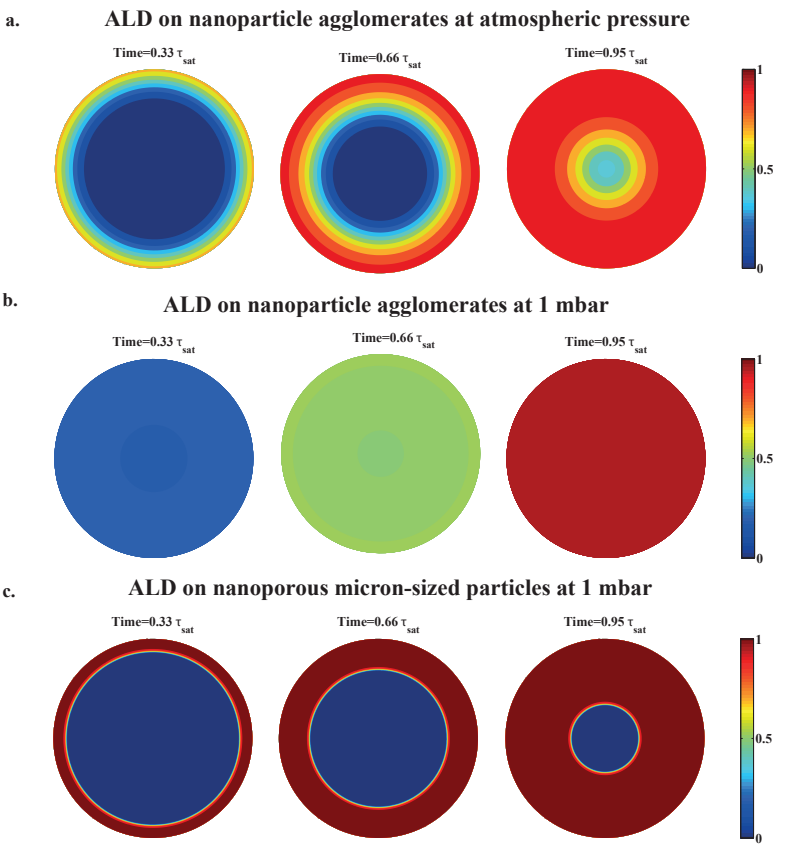

Figure 7.2: Surface coverage of methyl groups depicted in a 2D projection at different times for ALD on a nanoparticle agglomerate at atmospheric pressure (a.) and 1 mbar (b.), and for ALD on a nanoporous micron-sized particle at 1 mbar (c.).

does not limit the deposition process, and the breakthrough occurs when the adsorption reaction slows down in correspondence of an almost saturated surface.

For both pressures, the transport at the nanoparticle agglomerates scale has little to no influence on the precursor utilization efficiency, since the residence time in the emulsion phase τ_{em} is several orders of magnitude greater than the slowest transport time scale in the emulsion phase (see Table 7.4), even in the lab-scale reactor simulated here. This is also true for other types of nanoparticles which undergo a similar multi-level agglomeration, characterized by minimum fluidization velocities of the order of few centimeters per second. For this reason, fast ALD kinetics translate into a precursor concentration in the emulsion phase close to zero at a high surface conversions. If little to no precursor losses are expected from the emulsion phase, unreacted precursor molecules might still escape the reactor from the bubble phase. The residence time in the bubble phase τ_b can indeed be comparable to the inter-phase mass transfer time scale τ_{int} depending on the average properties of the

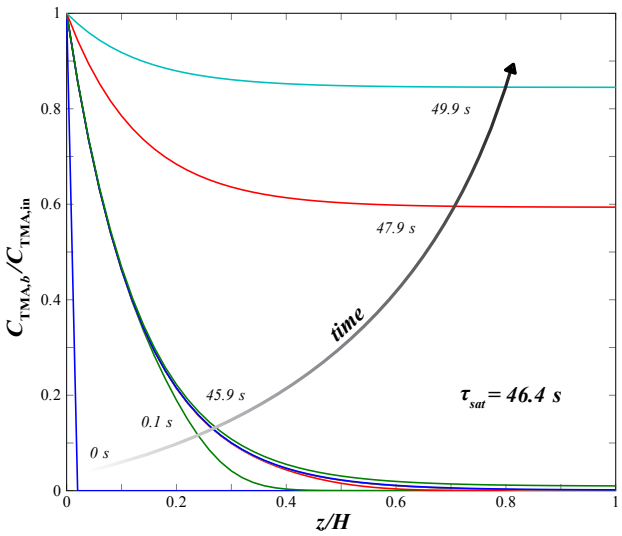

Figure 7.3: Normalized TMA concentration in the bubble phase as a function of the normalized reactor height at different times at atmospheric pressure. From left to right t=0 s, 0.1 s, 0.2 s, 0.9 s, 9.9 s, 19.9 s, 43.9 s, 44.9 s, 45.9 s, 47.9 s, 49.9 s (τ_{sat} = 46.4 s).

bubble phase, the height of the reactor, the superficial gas velocity and the operating pressure. Figure 7.3 shows the normalized TMA concentration in the bubble phase as a function of the reactor height, at different times, obtained for the case at atmospheric pressure. After a rapid transient, in this case of the order of 1 s, at the beginning of the pulse, the TMA concentration in the bubble phase approaches a quasi-steady state regime, in which the concentration remains almost constant till the particles surface reaches saturation at 46.4 s. During the quasi-steady state regime, the TMA concentration in the bubble phase decays exponentially along the reactor height. In this simulation, a reactor height of about 10 cm and an average bubble diameter of 1 cm result in a outlet TMA bubble concentration close to zero. Nevertheless, a shallower reactor bed or a larger average bubble diameter would result in the bypassing of part of the TMA feed rate, thus reducing the process efficiency. Hence, it is of interest to identify a set of operating parameters which minimizes precursor losses arising from insufficient residence time in the bubble phase. This can be done analytically by simplifying the model for the quasi-steady state period. As already discussed, during such period we can assume:

$$C_{TMA,em} \sim 0 \tag{7.48}$$

and therefore the mole balance for the bubble phase can be rewritten as:

$$u_b \frac{\partial C_{TMA,b}}{\partial z} = -K_{be} C_{TMA,b}, \quad \tau_b << t < \tau_{sat} \tag{7.49}$$

Hence, by integrating Eq. (7.49) and recalling Eq. (7.47) we obtain the TMA outlet concentration as:

$$C_{TMA,out} = \frac{u_b \delta}{u} C_{TMA,in} \exp\left[-HK_{be}/u_b\right] \tag{7.50}$$

Therefore the precursor conversion or precursor utilization efficiency during the quasi-steady state regime can be estimated as:

$$\eta = \frac{C_{i,in} - C_{i,out}}{C_{i,in}} = 1 - \frac{u_b \delta}{u} \exp\left[-HK_{be}/u_b\right] \tag{7.51}$$

It is worth noting that we could have come to the same expression by neglecting the terms relative to the diffusion limitations in the emulsion phase (α and β) in Eq. (7.45) derived for ALD on micron-sized nano-porous particles. Equation (7.51) could be used for conservative designs of both lab-scale and large-scale reactors, provided that the properties of the system (e.g. u_{mf}, d_b) are known. For example, by setting $\eta^* = 0.9999$, one can estimate the optimum reactor height H^* as a function of the the system properties:

$$H^* = \frac{u_b}{K_{be}} \ln\left[\frac{u_b \delta}{u_0(1-\eta^*)}\right] \tag{7.52}$$

Figure 7.4 shows the value of the estimated required bed height for the TMA half-reaction

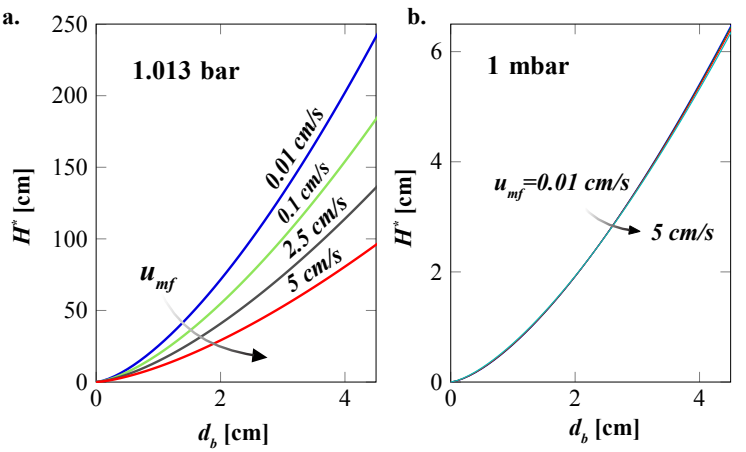

Figure 7.4: Estimated required bed height H^* to obtain the efficiency $\eta^* = 0.9999$ as a function of the average bubble diameter, for several minimum fluidization velocities at atmospheric pressure (a.) and 1 mbar (b.); $u_0 = 1.5u_{mf}$.

at both atmospheric pressure and 1 mbar as a function of the bubble diameter and for several minimum fluidization velocities. At atmospheric pressure, H^* increases with the average bubble diameter and decreases with the minimum fluidization velocity. On the other hand, at low pressure (P $\leqslant$ 1 mbar), the value of the minimum fluidization velocity has virtually no effect on H^*. In fact, the interphase mass transfer K_{be} defined in Table 7.1, is given by the superposition of a convective term, proportional to the minimum fluidization velocity, and a diffusive term, which is a function of the diffusion coefficient D_i. At atmospheric pressure, the gas diffusion is relatively slow and the interphase mass transfer occurs mainly through convection, whereas at low pressure the diffusion process is relatively fast and the diffusive

contribution dominates. As a result, at 1 mbar, a bubble with an average diameter of 4.5 cm would require a bed height of only 6.5 cm to be nearly depleted from TMA, whereas at atmospheric pressure, the same average bubble diameter would require an height of about 100 cm, for a minimum fluidization velocity of 5 cm/s. It must be kept in mind that these are conservative estimations based on the assumption of solid-free bubbles. Nevertheless, provided that the ALD reactions are not the limiting step, these figures suggest how, at low pressures, the bubbles are unlikely to play a role in determining the efficiency of the process, whereas the bypassing of precursor molecules through the bubble phase could be a concern in ALD at atmospheric pressure, especially for systems characterized by low minimum fluidization velocities.

7.3.2. ALD on micron-sized nano-porous particles

We now discuss the simulation results obtained for a small batch of micron-sized nanoporous γ-alumina particles (see Table 7.1). Figure 7.2c shows the evolution in time of the

$S_{BET}[\frac{m^2}{g}]$	$\varrho_b[\frac{kg}{m^3}]$	$d_p[\mu m]$	$u_{mf}[\frac{cm}{s}]$	$u[\frac{cm}{s}]$	$M_{Al_2O_3}$ [g]
150	800	120	5	10	1.3
$T[K]$	λ_p [nm]	ϵ_p [-]	H_0/d_t [-]	d_t[cm]	H/H_0 [-]
500	7	0.6	2	1	1.7

Table 7.1: Simulation parameters for ALD on micron-sized nanoporous γ-alumina particles.

methyl groups surface coverage during the TMA half-reaction within the particles obtained with the dynamic model at 1 mbar. In this case, as opposed to ALD on nanoparticles, the reaction proceeds towards the center of the particles in sharp reaction fronts and the deposition process is limited by the inter-particle diffusion. Such characteristic diffusion-limited regime arising from fast ALD kinetics could be exploited to fabricate eggs-hell catalysts by modulating the pulsing time and thereby the deposition depth.

Figure 7.5 shows how, for the simulated lab-scale reactor, the TMA breakthrough is seen already at around 50% of the saturation time as opposed to ALD on nanoparticles. In this case, the mass transfer limitations at the emulsion, bubble and particle scale can all affect considerably the precursor utilization efficiency. The predictions of the dynamic model are well approximated by the quasi-steady state model before saturation (see Fig. 7.5), and we can use Eq. (7.45) to estimate the effect of the precursor transport on the precursor utilization efficiency given the system properties. The same arguments put forward for the effect of bubbles on the precursor utilization efficiency for the nanoparticles case hold for micron-sized particles, with the only difference being the extra contribution due to the mass transfer limitations at the emulsion and particle scale. In particular, the mass transfer limitations at the particle scale can drastically decrease the efficiency for large particles $d_p > 300\ \mu$m and low effective diffusion coefficients $D_{i,p}$ (see Fig. 7.6 a.). Equation (7.45) can be also used to estimate the reactor height required to obtain the desired efficiency. For example, Fig. 7.6 b. shows how the efficiency scales with the reactor height for different average bubble diameters in FBRs of micron-sized particle of average radius $R_p = 200\ \mu$m and effective

diffusion coefficient $D_{i,p} = 5 \cdot 10^{-7}$ ($u = 1.5\ u_{mf}$, $u_{mf} = 5$ cm/s). Finally, precursor utilization efficiencies close to 100% for ALD on micron-sized nano-porous particles in FBRs are only possible if the reactor height is scaled by taking into account parameters such as the particle diameter, pore size, operating pressure and average bubble properties.

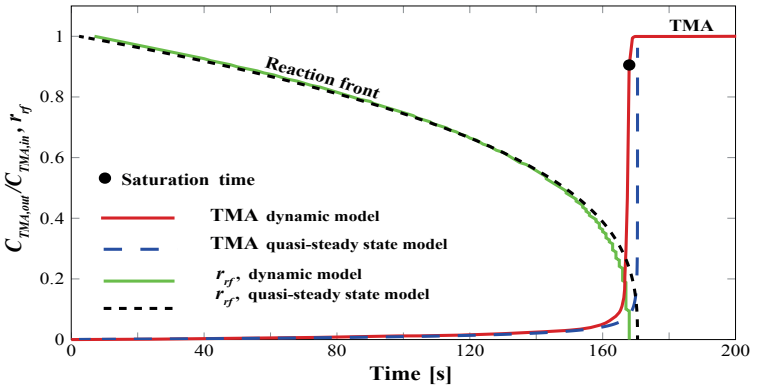

Figure 7.5: TMA breakthrough curve and normalized reaction front, calculated with both, the dynamic model and the quasi-steady state model, for ALD on nanoporous micron-sized γ-alumina particles at 1 mbar (for the dynamic model, the normalized reaction front position $f = r_{rf}/R_p$ is defined has the particle radius at which $\vartheta_{Me} = 0.5$).

7.3.3. Final remarks

The model presented here can be applied to other ALD reaction systems by retaining the precursor transport description and using an appropriate description of the ALD reaction kinetics and surface coverage dynamics. In our analysis, by using the TMA/H_2O ALD reaction system as a reference, we were able to examine a limiting case for the impact of the precursor transport on the precursor utilization efficiency. Other ALD reaction systems are likely to have slower kinetics and one can conclude that the precursor transport limitations will be even milder than the ones discussed here. Therefore, the precursor utilization efficiency in ALD in FBRs is likely to depend more on the ALD kinetics rather than on the gas-solid contact quality. Nevertheless, even with slower kinetics, ALD in FBRs on high-surface-area substrates is a forgiving process and the influence of ALD kinetics is expected to be dampened by the large minimum saturation time to average residence time ratio, as already pointed out in section 2.1.4.

7.4. Conclusions

In summary, we have developed a dynamic reactor model capable of describing the ALD dynamics for the TMA/H_2O system on nanoparticles in fluidized bed reactors at both reduced and atmoshperic pressure. Furthermore, an analytical model for ALD on nanoporous particles is derived. In light of the results obtained with these models we conclude that:

- At reduced pressure (~1 mbar), the multi-fractal structure of the nanoparticle agglomerates gives negligible resistance to the diffusion process, and provided that the ALD

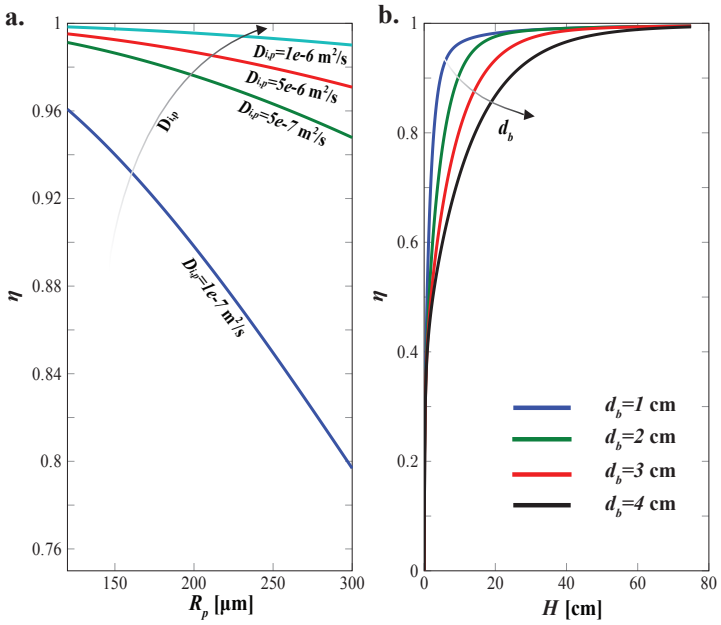

Figure 7.6: a. Efficiency as a function of R_p and $D_{i,p}$ at constant reactor height (H=1.5 H_0, H_0=10 cm). b. efficiency as a function of the reactor height for different average bubble diameters for $R_p = 200\,\mu$m and $D_{i,p} = 5 \cdot 10^{-7}$ m^2/s. In both cases P=1.013 bar and $u_0 = 1.5\ u_{mf}$, where $u_{mf} = 5$ cm/s.

7

reaction kinetics is relatively fast, ALD on nanoparticles in FBRs can be carried out with complete uptake of precursors at high surface area conversions. Furthermore, the possible presence of bubbles has little to no influence on the overall process efficiency. As a result this process is relatively insensitive to the reactor scale.

- At atmospheric conditions, the coating process is limited by the diffusion in the complex agglomerate level. For this reason, non-saturating regimes would result in an inhomogeneous product if the time scale of the break-up and rearrangement of nanoparticle agglomerates is greater than the saturation time. Nevertheless, provided that the ALD reaction is not the limiting step, the molar flux to the agglomerates is high enough to reduce the precursor concentration in the emulsion phase to zero, even at short gas residence times. In this case, the bubbles do have an influence on the process efficiency and the reactor design must take into account the effect of the bubble size and reactor height on the efficiency.

- ALD on nanoporous micron-sized particles in FBRs is limited by the inter-particle diffusion and the coating penetration depth can be tuned by modulating the pulsing time. At small scales this process has lower efficiency compared to ALD on nanoparticles in FBRs. Nevertheless, complete uptake of precursors at high surface area conversions can be easily achieved in larger reactors taking into account the mass

transfer limitations at the emulsion, bubble and particle scale.

Notation

C_i	Concentration of the i-th precursor	$[\mathrm{mol\,m^{-3}}]$
$C_{i,b}$	Concentration of the i-th chemical species in the bubbles	$[\mathrm{mol\,m^{-3}}]$
$C_{i,em}$	Concentration of the i-th chemical species in the emulsion	$[\mathrm{mol\,m^{-3}}]$
$C_{i,in}$	Inlet concentration of the i-th chemical species	$[\mathrm{mol\,m^{-3}}]$
$C_{i,out}$	Outlet concentration of the i-th chemical species	$[\mathrm{mol\,m^{-3}}]$
$C_{i,p}$	Concentration of the i-th chemical species in the particles	$[\mathrm{mol\,m^{-3}}]$
$C_{i,s}$	Concentration of the i-th chemical species at the outer surface of the nanoparticle agglomerates	$[\mathrm{mol\,m^{-3}}]$
D_i	Diffusion coefficient of the i-th chemical species	$[\mathrm{m^2\,s^{-1}}]$
$D_{f,j}$	Fractal dimension of the j-th level of the multi-level fractal structure of nanoparticle agglomerates	[-]
$D_{i,K}$	Knudsen diffusion coefficient of the i-th	$[\mathrm{m^2\,s^{-1}}]$
$D_{i,k}$	Effective diffusion coefficient of the i-th chemical species in the k-th level	$[\mathrm{m^2\,s^{-1}}]$
$D_{i,p}$	Effective diffusion coefficient of the i-th chemical species in the particles	$[\mathrm{m^2\,s^{-1}}]$
H	Reactor height	[m]
H^*	Required reactor height to obtain the desired efficiency	[m]
H_0	Initial reactor height	[m]
J	Molar flux	$[\mathrm{mol\,s^{-1}\,m^{-2}}]$
K_{be}	interphase mass transfer coefficient	$[\mathrm{s^{-1}}]$
K_{ga}	Emulsion-gas-to-agglomerates mass transfer coefficient	$[\mathrm{m\,s^{-1}}]$
K_{gp}	Emulsion gas to particles mass transfer coefficient	$[\mathrm{m\,s^{-1}}]$
$\mathcal{M}_i$	Molecular mass of the i-th chemical species	[kg]
P	Absolute pressure	[Pa]
$P_{i,in}$	Inlet partial pressure of the i-th precursor	[Pa]
R_p	Average particle radius	[m]
R_c	Average radius of the complex agglomerates	[m]
R_{sa}	Average radius of the simple agglomerates	[m]
S_p^{ext}	External particle surface area	$[\mathrm{m^2}]$
S_p^{tot}	Total particle surface area	$[\mathrm{m^2}]$
S_{BET}	Brunauer—Emmett—Teller (BET) surface area	$[\mathrm{m^2\,kg^{-1}}]$
T	Temperature	[K]
V	Reactor volume	$[\mathrm{m^3}]$
V_p	Particle volume	$[\mathrm{m^3}]$

d_j	Average diameter of the of the j-th level of the multi-level fractal structure of nanoparticle agglomerates	[-]
d_p	Particle diameter	[m]
d_t	Reactor diameter	[m]
d_{ag}	Average nanoparticles agglomerates diameter	[m]
d_b	Average bubble diameter	[m]
f	Nondimensional position of the reaction front	[-]
$\tilde{g}_{i,k}$	Linearised generation term with respect to the precursor concentration C_i at the k-th level of the multi-level fractal structure of nanoparticle agglomerates	$[\mathrm{mol\,s^{-1}}]$
g_i	Generation term of the i-th chemical species	$[\mathrm{mol\,s^{-1}}]$
k_b	Boltzmann constant	$[\mathrm{m^2\,kg\,s^{-2}K^{-1}}]$
k_j	Prefactor of the scaling law of density of the j-th level of the multi-level fractal structure of nanoparticle agglomerates	[-]
l	Molecules mean free path	[m]
n_p	Number of particles	[-]
n_{max}	Maximum number of precursor molecules that can be chemisorb per unit area of the particle surface	$[\mathrm{m^{-2}}]$
r	Radial coordinate	[m]
r_c	Radial coordinate at the complex agglomerate scale	[m]
r_{rf}	Position of the reaction front	[m]
r_{sa}	Radial coordinate at the simple agglomerate scale	[m]
t	Time	[s]
$\tilde{u}$	Equivalent superficial velocity that takes into account the gas flowing through the emulsion phase and the gas exchanged between emulsion and bubble phase	$[\mathrm{m\,s^{-1}}]$
u_0	Inlet superficial gas velocity	$[\mathrm{m\,s^{-1}}]$
u_b	Average bubble rising velocity	$[\mathrm{m\,s^{-1}}]$
u_{mf}	Minimum superficial gas velocity	$[\mathrm{m\,s^{-1}}]$
z	Axial coordinate parallel to the reactor height	[m]

Greek symbols

α	Nondimensional number relative to the diffusion limitations at the particle scale	[-]
β	Nondimensional number relative to the diffusion limitations at the emulsion scale	[-]
δ	Volume fraction of the fluidized bed occupied by the bubble phase	[-]
ϵ_c	Total porosity of the nanoparticle agglomerates	[-]
ϵ_i	Total porosity of the i-th level of the multi-level fractal structure of nanoparticle agglomerates	[-]
ϵ_c	Porosity of the complex agglomerate level	[-]
ϵ_{fb}	Average voidage of the fluidized bed	[-]
$\epsilon_{i,k}$	Effective porosity of the i-th level with respect to the k-th level of the multi-level fractal structure of nanoparticle agglomerates	[-]

ϵ_{mf}	Fluidized bed voidage in the minimum fluidization conditions	[-]
ϵ_{sa}	Porosity of the simple agglomerate level	[-]
η	Precursor utilization efficiency	[-]
λ	Average pore size	[m]
$\langle \nu'_k \rangle$	Average ALD reaction rate coefficient at the k-th level of the multi-level fractal structure of the nanoparticle agglomerates	[s^{-1}]
$\langle \tau \rangle$	Average reactor residence time	[s]
ν	ALD reaction rate	[$nm^{-2}\,s^{-1}$]
ϕ^*_k	Equivalent Thiele modulus	[-]
ϱ_j	Density of the j-th level of the multi-level fractal structure of nanoparticle agglomerates	[$kg\,m^{-3}$]
σ	Collision diameter	[m]
τ_k	Tortuosity of the k-th level	[-]
τ_b	Residence time in the bubble phase	[s]
τ_c	Diffusion time scale in the complex agglomerate level	[s]
τ_{em}	Average residence time in the emulsion phase	[s]
τ_{ga}	Emulsion gas to nanoparticle agglomerate mass transfer time scale	[s]
τ_{int}	Time scale of the interphase mass transfer	[s]
τ_{rxn}	ALD reaction time scale	[s]
τ_{sat}	Saturation time	[s]
τ_{sat}^{min}	Minimum saturation time (complete uptake of the precursor)	[s]
τ_{sa}	Diffusion time scale at simple agglomerate level	[s]
ϑ_{Me}	Surface coverage of methyl groups	[-]
ϑ_{OH}	Surface coverage of hydroxyl groups	[-]
ϑ_O	Surface coverage of oxygen groups	[-]

Dimensionless numbers

Kn	Knudsen number
Re	Reynolds number
Sc	Schmidt number
Sh	Sherwood number

References

[1] D. M. King, X. Liang, and A. W. Weimer, *Functionalization of fine particles using atomic and molecular layer deposition,* Powder Technology 221 (2012) (2012).

[2] J. R. van Ommen, C. U. Yurteri, N. Ellis, and E. M. Kelder, *Scalable gas-phase processes to create nanostructured particles,* Particuology 8, 572 (2010).

[3] A. Goulas and J. van Ommen, *Scalable production of nanostructured particles using atomic layer deposition,* KONA Powder and Particle Journal 31, 234 (2014).

[4] D. Longrie, D. Deduytsche, and C. Detavernier, *Reactor concepts for atomic layer deposition on agitated particles: A review,* Journal of Vacuum Science & Technology A 32 (2014).

[5] S. M. George, *Atomic Layer Deposition: An Overview,* Chemical Reviews 110 (2010).

[6] D. M. King, J. A. Spencer II, X. Liang, L. F. Hakim, and A. W. Weimer, *Atomic layer deposition on particles using a fluidized bed reactor with in situ mass spectrometry,* Surface and Coatings Technology 201, 9163 (2007).

[7] J. R. Ommen, J. M. Valverde, and R. Pfeffer, *Fluidization of nanopowders: a review,* Springer Netherlands , 1 (2012).

[8] X. Liang, Y. Zhou, J. Li, and A. W. Weimer, *Reaction mechanism studies for platinum nanoparticle growth by atomic layer deposition,* Journal of Nanoparticle Research 13, 3781 (2011).

[9] J. Li, X. Liang, D. M. King, Y.-B. Jiang, and A. W. Weimer, *Highly dispersed Pt nanoparticle catalyst prepared by atomic layer deposition,* Applied Catalysis B: Environmental 97, 220 (2010).

[10] A. Goulas and J. R. van Ommen, *Atomic Layer Deposition of Platinum Clusters on Titania Nanoparticles at Atmospheric Pressure,* Journal of Materials Chemistry 15, 4647–4650 (2013).

[11] R. Beetstra, U. Lafont, J. Nijenhuis, E. Kelder, and J. R. van Ommen, *Atmospheric pressure process for coating particles using atomic layer deposition,* Chemical Vapor Deposition 15, 227–233 (2009).

[12] Y. Zhou, D. M. King, X. Liang, J. Li, and A. W. Weimer, *Optimal preparation of Pt/TiO2 photocatalysts using atomic layer deposition,* Applied Catalysis B: Environmental 101, 54 (2010).

[13] R. L. Puurunen, *Surface chemistry of atomic layer deposition: A case study for the trimethylaluminum/water process,* Journal of Applied Physics 97 (2005) (2005).

[14] V. Miikkulainen, M. Leskelä, M. Ritala, and R. L. Puurunen, *Crystallinity of inorganic films grown by atomic layer deposition: Overview and general trends,* Journal of Applied Physics 113, 021301 (2013).

[15] D. Kunii and O. Levenspiel, *Fluidization Engineering* (Butterworth-Heinemann, 1991).

[16] J. Shabanian, R. Jafari, and J. Chaouki, *Fluidization of ultrafine powders,* International Review of Chemical Engineering 4, 16–50 (2012).

[17] W. Yao, G. Guangsheng, W. Fei, and W. Jun, *Fluidization and agglomerate structure of SiO2 nanoparticles,* Powder Technology 124, 152 (2002).

[18] C. Zhu, Q. Yu, R. N. Dave, and R. Pfeffer, *Gas fluidization characteristics of nanoparticle agglomerates,* AIChE Journal 51, 426 (2005).

[19] S. Morooka, K. Kusakabe, A. Kobata, and Y. Kato, *Fluidization state of ultrafine powders,* J. Chem. Eng. J. 21, 41 (1988).

[20] J. W. Elam, D. Routkevitch, P. P. Mardilovich, and S. M. George, *Conformal Coating on Ultrahigh-Aspect-Ratio Nanopores of Anodic Alumina by Atomic Layer Deposition,* Chemistry of Materials 15, 3507 (2003).

[21] R. Gordon, D. Hausmann, E. Kim, and J. Shepard, *A Kinetic Model for Step Coverage by Atomic Layer Deposition in Narrow Holes or Trenches,* Chemical Vapor Deposition 9, 73 (2003).

[22] H.-Y. Lee, C. J. An, S. J. Piao, D. Y. Ahn, M.-T. Kim, and Y.-S. Min, *Shrinking Core Model for Knudsen Diffusion-Limited Atomic Layer Deposition on a Nanoporous Monolith with an Ultrahigh Aspect Ratio,* The Journal of Physical Chemistry C 114, 18601 (2010).

[23] P. Poodt, J. van Lieshout, A. Illiberi, R. Knaapen, F. Roozeboom, and A. van Asten, *On the kinetics of spatial atomic layer deposition,* Journal of Vacuum Science & Technology A 31 (2013).

[24] L. de Martín, W. G. Bouwman, and J. R. van Ommen, *Multidimensional Nature of Fluidized Nanoparticle Agglomerates,* Langmuir 30, 12696 (2014).

[25] L. de Martín, A. Fabre, and J. R. van Ommen, *The fractal scaling of fluidized nanoparticle agglomerates,* Chemical Engineering Science 112, 79 (2014).

[26] C. D. Travis and R. A. Adomaitis, *Modeling ALD Surface Reaction and Process Dynamics using Absolute Reaction Rate Theory,* Chemical Vapor Deposition 19, 4 (2013).

[27] C. D. Travis and R. A. Adomaitis, *Dynamic Modeling for the Design and Cyclic Operation of an Atomic Layer Deposition (ALD) Reactor,* Processes 1, 128 (2013).

[28] C. D. Travis and R. A. Adomaitis, *Modeling alumina atomic layer deposition reaction kinetics during the trimethylaluminum exposure,* Theoretical Chemistry Accounts 133, 1 (2013).

[29] A. Yanguas-Gil and J. W. Elam, *Simple model for atomic layer deposition precursor reaction and transport in a viscous-flow tubular reactor,* Journal of Vacuum Science & Technology A 30 (2012).

[30] A. Yanguas-Gil and J. W. Elam, *Self-Limited Reaction-Diffusion in Nanostructured Substrates: Surface Coverage Dynamics and Analytic Approximations to ALD Saturation Times,* Chemical Vapor Deposition 18, 46 (2012).

[31] A. Yanguas-Gil and J. W. Elam, *Analytic expressions for atomic layer deposition: Coverage, throughput, and materials utilization in cross-flow, particle coating, and spatial atomic layer deposition,* Journal of Vacuum Science & Technology A 32 (2014).

[32] S. Yagi and D. Daizo Kunii, *Studies on combustion of carbon particles in flames and fluidized beds,* Symposium (International) on Combustion 5, 231 (1955).

[33] R. D. Toomey and H. P. Johnstone, *Gaseous fluidization of solid particles,* Chemical Engineering Progress 48, 220 (1952).

[34] S. Sit and J. Grace, *Effect of bubble interaction on interphase mass transfer in gas fluidized beds,* Chemical Engineering Science 36, 327 (1981).

[35] C. R. Wilke and C. Y. Lee, *Estimation of Diffusion Coefficients for Gases and Vapors,* Industrial & Engineering Chemistry 47, 1253 (1955).

[36] W. Yang, *Handbook of Fluidization and Fluid-Particle Systems*, Chemical Industries (Taylor & Francis, 2003).

[37] R. H. Perry and D. W. Green, *Perry's Chemical Engineers' Handbook*, 8th ed. (McGraw-Hill, New York, 2008).

[38] M. Tahmasebpoor, L. de Martín, M. Talebi, N. Mostoufi, and J. R. van Ommen, *The role of the hydrogen bond in dense nanoparticle-gas suspensions,* Phys. Chem. Chem. Phys. 15, 5788 (2013).

[39] L. F. Hakim, J. L. Portman, M. D. Casper, and A. Weimer, *Aggregation behavior of nanoparticles in fluidized beds,* Powder Technology 160, 149 (2005).

[40] R. Aris, *The mathematical theory of diffusion and reaction in permeable catalysts*, Vol. I (Oxford University Press, New York, 1975).

[41] C. N. Satterfield, *Mass transfer in heterogeneous catalysis* (MIT, Cambrige, 1970) p. 43.

[42] R. S. Brodkey and H. C. Hershey, *Transport Phenomena: A Unified Approach* (McGraw-Hill, 1988) p. 183.

[43] N. Wakao and J. M. Smith, *Diffusion and Reaction in Porous Catalysts,* Industrial & Engineering Chemistry Fundamentals 3, 123 (1964).

[44] T. Doğu, *Diffusion and Reaction in Catalyst Pellets with Bidisperse Pore Size Distribution,* Industrial & Engineering Chemistry Research 37, 2158 (1998).

[45] N. Örs and T. Doğu, *Effectiveness of bidisperse catalysts,* AIChE Journal 25, 723 (1979).

[46] M. Juppo, A. Rahtu, M. Ritala, and M. Leskelä, *In Situ Mass Spectrometry Study on Surface Reactions in Atomic Layer Deposition of Al2O3 Thin Films from Trimethylaluminum and Water,* Langmuir 16, 4034 (2000).

[47] S. D. Elliott and J. C. Greer, *Simulating the atomic layer deposition of alumina from first principles,* J. Mater. Chem. 14, 3246 (2004).

[48] R. L. Puurunen, *Correlation between the growth-per-cycle and the surface hydroxyl group concentration in the atomic layer deposition of aluminum oxide from trimethylaluminum and water,* Applied Surface Science 245, 6 (2005).

[49] R. Puurunen, *Growth Per Cycle in Atomic Layer Deposition: Real Application Examplesof a Theoretical Model,* Chemical Vapor Deposition 9, 327 (2003).

[50] R. A. Wind and S. M. George, *Quartz Crystal Microbalance Studies of Al2O3 Atomic Layer Deposition Using Trimethylaluminum and Water at 125 °C,* The Journal of Physical Chemistry A 114, 1281 (2010).

[51] R. Puurunen, *Growth Per Cycle in Atomic Layer Deposition: Real Application Examples of a Theoretical Model,* Chemical Vapor Deposition 9, 327 (2003).

Piramide, Roma 2016.

8

Conclusions and Outlook

And no one showed us to the land
And no one knows the wheres or whys
But something stirs and something tries
And starts to climb towards the light

excerpt from "Echoes"
Roger Waters (Pink Floyd)

The overarching themes of this thesis are: atomic-scale control and scalability. The first theme finds expression in the quest for a fundamental understanding of how atoms spontaneously organize over surfaces. Most of this thesis is in fact dedicated to the question: What are the atomistic processes that lead to the aggregation of adatoms into nanoparticles (NPs) and nanorods during atomic layer deposition (ALD)? Hence the title: "Aggregation Phenomena in Atomic Layer Deposition". Answering such a question has not only an intrinsic fundamental value but also a practical one. This is because the nature of the dominant growth mechanisms can inform strategies for steering the process towards the desired path, that is, the one enabling atomic-scale control. In addition, this thesis is also concerned with reconciling atomic-scale control with the fabrication of nanostructured materials on an industrial scale. A considerable part of the experimental and modeling work of this thesis is in fact dedicated to ALD performed in fluidized bed reactors, which lend themselves to the processing of bulk quantities of powders, and thus to large surface areas. Hence, the subtitle "Bridging Macro and Nano". In sum, this thesis is an attempt to gain an atomic-scale understanding while having in mind the reactor scale.

8.1. Main Contributions

1. This thesis provides fundamental insights into NP formation and growth during ALD. Prior to this work, the understanding of ALD was mostly framed in terms of self-limiting surface reactions leading to a layer-by-layer growth of conformal layers. The formation of NPs during the early stages of certain ALD processes, such as Pt ALD on oxides, was attributed to the poor thermodynamic affinity between the ALD-grown material and the substrate [1–3]. Yet, the nature and the role of the kinetic processes behind the formation and growth of NPs were poorly understood. For the first time, we describe the formation and growth of NPs in terms of

atomistic processes that go beyond ALD surface reactions: surface diffusion, atom attachment/detachment and aggregation, and NP diffusion and coalescence. We do so by means of a mean-field population-balance model. Our model allows us to evaluate the effect of different growth mechanisms on the evolution of the following observables: (i) particle size distribution (PSD), (ii) amount of deposited material, and (iii) number of NPs per unit area (number density). An analysis aimed at assessing the impact of different growth mechanisms on experimental observables allowed us to conclude that:

(a) The particle size distribution is the "signature" of the growth mechanism in that it is the observable that is most affected by it.

(b) A constant number density is not a sufficient condition for ruling out Ostwald ripening and dynamic coalescence as dominant mechanisms.

(c) The cyclic deposition of single atoms in concomitance with the occurrence of Oswald ripening should result in a narrowing (focusing), rather than in a broadening (defocusing), of the PSD.

2. One of the main findings of this thesis is that Smoluchowski aggregation (i.e., dynamic coalescence) is an important mechanism in ALD of NPs. In fact, modeling of our experiments shows that it is the dominant mechanism in the growth of platinum NPs during $MeCpPtMe_3/O_2$ ALD on graphene nanoplatelets. Previously, the growth of Pt nanoparticles was rationalized in terms of single atoms processes such as single atom diffusion and attachment, and Ostwald ripening, or layer-by-layer growth [2, 4–6]. Also, we find that the NPs form and grow mostly during the ligand-removal step. We therefore propose that the local pressure and temperature gradients caused by the combustion of the ligands induce transient adatom and NP mobility.

3. By leveraging our atomic-scale understanding of Pt ALD, we fabricated gram-scale batches of catalysts based on supported Pt NPs with tailored PSDs. Crucially, we show that the deposition temperature affects the extent of Smoluchowski aggregation and thus the broadness of the PSD. Low deposition temperatures ($< 150\ ^\circ C$) limit the mobility of the NPs and thus result in narrow PSDs, whereas high deposition temperatures ($\geq 150\ ^\circ C$) promote the migration of large NPs and thus lead to broad PSDs. Our findings are further corroborated by recent work by Yan et al.[7] who used low deposition temperatures to suppress the aggregation process to such an extent that they could synthesize platinum dimers on graphene after two ALD cycles. By tailoring the PSD at a given Pt loading we find that narrow PSDs result in more active and stable catalysts against propene oxidation. Our proof-of-concept study illustrates how ALD can be used not only to optimize catalysts but also to investigate structure-dependent properties. In fact, the knowledge of the mass-based PSD after the catalytic test allowed us to test a simple geometrical model, which showed that integral properties such as average diameter and dispersion are poor descriptors of the catalytic activity. Our results can find application in the optimization of noble-metal catalysts.

4. A systematic study of the effect of the oxygen exposure (P_{O_2} x time) on the formation of Pt NPs during $MeCpPtMe_3/O_2$ ALD on TiO_2 nanopowders allowed us to shed

light on the discrepancies between the literature on ALD on flat substrates and that on ALD on high-surface-area substrates such as powders. We find that, at a given number of cycles, the Pt loading, and thus the extent of the ligand-removal step, exhibits a sigmoidal (S-shaped) kinetic curve as a function of the oxygen exposure. This is in agreement with the autocatalytic nature of combustion reactions. In particular, the oxygen exposures typically used for ALD on flat substrates result in an incomplete removal of the precursor ligands. This hinders Pt deposition after the first cycle. Furthermore, the Pt deposited after the first cycle remains mostly atomically dispersed. On the other hand, the high oxygen exposures (» 120 mbar s) that are typically used for ALD on powders effectively remove the precursors ligands, thus allowing the deposition of more platinum after the first cycle. As a result, NPs as large as 5-6 nm can form even after only 5 cycles. Crucially, high oxygen exposures suppress metal aggregation and can be thus used to synthesize NPs with narrow PSDs.

5. Another important finding of this thesis is the formation of TiO_2 nanorods during $TiCl_4/H_2O$ ALD on graphene nanoplatelets and the occurrence of oriented attachment of individual TiO_2 crystals. The latter is a variant of Smoluchowski aggregation where individual nanocrystals not only diffuse and collide but also align and fuse across a preferred crystallographic orientation. Interestingly, the lattices of the TiO_2 nanorods and graphene nanoplatelets are found to be in a rotational alignment driven by lattice matching. This strongly suggests that the aggregation process is substrate-mediated. Furthermore, we find that the fraction of nanorods is a non-linear function of the exposure time of both precursors. Such insights further emphasize the importance of non-equilibrium processes in ALD. Clearly, an understanding of such processes informs strategies for controlling not only the size of ALD-grown nanostructures but also their shape. In addition, we believe that understanding how the adlayer-substrate interaction can impart directionality to the aggregation process is instrumental to the rational synthesis of asymmetric supported nanostructures, especially on 2D materials.

6. The scalability and feasibility of ALD perfomed in fluidized bed reactors on nanostructured materials strongly depends on the efficiency with which ALD precursors are used. A conservative analysis based on a multi-scale reaction engineering model shows that precursor utilization efficiencies close to 100% can be obtained even in the presence of mass-transfer limitations. In fact, the precursor utilization is expected to be mostly affected by the kinetics of ALD surface chemistry. Nonetheless, given the typically fast ALD kinetics, we conclude that ALD on high-surface-area powders performed in fluidized bed reactors is in general a forgiving process. However, modeling of the precursor transport clearly shows that performing the process at relatively high pressures (~ 1 bar) can result in an inhomogeneous coating process if the ALD reactions are not run to completion. This is because high-surface-area powders typically present a porous structure through which the precursor has to diffuse before reaching the active sites. As a result, the available surface is not exposed homogeneously to the precursor. Instead, the precursor first saturates the outer surface of the powder porous structure. The saturation front then gradually proceeds toward the center of the porous structure. While an inhomogenous deposition process can be detrimental

to some applications, diffusion-limited ALD can be rationally used to functionalize the outer part of porous catalysts particles, or even to introduce discontinuities in the pore size along the particle radius.

8.2. Opportunities, limitations, and outlook

8.2.1. Sintering mechanisms in ALD: a curse or a blessing?

In this thesis we have shown that in several cases the growth of NPs during ALD is dominated by sintering mechanisms such as dynamic coalescence. At first sight this might appear as a major shortcoming of ALD of NPs, as sintering tends to broaden the PSD. Nonetheless, sintering mechanisms, if properly understood, can be turned into powerful synthetic routes. In fact, Ostwald ripening and dynamic coalescence (provided that the NP mobility is strongly size-dependent) can result in the focusing of the PSD on short time scales. This is because both mechanisms act as size selectors: small NPs shrink, and eventually disappear, at a faster rate than large NPs grow. Inevitably, after a transient focusing, the PSD eventually broadens, thus an optimum has to be found [8]. Hybrid ALD schemes that include a combination of ALD cycles and extra annealing/focusing steps can be beneficial to ALD of NPs in general. An ideal ALD scheme would consist of alternating series of deposition and focusing steps, such that the broadening resulting from the formation of new NPs in every cycle is compensated by a subsequent sintering step where the NP ensemble grows at the expenses of the small NPs. Similar concepts have already been employed in the synthesis of colloidal NPs [9, 10]. This strategy is especially relevant to the deposition of NPs on nanopowders. This is because they typically consist of agglomerates of distinct particles that have a well-defined surface area. If the single atoms and the NPs adsorbed on each particle do not interact with the ones adsorbed on neighboring particles, then an extended sintering step would lead to the formation of a single NP per particle. Therefore, the size of each NP will depend exclusively on the surface, and thus the size of the support particle, the number of cycles, and the number of atoms deposited per cycle on the support. An analogous strategy was also proposed in a recent work by Van Den Berg et al. [11], where the confinement of surface diffusion arising from the plate-like structure of the solid precursor itself was found to affect the size of the NPs forming during the precursor reduction. Yet, exploiting sintering mechanisms poses a fundamental challenge in that one has to find the operating conditions (e.g., temperature, chemical atmosphere, pressure) under which the sintering process steers in the desired direction. Certainly, the extensive body of literature dedicated to NP sintering can inform the field of ALD of NPs, especially with regard to the effect of the temperature and the substrate, and the choice of co-reactants [12–17].

ALD of Bimetallic NPs and Area-Selective ALD

ALD of bimetallic NPs and area-selective ALD could also benefit from a rational exploitation of NP sintering and surface diffusion in general. A great deal of research has in fact been dedicated to the development of complex ALD routes for the deposition of bimetallic NPs [18–22]. Most routes focus on the suppression of the deposition on the support so that one metal can be selectively deposited onto the other (area-selective ALD). Some rely on dedicated surface chemistries that are inherently selective only in one deposition step or on more complex strategies involving surface inhibitors such as self-assembled monolayers. The idea is that, by doing so, all the metal is found in bimetallic NPs. Yet, it is evident from

the shape of the NPs and of their PSDs that at any rate the NPs do undergo sintering during such processes [18]. Therefore, instead of resorting to complex ALD schemes, one could deposit the two metals one after the other and then add an annealing step in which the two metals aggregate in a controlled fashion. Again, strategies involving sintering steps require a deep understanding of how the process conditions can be tuned in order to promote either Ostwald ripening or strongly size-dependent dynamic coalescence.

Single-atom-catalysts

In this thesis, the emphasis is on elucidating the mechanisms and to use this as part of the toolbox for controlling the PSD of supported NPs. Recently, a lot of attention is given to "single-atom-catalysts", catalysts with the maximum degree of dispersion. They are the ideal examples of excellent homogeneous catalysts on a support [22, 23]. A good illustration of the potential of single-atom-catalysts can be found in electrocatalysis, where the catalyst activity is of crucial importance. This is because in many instances, the price of the employed noble metals is disruptive to the scaling up to practical applications [23]. Thus, in this field, single-atom-catalysts could be game-changers. The question arises whether the results of this thesis give clues relevant to the synthesis of single-atom catalysts. Ideally, in the first cycle a perfect distribution of single atoms can be realized, even in the case where several cycles result in supported particles. For example, in ALD of Pt on graphene nanoplatelets the first half cycle, that is, the precursor chemisorption, precursor takes place with virtually no sintering [24]. The second half of the cycle where the carbon ligands are destroyed by oxidation at elevated temperature should be avoided or changed into a subtle conversion method. In general, the diffusion rate is size-dependent (atoms diffuse and aggregate relatively fast, the larger the NP the slower the rate of diffusion). In aiming at single-atom systems, the rate of diffusion should be minimized. This will be the case when the metal-support interaction is very strong. Yan et al. [25] demonstrated for Pd/graphene systems single-atom-catalyst can be synthesized by ALD, provided that the nature of the oxygen functional groups at the graphene surface is carefully tuned. They conclude that isolated phenol groups result in single Pd sites and no apparent NP formation. This conclusion is corroborated by a recent work [7] where it is shown that metal atoms anchored to carboxyl groups exhibit low lateral interactions, and as a consequence NP formation is suppressed. Clearly, the rate of diffusion is a handle in the rational catalyst design by ALD. Following-up on the above discussion on the synthesis of bimetallic NPs, the approach discussed here could be applied for the rational design of another class of bimetallic nanostructured catalysts consisting of well-defined NPs of metal A in a "sea" of single atoms species of metal B.

8.2.2. Population-Balance Growth Model: Opportunities and Limitations

Our analysis and the population-balance model on which it is based present both opportunities and limitations. For example, the model can be used to study the experimental evolution of the PSD of NPs deposited with ALD processes other than Pt ALD. The model can in fact be used to assess the relative importance of different kinetic mechanisms in all those processes leading to the formation of 3D NPs. In particular, given a certain ALD process, the model can interpret the effect of different operating conditions (e.g., temperature, co-reactant, pressure) and different substrates on the dominant mechanism. Furthermore,

population-balance models can provide valuable insights into the effect of different reaction environments on sintering mechanisms. Yet, most of the sintering literature still relies on simple models based on average quantities such as the average diameter and dispersion, which are known to bear little information about the sintering mechanism [14]. We therefore hope that our work will invite other researchers in the NP sintering community to adopt population-balance models. As to the limitations of our analysis, we mention four aspects that were not considered here:

(a) The effect of attractive/repulsive forces between surface species

(b) Local effects introduced by surface heterogeneities

(c) The effect of size-dependent reactivity of the NPs against precursor chemisorption

(d) The simultaneous occurrence of dynamic coalescence and Ostwald ripening

Our analysis is based on the assumption that the aggregation process is purely diffusive, and thus random in nature. However, the aggregation of adsorbates can also be driven and mediated by short- and long-range attractive/repulsive forces [26–30]. For example, adsorbates can deform the lattice of the underlying substrate thereby inducing a strain field that in turn can bring about long-range interactions between adsorbates [27, 28]. Long- and short-range interactions can also arise if the NPs are charged [15, 31]. At any rate, adsorbates in close proximity are bound to experience van der Waals interactions [32]. Moreover, directional inter-particle interactions can result in the self-organization of NPs in asymmetric nanostructures such as nanorods. This has been receiving growing attention not only in the field of crystal growth but also in the ALD community [33–35]. Yet, population-balance models are not suitable for the explicit treatment of inter-particle interactions, which are easier to capture with Kinetic Monte Carlo (KMC) or level-set models [29].

Our model, given its mean-field nature, cannot account for local effects and, in particular, the effect of surface heterogeneities. The latter are relevant to not only the synthesis of catalysts, since most supports have an heterogeneous surface [36], but also area-selective ALD, which inherently involve patterned surfaces [37–39]. Surface heterogeneities can in fact affect surface diffusion, NP stability, and G_s (the number of single atoms deposited on the substrate surface in each cycle).

Here we considered that the amount of material deposited on the NPs (G_p) is independent of the size of the NPs. However, the chemisorption of precursors on the surface of NPs is bound to be size-dependent, especially when the chemisorption involves combustion-like reactions [18, 40]. In particular, we expect that, in the case of ALD of noble metals based on oxidative chemistries, the NPs will grow due to ALD reactions after reaching a critical size. This is because NPs of noble metals such as Pt are active against combustion reactions once they are faceted [41, 42]. This aspect should be considered in follow-up works.

For sake of simplicity, here we considered growth scenarios where either dynamic coalescence and Ostwald ripening are at play. Yet, in general, there is no reason why dynamic coalescence and Ostwald ripening should not take place at the same time. Nonetheless,

the two processes are usually characterized by well separated time scales. At any rate, we expect that the competition between these mechanisms would spawn intermediate regimes where Ostwald ripening works against dynamic coalescence in that it leads to narrower PSDs depending on how the NP mobility scales with NP size and on the likelihood of atom detachment. Certainly, the rich dynamics stemming from the interplay between Ostwald ripening and dynamics coalescence merits further research.

An Epistemological Problem as the Basis for a New Line of Research

The model presented in this thesis is *phenomenological* in that, despite having theoretical grounds and relating experimental properties, is not derived from first principles. As a result, its predictive power is rather limited. It is therefore desirable to develop an understanding that does not rely on "fitting parameters". Here, we propose a line of research aimed at achieving an *a priori* understanding of the growth and assembly of atoms and NPs based on a two-level approach:

1. "Particle level": Molecular dynamics simulations (MD) based on force fields derived from density functional theory (DFT) aimed at understanding how atoms and clusters of atoms A behave on a surface B exposed to a chemical atmosphere C. Such simulations would allow the formulation of "interaction rules", that is, the events that capture the general behavior of atoms and clusters, and the rates associated with them.

2. "Ensemble level": Implementation of the "interaction rules" in a KMC or mean-field model to study the collective behavior of atoms and clusters of atoms over surfaces.

8.2.3. On ALD in Fludized Bed Reactors

The multi-scale reaction engineering model presented here clearly predicts poor homogeneity of the deposition process if ALD is performed on porous powders and the ALD reactions are not run to completion. Furthermore, this model assumes perfect mixing of the powder within the bed. Assessing the homogeneity of the deposition process is certainly crucial to its scale-up. Yet, to the best of our knowledge no experimental study was dedicated to the assessment of the uniformity of the ALD process at both reactor and particle scales. For example, it would be of interest to sample the fluidized bed reactor at different bed heights at different phases of the ALD process. The powders thus sampled can then be characterized by means of elemental analysis (e.g., inductively coupled plasma atomic emission spectroscopy (ICP-AES) and time-of-Flight Secondary Ion Mass Spectrometry (TOF-SIMS)) and transmission electron microscopy. By doing so, one can quantify the degree of inhomogeneity of the deposition process at the reactor scale as well as the particle scale as a function of the operating conditions and the nature of the ALD process at hand. The same study can be carried out using reactors of different scales and assisting methods that provide different degree of mixing within the bed (e.g., vibration, stirring, microjets) [43].

8.2.4. On the Fluidization of nanopowders

Fluidized bed reactors are excellent reactors for performing ALD on NPs [44–46]. The latter are not fluidized individually but in the form of highly porous agglomerates that can be as large as few millimiters [43, 47–52]. The size of such agglomerates exhibits broad PSDs

arising from a dynamic equilibrium between agglomeration and fragmentation [43, 47–50]. The fluidization behaviour and the mass-transfer within such agglomerates clearly depend on their PSD. Population balance models as the one used for describing the formation and growth of NPs during ALD can also be adapted to describe the dynamic agglomeration and fragmentation of NP agglomerates during fluidization. Such models can be used as a tool for understanding how the interparticle forces, superficial gas velocity, and NP properties affect the PSD of the fluidized agglomerates and thus the fluidization behaviour. Furthermore, such models could answer the fundamental question: What are the properties that the nanopowder must have for a dynamic equilibrium between agglomeration and fragmentation to exists?

References

[1] R. L. Puurunen, *Surface chemistry of atomic layer deposition: A case study for the trimethylaluminum/water process,* Journal of Applied Physics 97 (2005).

[2] A. J. Mackus, M. A. Verheijen, N. Leick, A. A. Bol, and W. M. Kessels, *Influence of oxygen exposure on the nucleation of platinum atomic layer deposition: Consequences for film growth, nanopatterning, and nanoparticle synthesis,* Chemistry of Materials 25, 1905 (2013).

[3] H. Van Bui, F. Grillo, and J. R. van Ommen, *Atomic and molecular layer deposition: off the beaten track,* Chem. Commun. 53, 45 (2017).

[4] N. Cheng, Y. Shao, J. Liu, and X. Sun, *Electrocatalysts by atomic layer deposition for fuel cell applications,* Nano Energy 29, 220 (2016), electrocatalysis.

[5] Y. Zhou, C. L. Muhich, B. T. Neltner, A. W. Weimer, and C. B. Musgrave, *Growth of pt particles on the anatase tio2 (101) surface,* The Journal of Physical Chemistry C 116, 12114 (2012).

[6] K. Kim, H. B. R. Lee, R. W. Johnson, J. T. Tanskanen, N. Liu, M. G. Kim, C. Pang, C. Ahn, S. F. Bent, and Z. Bao, *Selective metal deposition at graphene line defects by atomic layer deposition,* Nature Communications 5, 4781 (2014).

[7] H. Yan, Y. Lin, H. Wu, W. Zhang, Z. Sun, H. Cheng, W. Liu, C. Wang, J. Li, X. Huang, T. Yao, J. Yang, S. Wei, and J. Lu, *Bottom-up precise synthesis of stable platinum dimers on graphene,* Nature Communications 8 (2017).

[8] D. V. Talapin, A. L. Rogach, M. Haase, and H. Weller, *Evolution of an ensemble of nanoparticles in a colloidal solution: Theoretical study,* Journal of Physical Chemistry B 105, 12278 (2001).

[9] P. Dagtepe and V. Chikan, *Quantized Ostwald ripening of colloidal nanoparticles,* Journal of Physical Chemistry C 114, 16263 (2010).

[10] N. J. J. Johnson, A. Korinek, C. Dong, and F. C. J. M. Van Veggel, *Self-focusing by Ostwald ripening: A strategy for layer-by-layer epitaxial growth on upconverting nanocrystals,* Journal of the American Chemical Society 134, 11068 (2012).

[11] R. Van Den Berg, C. F. Elkjaer, C. J. Gommes, I. Chorkendorff, J. Sehested, P. E. De Jongh, K. P. De Jong, and S. Helveg, *Revealing the Formation of Copper Nanoparticles from a Homogeneous Solid Precursor by Electron Microscopy,* Journal of the American Chemical Society 138, 3433 (2016).

[12] E. D. Goodman, J. A. Schwalbe, and M. Cargnello, *Mechanistic understanding and the rational design of sinter- resistant heterogeneous catalysts,* ACS Catalysis 7, 7156 (2017).

[13] F. Behafarid and B. R. Cuenya, *Coarsening phenomena of metal nanoparticles and the influence of the support pre-treatment: Pt/TiO2(110),* Surface Science 606, 908 (2012).

[14] E. E. Finney and R. G. Finke, *Catalyst Sintering Kinetics Data: Is There a Minimal Chemical Mechanism Underlying Kinetics Previously Fit by Empirical Power-Law Expressions - And if So, What Are Its Implications?* Industrial and Engineering Chemistry Research 56, 10271 (2017).

[15] I. V. Yentekakis, G. Goula, P. Panagiotopoulou, S. Kampouri, M. J. Taylor, G. Kyriakou, and R. M. Lambert, *Stabilization of catalyst particles against sintering on oxide supports with high oxygen ion lability exemplified by Ir-catalyzed decomposition of N2O,* Applied Catalysis B: Environmental 192, 357 (2016).

[16] L. Luo, M. H. Engelhard, Y. Shao, and C. Wang, *Revealing the Dynamics of Platinum Nanoparticle Catalysts on Carbon in Oxygen and Water Using Environmental TEM,* ACS Catalysis 7, 7658 (2017).

[17] T. W. Hansen, A. T. Delariva, S. R. Challa, and A. K. Datye, *Sintering of catalytic nanoparticles: Particle migration or ostwald ripening?* Accounts of Chemical Research 46, 1720 (2013).

[18] A. J. M. Mackus, M. J. Weber, N. F. W. Thissen, D. Garcia-Alonso, R. H. J. Vervuurt, S. Assali, A. A. Bol, M. A. Verheijen, and W. M. M. Kessels, *Atomic layer deposition of Pd and Pt nanoparticles for catalysis: on the mechanisms of nanoparticle formation,* Nanotechnology 27, 034001 (2016).

[19] S. T. Christensen, H. Feng, J. L. Libera, N. Guo, J. T. Miller, P. C. Stair, and J. W. Elam, *Supported Ru-Pt bimetallic nanoparticle catalysts prepared by atomic layer deposition,* Nano Letters 10, 3047 (2010).

[20] J. Lu, K.-B. Low, Y. Lei, J. A. Libera, A. Nicholls, P. C. Stair, and J. W. Elam, *Toward atomically-precise synthesis of supported bimetallic nanoparticles using atomic layer deposition,* Nature Communications 5, 3264 (2014).

[21] Y. Lei, B. Liu, J. Lu, R. J. Lobo-Lapidus, T. Wu, H. Feng, X. Xia, A. U. Mane, J. A. Libera, J. P. Greeley, J. T. Miller, and J. W. Elam, *Synthesis of Pt-Pd core-shell nanostructures by atomic layer deposition: Application in propane oxidative dehydrogenation to propylene,* Chemistry of Materials 24, 3525 (2012).

[22] K. Cao, Q. Zhu, B. Shan, and R. Chen, *Controlled Synthesis of Pd/Pt Core Shell Nanoparticles Using Area-selective Atomic Layer Deposition,* Scientific Reports 5, 8470 (2015).

[23] C. Zhu, S. Fu, Q. Shi, D. Du, and Y. Lin, *Single-Atom Electrocatalysts,* (2017).

[24] F. Grillo, H. Van Bui, J. A. Moulijn, M. T. Kreutzer, and J. R. Van Ommen, *Understanding and Controlling the Aggregative Growth of Platinum Nanoparticles in Atomic Layer Deposition: An Avenue to Size Selection,* Journal of Physical Chemistry Letters 8, 975 (2017).

[25] H. Yan, H. Cheng, H. Yi, Y. Lin, T. Yao, C. Wang, J. Li, S. Wei, and J. Lu, *Single-Atom Pd_1/Graphene Catalyst Achieved by Atomic Layer Deposition: Remarkable Performance in Selective Hydrogenation of 1,3-Butadiene,* Journal of the American Chemical Society 137, 10484 (2015).

[26] D. S. Sholl and R. T. Skodje, *Late-stage coarsening of adlayers by dynamic cluster coalescence,* Physica A: Statistical Mechanics and its Applications 231, 631 (1996).

[27] X. L. Li, C. X. Wang, and G. W. Yang, *Thermodynamic theory of growth of nanostructures,* Progress in Materials Science 64, 121 (2014).

[28] P. Xu, L. Dong, M. Neek-Amal, M. L. Ackerman, J. Yu, S. D. Barber, J. K. Schoelz, D. Qi, F. Xu, P. M. Thibado, and F. M. Peeters, *Self-organized platinum nanoparticles on freestanding graphene,* ACS Nano 8, 2697 (2014).

[29] C. Ratsch and J. A. Venables, *Nucleation theory and the early stages of thin film growth,* Journal of Vacuum Science & Technology A: Vacuum, Surfaces, and Films 21, S96 (2003).

[30] W. C. Yang, M. Zeman, H. Ade, and R. J. Nemanich, *Attractive Migration and Coalescence: A Significant Process in the Coarsening of Islands on the Si(111) Surface,* Physical Review Letters 90, 4 (2003).

[31] I. V. Yentekakis, G. Goula, S. Kampouri, I. Betsi-Argyropoulou, P. Panagiotopoulou, M. J. Taylor, G. Kyriakou, and R. M. Lambert, *Ir-Catalysed Nitrous oxide (N2O) Decomposition: Effect of Ir Particle Size and Metal–Support Interactions,* (2017).

[32] J. Hermann, R. A. DiStasio, and A. Tkatchenko, *First-Principles Models for van der Waals Interactions in Molecules and Materials: Concepts, Theory, and Applications,* (2017).

[33] J. J. De Yoreo, P. U. Gilbert, N. A. Sommerdijk, R. L. Penn, S. Whitelam, D. Joester, H. Zhang, J. D. Rimer, A. Navrotsky, J. F. Banfield, A. F. Wallace, F. M. Michel, F. C. Meldrum, H. Cölfen, and P. M. Dove, *Crystallization by particle attachment in synthetic, biogenic, and geologic environments,* Science 349 (2015).

[34] J. Shi, Z. Li, A. Kvit, S. Krylyuk, A. V. Davydov, and X. Wang, *Electron microscopy observation of TiO2 nanocrystal evolution in high-temperature atomic layer deposition,* Nano Letters 13, 5727 (2013).

[35] K. Wen and W. He, *Can oriented-attachment be an efficient growth mechanism for the synthesis of 1D nanocrystals via atomic layer deposition?* Nanotechnology 26, 382001 (2015).

[36] V. P. Zhdanov, *Two-dimensional Ostwald ripening on a patterned support and in a mixed overlayer,* Surface Science 644, 191 (2016).

[37] A. Mameli, M. J. Merkx, B. Karasulu, F. Roozeboom, W. E. M. Kessels, and A. J. Mackus, *Area-Selective Atomic Layer Deposition of SiO2 Using Acetylacetone as a Chemoselective Inhibitor in an ABC-Type Cycle,* ACS Nano 11, 9303 (2017).

[38] F. S. Minaye Hashemi, C. Prasittichai, and S. F. Bent, *Self-Correcting Process for High Quality Patterning by Atomic Layer Deposition,* ACS Nano 9, 8710 (2015).

[39] H. B. R. Lee and S. F. Bent, *Nanopatterning by Area-Selective Atomic Layer Deposition,* in *Atomic Layer Deposition of Nanostructured Materials* (2012) pp. 193–225.

[40] A. J. M. Mackus, N. Leick, L. Baker, and W. M. M. Kessels, *Catalytic combustion and dehydrogenation reactions during atomic layer deposition of platinum,* Chemistry of Materials 24, 1752 (2012).

[41] L. M. Carballo and E. E. Wolf, *Crystallite size effects during the catalytic oxidation of propylene on Pt/Al2O3,* Journal of Catalysis 53, 366 (1978).

[42] H. Van Bui, F. Grillo, S. S. Kulkarni, R. Bevaart, N. Van Thang, B. van der Linden, J. A. Moulijn, M. Makkee, M. T. Kreutzer, and J. R. van Ommen, *Low-temperature atomic layer deposition delivers more active and stable Pt-based catalysts,* Nanoscale (2017).

[43] J. R. van Ommen, J. M. Valverde, and R. Pfeffer, *Fluidization of nanopowders: a review,* (2012).

[44] D. Longrie, D. Deduytsche, and C. Detavernier, *Reactor concepts for atomic layer deposition on agitated particles: A review,* Journal of Vacuum Science & Technology A: Vacuum, Surfaces, and Films 32, 010802 (2014).

[45] D. M. King, X. Liang, and A. W. Weimer, *Functionalization of fine particles using atomic and molecular layer deposition,* (2012).

[46] A. Goulas and J. R. van Ommen, *Scalable production of nanostructured particles using atomic layer deposition,* KONA Powder and Particle Journal 31, 234 (2014).

[47] H. Liu, L. Zhang, T. Chen, S. Wang, Z. Han, and S. Wu, *Experimental study on the fluidization behaviors of the superfine particles,* Chemical Engineering Journal 262, 579 (2015).

[48] X. Zhu, Q. Zhang, Y. Wang, and F. Wei, *Review on the nanoparticle fluidization science and technology,* Chinese Journal of Chemical Engineering 24, 9 (2016).

[49] L. F. Hakim, J. L. Portman, M. D. Casper, and A. W. Weimer, *Aggregation behavior of nanoparticles in fluidized beds,* Powder Technology 160, 149 (2005).

[50] L. De Martín, W. G. Bouwman, and J. R. Van Ommen, *Multidimensional nature of fluidized nanoparticle agglomerates,* Langmuir 30, 12696 (2014).

[51] J. R. Van Ommen, C. U. Yurteri, N. Ellis, and E. M. Kelder, *Scalable gas-phase processes to create nanostructured particles,* Particuology 8, 572 (2010).

[52] L. F. Hakim, J. H. Blackson, and A. W. Weimer, *Modification of interparticle forces for nanoparticles using atomic layer deposition,* Chemical Engineering Science 62, 6199 (2007).

Porto, Portugal 2017.

Final Elucubration and Acknowledgements

We are what we remember
The brain creates fake memories
Everything is relation

Some say that our perception of time is dictated by the rate at which our brain is fed with new information. The more your brain processes "unfamiliar" experiences the more time seems to slow down. When I think of this, I cannot help but recall the lysergic lyrics of the song "white rabbit" from the Jefferson Airplane:

"..When logic and proportion have fallen sloppy dead
And the white knight is talking backwards
And the red queen's off with her head
Remember what the dormouse said
Feed your head, feed your head.."

I have heard many of my peers reciting the old adage "four years are nothing, time flies". I could not disagree more. Four years of PhD fed my head with such a multitude of unfamiliar experiences that I feel as though an entire lifetime stands in between my current and my past self. Such is the distance that trying to project my past self upon the screen of consciousness is no more than a flight of fantasy. The continuity between the life before and after the PhD is a but a mere assumption. Whether a broken continuity makes for better or worse I still cannot tell. What I know with a certain degree of certainty is that every gain comes at a cost.

It always struck me how for some people the world is "no bigger than a couple of blocks". They are born, they live, and they die within a radius of just a few kilometers. As a kid my world was no different. As far as I can recall, my universe fitted in one room and a yard enclosed between two rows of houses, a gate, and a patch of wasteland. A rather small world. Yet, back then, it amounted to about all that ever was, and it was enough. Four years of PhD have certainly expanded my universe. I visited more countries that my parents, and my extended family combined, for that matter, have ever and probably will ever visit in their lifetime. I wonder, though, whether I now know any of those places, where have been and lived, better than I used to know my yard. I remember spending endless hours fathoming every single square centimeter of that yard. I knew it so well that it was alive to me. It was alive because from day to day I could discern the slightest changes in its appearance, I could resolve, in other words, its "motion". A type of motion that is invisible to the eye of the occasional visitor. The PhD consolidated in me the notion that the human condition is inextricably bound to a great degree of superficiality. We live most of our lives barely scratching the surface of things. At times it seems to me that adulthood is the festival of superficiality. Nonetheless, far be it from me to say that childhood is the state of mind that

brings one closer to the truth, that would be delusional. For one thing, whenever I "go back to my roots" I feel as though I understand them better. As if my yard acquires more meaning and depth the more I can put it in relation with the places that are most distant from it. I like to think of childhood and adulthood in dialectical terms, that is, as thesis and antithesis. Neither childhood nor adulthood contains the truth, yet a careful synthesis of the two can certainly bring one closer to it. If childhood is home to what is most familiar and adulthood is the Odyssey of the common man, then I find that the dialectical tension of above is best summarized by two of my favorite quotes:

Places where I am all the time I know too much and not enough
and to be lucid about is the most difficult
Henri Cartier-Bresson

We shall not cease from exploration
And the end of all our exploring
Will be to arrive where we started
And know the place for the first time
T.S. Eliot

I wrote about places, it is time to write about people. This journey started thanks to my supervisor and later promotor Ruud. You believed in me despite my not so excellent communication skills. Had it not been for your support, the superficiality of men would have put me on a very different path. I shall not forget that. We had our disagreements and a couple of accidents. That I cannot deny. Yet, I do understand that a PhD at TU Delft without a pinch of drama is not worth the title. From you I certainly learned the value of diplomacy. You have a great heart, thank you Ruud!
A crucial figure in my PhD was certainly that of my copromotor Michiel. I am really grateful for all the time you dedicated to me despite all your commitments. I do not know of many heads of department who manage to actually contribute to the research of PhD students. Thanks you for your striving for excellence. I learned a great deal of scientific writing with you. Thanks for finding the time to meet me even outside of the office when I needed help. Thank you also for all the Christmas dinners!
Jacob, despite being neither a supervisor nor a promotor you had a major impact on my research. Your enthusiasm for my work was an incredible drive for me. In several occasions your vast knowledge made you the perfect deus-ex-machina mentor. Thank you for all the support!
Hao, I will never forget all those nights spent in the office working back-to-back. We achieved a great deal together. At times our work relationship would be of the love-hate type, nonetheless we had a great time and we learned a lot from each other. I think we both learned that ambition is indeed key to success, but if it is not followed by competence, then it is only a recipe for disaster. Thank you Hao, me and Damiano really missed you when you left the office.
Damiano, you deserve a special mention. I can safely say that if it was not for your presence I might have dropped the PhD along the way. Your support was invaluable. We are very different people but somehow we found our sinergy. You were a great friend and a great collaborator. Neither our friendship nor our collaboration will end with my PhD. Grazie zi'.

I would like to thank all those people that keep the show running behind the scenes. I thank our secretaries Astrid and Elly for their prompt help in the moments of need. Thanks Elly for that time in which you unconsciously contributed to an experiment. I was looking for cotton wool to improvise a powder filter and you instead suggested to use earplugs. They worked like a charm. Thanks! I would like to thank our technicians, and in particular, Mojgan. Thank you for your help, especially at the very beginning.

I thank my collaborators and instructors. Thank you Patricia for introducing me to TEM, you were very kind to me, I won't forget that! You even helped me to prepare my first form for claiming expenses. Thank you Bart for helping me with XPS, I really appreciate your patience. Thank you Alexey and thank you Tom from the University of Twente. Tom, if all the technicians were like you, academia would be a better place. Thank you Michiel Makkee! I really appreciate your legendary critical attitude. I can see a bit of myself in your destructive criticism. Thank you Job and Annelies for seeing potential in my work, I hope to keep collaborating with you in the future.

I thank all my students: Sara, Mate, Ryan, Damiano, Paul, Karthik, Vikram and Esteban. I learned a lot from you and from the process of mentoring you. Thank you Karthik for all the effort you put in your work, I am really proud of what you achieved. Thank you Esteban for all the passion you put in the project I proposed to you. It was not easy but in the end all the effort bore fruit. Also thank you for being so thankful.

I will always cherish the memory of the time I spent with the people of the "early" PPE: Aris, Andrea, David, Yogesh, Durghesh, Dayinta, Wenjie, Floris, Hrushikesh, and later Samir. Looking back to those times really feels like evoking memories from a previous life. It seems that life put us on different tracks, but back then it was great. Thank you all! How can I forget: the intoxicating dinners at David's, the improbable food, the philosophical discussions with Yogesh on the nature of reality and the relation between Indian theology and modern science, the unreasonably hot cuisine of Durgesh, the summer schools, the Christmas dinner, the Luxembourg/Belgium/Germany trip culminating with a return trip with a broken window and Samir's Bazooka, and the unbearable lightness of Andrea. Our toxic relationship was brief but intense, it definitely left a mark for better or worse. Had it not been for you I would have probably never got to know, among other things, Mexico, thank you Andrea!

Aris, you were one of the first persons with whom I started hanging out when I moved to the Netherlands. It is safe to say that that first connection with you shaped my entire social network during my PhD. In one way or the other most of the people I met in the Netherlands I met them through you. For that alone I owe you a lot, although I must admit that there is not much merit in it. What I am really thankful for is having found somebody with whom I can connect in terms of outlook on life and past experiences. Thank you also for inviting me to your village, it was a cathartic experience.

I also thank the "later" PPE: Dominik, Shaurya, Maulik, Aswin, Karthik, Serhii, Melvin, Jing, Yujie, and Fatemeh. For one reason or another I didn't get to spend as much time with you as I did with the "early" PPE. This has mostly to do with the increasingly demanding nature of the second half of the PhD and the limited number of hours in a day. I am sure that in a parallel universe in which I spent more time with you I had a great time! Melvin, you deserve a special mention because you saved my life but translating the summary of my thesis in no time, I will be forever grateful for that!

Outside the office I had quite a colorful life, with many people contributing to my color palette. It is hard to mention all the names, but I will try my best. The life of the international student is inevitably punctuated by cyclic farewells and the emergence of new friendships. At the very beginning I had a great time with the "early" Italian crew: Marko, Silvia, Giulia, Claudia, Pasquale, Daniele, Giorgio, Gabriele, and Enrico. Thank you Marko for coming to my defense, your presence is quite significant because you'll always hold against me the fact that while I was writing my master's thesis I repeatedly told you that I would never ever pursue a PhD. Thank you all for the homemade pasta sessions and the "pranzo della domenica". Gabriele deserves a special mention as he was my roommate for almost 4 years. Somehow we managed to live together without much drama, thank you! When most of the "early" Italian crew underwent a diaspora the Turkish, the Greek, and the "late" Italian crew took over. Thank you Cansin, Tilbe, Burak, Musti, Onursal, Burak, Emre, Argun, Ezgi you made my day everyday our path crossed. Thank you for all the noise, the joy, the food, the Turkish touch of spice, the Menemen, the boat trips in Kas. Thank you Faidra, Giannis, Aris, Stefanos, Maria, Giulia, Elly, Martino, Alessandro 1, Alessandro 2, and Francesco. Thank you for Budapest, Amorgos, the beers at the "usual" place, the Mediterranean dinners, and the hopeless philosophical discussions. Thank you for populating some of the best moments I had during the past four years.

Giulia, I was very happy when I first got to know you, although when I first met you I didn't really like you. You tend to do that to people, don't you? I was happy because I had found somebody who has a sensibility for complexity, somebody I could talk to in my mother tongue using my own language. I was happy also because underneath that thick skin of layered misfortunes and bitterness there is a great heart. I wish you that somewhere in the near future you'll be able to shed that thick skin so that you won't scare off people at first sight. Thank you also for bringing along your lovely twin Elly. I am thankful for having met you both. Thank you also for introducing me to Alessandro C., a great Roman. If he could resist the charm of consumerism, he would be perfect.

Thank you Moreno! Somehow you defy the above classifications. We did not manage to spend much time together, but I did appreciate your advice and our brave excursions to the international film festival of Rotterdam. I wish you all the best with Anja!

Grazie Paolo, the understanding between us is quite rare and I really cherish it. I am glad we stay in touch despite the distance. Thank you for all the support, the walks in Camden Town, Scotland, the "cultural" excursions in Italy, and for sharing your passion for photography with me.

Grazie Ilario. Ci conosciamo ormai da più di venti anni. Anche se ci sentiamo e vediamo di rado, il tempo tra noi è come se non passasse mai. Per me sei quel che Dino Giuffrè è per Titta di Girolamo in "Le conseguenze dell'amore". E ora che vivo in Svizzera, questo parallelismo è più significativo che mai.

Grazie Sante. La tua esistenza mi ricorda sempre che il grado di istruzione misurato dal numero di titoli di studio non ha alcun significato. Sei una delle persone più intelligenti che conosca, mi sento fortunato d'averti conosciuto. Parlare con te è sinonimo di casa.

Grazie Andrea, per me sei in qualche modo un pilastro di quel che chiamo casa.

Grazie Ginevra per essere venuta fino in Olanda per esserci. Lo apprezzo molto.

Grazie mamma e papà. Sebbene non abbiate la più pallida idea di quel che faccio nella vita, so che siete comunque contenti di quel che faccio, e questo mi basta per esser contento

anch'io.
Vana, at the end of all my exploring I finally found somebody that I do not wish to change. That to me means everything. Thank you.

De Proeffabriek, Delft, The Netherlands 2016.

Curriculum Vitæ

Fabio Grillo

05-05-1989 Born in Anzio, Italy.

Education

02/2014–02/2018	PhD in Chemical Engineering Delft University of Technology, The Netherlands
11/2011–01/2014	Msc in Chemical Engineering, 110/110 *cum laude* University of Rome: La Sapienza, Italy Guest researcher (5 months) Delft University of Technology, The Netherlands Erasmus exchange student (6 months) KTH: Royal Institute of Technology, Sweden
10/2008–07/2011	Bsc in Chemical Engineering, 110/110 *cum laude* University of Rome: La Sapienza, Italy

Awards and Scholarships

2017	Paper selected for the Spotlights section of The Journal of Physical Chemistry Letters
2017	Travel award granted by Elsevier for the 5th Nano Today conference
2016	3rd prize for the best student talk at the 16th International Conference on Atomic Layer Deposition, Dublin
2013	6-months scholarship awarded by the University of Rome: La Sapienza for writing the master's thesis abroad
2011	Cash award granted by the foundation: "Fondazione Ingegnere Davide Caligiore Onlus" for the quality of the academic achievements attained during the bachelor studies
2011	6-months scholarship granted by the Erasmus program for an exchange period at KTH: Royal Institute of Technology
2010	1-year student-collaboration scholarship awarded to outstanding students for working at the main library "Boaga" of the Faculty of Engineering of the University of Rome: La Sapienza

List of Publications

8. F. Grillo, D. La Zara, P. Mulder, M. T. Kreutzer, and J. R. van Ommen, *Self-Organized Growth of TiO_2 Anatase Nanorods on Graphene Nanoplatelets by Atomic Layer Deposition*, Submitted.

7. J. Soethoudt, F. Grillo, E. A. Marques, R. van Ommen, Y. Tomczak, L. Nyns, S. Van Elshocht, A. Delabie, *Ruthenium Atomic Layer Deposition on Dielectrics: Insights into sur-face dependence and diffusion-mediated growth mechanisms*, Submitted

6. F. Grillo, H. Van Bui, D. La Zara, A. A. I. Aarnink, A. Y. Kovalgin, P Kooyman, M. T. Kreutzer, and J. R. van Ommen, *From Single atoms to Nanoparticles: Autocatalysis and Metal Aggregation in Atomic Layer Deposition of Pt on TiO_2 Nanopowder*, Small (2018, accepted for publication.

5. F. Grillo, J. A. Moulijn, M. T. Kreutzer, J. R. van Ommen, *Nanoparticle Sintering in Atomic Layer Deposition of Supported Catalysts: Kinetic Modeling of the Size Distribution*, Catalysis Today, (2018).

4. H. Van Bui*, F. Grillo*, S. S. Kulkarni, R. Bevaart, N. Van Thang, B. van der Linden, J. A. Moulijn, M. Makkee, M. T. Kreutzer and J. R. van Ommen, *Low-Temperature Atomic Layer Deposition Delivers More Active and Stable Pt-Based Catalysts*, Nanoscale 9, (2017). [*equal contribution]

3. F. Grillo, H. Van Bui, J. A. Moulijn, M. T. Kreutzer, and J. R. van Ommen, *Understanding and Controlling the Aggregative Growth of Platinum Nanoparticles in Atomic Layer Deposition: An Avenue to Size Selection*, Journal Physical Chemistry Letters 5, 8 (2017).

2. H. Van Bui, F. Grillo, and J. R. van Ommen, *Atomic Layer and Molecular Deposition: Off the Beaten Track*, Chemical Communications 53, (2017).

1. F. Grillo, M. T. Kreutzer, J. R. van Ommen, *Modeling the Precursor Utilization in Atomic Layer Deposition on Nanostructured Materials in Fluidized Bed Reactors*, Chemical Engineering Journal 268, (2015).

In preparation

(i) F. Grillo, K. Chidambaram, L. De Martin, A. Fabre, and J. R. van Ommen, *Universal Scaling of the Size Distribution of Fluidized Nanoparticle Agglomerates from Dynamic Agglomeration and Fragmentation*.

(ii) D. La Zara, F. Grillo, J. R. van Ommen, *Fluidization of Graphene Nanoplatelets: From Microstructure to Hydrodynamics*.